Measurement and Understanding of Emissions over London and Southern England by Airborne Eddy-Covariance

Adam Robert Vaughan

PhD

University of York

Chemistry

March, 2017

Dedication

I dedicate this thesis to my family. Thank you for all your support throughout my PhD.

Abstract

High anthropogenic emissions are a global problem with clear links existing between poor air quality and premature mortality, which is of great alarm to organisations such as the World Health Organisation (WHO). In Europe, high emissions of nitrogen oxides (NO_x) are a concern with concentrations plateauing over the last 15 years. Emission assessment is a key part of the UK's air quality strategy; this is done so by using tools such as the National Atmospheric Emissions Inventory (NAEI), to report annual emissions to the EU to meet strict air quality regulations. Due to the high importance placed on inventories such as the NAEI, their accuracy is vital.

This thesis details the development and implementation of an airborne eddy−covariance (AEC) strategy to measure anthropogenic fluxes over highly polluted areas, and compare these findings to UK emission inventories. The Ozone Precursor Fluxes in an Urban Environment (OPFUE) campaign was run over two consecutive years, aiming at evaluating emissions from London and Southern England. NO_x emissions were evaluated over London showing high emissions coming from central areas. Comparison to the NAEI found NO_x emissions were being underestimation by up to a factor of 2. Refinement using the NAEI + road transport estimates scaled via road side measurements showed good improvement, suggesting the need to refine road transport estimates used in the NAEI.

A variety of VOC emissions were also measured over London and Southern England. Measured VOCs over London showed good agreement to the NAEI, and highlighted the successful reduction of VOC emissions through air quality strategies. Measured biogenic emissions of isoprene were found to be higher than air quality model estimates, which could have implications towards regional air quality due to ground level ozone formation. Overall, the described methodology allows for real-time assessment of emission inventories which is key if the UK is to see improvements in its air quality.

List of Contents

Abstract **3**

List of contents **5**

List of figures **9**

List of tables **21**

Acknowledgements **23**

Declaration **25**

1 Introduction **27**

1.1 Motivation 28

1.2 The Atmosphere 29

1.3 Health Effects of Poor Air Quality 31

1.3.1 Health Effects of NO_2, O_3 and $PM_{2.5}$ 33

1.4 UK Air Quality Strategy 36

1.4.1 National Atmospheric Emissions Inventory 36

1.5 Sources of Nitrogen Oxides 39

1.5.1 NO_x Trends in London 42

1.5.2 Vehicle Emissions of NO_x 43

1.5.3 Vehicle Types and Emission Control Strategies 45

1.5.4 Vehicle Emission Rigging 49

1.6 NO_x Chemistry 51

1.7 Summary 59

1.8 Thesis Outline 60

2 Methodology for Airborne Measurement of Nitrogen Oxides 61

2.1 Introduction . . . 62

2.2 NO_x Chemiluminescence . . . 64

2.3 Fast−AQD−NO_x system . . . 66

2.3.1 Flow Diagram . . . 67

2.3.2 Control Unit . . . 68

2.3.3 Photolytic Converter . . . 69

2.3.4 Detector Unit . . . 71

2.3.5 Ozoniser Unit . . . 73

2.3.6 Pump Unit . . . 74

2.4 Research Flight Operation . . . 75

2.5 Calibration Strategy . . . 78

2.6 O_3 Water Vapour Addition . . . 81

2.7 Error Analysis . . . 82

2.8 Conclusions . . . 86

3 Methodology for Airborne Flux Calculation and Surface Layer Interaction 87

3.1 Introduction . . . 88

3.2 Airborne Eddy-Covariance . . . 91

3.2.1 Introduction to Wavelets . . . 91

3.2.2 Eddy-Covariance Continuous Wavelet Transform . . . 93

3.3 Eddy-Covariance Algorithm . . . 95

3.3.1 Data Section and Resampling . . . 95

3.3.2 De−Trending and Lag−Time Correction . . . 97

3.3.3 CWT Parameterisation . . . 98

3.3.4 Frequency Analysis . . . 100

3.3.5 Cone of Influence . . . 102

3.3.6 Flux Errors . . . 103

3.4 Footprint Model . . . 106

3.5 Aircraft Footprint Model . . . 109

3.6 Footprint Calculation . . . 112

3.6.1 Model Parameterisation . . . 113

3.7 Footprint Parameter Analysis . . . 114

3.7.1 Aerodynamic Roughness Length . . . 114
3.7.2 Friction Velocity . . . 117
3.7.3 Planetary Boundary Layer . . . 119
3.7.4 Measurement Height . . . 121
3.7.5 Standard Deviation of Horizontal and Vertical wind . . . 123
3.8 Conclusions . . . 125

4 Airborne Eddy-Covariance Measurements of NO_x Fluxes over London during 2013 and 2014 127
4.1 Introduction . . . 128
4.2 Overview . . . 131
4.2.1 Research Flights . . . 132
4.3 Experimental . . . 134
4.3.1 Eddy-Covariance Fluxes . . . 134
4.3.2 Flux Calculation . . . 135
4.3.3 Footprint model . . . 137
4.4 Results and Discussion . . . 139
4.4.1 Spatially Resolved Flux Observations . . . 139
4.4.2 Comparison to the National Atmospheric Emissions Inventory . . . 142
4.4.3 Measurement Uncertaines . . . 147
4.4.4 The London Atmospheric Emissions Inventory . . . 149
4.4.5 Breakdown of London's Road Transport Emissions . . . 155
4.5 Conclusions . . . 159

5 Airborne Eddy-Covariance Measurements of VOC Fluxes over London and Southern England during 2013 and 2014 161
5.1 Introduction . . . 162
5.2 Methodology . . . 164
5.2.1 Flight Strategy . . . 164
5.2.2 Flight Meteorology . . . 166
5.2.3 Scientific Payload . . . 167
5.2.3.1 Scientific Payload . . . 167
5.2.3.2 Volatile Organic Compound Measurements . . . 167
5.2.3.3 PTR−MS Calibration . . . 169

5.2.4 Disjunct Eddy-Covariance . . . 170
5.2.5 Isoprene Loss Correction . . . 173
5.2.6 Footprint Calculation . . . 175
5.2.7 NAEI Comparison . . . 177
5.2.8 EMEP Comparison . . . 178
5.3 Results and Discussion . . . 179
5.3.1 Anthropogenic VOC fluxes over London . . . 179
5.3.2 NAEI Comparison . . . 183
5.3.2.1 Eddy-Covariance Flux Errors . . . 186
5.3.3 Biogenic VOC Fluxes . . . 187
5.3.4 EMEP model comparison . . . 191
5.4 Conclusions . . . 193

6 Conclusions and Future work 195
6.1 Conclusions . . . 196
6.2 Uncertainties in Airborne Flux Measurements . . . 199
6.3 Future work . . . 200

Appendix A Footprint Weighting Matrices 201

Appendix B Continuous Wavelet Transform Cross−Spectrums 215

Appendix C Continuous Wavelet Transform Co and Cumulative Co-Spectra 225

Abbreviations 229

References 232

List of Figures

1.1 News articles focusing on air pollution in the UK and Beijing from various media sources [1, 2, 3, 4]. 28
1.2 Structure of the atmosphere in relation to pressure, temperature and altitude. Taken from Seinfeld & Pandis. (2006) [6]. 29
1.3 Infographic of key pollutants, main transportation types and key governmental legislation as a function of time. Adapted from RCP. (2016) [8]. . . 32
1.4 Infographic of PM scales against fine beach sand and human hair. Taken from EPA. (2017) [25]. 34
1.5 Annual emission estimates for NO_x at 1 km^2 resolution for the entire of the UK region. Taken from NAEI UK emissions interactive map [31]. 37
1.6 NAEI emission source types being summed up to generate total annual emission grids for the UK. Taken from DEFRA. (2016) [32]. 38
1.7 Global NO_2 column from SCIAMACHY instrument on−board the European Environment Satellite, as an average from 2002 to 2012. Take from Schneider et al. (2015) [39]. 40
1.8 European average NO_x trends from 1990. Left axis shows emissions decreasing from 100% starting from 1990. The right axis shows NO_x emissions in kilotones per year. Taken from EEA. (2010) [40]. 41
1.9 European percentage averages for NO_x emissions from 8 key contributing sources. Taken from EEA. (2010) [40]. 41
1.10 NO_x (left) and NO_2 (right) trends in London from road side measurements. Taken from Carslaw et al. (2016) [43]. 42
1.11 Annual 2013 surface NO_2 concentrations for greater London at 20 m^2 resolution. Taken from ERG. (2016) [44]. 43

1.12 a) average European NO_x emissions from vehicles, b) emissions of NO_2 from 10 European countries, c) percentage proportion of NO_x emitted as NO_2. Taken from Carslaw et al. (2011) [45]. 44
1.13 Generated concentrations of NO, CO and HCs for a range of fuel to air ratios. Taken from Chigier. (2013) [46]. 46
1.14 Three−way catalytic conversion efficiency in terms of NO_x, CO and HCs. Taken from Farrauto & Heck. (1999) [47]. 46
1.15 Euro class diesel vehicle emissions of NO_2, and the introduction of specific emission control systems. Taken from Carslaw et al. (2016) [43]. 47
1.16 News articles on the VW diesel vehicle emissions scandal. Taken from The Guardian and BBC News [54, 55]. 49
1.17 Simplistic NO_x reaction schemes, left) oxidative reaction between NO, NO_2 and O_3 in the presence of sunlight. Right) reaction scheme between NO and NO_2 and other oxidative species. Taken from Atkinson. (2000) [58]. . 52
1.18 Basic VOC reaction scheme with OH, resulting in the formation of O_3 as a by−product. Taken from MCMv3.3.1 website [59]. 53
1.19 Nocturnal radical reaction chemistry of NO_x. Taken from Brown & Stutz. (2012) [60]. 54
1.20 Formation of PAN from oxidation of non-methane VOCs. Taken from Phillips et al. (2013) [69]. 58

2.1 Diagram of NO_x measurement techniques using; passive, active or remote-sensing approaches. Taken from the World Meteorological Organization Global Atmospheric Watch's (WMO/GAW) report on making long-term NO_x measurements [71]. 62
2.2 a) front view of Fast−AQD−NO_x system mounted in a flight rack for operation on NERC Dornier−228 aircraft, b) rear view of system showing sample lines and ozone humidification. 66
2.3 Flow diagram of the Fast−AQD−NO_x instrument containing: gas cylinders, flow−controllers (FC), mass−flow controllers (MFC), blue−light photolytic converter (blue−light PLC), pressure−controller (PC), zero−volume (ZV), reaction−vessel (RV), corona discharge units (CD), by−pass and scroll pumps. 67

2.4 Control unit containing: a pressure control, mass−flow controllers, blue−light PLC, calibration system, control systems and LabJack unit. 68
2.5 Quantum yield of photolysis products in relation to three PLC systems at different wavelengths. Taken from Pollack et al. (2010) [92]. 69
2.6 Photolytic converter cooled using Peltier coolers. Irradiation chamber shown as dotted purple area. 70
2.7 Detector Unit containing: dual photomultiplier tube (PMT) system with Peltier cooling, two high voltage supplier for the PMTs, reaction vessels and zero-volumes. 71
2.8 Front facing photomultiplier tube showing signal amplification as electrons move toward the anode from each dynode. Adapter from Borlinghaus. (2015) [95]. 72
2.9 Ozoniser unit containing: two coronal discharge units, high voltage power supply, pressure gauges for each O_3 supply, two way valves and electronic switches. 73
2.10 Aircraft pump tray containing high performance scroll pump with ozone scrubber, by−pass pump and gas cylinder mounts. 74
2.11 Background count rates of both channels decreasing as the PMT temperature drops due to dry ice cooling. 75
2.12 Stabilisation of the NO calibration signal, flowing through both channels for 30 minutes. 5 sccm of NO/N_2 added to a 'zero air' flow of 1500 sccm. . 76
2.13 Schematic of a Fast−AQD−NO_x research flight. Red areas represent pre and post−flight when the instrument was calibrated. Blue areas show high altitude transits. Green areas show low altitude measurement periods. . . 77
2.14 Calibration structure for Channel 1 and 2 containing two stages. The first assesses the conversion efficiency by blue−light PLC. The second calculates the nominal sensitivities of each PMT. 79
2.15 NO and NO_2 'zero air' data from a two hour period. Average NO of 25.13 ppt and NO_2 of -12.67 ppt, suggesting the NO_2 is below the instruments limit of detection. 83
2.16 Top) Frequency distributions for 1 Hz NO and NO_2 [ppt] 'zero air' data over a two hour period. Bottom) Frequency distributions for 9 Hz NO and NO_2 [pptv] 'zero air' data over the same period. 83

3.1 Atmospheric transport eddies moving across a vegetated region, varying in size and direction of rotation. Taken from Burba. (2013) [108]. 89
3.2 Representation of emission and deposition via eddy−movement. Eddy 1 shows the movement of concentration 1 (C_1) downwards, and eddy 2 the movement of concentration 2 (C_2) upwards. Taken from Burba. (2013) [108]. 89
3.3 Wavelet waveforms in the time domain. a) Morlet wavelet, b) Paul wavelet, c) DOG wavelet m=2, d) DOG wavelet m=6. m represents the wavelet function parameter. The solid line shows the real part of the wavelet and the dotted the imaginary. Adapted from Torrence & Compo. (1998) [127]. 92
3.4 Top) roll degree of the aircraft (green), ground altitude/100 (black) at 360 m and NO_2 concentration in mg m^3. The selected region for AEC is shown in the box. Middle) vertical wind speed in m s^{-1}. Bottom) flight track with selected region highlighted in red. 96
3.5 Normalised correlation coefficient between vertical wind speed and instantaneous concentration, showing no lag between the two variables and maximum correlation at time 0. 97
3.6 a) Variance of C_2 alkyl−benzenes and vertical wind speed, b) time resolved wavelet power spectrum with cone of influence shown as black dotted line, c) the average cross−variance between C_2 alkyl−benzenes and vertical wind. 99
3.7 a) co−spectra of C_2 alkyl-benzenes and temperature flux using CWT and FFT methods, b) cumulative co−spectra for C_2 alkyl−benzenes and temperature flux using CWT and FFT methods. Black line represents Nyquist frequency and dotted lines being the contributing frequency boundaries. . 100
3.8 Wavelet cross−spectrum for 0−32, 0−64 and 0−128 s frequency period bandwidths. Average flux contributions along total flight track for each frequency period bandwidths. 101
3.9 a & b) Calculated random and systematic errors for two PBL heights as a function of flux averaging scales, c) systematic error at two PBL heights as a function of flux averaging scales, d) random error at two PBL heights as a function of flux averaging scales. 104
3.10 Random and systematic errors as a function of Z_M/Z_i for a range of flux averaging scales (1, 5, 12 and 50 km). 104

3.11 Total flux error accounting for random and systematic errors as a function of averaging scales, at two PLB heights and a fixed flight altitude (360 m). 105
3.12 Footprint influence area in x and y directions from point of measurement, grey shaded area showing region of highest source influence. Taken from Schmid. (1994) [134]. 106
3.13 Footprint based on a backwards Lagrangian simulation using particle release ideology. Taken from Flesch. (1996) [143]. 107
3.14 Dependence of fitting parameters a, b, c, d on aerodynamic surface roughness length at different atmospheric conditions. Z_0 range from 0.007 to 2.72 m. Taken from Kljun et al. (2004) [151]. 111
3.15 Footprint weighting matrix of 1 km^2 cell size, equal to a unity value of 1. Position of flux measurement at the centre of the grid (Northing 0, Easting 0). 112
3.16 Aerodynamic roughness lengths for greater London, accounting for easterly and westerly wind directions [154]. 115
3.17 Effect of aerodynamic roughness length on alongwind footprint influence up to 100% influence. 116
3.18 Effect of friction velocity on alongwind footprint influence up to 100% influence. 118
3.19 Effect of PBL height (500, 1,000, 1,500 and 2,000 m) on alongwind footprint influence up to 100% influence. 120
3.20 Effect of measurement height on alongwind distance footprint influence up to 100% influence. 121
3.21 Effect of σ_v on horizontal and perpendicular wind direction footprint influence. Increasing σ_v acts to stretch the footprint along the y−axis (Northing plane). 123
3.22 Effect of σ_w on alongwind footprint influence up to 100% influence. 124

4.1 left) Trends in the mean concentration of NO_x across 35 roadside sites in Greater London with at least 10 years of data capture, right) projected change in urban road transport emissions split by main vehicle type from the NAEI using 2002 as a base year. 128
4.2 left) NERC Dornier 228 aircraft in−flight, right) schematic of aircraft. Taken from NERC Airborne Research and Survey Facility's Website [169]. 131

4.3 OPFUE 2013 flight transects over the Greater London region, right) OPFUE 2014 flight transects over the Greater London region. 132

4.4 (a) Variation of NO_2 concentration from the mean and variance of vertical wind speed from the mean, (b) time resolved wavelet cross-spectrum, (c) the average cross−covariance between NO_2 concentration and vertical wind, for a typical NE to SW run across London. 136

4.5 The contributing footprint area to a typical flight track, dependent on the prevailing wind direction and altitude of flight. The footprint is overlaid onto the NAEI at 1 km^2 grid resolution, coloured to annual NO_x tonnage emission estimates. 138

4.6 500 m fluxes calculated from all 2013 flight transects using inverse distance weighting (IDW) in ArcGIS. a) average instantaneous NO flux at 500 m resolution, b) average instantaneous NO_2 flux at 500 m resolution, c) average instantaneous NO_x flux at 500 m resolution. 140

4.7 500 m fluxes calculated from all 2014 flight transects using inverse distance weighting (IDW) in ArcGIS. a) average instantaneous NO flux at 500 m resolution, b) average instantaneous NO_2 flux at 500 m resolution, c) average instantaneous NO_x flux at 500 m resolution. 141

4.8 Average for Flights 5, 7 and 12 (2013), measured NO_x flux plotted in blue with standard error shown as the shaded blue area. Calculated NAEI estimates using the described footprint methodology for NO_x are plotted in red, with standard error shown as the shaded red area. NAEI estimates have been scaled to account for month, day and hour temporality. 143

4.9 Calculated emission source contributions from the NAEI plotted on the first y axis, with sources being broken down into road transport; other transport (such as rail), domestic and commercial combustion, industrial combustion and other sources. Also plotted on the second y axis as white squares is the ratio of measured to NAEI estimated NO_x flux, with the error bars denoting the standard error of all points included. The flight is broken into 4 zones, with 1 and 2 being SW outer London, 3 central London and 4 NE outer London. 144

4.10 Average measured NO_x flux (blue) and time−of−day scaled NAEI estimates (red) for 2013 and 2014 flights against latitude with standard error shown as shaded area. 146
4.11 Average for Flights 5, 7 and 12 (2013), measured NO_x flux plotted in blue with standard error shown as the shaded blue area. Calculated and scaled 'enhanced' NAEI estimates of NO_x emission are plotted in red, with standard error shown as the shaded red area. 150
4.12 Calculated emission source contributions from the 'enhanced' NAEI (see text for details) plotted on the first y axis, with sources being broken down into road transport; other transport (such as rail), domestic combustion, industrial combustion, other sources and non−road mobile machinery (NRMM). Also plotted on the second y axis as white squares is the ratio of measured to enhanced NAEI estimated NO_x flux, with the error bars denoting the standard error of all points included. The flight is broken into 4 zones, with 1 and 2 being SW outer London, 3 central London and 4 NE outer London. 152
4.13 Average measured NO_x flux (blue) and time−of−day scaled enhanced NAEI estimates (red) against latitude with shaded area as standard error, for 2013 and 2014 flights. 154
4.14 RSD percentage contribution of each vehicle type to road transport emissions at 1 km^2 resolution for the whole of greater London. 155
4.15 'enhanced' NAEI road transport emission contribution for each vehicle type across London. 157
4.16 Percentage contribution of each 'enhanced' NAEI emission source sector, with specific breakdown of road transport into individual vehicle types. . . 158

5.1 a) Research flight (RF) transects over London during July 2013, and b) July 2014. c) RF biogenic transects over South Sussex region during July 2013, d) July 2014. 165
5.2 a) instantaneous changes of vertical wind and C_2 alkyl-benzenes concentration from their respective means, b) global cross−spectrum of eddy contributions integrated over all frequency periods along flight track, c) average cross variance along flight track. 171

5.3 Top left) co-spectra of temperature and C_2 alkyl-benzenes flux across all frequencies using CWT and FFT methods. Top right) measured CWT flux in blue and FFT flux in red against day of year time (DOY). Bottom left) cumulative co-spectra of temperature and C_2 alkyl-benzenes flux across all frequencies using CWT and FFT methods. Bottom right) flight path over London coloured by measured C_2 alkyl-benzenes flux. 172

5.4 Left) isoprene oxidation pathways showing intermediates and the formation of MACR and MVK. Right) Molar yield of isoprene oxidation products as a function of NO mixing ratio. Adapted from Jenkin et al. (2015) [202]. . 174

5.5 Correction of isoprene flux due to chemical loss via OH oxidation. 174

5.6 Example footprint for 2014 RF transect over London showing the 30, 60, 90% footprint influence areas from flight track (white), overlaid onto 1 km^2 NAEI total NMHC emission estimates. 176

5.7 Left) EMEP4UK isoprene emission estimates at 5 km^2 resolution for entire of the UK. Right) South Sussex region EMEP4UK Isoprene emission estimates showing a maximum of 2.1 mg m^{-2} h^{-1}. 178

5.8 Measured instantaneous anthropogenic fluxes of a) benzene (2013), b) toluene (2013), c) C_2 alkyl-benzenes (2014), d) toluene (2014) and e) C_3 alkyl-benzenes (2014), interpolated at 500 m using inverse distance weighting from all RF transects.. 182

5.9 Latitude averaged (1 km) MTBE* (grey) and toluene flux (blue) with standard deviation (shaded area). 183

5.10 Latitude averages (1 km) for: a) benzene flux (2013), b) C_2 alkyl−benzenes flux (2014), c) toluene flux (2013) and d) toluene flux (2014) shown in blue, with footprint NAEI estimates in red. Shaded areas being calculated standard deviation of all RF transects. 185

5.11 RF flight track during 2013 flight over South Sussex region. Left) Calculated footprint extent 30, 60, 90% from flight track, overlaid onto EMEP4UK isoprene emission grid. Right) footprint extent 30, 60, 90% from flight track, overlaid onto UK National Land Class Inventory 2012 at 25 m^2 resolution. 187

5.12 Measured biogenic instantaneous fluxes of a) isoprene (2013), b) isoprene (2014), c) monoterpenes (2013) and d) monoterpenes (2014), interpolated at 500 m using inverse distance weighting from all RF transects. 189

5.13 Mean isoprene emissions from 3 OPFUE (July 2013) identical flight transects conducted on 3 consecutive days (7/7/13−9/7/13), each flight consisting of 1.5 hours of data and ∼40 km repeated flight legs. Mean isoprene emission in the dense broadleaved woodland area displayed a dependence on photo−synthetically active radiation (PAR) (black) and ground temperature (grey). Ground PAR and temperature data is from the Goodwood AURN site. 190

5.14 Latitude averaged (1 km) of measured isoprene flux (blue) and EMEP4UK isoprene emission (red) with shaded standard deviation for 2013 and 2014. 192

A.1 Footprint weighting matrix for set Z_i of 500 and 750 m. All other footprint parameters set constant. 202

A.2 Footprint weighting matrix for set Z_i of 1,000 and 1,250 m. All other footprint parameters set constant. 202

A.3 Footprint weighting matrix for set Z_i of 1,500 and 1,750 m. All other footprint parameters set constant. 203

A.4 Footprint weighting matrix for set Z_i of 2,000 m. All other footprint parameters set constant. 203

A.5 Footprint weighting matrix for set σ_v of 0.2 and 0.4 m s^{-1}. All other footprint parameters set constant. 204

A.6 Footprint weighting matrix for set σ_v of 0.6 and 0.8 m s^{-1}. All other footprint parameters set constant. 204

A.7 Footprint weighting matrix for set σ_v of 1.0 and 1.2 m s^{-1}. All other footprint parameters set constant. 205

A.8 Footprint weighting matrix for set σ_w of 0.2 and 0.4 m s^{-1}. All other footprint parameters set constant. 206

A.9 Footprint weighting matrix for set σ_w of 0.6 and 0.8 m s^{-1}. All other footprint parameters set constant. 206

A.10 Footprint weighting matrix for set σ_w of 1.0 m s^{-1}. All other footprint parameters set constant. 207

A.11 Footprint weighting matrix at set u_* of 0.2 and 0.4 m s^{-1}. All other footprint parameters set constant. 208

A.12 Footprint weighting matrix at set u_* of 0.6 and 0.8 m s^{-1}. All other footprint parameters set constant. 208

A.13 Footprint weighting matrix at set u_* of 1.0 and 1.2 m s^{-1}. All other footprint parameters set constant. 209
A.14 Footprint weighting matrix at set Z_0 of 0.1 and 0.2 m. All other footprint parameters set constant. 210
A.15 Footprint weighting matrix at set Z_0 of 0.4 and 0.8 m. All other footprint parameters set constant. 210
A.16 Footprint weighting matrix at set Z_0 of 1.6 and 3.2 m. All other footprint parameters set constant. 211
A.17 Footprint weighting matrix at set Z_0 of 6.4 m. All other footprint parameters set constant. 211
A.18 Footprint weighting matrix at set Z_M of 100 and 150 m. All other footprint parameters set constant. 212
A.19 Footprint weighting matrix at set Z_M of 200 and 250 m. All other footprint parameters set constant. 212
A.20 Footprint weighting matrix at set Z_M of 300 and 350 m. All other footprint parameters set constant. 213
A.21 Footprint weighting matrix at set Z_M of 400 and 450 m. All other footprint parameters set constant. 213

B.1 (a) Variation of NO_2 concentration from the mean and variance of vertical wind speed from the mean, (b) time resolved wavelet cross spectrum, (c) the average cross−covariance between NO_2 concentration and vertical wind, for a typical NE to SW run across London. 216
B.2 (a) Variation of benzene concentration from the mean and variance of vertical wind speed from the mean, (b) time resolved wavelet cross spectrum, (c) the average cross−covariance between benzene concentration and vertical wind, for a typical NE to SW run across London. 217
B.3 (a) Variation of toluene concentration from the mean and variance of vertical wind speed from the mean, (b) time resolved wavelet cross spectrum, (c) the average cross−covariance between toluene concentration mixing ratio and vertical wind, for a typical NE to SW run across London. 218

B.4 (a) Variation of C_2 alkyl−benzenes concentration from the mean and variance of vertical wind speed from the mean, (b) time resolved wavelet cross spectrum, (c) the average cross−covariance between C_2 alkyl−benzenes concentration and vertical wind, for a typical NE to SW run across London. 219

B.5 (a) Variation of C_3 alkyl−benzenes concentration from the mean and variance of vertical wind speed from the mean, (b) time resolved wavelet cross spectrum, (c) the average cross−covariance between C_3 alkyl−benzenes concentration and vertical wind, for a typical NE to SW run across London. 220

B.6 (a) Variation of isoprene concentration from the mean and variance of vertical wind speed from the mean, (b) time resolved wavelet cross spectrum, (c) the average cross−covariance between isoprene concentration and vertical wind, for a typical run across Southern England. 221

B.7 (a) Variation of MVK/MACR concentration from the mean and variance of vertical wind speed from the mean, (b) time resolved wavelet cross spectrum, (c) the average cross−covariance between MVK/MACR concentration and vertical wind, for a typical run across Southern England. 222

B.8 (a) Variation of monoterpenes concentration from the mean and variance of vertical wind speed from the mean, (b) time resolved wavelet cross spectrum, (c) the average cross−covariance between monoterpenes concentration and vertical wind, for a typical run across Southern England. 223

C.1 left) co−spectra of NO_2 and temperature flux using CWT and FFT methods. Right) cumulative co−spectra for NO_2 and temperature flux using CWT and FFT methods. 226

C.2 left) co−spectra of benzene and temperature flux using CWT and FFT methods. Right) cumulative co−spectra for benzene and temperature flux using CWT and FFT methods. 226

C.3 left) co−spectra of toluene and temperature flux using CWT and FFT methods. Right) cumulative co−spectra for toluene and temperature flux using CWT and FFT methods. 226

C.4 left) co−spectra of C_2 alkyl-benzenes and temperature flux using CWT and FFT methods. Right) cumulative co−spectra for C_2 alkyl-benzenes and temperature flux using CWT and FFT methods. 227

C.5 left) co−spectra of C_3 alkyl-benzenes and temperature flux using CWT and FFT methods. Right) cumulative co−spectra for C_3 alkyl-benzenes and temperature flux using CWT and FFT methods. 227

C.6 left) co−spectra of isoprene and temperature flux using CWT and FFT methods. Right) cumulative co−spectra for isoprene and temperature flux using CWT and FFT methods. 227

C.7 left) co−spectra of MVK/MACR and temperature flux using CWT and FFT methods. Right) cumulative co−spectra for MVK/MACR and temperature flux using CWT and FFT methods. 228

C.8 left) co−spectra of monoterpenes and temperature flux using CWT and FFT methods. Right) cumulative co−spectra for monoterpenes and temperature flux using CWT and FFT methods. 228

List of Tables

2.1 Errors associated with 1 Hz measurements of NO. 85
2.2 Errors associated with 1 Hz measurements of NO_2. 85
2.3 Errors associated with 9 Hz measurements of NO. 85
2.4 Errors associated with 9 Hz measurements of NO_2. 85

3.1 Matlab^{TM} CWT analysis parameters 98
3.2 Aerodynamic roughness length statistics of maximum flux influence distance and percentage, 80 and 100% footprint influence distance. 116
3.3 Friction velocity statistics of maximum flux influence distance and percentage, 80 and 100% footprint influence distance. 118
3.4 Measurement height statistics of maximum flux influence distance and percentage, 80% and 100% footprint influence distance. 122

4.1 Upper) Average measured NO_x flux and time−of−day NAEI estimate during 2013 and 2014 flights with subsequent breakdown into four regions of London. Lower) Average ratio of measured flux to NAEI estimate with breakdown of four regions of London 146
4.2 Upper) Average measured NO_x flux and time−of−day enhanced NAEI estimate during 2013 and 2014 flights with subsequent breakdown into four regions of London. Lower) Average ratio of measured flux to enhanced NAEI estimate with breakdown of four regions of London 154

5.1 Top) Meteorological conditions during all biogenic RF's over Southern Sussex (July 2013 & 2014). Bottom) Meteorological conditions during anthropogenic RF's over greater London (July 2013 & 2014). 166

5.2 Averaged flux and footprint estimates during 2013 and 2014 for each London zone. Suburban London latitudes (51.30−51.35^o), Southwest Greater London latitudes (51.35−51.42^o), Central London latitudes (51.42−51.56^o), Northeast Greater London latitudes (51.56−51.60^o). 185

5.3 Average flux/NAEI ratio for each London zone. Suburban London latitudes (51.30−51.35^o), Southwest Greater London latitudes (51.35−51.42^o), Central London latitudes (51.42−51.56^o), Northeast Greater London latitudes (51.56−51.60^o). 185

5.4 Calculated flux errors for each VOC compound for systematic, random and disjunct error as an average for each flight transect (50 km resolved fluxes). 186

5.5 Measured biogenic flux statistics during both campaigns for isoprene, total monoterpenes and MVK/MACR. 190

5.6 Statistics for measured flux and footprint model generated EMEP4UK emission estimates of isoprene during both field campaigns. 192

Acknowledgements

Firstly, I would like to thank NERC for funding my PhD.

Secondly, I would like to thank Prof. James Lee and Prof. Lucy Carpenter for all their support and guidance over the last 4 years. It has been a great privilege to have had them as scientific supervisors and I will be forever grateful to them for giving me the opportunity to do this PhD and all the research it has involved.

A massive thanks must also go to Dr. Stephane Bauguitte at FAAM for all his help, support and training on using the NO_x chemiluminescence instrument over the last 4 years.

I would also like to thank the entire Atmospheric Chemistry group at York for their support during my research. They are a brilliant and inspiring group to work with.

A special thanks must also go to my girlfriend, Lauren, who has put up with me throughout my PhD, even when I was stressed and grumpy.

Finally, a massive thanks must go to my Mum and Dad. You have always supported me with my ambitions and encouraged me to do my best. You are both such an inspiration and I'm so grateful for all the help you've given me along the way.

Declaration

The research described in this thesis is original work, which I undertook whilst at the University of York from 2013 to 2017. Unless when stated, all the work in this thesis represents the original contribution of the author. Some parts of this thesis have been published in journals whereupon I was the author. Publications are listed at the beginning of the Chapter to which they relate. The work presented here has not been submitted in full or part for any other degree.

Chapter 1

Introduction

1.1 Motivation

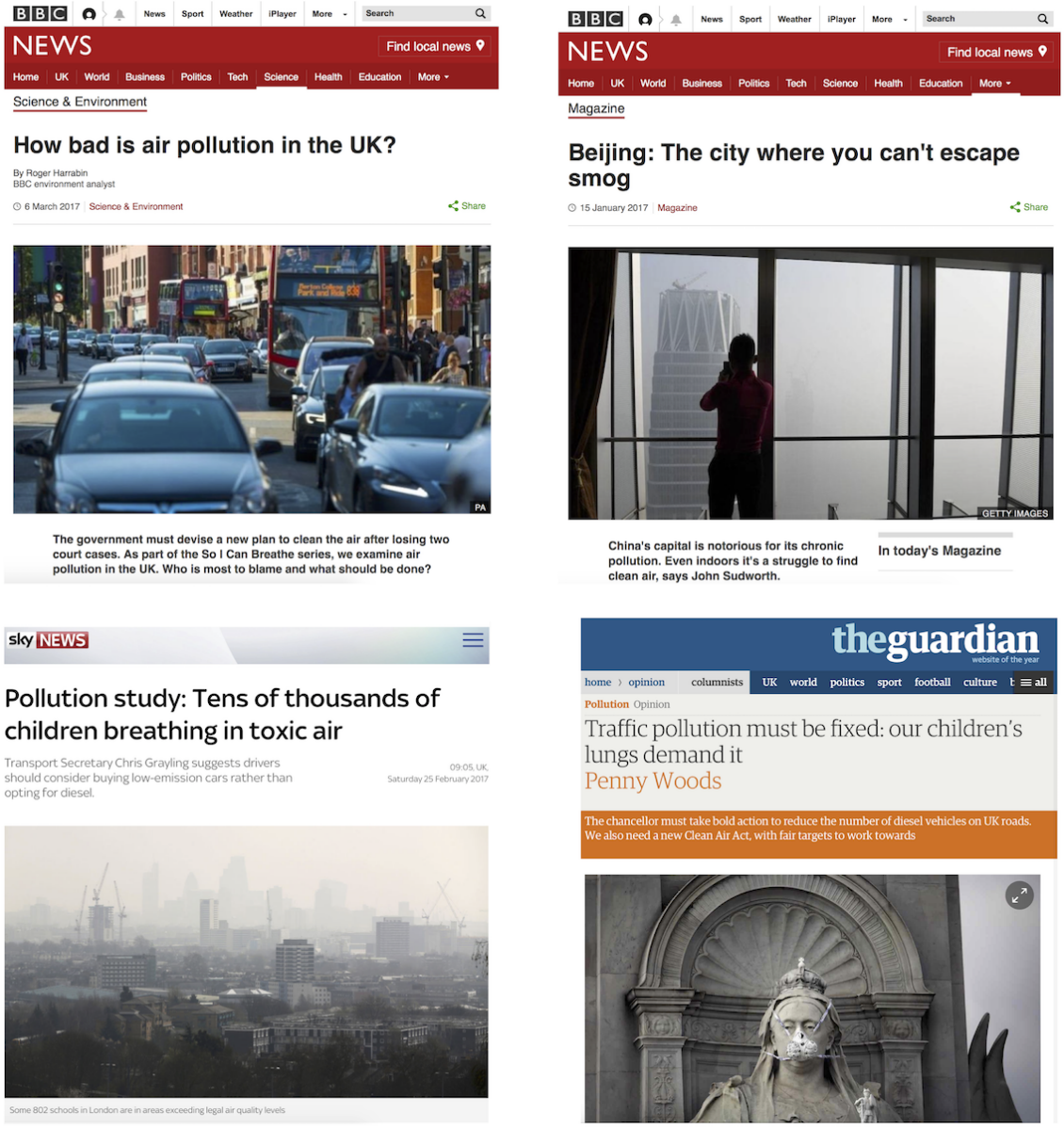

Figure 1.1: News articles focusing on air pollution in the UK and Beijing from various media sources [1, 2, 3, 4].

Air pollution is a global problem, with the World Health Organisation (WHO) considering it one of the top risks to global health. It is now estimated that 1.7 million children per year die as a direct consequence of environmental pollution, of which approximately 600,000 can be attributed to poor air quality and other sources such as second-hand smoke [5]. Greater public awareness of air pollution has been driven by frequent news publications, by sources such as the BBC and major British newspapers. Figure 1.1 shows a few examples of media publications on air quality, focussing mainly on the UK and Beijing [1, 2, 3, 4].

Reducing the pollution emitted into the atmosphere is vital if global mortalities rates are to continue falling in the future. The task of doing so is highly complex with individual regions having different pollution problems and potential solutions.

1.2 The Atmosphere

Humans inhabit the troposphere which is the lowest layer in the atmosphere. The troposphere contains around 80% of the atmosphere's mass and is where most of the earth's weather systems takes place. Figure 1.2, shows a diagrammatic representation of the atmospheres layers in relation to altitude, temperature and pressure.

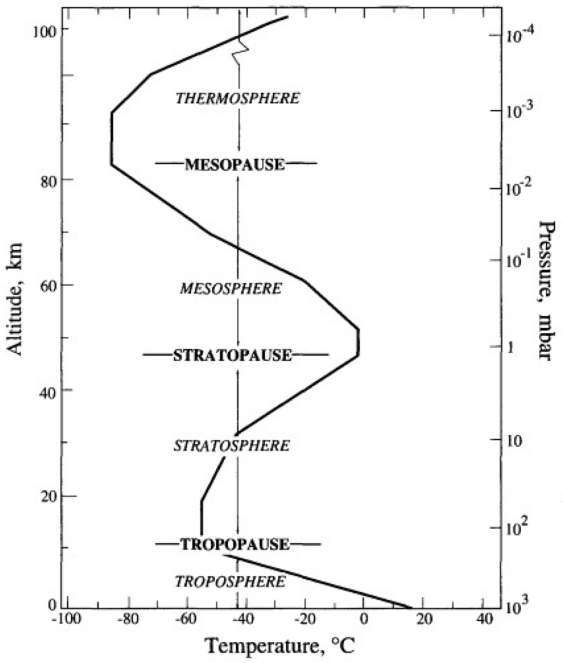

Figure 1.2: Structure of the atmosphere in relation to pressure, temperature and altitude. Taken from Seinfeld & Pandis. (2006) [6].

Humans are having a direct impact on the earth's atmosphere. High anthropogenic emissions into the troposphere from the Industrial Revolution onwards, are changing the earth's atmosphere at a rate not previously observed for millions of years. One such change is the rapidly increasing CO_2 concentrations from anthropogenic sources. This increase is driving global rises in surface temperatures which is a major concern in relation to the earth's climate. The earth's atmosphere consists of mainly nitrogen (78%), oxygen (20%) and Argon (1%) [6]. The remaining composition is made up of traces gases such as CO_2, NO, NO_2, VOCs and other molecules. Trace gases have both natural and anthropogenic

sources; however, man-made sources are influencing air quality at a far faster rate. This effect is both changing the dynamics of the atmosphere and also the quality of the air within the troposphere.

1.3 Health Effects of Poor Air Quality

The effect of poor air quality on human health has always been an important issue and one which is at the forefront of medical research today. Not all regions worldwide have seen improvements in air quality. China has observed major decreases in its air quality over the last 20 to 30 years, due mainly by population growth and changes in energy production and industrial modernisation. From the late 1970s into the 21^{st} Century, oil usage and road vehicle numbers in Beijing has increased exponentially. Tang et al. correlating the usage of such fuels and increasing vehicle use with heightened levels of cardiovascular disease [7]. Liu et al. estimates that on a national scale for China the mortality rates from $PM_{2.5}$ has increased from 800,000 in 2004 to over 1.2 million in 2012. Such statistics further strengthen the need for areas such as these to dramatically change their approach to air pollution and thus improve their populations life expectation.

A report by the Royal College of Physicians (RCP) and Royal College of Paediatrics and Child Health (RCPCH) in 2016, examined the impact air pollution has on human health over a life time [8]. The report estimated current death rates attributed to poor outdoor air quality is approximately 40,000 a year for the UK. This figure only accounts for outdoor exposure deaths in relation to fine particles such as $PM_{2.5}$ and Nitrogen Dioxide (NO_2). Higher mortality rates can be expected when other pollutant types such as Ozone (O_3) and indoor environments are also accounted for.

The detrimental effect air pollution has on a major city such as London is a long-standing problem. The London smog event of 1952 claimed an estimated 12,000 lives and helped usher in the Clean Air Act (CAA) aimed at reducing London air pollution for the next three decades [9]. The UK's air quality has changed a lot over the last 100 years alone, with stricter legislation bringing with it improvements. The CAA of 1956 helped reduce the smog problems of the 1950s with stricter legislation focused towards cleaner burning fuels, such as 'smokeless fuels' and heating using electricity and gas. The act also setup smoke control areas and removal of power generation within London to further reduce emissions of soot and Sulphur Dioxide (SO_2) [10].

From the 1960s to 1980s air quality improvements were starting to become apparent but other challenges were being discovered. Lead was a key additive in petrol fuel in the UK and around the world. Added as tetraethyl lead, it helped to increase the octane rating of the fuel. The main problem with its use in petrol was the high levels of lead metal being emitted from vehicle exhausts after combustion, resulting in elevated exposure levels

around main roads and filling stations. Lead once inside the body has toxic effects and can build up within bone density and pass into the brain. Extensive research was conducted around the dangers of lead as a petrol additive, with findings showing dangerous amounts of lead being up taken into the human body resulting in its complete removal from petrol by the late 1990s [11, 12, 13]. Lead has now been replaced by other fuel additives such as methyl tert−butyl ether (MTBE) and ethanol.

Into the 2000s particulates and NO_2 emissions have increased greatly due mainly to increased use of diesel fuel over petrol. Diesel fuel releases lower CO_2 emissions than petrol due to higher temperature fuel combustion in a diesel engine. The downside of which is Oxides of Nitrogen (NO_x) and fine particles ($PM_{2.5}$) are released at much higher rates than from petrol engines. Figure 1.3 depicts key dates of legislation aimed at reducing pollution and the main pollution types as a timeline [8].

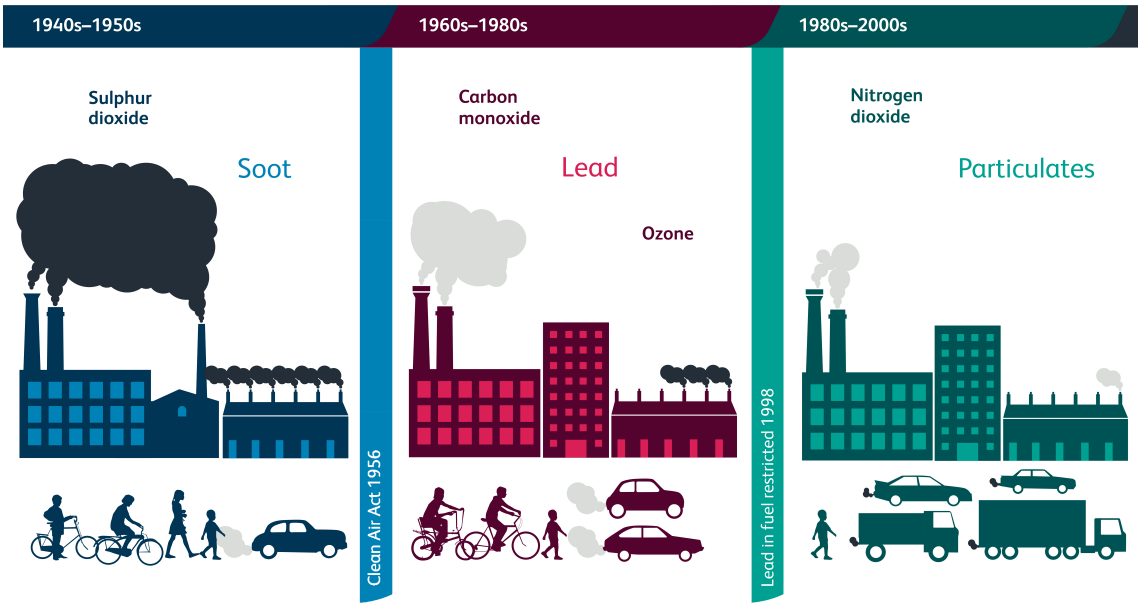

Figure 1.3: Infographic of key pollutants, main transportation types and key governmental legislation as a function of time. Adapted from RCP. (2016) [8].

1.3.1 Health Effects of NO_2, O_3 and $PM_{2.5}$

NO_2 as a pollutant has become a growing problem for the 21^{st} Century. Use of diesel fuel has become more common place due to it's high efficiency and lower CO_2 emissions than petrol. The high temperatures in diesel combustion engines produce NO_2 from oxygen and nitrogen in the air. NO_2 can actively promote the formation of other pollutants which is discussed in Section 1.6.

The effect NO_2 has on human health has gained attention from scientists and medical professionals over the last 20 years. NO_2 has been observed to effect two areas of the human body in particular. NO_2 enters the body through inhalation into the lungs and has been found to directly affect normal lung function. Studies have shown that NO_2 can lead to several repertory issues ranging from inflammation, bronchial reactivity and significant reduction in lung capacity [14, 15, 16].

Gauderman et al. investigated the effect NO_2 pollution has on lung development between the ages of 10 to 18. They found significant reduction in Forced Expiratory Volume in the first second (FEV_1) for both girls and boys [17]. A further in−depth review conducted by Götschi et al. analysed a range of previous studies, concluding clear links exist between NO_2 and a range of lung related problems. They again stressed importance that elevated NO_2 pollution has a direct effect on children repertory system development [18]. In addition to causing lung problems, exposure to NO_2 has been clearly linked to promoting cardiovascular disease. Studies such as by Chang et al. found strong evidence between increased NO_2 levels and hospital admissions in Taiwan due to cardiovascular diseases [19]. Work by Wong et al. in Hong Kong found strong correlation between ischaemic heart disease and long−term exposure to high NO_2 levels [20].

The full effects of NO_2 on the heart is still to be fully understood. One such pathway, as discussed by O'Toole et al., involves inhaled NO_2 passing through the epithelium (interior surface of blood vessels) which can promote an inflammatory responses by the cardiovascular system and also generate reactive radicals within the system causing further damage [21, 22]. NO_2 has also been shown to affect over 65s to a higher degree in relation to cardiovascular promotion, as discussed by Wong et al. [23]. Significant correlation was found between increased age, daily concentrations of NO_2 and adverse health effects recorded from hospital admissions in Hong Kong.

In addition to NO_2 and O_3, PM also plays a key role in affecting human health. Although there are many different sizes of PM, only $PM_{2.5}$ will be discussed here. Sources of

$PM_{2.5}$ are both natural and manmade. Figure 1.4 shows the relative scale of $PM_{2.5}$ against a grain of sand and a human hair. Dust storms which effect the equatorial latitudes greatest are a major source of $PM_{2.5}$ and can present health problems. For regions such as Beijing where concentrations of $PM_{2.5}$ regularly exceed safe limits, understanding where regional or transportation sources are to blame is of high importance. Yu et al. concluded that a range of sources were responsible for Beijing's $PM_{2.5}$, ranging from biomass burning, soil dust, transport and other major industrial processes [24]. Seasonality was also observed to effect sources of $PM_{2.5}$, with spring conditions highlighting dust as a major source compared to winter conditions where biomass burning was the main source.

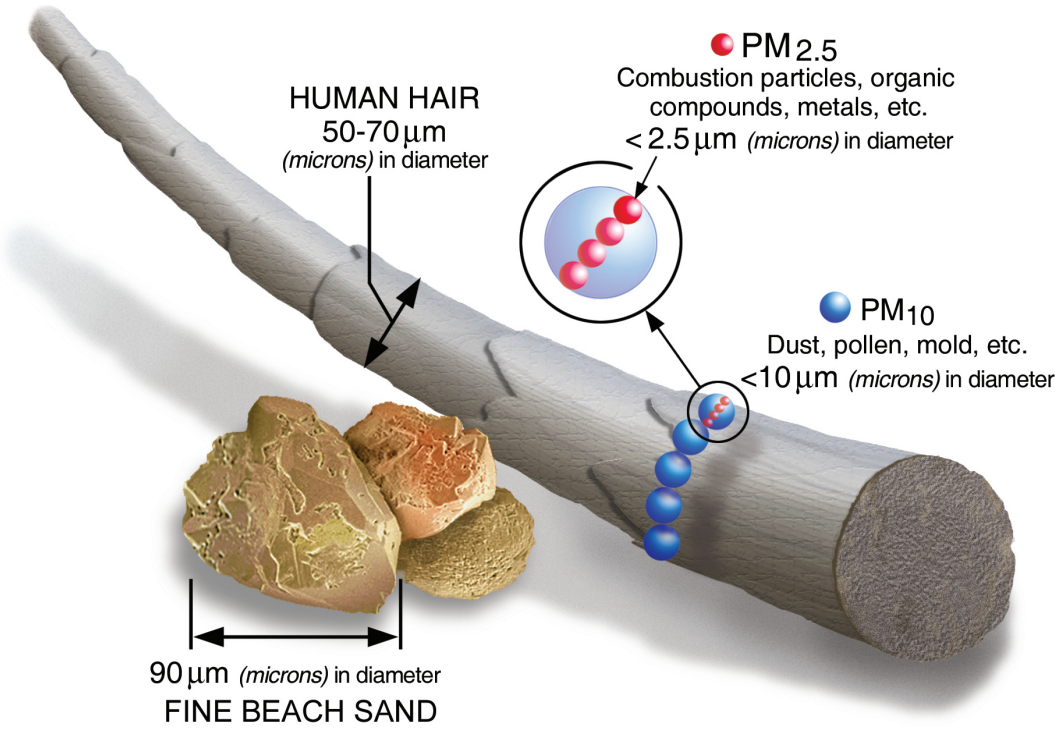

Figure 1.4: Infographic of PM scales against fine beach sand and human hair. Taken from EPA. (2017) [25].

Extensive medical studies have strongly linked $PM_{2.5}$ exposure to similar medical conditions to those already discussed for NO_2. Due to its small size, $PM_{2.5}$ can easily make its way down into the lower lung region of the respiratory system and cause lung function degradation. Further health problems have also been observed if particles pass into the blood stream and make their way to the cardiovascular system. Clear evidence was presented by the Committee on Medical Effects of Air Pollution in 2009, linking increased mortality rates in the UK with long−term exposure to elevated levels of $PM_{2.5}$ [26]. The

main mortality pathways linked to $PM_{2.5}$ by the committee, were mortality by either cardiopulmonary or lung cancer. There is little doubt that increased exposure to PM is a major health concern, with the EU setting strict air quality standards (EU Directive on Ambient Air Quality and Cleaner Air for European (2008/50/EC)) which now form UK law as of 2010 (Air Quantity Standard Regulations 2010). The directive clearly states that for a healthy exposure limit the UK should have an annual mean $PM_{2.5}$ concentration of $\leq$25 μg m^{-3} to be met by 2020 [27, 28]. Although extensive research has been conducted into the health effects of the total class of $PM_{2.5}$, current understanding of individual $PM_{2.5}$ chemical composition towards health is still limited.

1.4 UK Air Quality Strategy

As previously discussed, NO_x levels in the UK pose a serious air quality problem. Air quality management for the UK is overseen by the Department of Environmental, Food and Rural Affairs (DEFRA). DEFRA's air quality mandate is to measure and assess air quality trends throughout the UK with the aim of identifying ways of improving the UK air quality. The UK has a range of systems in place to analysis UK air quality with specific strategy published by DEFRA as outlined in 'The Air Quality Strategy for England, Scotland, Wales and Northern Ireland and the 2010 to 2015 government policy on environmental quality' [29, 30].

At a high level, DEFRA provides a daily pollution forecast for the entire UK region in collaboration with the Met Office. The forecast gives an air quality measure for the UK region for the next 5 days, ranging from low, moderate, high and in extreme cases very high ranking of overall pollution levels. It also issues health advice directly aimed as those who maybe more susceptible to high pollution events such as asthmatics. The forecasts are generated by the Meteorological Office (Met Office) using the Air Quality configuration of the Unified Model (AQUM). The model accounts for emission rates of pollutants, transportation rate due to meteorology and chemical reactivity within the atmosphere. One of DEFRA's more important mandates includes having to ensure the UK meets strict international obligations for air quality as legislated by the European Commission.

1.4.1 National Atmospheric Emissions Inventory

Annual assessment of UK emissions by DEFRA is achieved through the National Atmospheric Emissions Inventory (NAEI), which is produced for important greenhouse gases and key pollutants. The NAEI is developed and maintained by Ricardo Energy & Environment on an annual basis, feeding directly into DEFRA's analysis strategy on UK emissions. Figure 1.5 shows for the entire UK annual NO_x emission estimates at 1 km^2 resolution. The UK's major road network and large cities can be clearly seen. The NAEI is a highly valuable tool which allows the UK to assess its emissions. It is used on both a UK and a Devolved Administration (DA) scale, which allows individual councils to assess their air quality. The NAEI also feed into DEFRA's air quality models, which can assess current and future air quality trends for the UK [31]. The NAEI is a vital tool used by the UK government in reporting its emission to the EU. The UK has a commitment to

report its emissions to meet strict legislation regarding the Convention on Long−Range Transboundary Air Pollution (CLRTAP). All reported data from the CLRTAP is fed into air quality models such as EMEP, which forms the basis of air quality predictions for the UK and Europe [31].

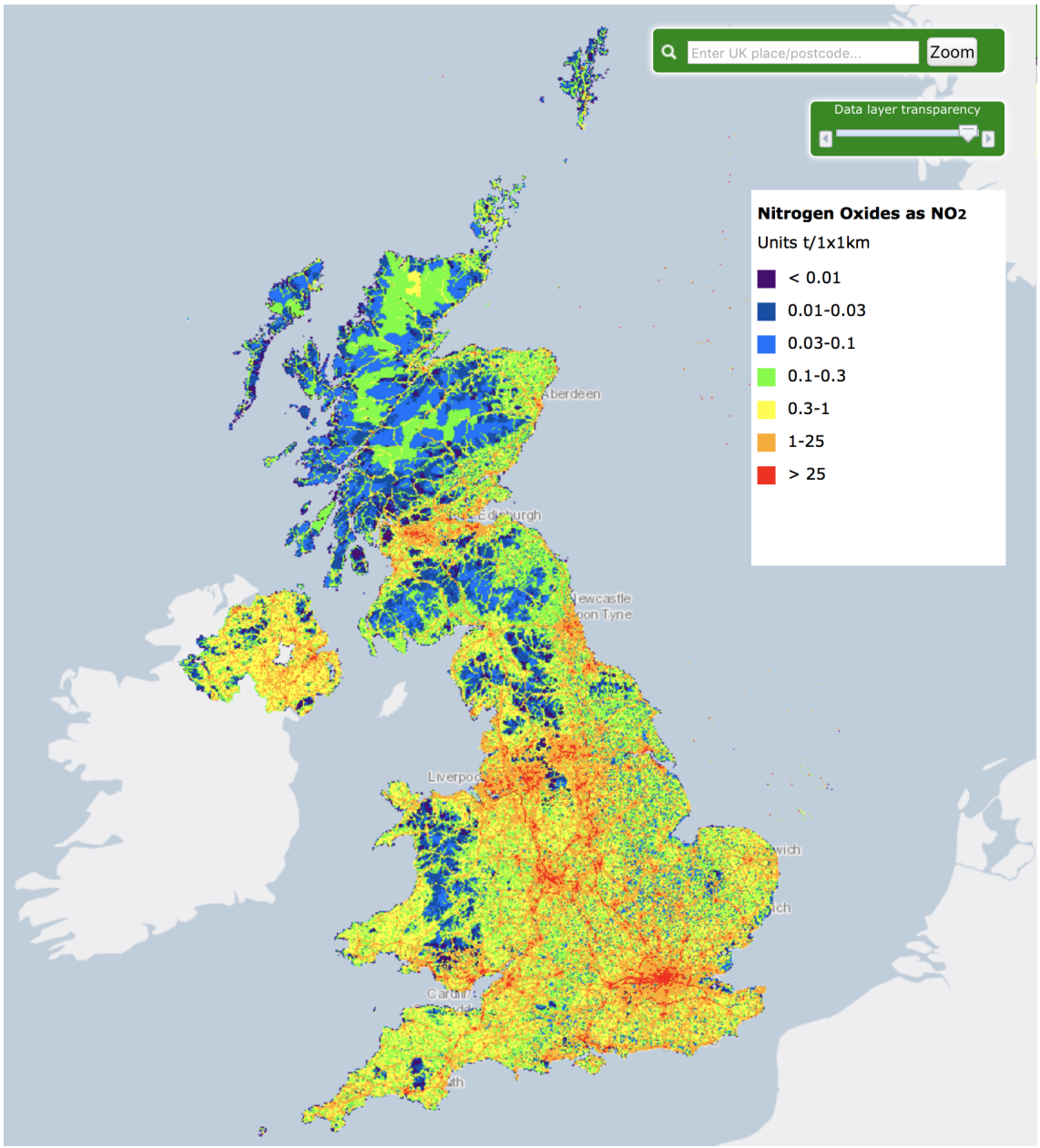

Figure 1.5: Annual emission estimates for NO_x at 1 km^2 resolution for the entire of the UK region. Taken from NAEI UK emissions interactive map [31].

The NAEI considers three main emission types: UK's road network, area specific emissions and large point sources. Examples of point sources include major industry, oil refineries and power stations. Figure 1.6 shows each of the three sources being combined to give gridded emissions for the entire UK [32]. Data is also drawn from sources such as the AURN network to make the inventory as realistic as possible. For road transport emission estimates, highway dynamics and fleet composition is considered to help improve the realism of estimates fed into the inventory. Overall, the inventory breaks down annual total emissions into 12 United Nations Economic Commission for Europe (UNECE) selected nomenclature for reporting of air pollutants (SNAP) sectors. These 11 SNAP sectors account for a range of different sources from road transport, solvent use to production processes all at 1 km^2 resolution [33].

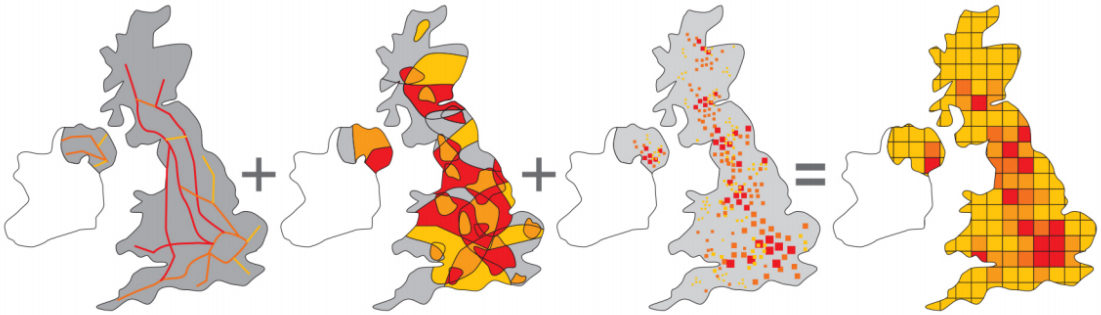

Figure 1.6: NAEI emission source types being summed up to generate total annual emission grids for the UK. Taken from DEFRA. (2016) [32].

1.5 Sources of Nitrogen Oxides

Oxides of nitrogen (NO + NO_2 = NO_x) play an important role in global air quality. NO_x can arise from a range of natural and made−made sources. A major nature source is lightning. Being one of the most energetic processes to occur in the atmosphere, it can split N_2 and O_2 into molecular N and O, which then goes on to form 2 molecules of NO. Globally lightning is estimated to contribute approximately 3.6 Tg N yr^{-1} of NO_x [34, 35]. For remote areas, such as oceanic and the tropics, lightning will be the main source of NO in the absence human activity.

Snow is also a key NO emitter, especially in regions such as Antarctic where there are no anthropogenic influences. Studies within the continent have observed high mixing ratios of NO > 500 pptv which can have possible implications on atmospheric photochemistry above the region. Microbial activity has also been shown to emit NO_x from the soil surface during the nitrification processes [36]. On a global scale, it has been estimated that emissions from this source alone can contribute to between 4 to 15 Tg N yr^{-1}. This estimate has been further refined, such as the work by Vinken et al., using the GEOS−Chem model which has estimated soil emissions of NO_x globally contribute around 13 Tg N yr^{-1} to the total NO_x emission budget [37].

Although all the listed natural sources of NO_x are lower when compared to predicted global emission of anthropogenic NO_x, they collectively play an important role influencing tropospheric and stratospheric chemistry with a total collective emission range of $12 - 35$ Tg N yr^{-1} [37]. Globally, anthropogenic sources of NO_x are the single largest contributor to the global NO_x budget, overtaking lightning as the largest source. Predicted global emission of NO_x from anthropogenic processes is thought to be in the range of $21 - 28$ Tg N yr^{-1} [38]. Key anthropogenic sources include: energy production and extract, industrial processes, road transport and other transport types such as aviation and rail. Measured NO_2 columns from the European Environment Satellite using the SCIAMACHY instrument clearly highlight 4 main regions where anthropogenic levels are well above the norm. As shown in Figure 1.7, the Western coast of America, Europe, South Africa and China all show high NO_2 concentrations as an average over 10 years (2002 to 2012) [39]. China shows the strongest levels of NO_2, which is due to fast modernisation of industry and vehicle use.

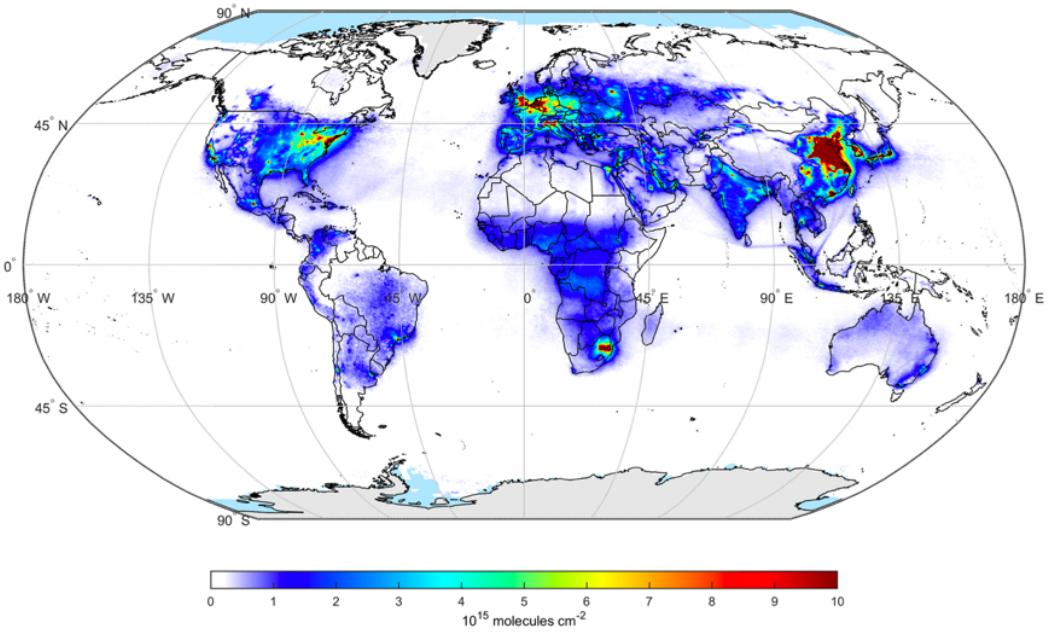

Figure 1.7: Global NO_2 column from SCIAMACHY instrument on−board the European Environment Satellite, as an average from 2002 to 2012. Take from Schneider et al. (2015) [39].

Over the last 20 years NO_x levels throughout Europe have decreased, as shown in Figure 1.8, by an average of 50% for EU28 countries and 40% for EEA33 countries. The overall reduction in NO_x emission has been driven by improvements in energy production, energy use in industry and road transport technology [40]. Although improvements have been observed for many regions of Europe, the UK has seen NO_x concentrations deviate from predicted reductions. As discussed by Carslaw et al., concentrations followed a strong decreasing trend from the 1990s until about 2004 after which point concentrations plateaued, which may be due to changes in the UK's vehicle fleet, such as increased use of diesel [41].

Anthropogenic NO_x in Europe has many sources, with percentage contributions being highly area dependent. As an average for all European countries, road transport makes up nearly 50% of all anthropogenic NO_x emissions with other sources such as energy production, industrial and commercial process also contributing (Figure 1.9). As early as 2005, increasing emission rates of NO_x were being attributed to increasing usage of diesel, with particulate filter technology playing an important role in controlling particulate matter removal whilst increasing NO_x emissions [42].

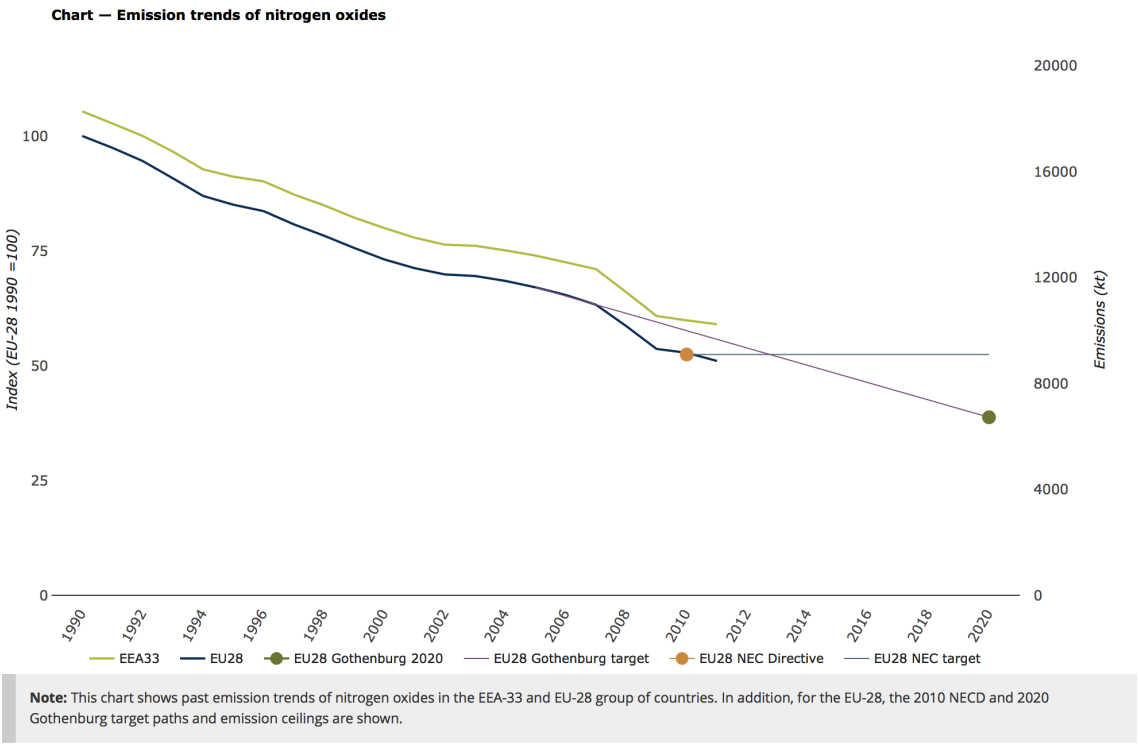

Figure 1.8: European average NO_x trends from 1990. Left axis shows emissions decreasing from 100% starting from 1990. The right axis shows NO_x emissions in kilotones per year. Taken from EEA. (2010) [40].

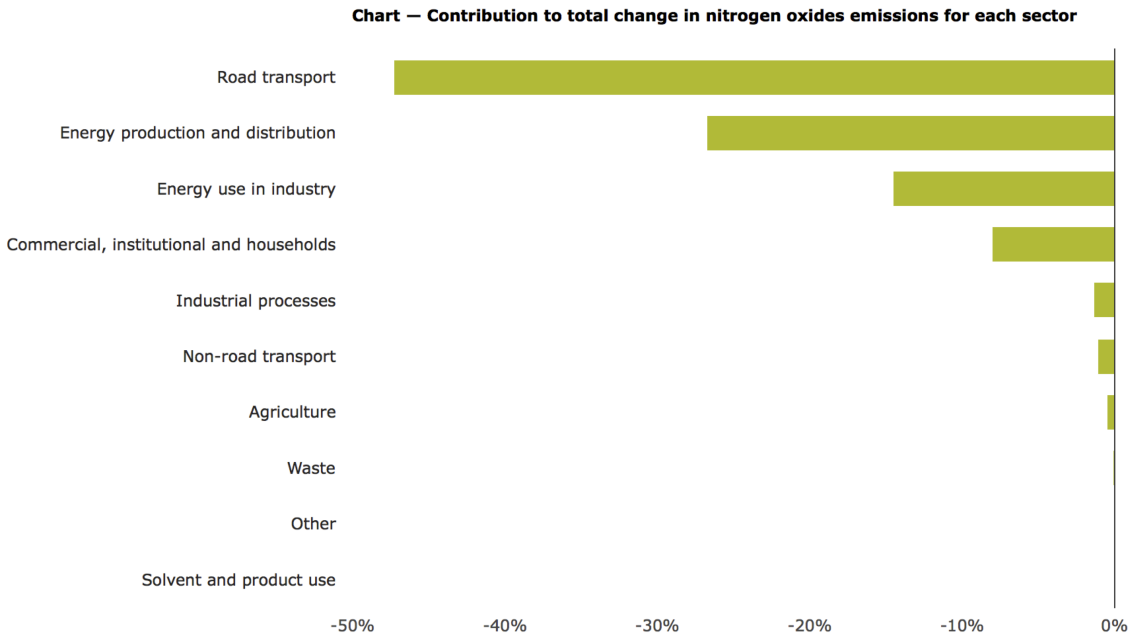

Figure 1.9: European percentage averages for NO_x emissions from 8 key contributing sources. Taken from EEA. (2010) [40].

1.5.1 NO_x Trends in London

Concentrations of NO_x in London readily exceed safe limits set by the EU. Current legislation states that concentration of NO_2 according to Directive 2008/50/EC, should not exceed an annual value of 40 μg m^{-3} and an hourly value of 200 μg m^{-3}. Up until 2000, emission reduction strategies were helping to bring London's NO_x levels to a safer level which can be seen in the step downward trend in Figure 1.10 (left). From 2000 onwards; however, NO_x levels plateaued [43]. This plateauing effect is a direct effect of increased emissions of primary NO_2. Measured concentrations from 1995 to 2015 have not dropped below the 50 μg m^{-3}, and have only decreased by around 10 μg m^{-3}.

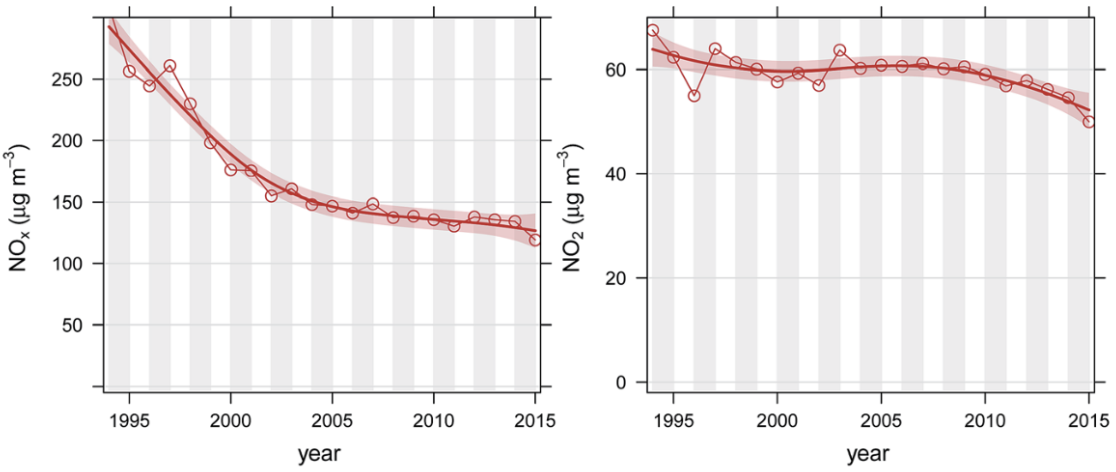

Figure 1.10: NO_x (left) and NO_2 (right) trends in London from road side measurements. Taken from Carslaw et al. (2016) [43].

Concentrations of NO_2 in London show a complex structure, with outer areas meeting annual EU regulations. Central London; however, greatly exceeded the 40 μg m^{-3} annual limit. Its major road network is clearly visible on the London Atmospheric Emission Inventories concentration map, which gives 20 m^2 annual concentration data for the entire of London. Concentrations along these main roads well exceed the safe limit, and highlights one of London's main emission problems. Road vehicles in London are a major anthropogenic source of NO_x. Over the last 20 years diesel vehicle use has rapidly increased due to better fuel efficiency and lower CO_2 emissions. The downside has been increased emission rates of primary NO_2.

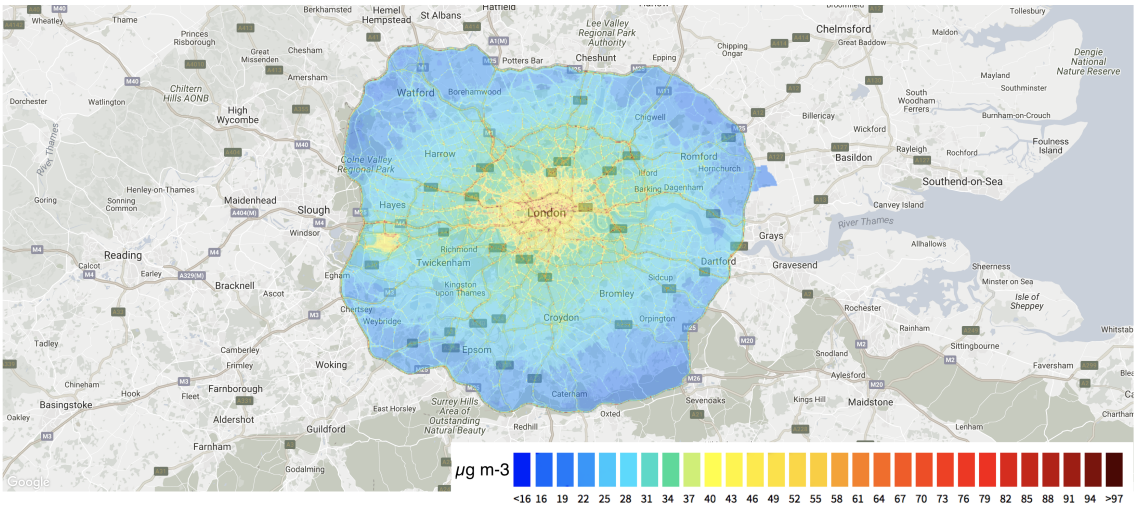

Figure 1.11: Annual 2013 surface NO_2 concentrations for greater London at 20 m^2 resolution. Taken from ERG. (2016) [44].

1.5.2 Vehicle Emissions of NO_x

NO_x emitted as NO can go on to form NO_2 through reaction with O_3, (see Section 1.6). Under these conditions O_3 is the limiting factor towards increasing concentrations of NO_2. The emission of NO_x from diesel vehicles; however, has been measured to emit increased proportions of NO_x as NO_2 which can perturb the reaction cycle, leading to elevated concentrations of NO_2 from direct emission [45]. Figure 1.12a shows predicted reductions in NO_x emissions from vehicles as an average for all European countries. However, as highlighted in Figure 1.12c, the proportion of NO_x emitted as NO_2 has increased by nearly 30%. This increase in NO_2 emissions has important health implications, even with the overall reduction in NO_x emissions.

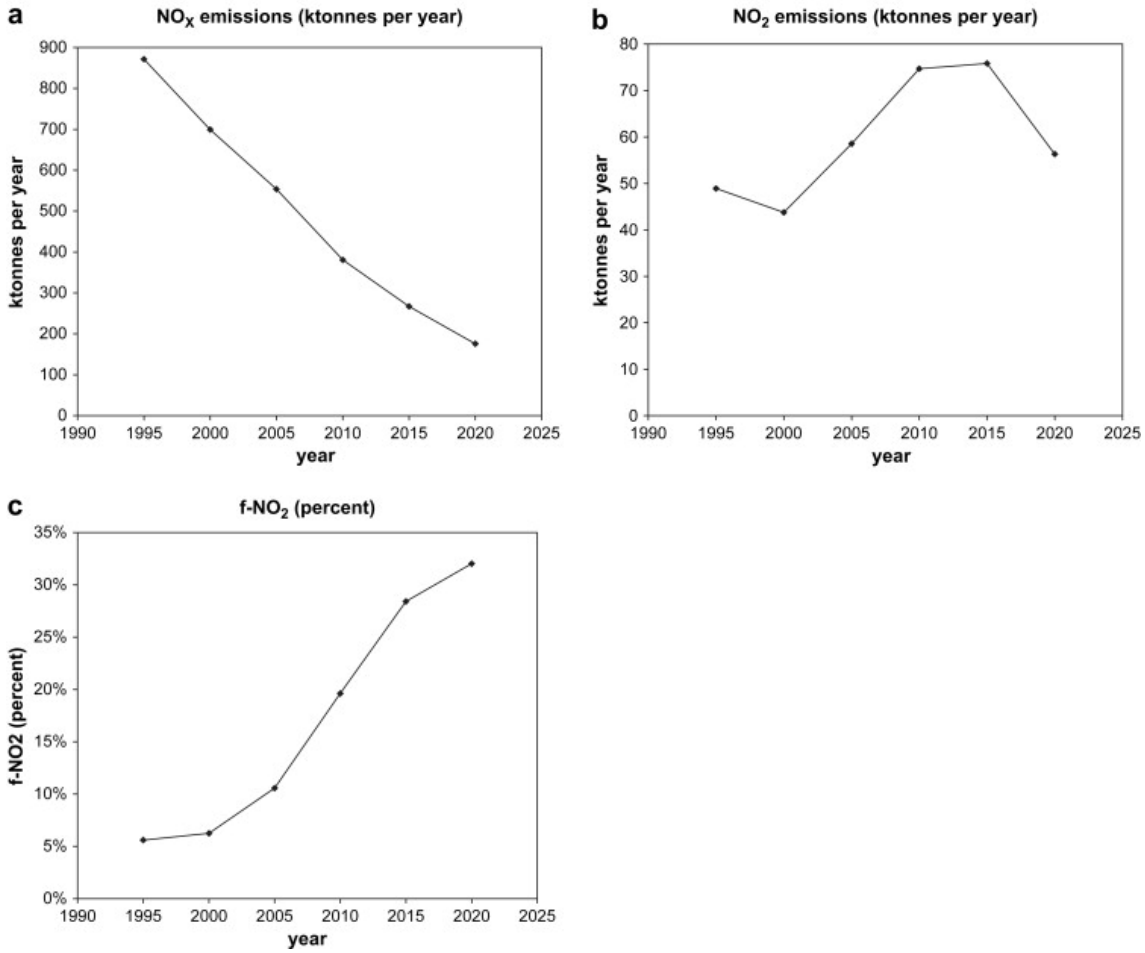

Figure 1.12: a) average European NO_x emissions from vehicles, b) emissions of NO_2 from 10 European countries, c) percentage proportion of NO_x emitted as NO_2. Taken from Carslaw et al. (2011) [45].

1.5.3 Vehicle Types and Emission Control Strategies

NO is formed in the combustion engine from N_2 and O_2 present in the injected air. The high temperature and pressure found inside pistons cause N_2 and O_2 to atomise and can then react to form NO. The two main engine types, gasoline and diesel, operate under different conditions and so can affect the amount of NO_x produced. Gasoline engines run close to the stoichiometric ratio, with a fuel to air ratio of 1 allowing for complete combustion of all fuel. Changes in the ratio used can have implications towards generated concentrations of NO and other combustion products such as CO and hydrocarbons (HCs). At higher fuel to air ratios 'rich', NO concentrations drop; however, CO and HCs concentration can increase greatly [46]. Figure 1.13 shows the formation of these three main combustion products in relation to the fuel to air ratio.

Gasoline engines operating at a fuel to air ratio of 1 can lead to a significant amount of NO and HCs being generated, Figure 1.13. Due to this gasoline vehicles have operated for the last 30 years with specific catalytic methodologies to reduce these pollutants. A three-way catalytic converter system is used to remove excess NO_x, CO and unburnt HCs from the vehicle exhort. The system involves a reduction process to convert any NO_x to O_2 and N_2, an oxidation process to convert CO to CO_2 and a final oxidation process to convert any remaining HCs to CO_2 and H_2O [47]. The efficiency of such a catalyst is shown in Figure 1.14, with a gasoline engine operating in the Air-Fuel ratio shown. NO_x removal is predicted to be $80 - 90\%$ within the operation window.

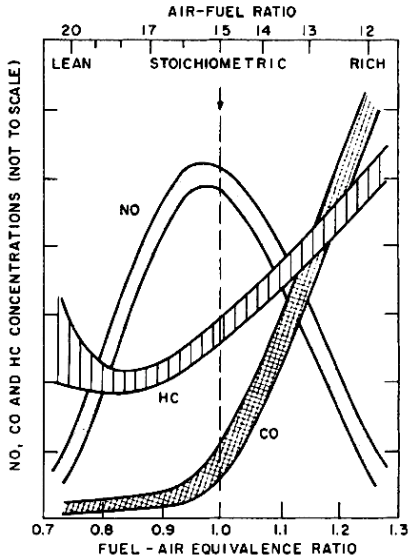

Figure 1.13: Generated concentrations of NO, CO and HCs for a range of fuel to air ratios. Taken from Chigier. (2013) [46].

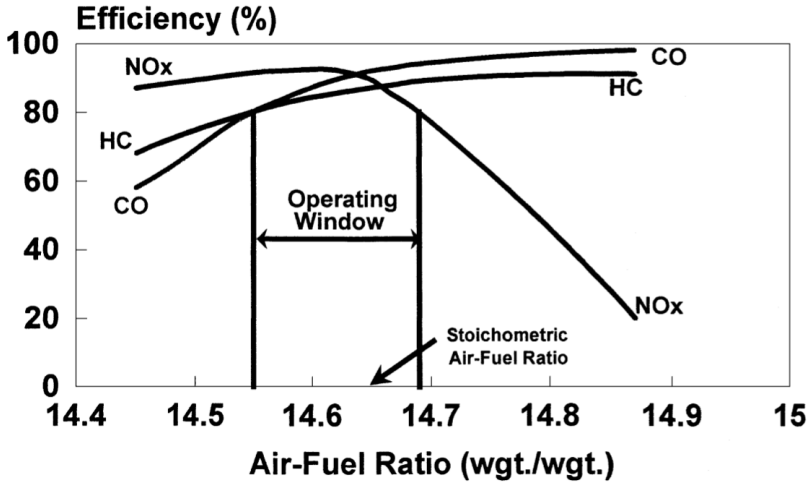

Figure 1.14: Three−way catalytic conversion efficiency in terms of NO_x, CO and HCs. Taken from Farrauto & Heck. (1999) [47].

Diesel vehicles, on the other hand, operate in a different manner. The engine design is more efficient than a gasoline vehicle, normally operating within the 'lean' zone which allows for complete combustion of all fuel with air in excess, Figure 1.13. The downside of having air in excess is that higher levels of NO can form. Higher levels of NO emission were not a problem for earlier Diesel vehicle types (Pre-Euro1, Euro1 and Euro 2) due to less strict PM controls. The development of diesel vehicle after-treatment technology has led to the increased emissions of NO_2. Since Euro 3, diesel vehicles have had oxidation catalysts (DOC) installed. They act to oxidise excess NO to NO_2, which can further oxidise any PM emission in the exhaust. The main downside of this process being increased formation of NO_2 [43]. The addition of the diesel particulate filter (DPF) in Euro 4 onwards helped to further reduce PM emission; however, NO_2 emissions have continued to increase with the dual system (DOC + DPF) [48]. Figure 1.15 shows diesel vehicle types and their NO_2 emissions, with specific emission control technologies listed above.

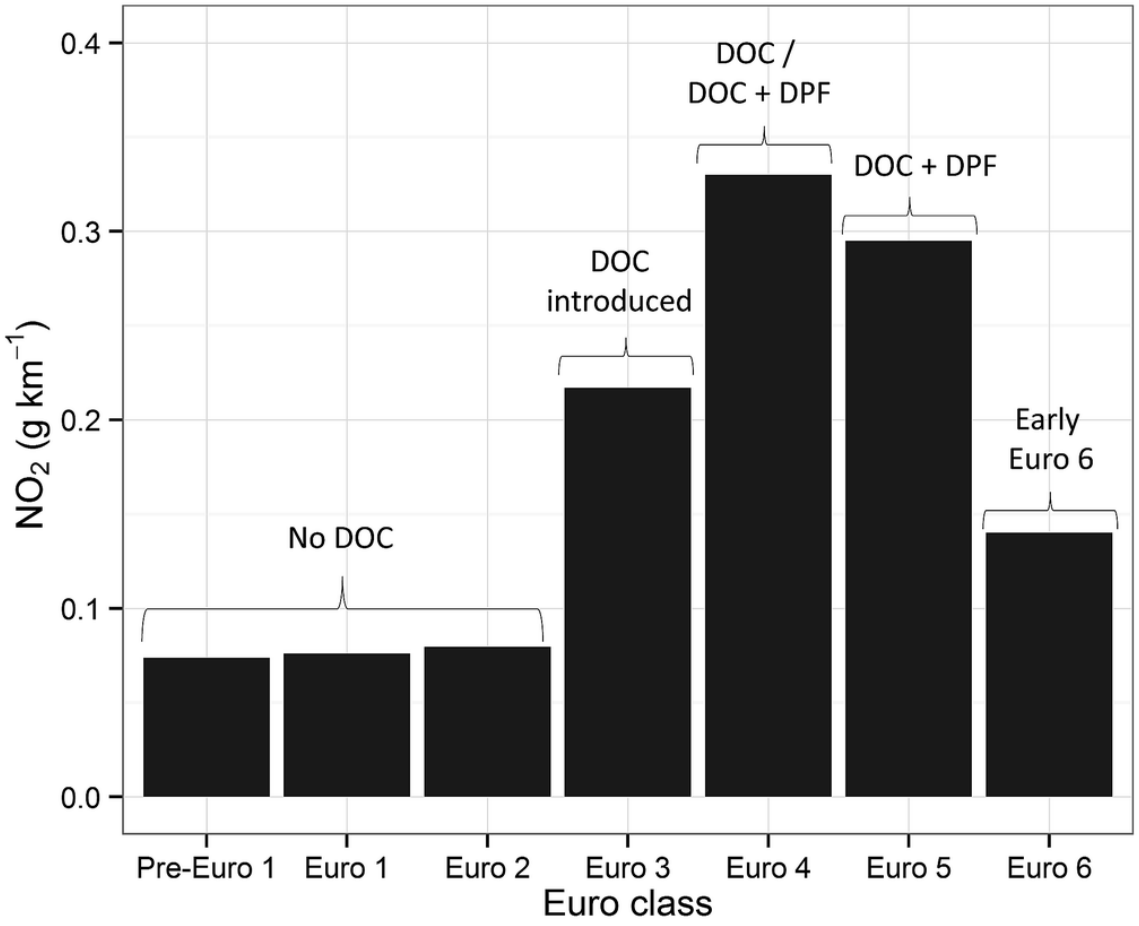

Figure 1.15: Euro class diesel vehicle emissions of NO_2, and the introduction of specific emission control systems. Taken from Carslaw et al. (2016) [43].

The reduction in NO_2 emissions as seen for Euro 6 vehicles is down to the introduction of emission control strategies aims at controlling NO_x emissions. Such technologies include Lean NO_x Trap (LNT) and Selective Catalytic Reduction (SCR) systems. SCR has been implemented in heavy-duty vehicles for a while now, with light-vehicles such as passenger cars only recently using such a device. The SCR approach is to add Urea into the tailpipe with a catalyst, which converts any NO_x into N_2 and H_2O [49, 50]. The LNT system is slightly more complex involving a multi-step strategy. Firstly, NO is oxidised to NO_2 and deposits onto the catalytic surface as nitrate/ nitrate. The nitrite/ nitrate is then released as NO_x which is reduced to form N_2 [51]. Both approaches give efficient NO_x removal. The addition of such to Euro 6 and above diesel vehicles will be key if any drop in NO_2 emissions from vehicles is to occur.

1.5.4 Vehicle Emission Rigging

Diesel vehicle numbers have increased in the UK throughout the 2000s which is mainly due to fuel efficiency and reduced CO_2 emissions. A key turning point came on the 18^{th} of September 2015, with a report published by the United States Environmental Protection Agency (EPA) reporting that Volkswagen (VW) Group Inc. manufactured cars were in violation of the US Clear Air Act. The EPA in this notification showed specific evidence that many of VW and Audi diesel cars were implementing software capable to forging emission test cycles [52].

A settlement was reached, removing affected cars from the roads and resolving the emission performance of those vehicles. The settlement involved the payment of a large fine for purposely breaking the CCA and required VW to commit to the investment of low emission strategies, a grand total of which is reported to run into billions of US dollars [53]. In the UK and Europe, VW vehicles were also found to breach emission limits with vehicles also recalled for emission performance corrections, Figure 1.16.

Figure 1.16: News articles on the VW diesel vehicle emissions scandal. Taken from The Guardian and BBC News [54, 55].

A major positive to come from the scandal in the UK is the advanced introduction of real world test cycles for vehicles. These test cycles ensure vehicles perform correctly under driving conditions in the real world, as discussed by the House of Commons Transport Committee into VW Inc.'s conduct around the emission scandal in the UK and Europe [56]. Due to the excessive emission coming from such vehicles, the potential for NO_x emissions to have plateaued is credible if such vehicles do not perform as they should. Although this hypothesis may not completely account for the UK's persistently high NO_x levels, it may go some way to explaining why emission strategies have failed to bring down emissions.

1.6 NO_x Chemistry

Anthropogenic NO_x emissions as previously discussed, are highly important when considering air quality. NO_x emitted into the atmosphere can undergo chemical reactions which can lead to further reductions in air quality. NO and NO_2 coexist in the atmosphere in an equilibrium state with O_3, under the reaction conditions defined in Equations 1.1−1.3 [57]. During the day, ultra violet (UV) light at wavelengths below 400 nm causes emitted NO_2 to undergo photodegradation, forming NO and molecular oxygen in the ground state $O(^3P)$. Due to $O(^3P)$ being highly reactive, it can react with O_2 and form a molecule of O_3. As a pollutant, O_3 has no direct emission sources, and is formed only through chemical reactions in the atmosphere. High concentrations of tropospheric O_3 can form in areas of enhanced NO_x emissions, which is of concern as O_3 is a known respiratory irritant (Section 1.3). Formed O_3 can also be lost during the day. As O_3 is highly reactive it can react with emitted NO to reform NO_2 and the O_2 molecule originally lost. Figure 1.17 left, shows the NO_x cycle with O_3.

$$NO_2 \overset{h\nu}{\rightarrow} NO + O\left(^3P\right) \tag{1.1}$$

$$O\left(^3P\right) + O_2 + M \rightarrow O_3 + M \tag{1.2}$$

$$NO + O_3 \rightarrow NO_2 + O_2 \tag{1.3}$$

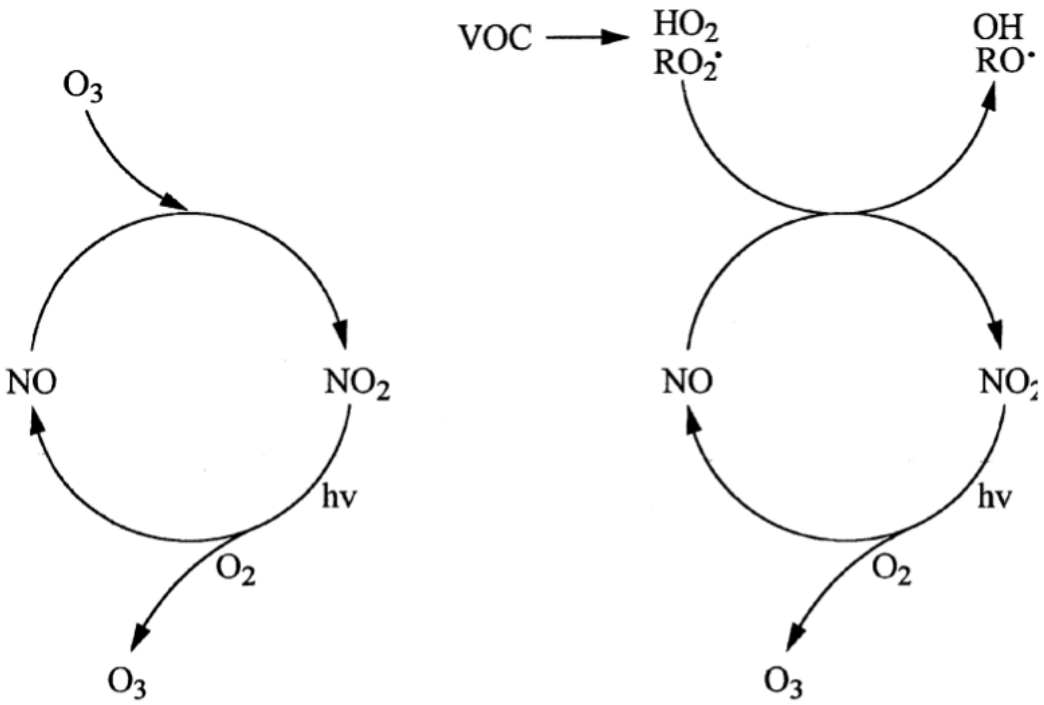

Figure 1.17: Simplistic NO_x reaction schemes, left) oxidative reaction between NO, NO_2 and O_3 in the presence of sunlight. Right) reaction scheme between NO and NO_2 and other oxidative species. Taken from Atkinson. (2000) [58].

In addition to NO_x, VOCs also play an important role in forming tropospheric O_3. VOC chemistry in the troposphere is intrinsically linked to NO_x and O_3. A simplistic reaction scheme is shown in Figure 1.18. Emitted VOCs can react with OH to form the RO_2 radical. This radical will then further react with NO, forming of O_3 and RO. Equations 1.4−1.5 describe the formation of NO_2 from OH oxidation of the primary VOC. Further reactions as shown in Equations 1.6−1.7, involve the generation of a secondary VOC carbonyl and HO_2 from RO. HO_2 radical leads to the regeneration of the OH radical and NO_2 formation via reaction with NO. Collectively, the reaction cycle can generate two O_3 molecules from one VOC, although this scheme is highly simplified without other molecules interacting. The outlined mechanism is highly important in the troposphere, both in the removal of emitted VOCs and in the production of tropospheric NO_x and O_3.

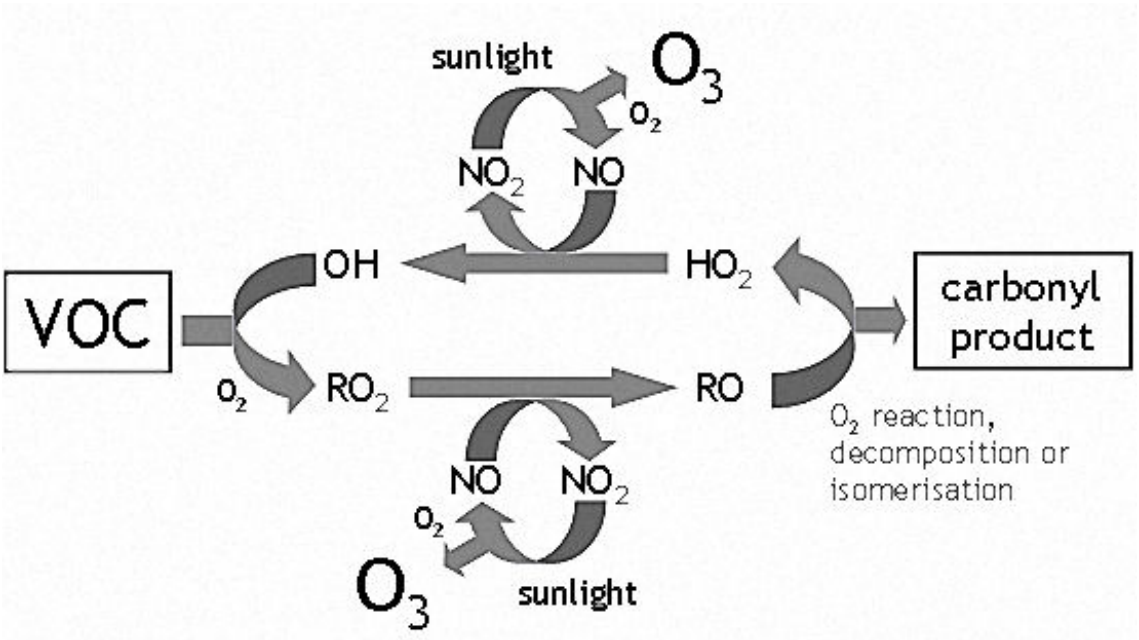

Figure 1.18: Basic VOC reaction scheme with OH, resulting in the formation of O_3 as a by−product. Taken from MCMv3.3.1 website [59].

$$VOC + OH \overset{O_2}{\rightarrow} RO_2^{\cdot} + H_2O \tag{1.4}$$

$$RO_2^{\cdot} + NO \overset{O_2}{\rightarrow} NO_2 + RO^{\cdot} \tag{1.5}$$

$$RO^{\cdot} + O_2 \rightarrow carbonyl + HO_2 \tag{1.6}$$

$$HO_2 + NO \rightarrow OH + NO_2 \tag{1.7}$$

$$NO_2 + hv \overset{O_2}{\rightarrow} NO + O_3 \tag{1.8}$$

The chemistry occurring during the night-time has a different dynamic than that observed during the day with the main difference being the removal of photolysis reactions. Without UV light, high order compounds containing more than one nitrogen atom can last orders of magnitude longer. During the daytime, NO and NO_2 are the dominant forms of nitrogen oxides and drive chemistry through their reactions with O_3 and other oxidising compounds such as the OH radical. At night, nitrogen trioxide (NO_3) and dinitrogen pentoxide (N_2O_5) can form without being quickly photolysed. Figure 1.19 depicts the reaction cycle of high order nitrogen oxides with other radical species during nocturnal hours [60].

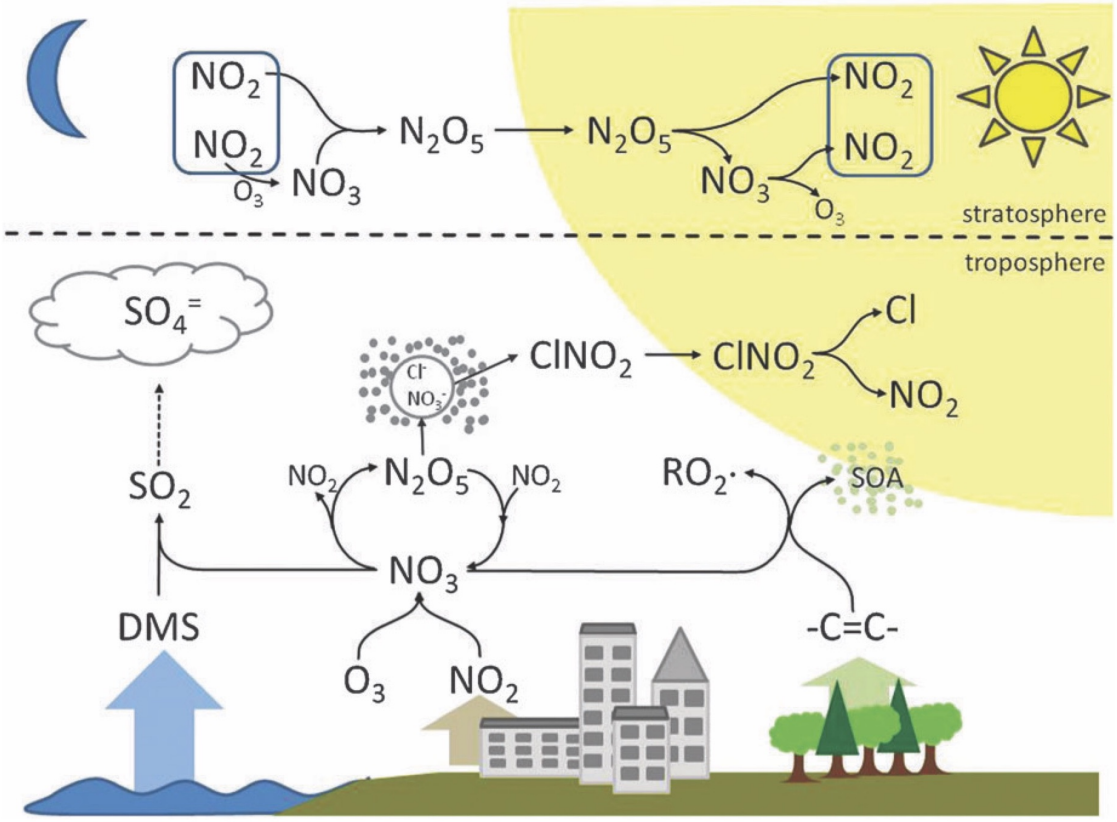

Figure 1.19: Nocturnal radical reaction chemistry of NO_x. Taken from Brown & Stutz. (2012) [60].

During the night, emitted NO can react with O_3 to form NO_2. This reaction can lead to highly reduced NO concentrations as photolysis cannot drive back the formation of NO. NO_2 either formed or directly emitted can go on to further react with O_3 to form NO_3 and O_2. NO_3 formation is possible during the daytime; however, it is readily photolysed back to NO_2 and molecular oxygen which can then go on to form O_3. Equations 1.9−1.11 show night-time formation of NO_3 and its loss during daytime conditions through UV photolysis and also reaction with NO [60]. Most photolysed NO_3 will form NO_2 (90 %) in comparison to NO (10 %) [58].

$$NO_2 + O_3 \rightarrow NO_3 + O_2 \tag{1.9}$$

$$NO_3 + hv \rightarrow NO + O_2 \tag{1.10}$$

$$NO_3 + hv \rightarrow NO_2 + O\left(^3P\right) \tag{1.11}$$

$$NO_3 + NO \rightarrow 2NO_2 \tag{1.12}$$

$$NO_2 + NO_3 + M \rightarrow N_2O_5 + M \tag{1.13}$$

$$N_2O_5 + M \rightarrow NO_2 + NO_3 + M \tag{1.14}$$

NO_3 can go onto react with a range of other atmospheric components as depicted in Figure 1.19. One reaction involves the formation of N_2O_5, as shown in Equation 1.13. The formation of N_2O_5 is in equilibrium, with Equation 1.14 showing the reformation of NO_3 from N_2O_5. The equilibrium partitioning of NO_3 to N_2O_5 has previously been investigates by Benton et al. from the BT Tower in London using broadband cavity enhances absorption spectroscopy (BBCEAS) [61]. They found a strong anti-correlation between measured NO_3/ N_2O_5 and NO/ NO_2, indicative of Equations 1.9 and 1.11. Ratio of formed NO_3/N_2O_5 was found to be 0.01 which strongly highlights a shift of the reaction equilibrium towards formation of N_2O_5.

NO_x emitted into the atmosphere can be lost through the chemical reactions already discussed or through sink processes. The main loss route for NO_x in the troposphere is the reaction of NO_2 with the OH radical to form nitric acid (HNO_3), as shown in Equation 1.15. Nitric acid can then be lost through dry or wet deposition [62]. During dry deposition HNO_3 can be converted into aerosols and then deposited onto surfaces. Wet deposition removes HNO_3 through absorption into a water droplet, which can then be rained out of the atmosphere. During the night, NO_x can form NO_3 and N_2O_5. These oxides can undergo similar loss processes, such as the reaction of N_2O_5 with H_2O forming two molecules of nitric acid. N_2O_5 is hydrolysed by aerosols in the atmosphere and is a key removal process during night-time conditions, when N_2O_5 product is at its maximum. Loss of N_2O_5 due to hydrolysis has been previously studied with Equations 1.16−1.17 defining formation of HNO3 through homogeneous and heterogeneous reaction pathways [63, 64, 65]. Through a heterogeneous pathway N_2O_5 gas can react with H_2O water vapour forming HNO_3 gas. HNO_3 can also form aerosol through uptake into water aerosol or secondary aerosol formation [66, 67]. NO_3 formed during night-time conditions can also react with an organic molecules (RH) leading to the production of nitric acid.

$$NO_2 + OH + M \rightarrow HNO_3 + M \tag{1.15}$$

$$NO_3 + VOC \rightarrow HNO_3 + R \tag{1.16}$$

$$N_2O_5 + H_2O \rightarrow 2HNO_3 \tag{1.17}$$

In addition to the discussed reaction processes, NO_x can also form other products which can act to remove it from the troposphere. The first is the formation of nitrous acid (HONO). HONO can be formed from to the reaction of NO with OH, as shown in Equation 1.18. This reaction is reversible in the daytime with ultraviolet light splitting the molecule back to NO and OH (Equation 1.19). HONO can also go on to reaction with another OH molecule forming H_2O and NO_2 [68]. Lee et al. suggested that HONO may also form via heterogeneous conversion of NO_2 on organic substrates which have photosensitivity. The study conducted in London highlighted that during the daytime, urban surface release of NO_2 due to photolysis maybe a significant source of HONO [68].

$$NO + OH + M \rightarrow HONO + M \tag{1.18}$$

$$HONO + hv \rightarrow OH + NO \tag{1.19}$$

$$HONO + OH \rightarrow H_2O + NO_2 \tag{1.20}$$

NO_2 can also go on to form peroxyacyl nitrates (PANs). PANs are formed from the reaction between peroxyacyl radicals and NO_2. Non-methane VOCs are a key source of peroxyacyl radicals, with isoprene and $\alpha-$pinene being two VOCs known to form PAN [69]. Figure 1.20 shows a few reaction pathways involving VOC oxidation and reaction with NO_2 to form PANs. The atmospheric lifetime of PANs can be very long and they act as a reservoir for NO_x in the atmosphere. PANS can eventually be removed from the atmosphere through dry deposition [70].

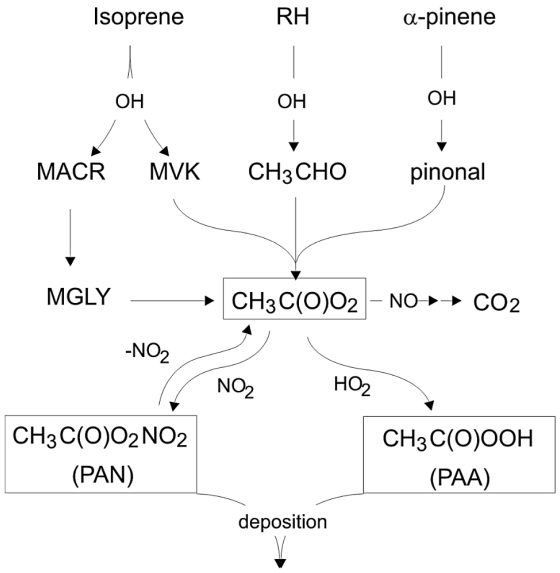

Figure 1.20: Formation of PAN from oxidation of non-methane VOCs. Taken from Phillips et al. (2013) [69].

1.7 Summary

Anthropogenic NO_x pollution in the UK is a major problem, with major cities such as London having some of the highest emissions in Europe. Levels of NO_x in London has been found to readily exceed the EU's annual exposure limit of 4 μg m^{-3} on a daily basis, which brings into question the effect such exposure will have on public health. Medical evidence over the last 20 years has shown a correlation between long term NO_2 exposure and increased numbers of respiratory and cardiovascular type diseases, strengthening the need for NO_x emission reductions.

The main sources of NO_x in the UK are thought to be: energy production, industrial applications and road transport, with diesel fuel usage being a particularly high emitter of NO_x. The UK assesses NO_x emissions on an annual basis via the NAEI. Emission estimates from the inventory are used towards meeting strict EU air quality legislation. Emission estimates are very difficult to get right and require measurements to authenticate them. To date, tower and point source measurements have been used to help refine such inventories; however, they cannot assess an entire city such as London. On the other hand, aircraft measurements have allowed for assessment of large areas, with advancements in instrumentation allowing for sub second sampling of atmospheric pollutants such as NO_x.

The research discussed in this thesis assesses the applicability for using a low flying aircraft over the UK to assess city wide emissions and the validity of emission estimates.

1.8 Thesis Outline

The work outlined in this thesis discusses measurements made during the Ozone Precursor Fluxes in an Urban Environment (OPFUE) field campaign and the development of an eddy-covariance methodology allowing for direct comparison between airborne flux measurements and key UK emission inventories for NO_x and VOCs.

Chapter 2 outlines the scientific methodology, instrument specification and calibration strategy of NO_x chemiluminescence on-board a research aircraft. The instrument was operated during the OPFUE campaign over London enabling the calculation of real-time NO_x fluxes.

Chapter 3 discusses airborne eddy-covariance theory and the specifications required for calculating high spatiality fluxes over a large city such as London. The described technique couples airborne eddy-covariance with a footprint model allowing for top-down comparison of emission inventories, with specific parameterisations for NO_x and VOCs.

Chapter 4 discusses calculated NO_x fluxes during the 2013 and 2014 OPFUE campaigns with comparison to the National and London Atmospheric Emissions Inventories (NAEI and LAEI).

Chapter 5 discusses calculated VOC fluxes during the 2013 and 2014 OPFUE campaigns over Southern England and London, with comparison to the NAEI and EMEP4UK inventories.

Chapter 6 discusses the main conclusions found during the development and implementation of airborne eddy-covariance from a low flying aircraft over England. It also discusses in detail the uncertainties and future work needed to further develop this research going forward.

Chapter 2

Methodology for Airborne Measurement of Nitrogen Oxides

This chapter discusses the measurement technique of NO_x chemiluminescence and how it was used to quantify nitrogen oxides over Greater London during the Ozone Precursor Fluxes in the Urban Environment (OPFUE) campaign 2013 and 2014.

2.1 Introduction

High emissions of nitrogen oxides (NO + NO_2 = NO_x) are a major air quality problem affecting many European cities such as London. NO_x concentrations regularly exceed safe limits, which makes measuring their abundance and emission rates key. Three measurement approaches have been used to assess NO_x concentrations on both local and global scales. Figure 2.1 shows the different measurement strategies previously used to measure NO_x [71].

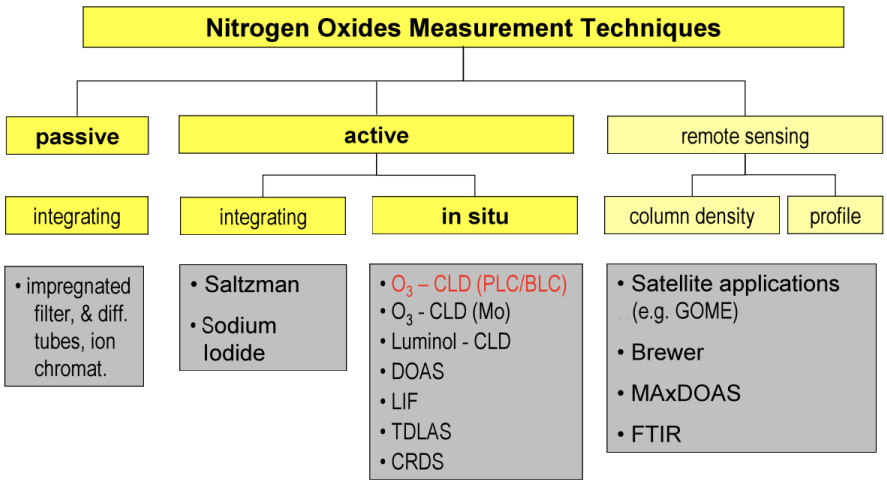

Figure 2.1: Diagram of NO_x measurement techniques using; passive, active or remote-sensing approaches. Taken from the World Meteorological Organization Global Atmospheric Watch's (WMO/GAW) report on making long-term NO_x measurements [71].

Passive sampling involves extracting NO_x from ambient air and integrating it onto a storage medium such as filter substrate. Diffusion tubes employ this kind of approach and allow for off-line extract and analysis of NO_x over a period of time. Work by Krochmal et al. investigated the use of triethanolamine as a trapping agent for nitrogen dioxide (NO_2) from an ambient sample and subsequent off-line quantification through either a spectrophotometrical approach with Saltzman solution or ion chromatography [72, 73]. Plaisance et al. also assessed the feasibility of using passive sampling for determination of ambient NO_2 concentrations [74]. A diffusion tube-sampler was used to trap NO_2 on a triethanolamine layer, with ion chromatography analysis of the NO_2 concentration bound as nitrite. For a two-week sampling period a detection limit of 2 μg m^{-3} was achievable using this method. Although passive sampling is a feasible method for assessing NO_2 levels, it lacks the capability to give high time resolution sampling and is limited by spatial confinement.

Remote sensing allows high resolution measurements on a global scale. The Global Ozone Monitoring Experiment (GOME) on-board the ESA ERS-2 satellite has previously been used to investigate NO_2 column densities, enabling direct assessment of global models [75]. Richter et al. investigated global NO_2 emissions through analysis of measurements made from both GOME and Scanning Imaging Absorption Spectrometer for Atmospheric Chartography (SCIAMACHY) instrument, evaluating column densities on a global scale [76]. The study showed decreasing NO_2 trends for parts of the USA and Europe, with increasing trends shown for areas such as China. Remote sensing is also possible through ground measurements. Systems such as multi-axis differential optical absorption spectroscopy (MAX-DOAS) can quantify vertical distributions of atmospheric tracers such as NO_2 [77]. It has previously been used to evaluate NO_2 from slant column densities [78, 79]. MAX-DOAS has also been used to assess vertical distributions of NO_2 on-board an aircraft. Dix et al. were able retrieve NO_2 column densities over 15 km in altitude with an uncertainty of 30% [80].

In-situ techniques offer high time resolution (<1 min) NO_x measurements. As shown in Figure 2.1, a number of different in-situ methods have previously been used. Spectroscopic techniques, such as cavity ring-down spectrometry (CRDS), have previously been used to assess concentrations of nitrogen and oxygen containing molecules (NO, NO_2, NO_3, N_2O_5) [81]. Osthoff et al. discussed the deployment of a CRDS instrument on-board an aircraft, being able to quantify NO_2 down to 40 ppt [81]. Other spectroscopic techniques such as differential optical absorption spectroscopy (DOAS), tuneable diode laser absorption spectroscopy (TDLAS) and Laser induced fluorescence (LIF) have also been used to quantify NO_2 concentrations at high time-resolution [82, 83, 84]. Fuchs et al. gives a detailed inter-comparison of a range of in-situ NO_2 techniques and highlights the pros and cons of each [85]. More recently, in-situ NO_x measurements have been made using ozone chemiluminescence, which will be discussed in this Chapter.

2.2 NO_x Chemiluminescence

Quantification of atmospheric NO_x, as discussed in Chapter 4, was achieved using a chemiluminescence approach. As discussed by Ridley et al., NO can be quantified through ozone chemiluminescence detection (O_3-CLD) [86]. Equations 2.1 and 2.2 describe the reaction of NO with O_3. NO reacts with O_3 to form NO_2, with a proportion being in an excited electronic state. As the excited state NO_2 is highly unstable, photonic emission can occur which returns the molecule to the ground energy state (Equations 2.3−2.4). The emission of a photon from the NO_2 molecule can be detected and used to directly calculate the NO concentration in the ambient sample.

$$NO + O_3 \xrightarrow{k_1} NO_2 + O_2 \tag{2.1}$$

$$NO + O_3 \xrightarrow{k_2} {NO_2}^* + O_2 \tag{2.2}$$

$${NO_2}^* \xrightarrow{k_3} NO_2 + hv \tag{2.3}$$

$${NO_2}^* + M \xrightarrow{k_4} NO_2 + M \tag{2.4}$$

Emission of a photon from excited NO_2 does not always occur. This is due to the presence of other atmospheric molecules, which are denoted as M in Equation 2.4. These other molecules can gain energy from the excited molecule and return it to the ground state without a photon being released. Equation 2.5 denotes the steady state formation of excited ${NO_2}^*$ from Equations 2.1−2.4. Increasing the concentration of O_3 will drive an increased formation of excited ${NO_2}^*$ [71].

$$[{NO_2}^*] = k_2 [NO] [O_3] / k_4 [M] \tag{2.5}$$

Quantification of NO_2 as discussed by Kley et al., can be achieved via photolytic ozone chemiluminescence detection (PLC-O_3-CLD) [87]. NO_2 does not chemiluminescence in its ground and so needs to be converted to NO first. Classically NO_2 has been converted using molybdenum converters (Equation 2.6), which operates at high temperatures ($300-350$ ^oC) [88]. The downside of using such a converter is interferences, with molybdenum converters being known to respond positively to NO_y species, such as nitric acid [89]. Photolytic conversion is now more mainstream with such converters utilising mercury lamps, Xenon arc lamps and UV$-$LEDs [87, 90, 91]. As described in Equation 2.7, using wavelength below 400 nm, NO_2 is photolytically converted to NO. Quantification then follows the same route as for NO with NO converted to excited $NO_2{}^*$ and release of a photon through relaxation to ground energy state (Equations $2.8-2.9$).

$$Mo + 3NO_2 \rightarrow MoO_3 + 3NO \tag{2.6}$$

$$NO_2 + hv \rightarrow NO + O\,(3_p) \tag{2.7}$$

$$NO + O_3 \rightarrow NO_2{}^* + O_2 \tag{2.8}$$

$$NO_2{}^* \rightarrow NO_2 + hv \tag{2.9}$$

2.3 Fast−AQD−NO_x system

The fast NO_x chemiluminescence instrument (Fast−AQD−NO_x) was built in 2012 by Air Quality Design Inc. (AQD), and is a dual channel instrument which can measure NO and NO_2 concurrently up to a rate of 10 Hz (Figure 2.2). Ambient NO is measured using O_3−CLD and NO_2 by PLC-O_3−CLD. The system has the capacity to operate using either dry-ice or Peltier cooling, which is used to reduce the dark counts on the photomultipliers which is discussed in more detail in Section 2.4.3. The instrument is specifically designed to operate on board the NERC Dornier 228 aircraft, and is housed in a specially designed flight rack. The system is split into three units (Control, Detector and Ozoniser) which house the instruments core parts. The modular design allows for easier replacement of parts should any fail during a field campaign.

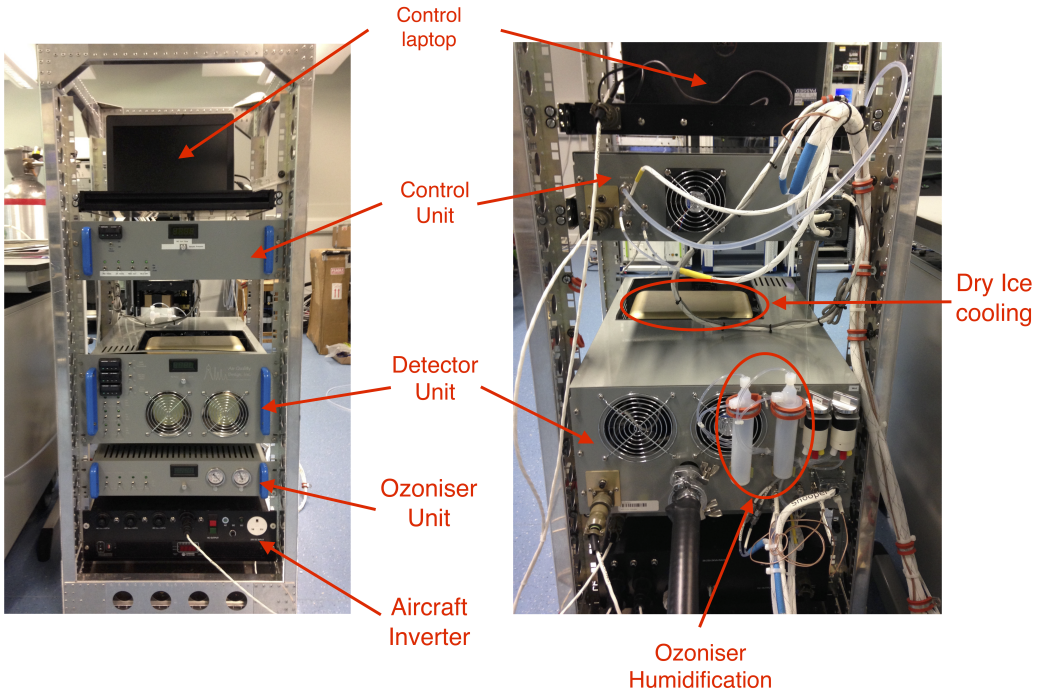

Figure 2.2: a) front view of Fast−AQD−NO_x system mounted in a flight rack for operation on NERC Dornier−228 aircraft, b) rear view of system showing sample lines and ozone humidification.

2.3.1 Flow Diagram

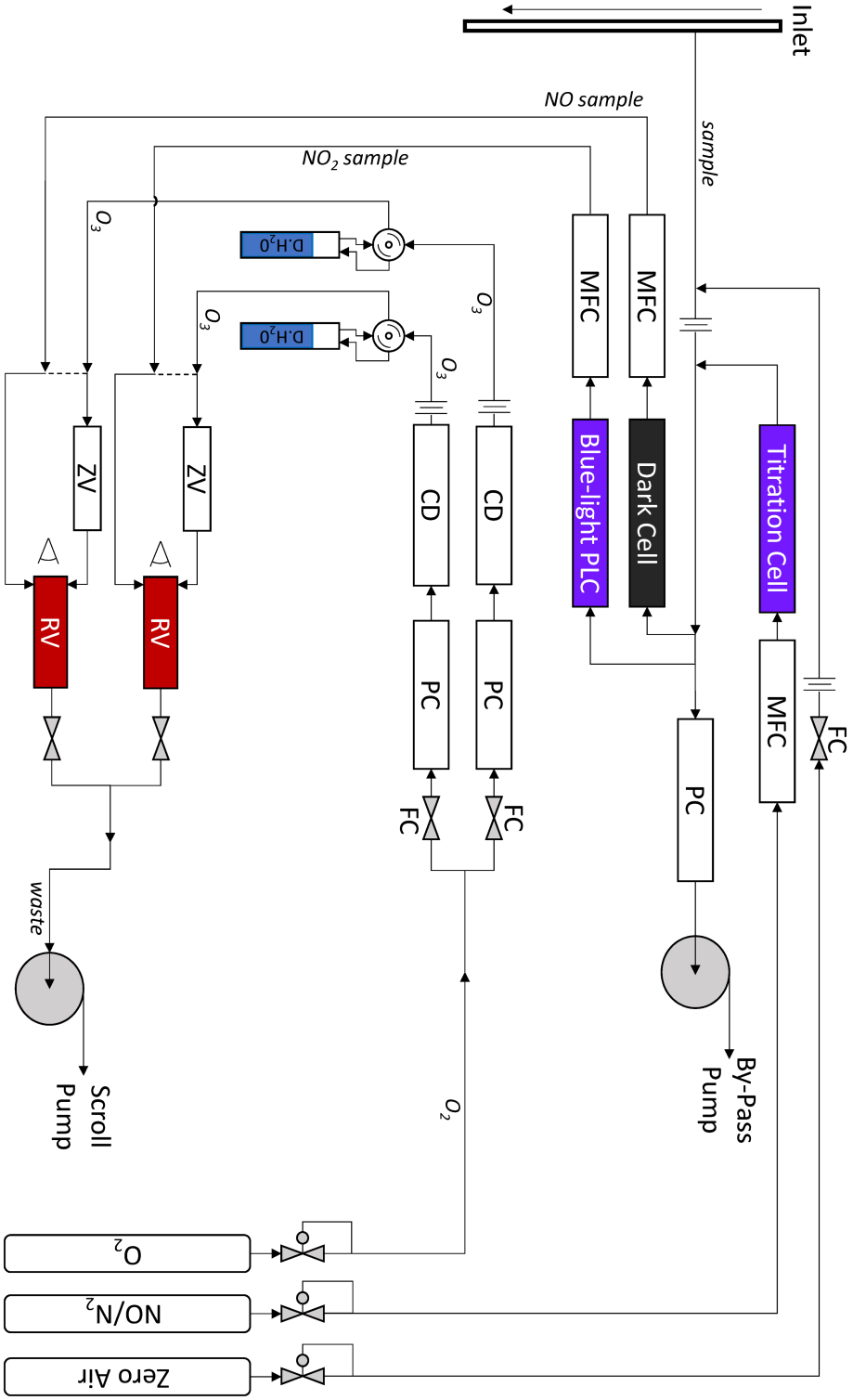

Figure 2.3: Flow diagram of the Fast−AQD−NO_x instrument containing: gas cylinders, flow−controllers (FC), mass−flow controllers (MFC), blue−light photolytic converter (blue−light PLC), pressure−controller (PC), zero−volume (ZV), reaction−vessel (RV), corona discharge units (CD), by−pass and scroll pumps.

2.3.2 Control Unit

The control unit (Figure 2.4) houses the main LabJack system which acts as interfaces between the control laptop and the instrument components. The unit houses pressure and mass−flow controllers which act to keep the entire system downstream at a constant pressure and flow rate for both channels. The system is pressure controlled via a MKS Type 640 pressure controller. At a constant pressure of 300 Torr the system remains independent of changes in altitude up to 23,000 ft. The control unit also houses mass−flow controllers which are used to keep the sample flow into each channel at 1,500 sccm. A high sample flow into each channel is essential for calculating fluxes from an aircraft. This is due to the need for the turbulent concentration structure of NO/ NO_2 needing to be retained if the eddy−covariance calculation is to work. The unit is also used to calibrate the instrument by controlling the addition of a calibration standard to each channel. For calibration of the NO_2 channel, a set amount of NO_2 is generated using a titration cell which makes O_3 to react with the NO calibration gas. This produced NO_2 can be used to assess the conversion efficiency of blue−light PLC which is also housed in the unit.

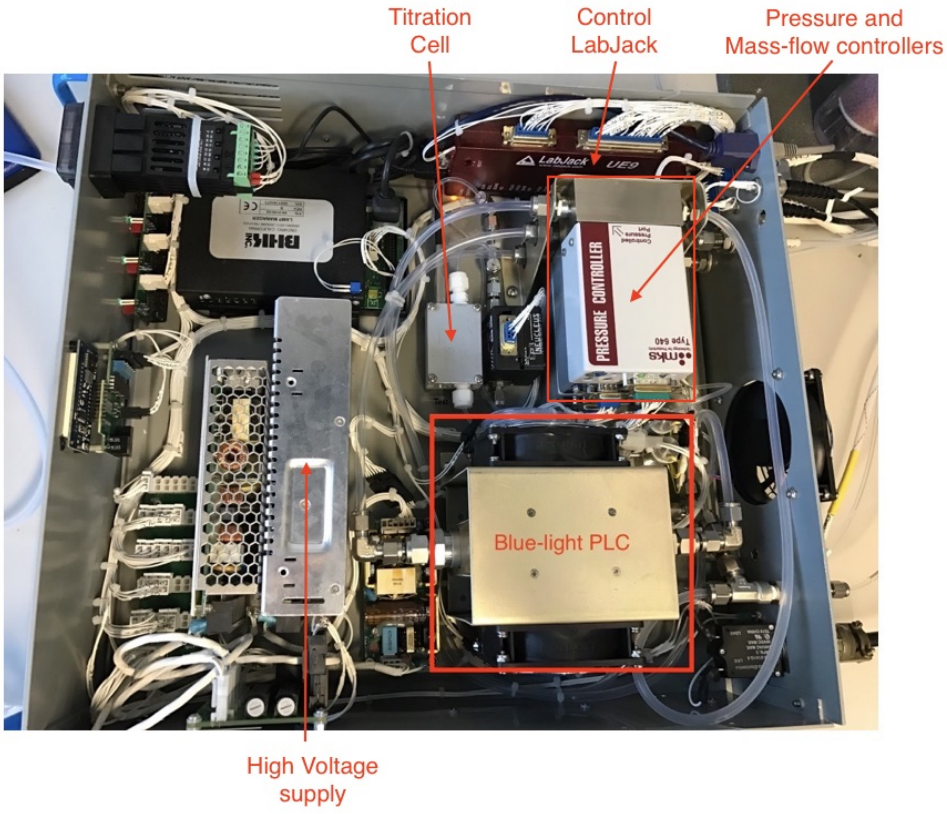

Figure 2.4: Control unit containing: a pressure control, mass−flow controllers, blue−light PLC, calibration system, control systems and LabJack unit.

2.3.3 Photolytic Converter

For detection of NO_2 a photolytic converter (PLC) is used to break apart NO_2 in the ambient sample to NO which can then be detected through O_3−CLD. Using a PLC brings enhancements over conventional methods such as molybdenum converters. Previous studies such as by Sadanaga et al. and Pollack et al. discussed the use of a PLC system in converting NO_2 to NO [91, 92]. Pollack et al. compared three LED converters which two centred at 365 nm and the other at 395 nm [92]. Figure 2.5 highlights the findings of the study in relation to NO_2 quantum yield and unwanted compounds, as a function of light wavelength. The lower wavelength LEDs encounter higher interferences from other NO containing molecules (HONO, $BrONO_2$ or $ClNO_2$) which could be photolysed. This could represent a major problem if such a system is being operated in a very low NO_2 environment, for example remote and tropical regions.

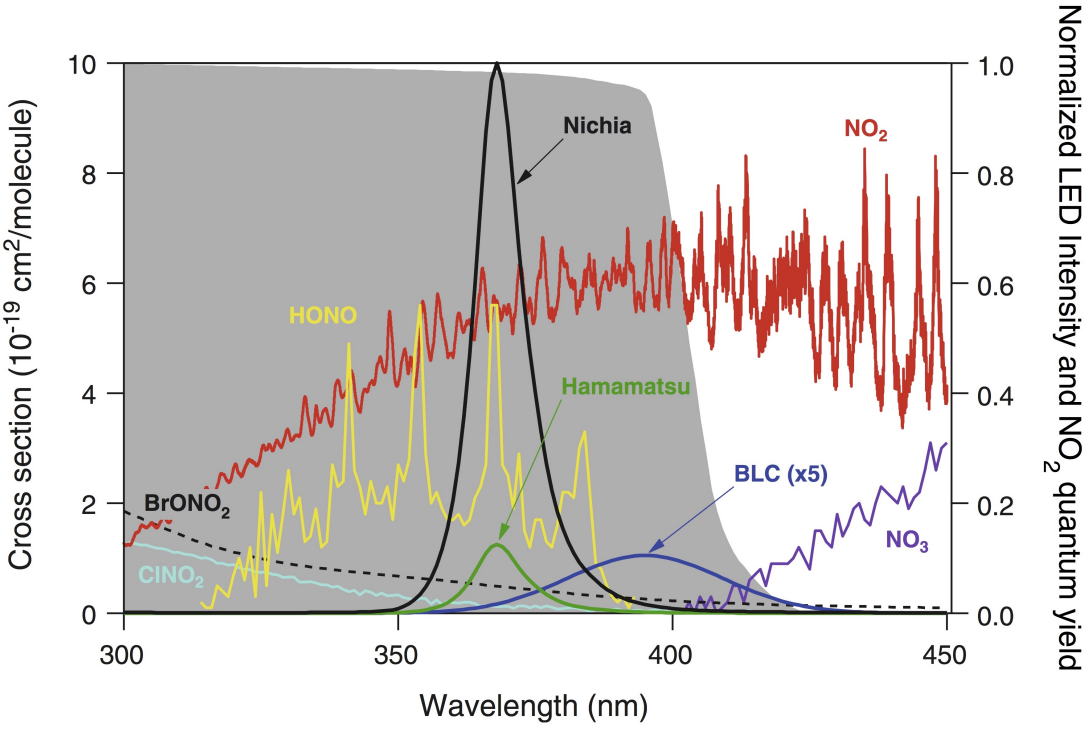

Figure 2.5: Quantum yield of photolysis products in relation to three PLC systems at different wavelengths. Taken from Pollack et al. (2010) [92].

In addition to photolysis compound inferences, thermal decomposition also plays a role in affecting the quality of NO_2 measurements using a PLC. The wavelengths used for most converters are < 400 nm. At these wavelengths, the LEDs release a large amount of heat which has the potential to thermally decompose certain compounds with in the

PLC. Laboratory studies have assessed the impact thermal decomposition have on NO_2 measurements. Reed et al. discussed the effect thermal decomposition of peroxyacetyl nitrate (PAN) has on measured NO_2, finding that 5% of the measured NO_2 was due to PAN [93]. For regions such as the remote tropics, concentrations of NO_x can be on the order of < 100 pptv, which makes understanding any potential interferences (both thermal and photolytic decomposition) highly important.

The PLC in this system is a blue−light photolytic converter housed in the control unit. It is designed to convert NO_2 to NO at an efficiency of $> 85\%$. The converter has a Teflon block with a milled cavity running down its centre, with 3 LEDs (395±20 nm) positioned on each side of the block. The Teflon acts to scatter light inside the cavity, ensuring maximum NO_2 to NO conversion. The volume within the cavity is 10 ml, and at a pressure of 300 Torr the resonance time is less than 0.2 s. The entire converter is enclosed with two Peltier coolers to keep the system at a lower temperature. This is due to the 6 LEDs expelling heat when operational. Figure 2.6 shows the Blue−light PLC with its enclosed Teflon block surrounded by two coolers.

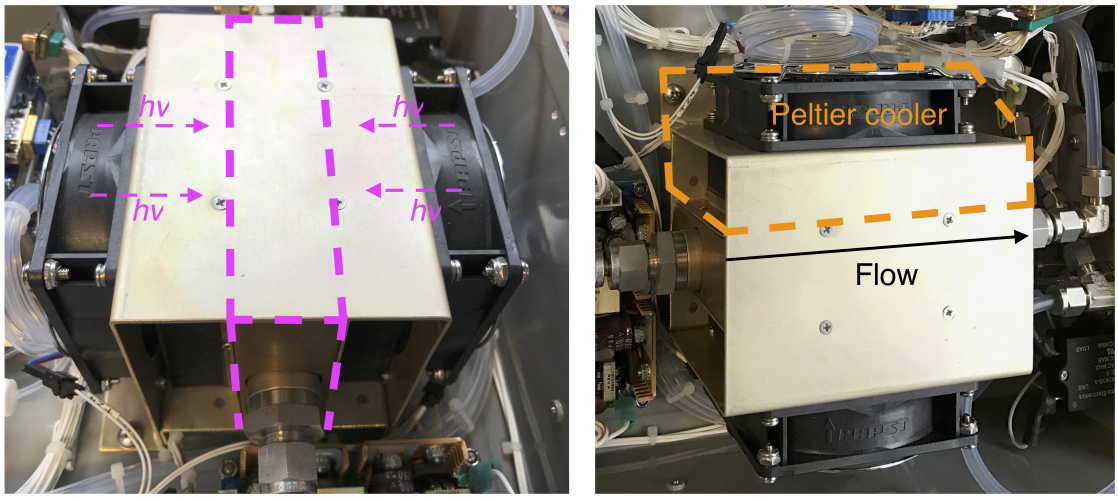

Figure 2.6: Photolytic converter cooled using Peltier coolers. Irradiation chamber shown as dotted purple area.

At a wavelength of 395 nm, the LEDs have low photolysis interferences. They are centred on a high NO_2 conversion peak and low peaks for; HONO, NO_3 and $ClNO_2$ (Figure 2.5). Under uncooled conditions the temperature inside the converter can rise to $> 70\ ^oC$ and so two Peltier coolers are used to keep the converter at between $35 - 50\ ^oC$. This ensures thermal decomposition interferences are kept to a minimum.

2.3.4 Detector Unit

The detector unit (Figure 2.7) contains the most vital components of the Fast−AQD−NO_x system. The unit houses the reaction vessels were ambient sample for each channel reacts with the O_3 supply leading to chemiluminescence reaction. The reaction vessels are situated right in front of the PMTs ensuring all chemiluminescence is measured. Each vessel is shielded from outside light interference which could potentially affect photons counted by the PMTs. Photons emitted from excited NO_2^* molecules are in the red-light region of the spectrum (> 600 nm) and travel to the surface of the PMT window. The photons pass through a red window and collide with the cathode generating a photoelectric current. This current is amplified as it passes along the PMT dynodes and is measured at the anode [94]. Figure 2.8 shows a schematic representation of a front facing PMT with current amplification occurring [95].

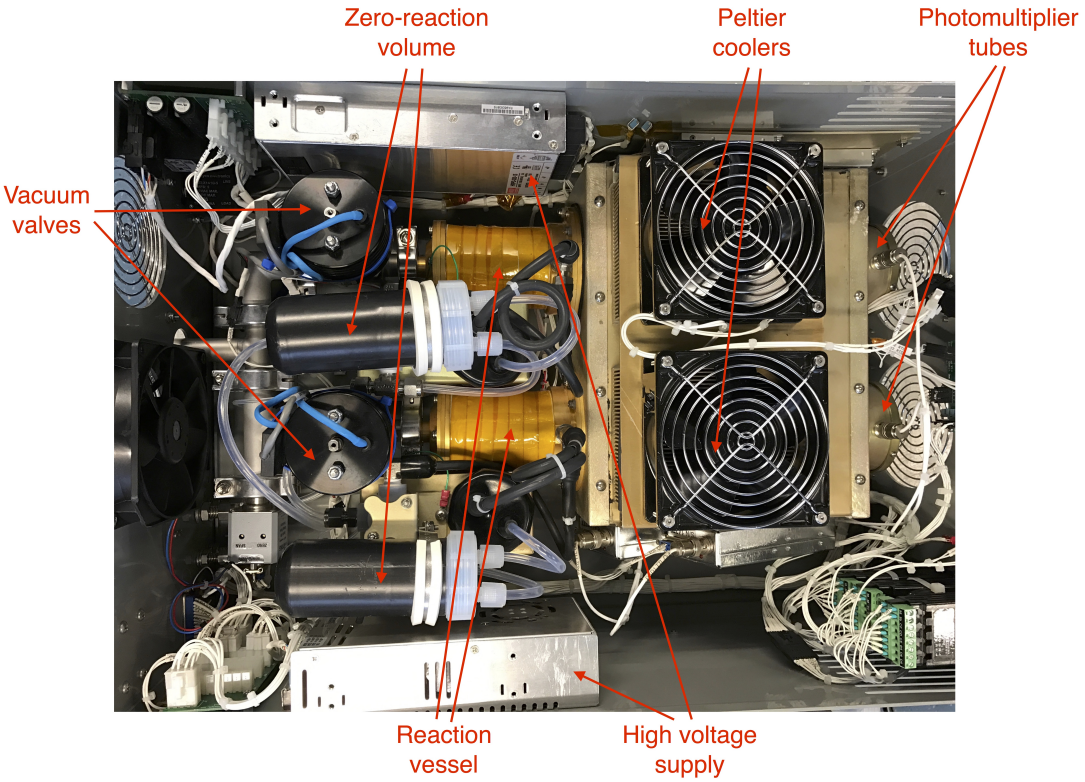

Figure 2.7: Detector Unit containing: dual photomultiplier tube (PMT) system with Peltier cooling, two high voltage supplier for the PMTs, reaction vessels and zero-volumes.

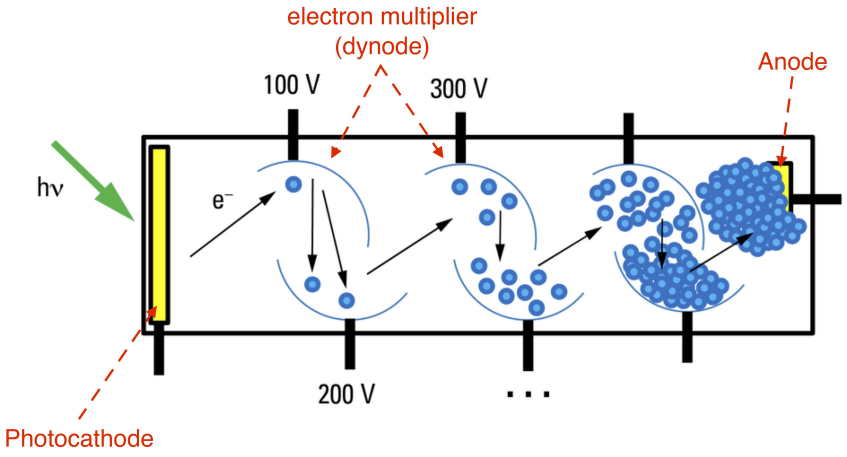

Figure 2.8: Front facing photomultiplier tube showing signal amplification as electrons move toward the anode from each dynode. Adapter from Borlinghaus. (2015) [95].

Photon counting is quantified using cooled PMTs at $<$ -50 ^{o}C. By cooling the PMTs down to sub−zero temperatures photoelectric events that are not the result of $NO_2{}^*$ chemiluminescence will be reduced. The main cause for this error is thermal noise, which is generated by electrons with enough thermal energy to escape from the cathode surface [96]. Also housed in the detector unit are two zero−volumes. Their purpose is to contain the reaction of the ambient sample with O_3 when the system is in zero mode, in order to assess the background count rate for each channel. Ambient sample reacts with the O_3 stream inside the zero−volume, meaning all the chemiluminescence will occur inside the zero−volume and not in front of the PMTs. Any measured counts within the reaction vessel now can be thought of as a base zero signal and incorporates the dark count on the PMTs.

2.3.5 Ozoniser Unit

The Ozoniser unit (Figure 2.9) supplies a constant feed of O_3 via coronal discharge reaction from a pure stream of O_2. Equations 2.10 and 2.11 define the generation of O_3 from O_2. A high voltage is passed over a dielectric surface, forming a coronal discharge within a glass tube. O_2 is flowed through the glass tube at a constant pressure. The O_2 molecules in the stream are broken apart by the coronal discharge giving 2 negatively charged oxygen atoms. These atoms react quickly with O_2 molecules forming O_3. Due to the Fast−AQD−NO_x system quantifying NO and NO_2 separately, two coronal discharge units are housed with the box giving a O_3 flow for each channel. O_3 flow pressure is kept constant, to allow for uniform chemiluminescence reaction.

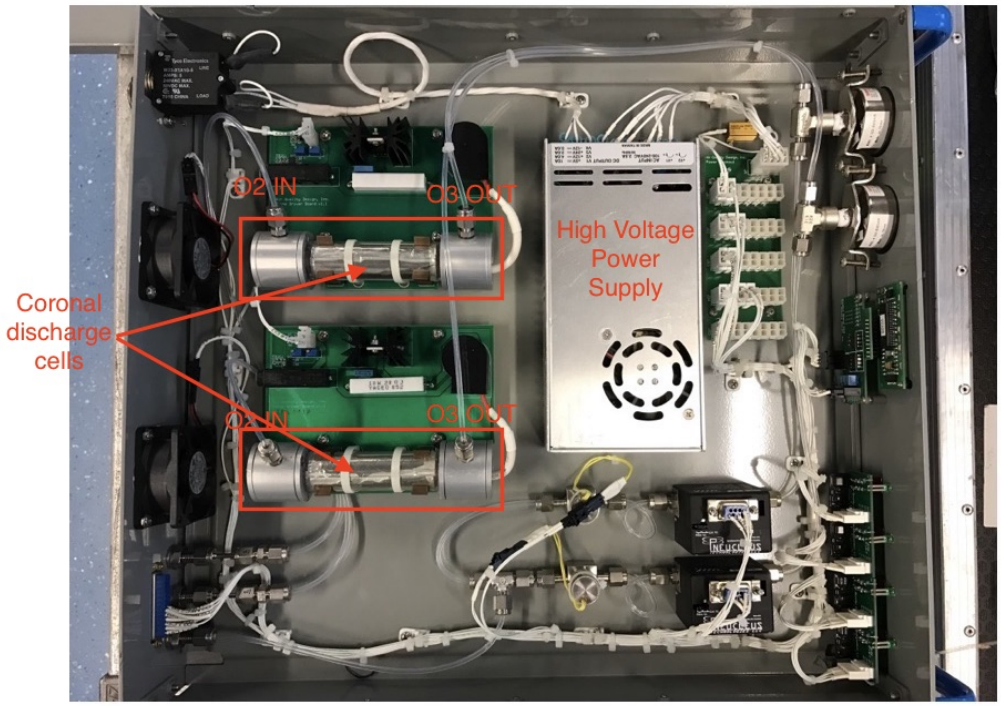

Figure 2.9: Ozoniser unit containing: two coronal discharge units, high voltage power supply, pressure gauges for each O_3 supply, two way valves and electronic switches.

$$O_2 + e^- \rightarrow 2O^- \tag{2.10}$$

$$O_2 + O^- \rightarrow O_3 \tag{2.11}$$

2.3.6 Pump Unit

Situated behind the main instrument rack on the aircraft is the pump tray. The tray houses two instrument pumps, both of which are shock mounted. The main instrument scroll pump, an Edward's nXDS 20, was specifically chosen due to its high efficiency and ability to handle humid ozone exhaust. The second pump, a by−pass pump, allows the system to stay at low pressure up to high altitude (approximately 23,000 ft). Due to the high levels of unreacted ozone in the waste sample, the instrument exhaust could not be vented to the atmosphere. A dry gas scrubber (Ozone Solutions) was attached to the scroll pump exhaust, with an ozone removal efficiency of 99.9%.

The plate also houses a 5 L pure O_2 cylinder required for ozone generation and a 5 L NO/N_2 calibration standard. Figure 2.10 shows the aircraft plate containing pumps, cylinders and circuit breakers.

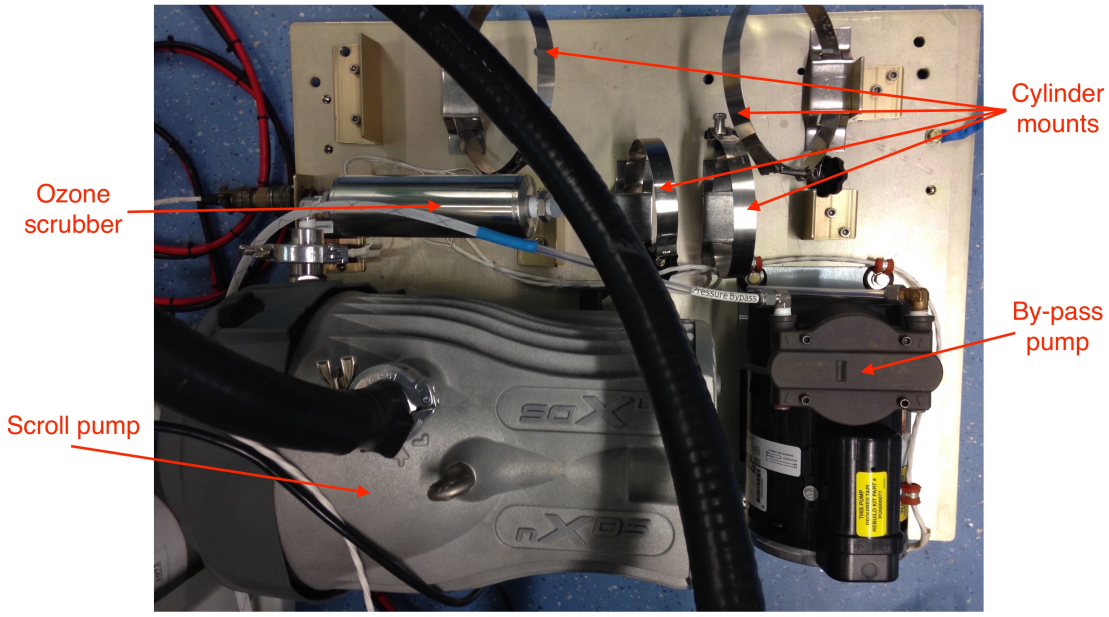

Figure 2.10: Aircraft pump tray containing high performance scroll pump with ozone scrubber, by−pass pump and gas cylinder mounts.

2.4 Research Flight Operation

A standard operating procedure (SOP) was followed when operating the Fast−AQD−NO_x. The SOP ensured the instrument was working at maximum efficiency and all data captured by the instrument has been correctly calibrated. Each flight would last a total of 9 hours; with 4 hours of instrument pre-flighting, 4 hours of science measurements and 1 hour of post-flight. The instrument is turned on 4 hours before take-off. Dry-ice is added to the metal reservoir above the PMTs cooling them down to $<$ -50 ^{o}C, taking around 2 hours. The 2 hours of cooling allowed the dark counts on each PMT to drop to below 5000 counts per second, giving a stable baseline. Figure 2.11 shows the first hour of cooling with the count rates of both PMTs dropping fast as the temperature decreases to below -50 ^{o}C.

The effect of water vapour is also considered in relation to the photon counting efficiency of each PMT. Water vapour acts as an excellent quencher of $NO_2{}^*$ chemiluminescence. As discussed by Boylan et al., water vapour is up to 10 times more effective than hydrogen and up to 3 time more effective than carbon dioxide at quenching chemiluminescence [97]. To account for quenching, a constant addition of deionised water vapour (d.H_2O) is added to each O_3 supply to negate the effect of changes in atmospheric water vapour. A full discuss of adding water vapour to O_3 can be found in Section 2.6.

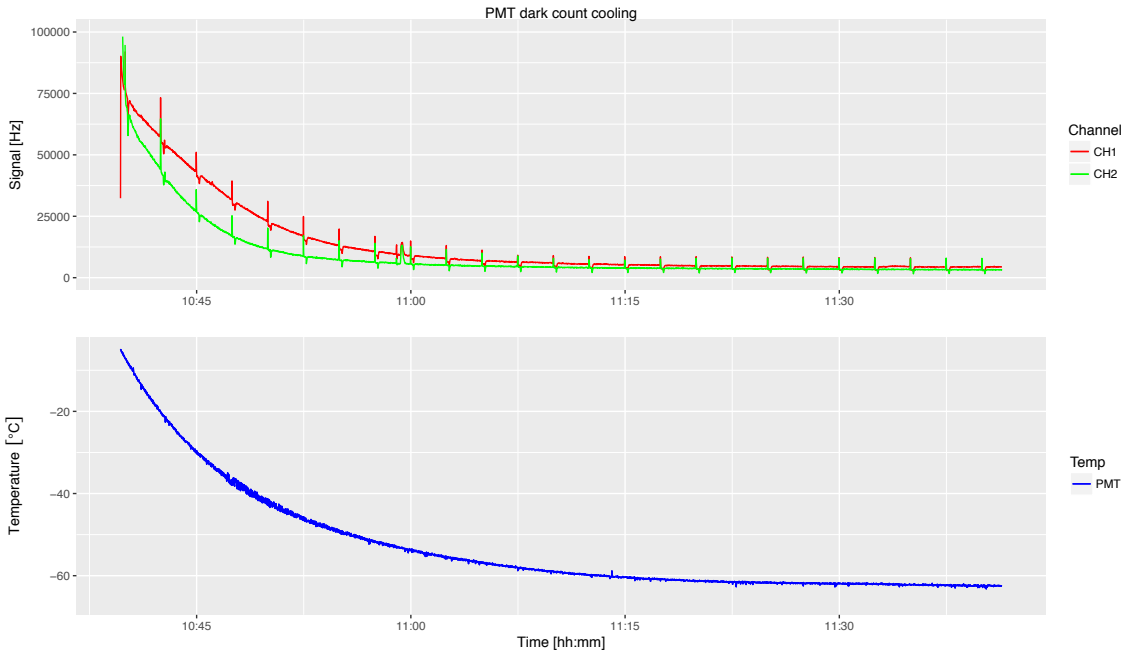

Figure 2.11: Background count rates of both channels decreasing as the PMT temperature drops due to dry ice cooling.

Whilst the instrument is on the ground, a zero-trap with particulate filter is attached to the sample inlet to give NO_x free air. The zero-trap has two components. The first; activated potassium permanganate reduced NO_2 to NO. The second component; activated charcoal, removes NO. The two components together remove all present NO_x from the ambient sample before it reaches the instrument and so giving a steady baseline. The zero−trap system also prevents the buildup of dust and other contaminate matter inside the instrument, which could affect the operation of the mass−flow controllers and instrument sensitivity through dust buildup on the red-windows of the PMTs.

After the instrument has reached a steady count rate on both channels (< 5000 counts per second), 4 pre−flight calibrations are done to ensure the instruments sensitivity is characterised before take−off. A full description of the calibration procedure is given in Section 2.5. Before calibrating for the first time, the calibration standards regulator is purged several times. This ensures any residual NO left inside the regulator overnight which may have reacted to form NO_2, is removed. Failure to do so may affect the accuracy of the calibration. The calibration line from the regulator to the instrument also requires conditioning before the first calibration can be conducted. The line may contain leftover calibration standard and so needed to be purged through for around 20 minutes, ensuring no loss of calibrant onto the line walls. Figure 2.12 shows the stabilisation of calibration gas signal over a 30 minute period. Higher signal is observed at the beginning due to possible residual NO_2 in the regulator.

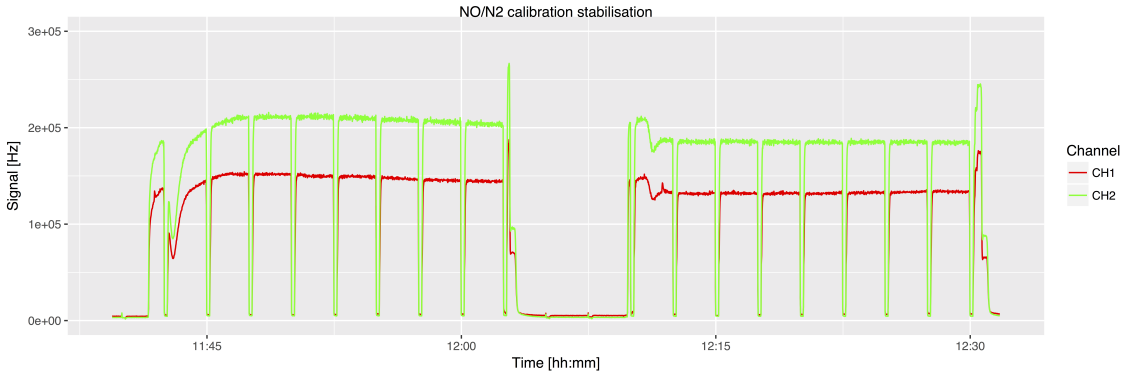

Figure 2.12: Stabilisation of the NO calibration signal, flowing through both channels for 30 minutes. 5 sccm of NO/N_2 added to a 'zero air' flow of 1500 sccm.

PLC−O_3−ClD is not an absolute technique with only a fraction of NO_2 being converted to NO by the blue−light PLC, requiring frequent calibrations to assess any changes in CE or sensitivity. Each calibration evaluates the sensitivities of each channel in counts per ppt and the CE of the blue light converter as a percentage. Section 2.5 gives an in−depth description of the calibration procedure. Typical channel sensitivity values were: 12 counts per ppt for Channel 1 and 9 counts per ppt for Channel 2. The CE was typically 85%.

After the system has been correctly calibrated, it is kept on the zero-trap until the plane has taken-off and cleared the influence of the airport, after which the main sample inlet can be connected. Further in−flight calibrations are conducted once an altitude of $>$ 5,000 m is reached. Calibrations need to be done as many time as possible during a flight in order to assess any changes in sensitivity. The data can then be used post-flight to correctly calculate NO and NO_2 mixing ratios. Figure 2.13 shows a schematic of a typical flight highlighting pre and post−flight calibrations, transit periods and low altitude measurements.

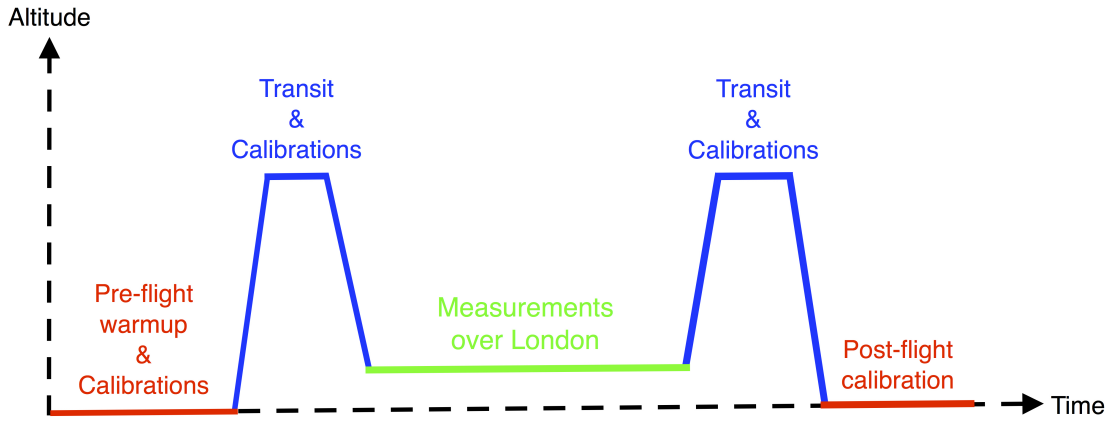

Figure 2.13: Schematic of a Fast−AQD−NO_x research flight. Red areas represent pre and post−flight when the instrument was calibrated. Blue areas show high altitude transits. Green areas show low altitude measurement periods.

2.5 Calibration Strategy

The calibration strategy for the Fast−AQD−NO_x is shown in Figure 2.14. Completion of the calibration takes 10 minutes. Controlled addition of the calibration gas is achieved using a mass−flow controller which is calibrated using a high accuracy gilibrator. Calibration of the mass-flow controller is conducted before and after a field campaign to ensure efficiency and flow volume has not changed during the campaign. Any deviations can be corrected for in post-campaign data analysis. Calibration gas (BOC supplied and calibrated) is added at a rate of 5 sccm to an ambient sample flow (zero−air) of 1500 sccm. A known concentration of NO/N_2 (5.0 ppm) is added to the ambient flow giving a NO dilution to 3.30 ppbv.

Further to adding a known amount of calibration gas to the instrument, a titration cell is also used to generate NO_2 from the calibration gas + O_2, in order to assess the blue−light PLCs convert efficiency. The cell houses a mercury pen lamp which generates UV light which generates O_3 from added O_2, which can react with the calibration gas to form NO_2. Generated NO_2 can then be using to evaluate the conversion efficiency of the blue−light PLC.

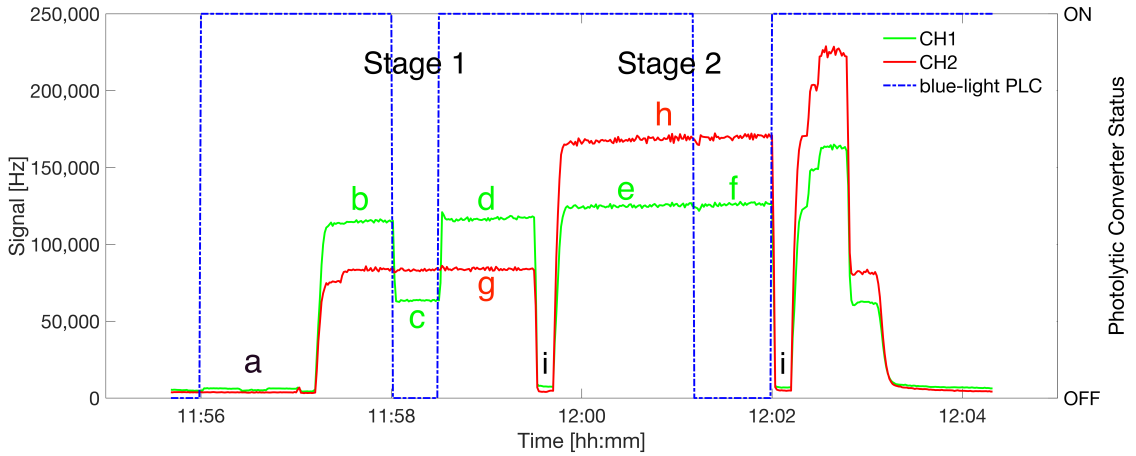

Figure 2.14: Calibration structure for Channel 1 and 2 containing two stages. The first assesses the conversion efficiency by blue−light PLC. The second calculates the nominal sensitivities of each PMT.

(a) Ambient sampling of 'zero air' containing low levels of NO_x

(b) Channel 1: blue−light PLC turned on, titration lamp making NO_2

(c) Channel 1: blue−light PLC turned off, titration lamp making NO_2

(d) Channel 1: blue−light PLC turned on, titration lamp making NO_2

(e) Channel 1: blue−light PLC turned on, titration lamp off

(f) Channel 1: blue−light PLC turned off, titration lamp off

(g) Channel 2: titration lamp is on

(h) Channel 2: titration lamp is off

(i) Channel 1 and 2 zero mode

The CE of the converter can be assessed as described in Equation 2.12. Step (e) defines the count rate of added NO standard without titration and the blue−light PLC turned on. This step can also be used to asses any impurities in the calibration standard. Higher counts will be measured during step (e) compared to (f) if NO containing impurities are present. Step (f) defines the count rate of NO without titration and the blue−light PLC turned off. Step (b) defines the count rate of NO + titrated NO2 with the blue−light PLC turned on. Step (c) defines the count rate of NO + titrated NO2 with blue−light PLC turned off.

$$CE = 1 - \frac{e - b}{f - c} \tag{2.12}$$

In addition to CE, the sensitivities of both PMTs requires constant assessment. PMT count rate is directly proportional to NO mixing ratio, following a linear relationship during chemiluminescence analysis when O_3 is in excess. Equation 2.13 defines the nominal sensitivity of Channel 1, which measures NO + converted fraction of NO_2. $NO2_{calconc}$ is the concentration of the standard once added to the ambient sample flow (3.3 ppbv). Equation 2.14 defines nominal sensitivity of Channel 2, which measured NO. $NO_{calconc}$ is the concentration of the standard added. Using the nominals and CE calculated during a calibration, NO and NO_2 mixing ratios can be evaluated as defined in Equations 2.15−2.16.

$$CH1_{nom} = \frac{e - i}{NO2_{cal\ conc}} \tag{2.13}$$

$$CH2_{nom} = \frac{h - i}{NO_{cal\ conc}} \tag{2.14}$$

$$NOppt = \frac{CH2_{Hz} - CH2_{background}}{CH2_{nom}} \tag{2.15}$$

$$NO_2ppt = \frac{\left(\frac{CH1_{Hz} - CH1_{background}}{CH1_{nom}}\right) - NOppt}{CE} \tag{2.16}$$

2.6 O_3 Water Vapour Addition

Water vapour is an excellent quencher of chemiluminescence and is known to affect the sensitivity of chemiluminescence instruments, such as the one discussed. Mathews discussed the effect interference molecules (third body quenchers) have on measured NO/ NO_2 chemiluminescence. These molecules include; CO_2, CO, O_2, H_2 and H_2O [98]. Equation's 2.17−2.19 describes the reaction of NO with O_3, resulting in either photonic emission (Equation 2.18) or collisional energy transfer (Equation 2.19) by which chemiluminescence does not occur. The intensity of the photoemission (I) is described in Equation 2.20, with M representing the interference molecule [98].

$$NO + O_3 \xrightarrow{k_1} NO_2^* + O_2 \tag{2.17}$$

$$NO_2^* \xrightarrow{k_2} NO_2 + hv \tag{2.18}$$

$$NO_2^* + M \xrightarrow{k_3} NO_2 + M \tag{2.19}$$

$$I = \frac{k_1 k_2 [NO][O_2]}{k_2 + \Sigma_M k_{3M}[M]} \tag{2.20}$$

Gerboles et al. found that increasing the absolute humidity up to 18 g m^{-3}, the measured NO concentration decreased by approximately 8% [99]. To account for changing atmospheric water vapour content during flights, the O_3 supplies to each channel are passed through deionised water head space gaining saturation. Ridley et al., advised adding at least 30 parts per thousand (ppth) of water vapour to chemiluminescence reaction vessels, in order to remove any instrument dependent on humidity [100].

To assess the amount of water vapour added to the reaction vessels, a known amount of water was added to each O_3 humidification volume. The instrument was then run for 5 hours under flight conditions with O_3 humidification turned on. After the 5 hour period each vessel was weighted using a 4 decimal place analytical balance and the amount of water removed from each vessel assessed. At a constant flow rate of 100 sccm per minute, the water vapour content of the humidified O_3 stream was found to be 35.5 ppth. After the O_3 enters the reaction vessel the water vapour content is diluted down into to an overall flow of 1600 sccm per minute, giving a water vapour content in the reaction vessels

of 32.3 ppth. During flights over London which are discussed in Chapters 4 and 5, the average water vapour content (20 ^{o}C, 50% relative humidity) was calculated to be 7 ppth which is considerably less than in the reaction vessels. The addition of 32.2 ppth of water vapour into the reaction vessels makes the instruments sensitivity independent on changing ambient water vapour.

2.7 Error Analysis

As with any scientific technique, understanding the error/ uncertainty associated with the measurement is vital. Two types of measurement error (precision and accuracy) affect the Fast−AQD−NO_x. The precision of a measurement quantifies the random error. As defined by Lee et al. (2009), the precision of a NO_x chemiluminescence instrument can be evaluated by analysing the zero−rate photon counting of each PMT [101].

Photon counting is a well−established technique, with statistics following a Poisson distribution [102, 103]. The precision for each channel is proportional to 2 times the standard deviation (2σ) of the zero−air count rate distribution, which is converted to ppt using calculated channel sensitivities. A Gaussian distribution is used here over a Poisson distribution due to the count rate ($>$ 3000 counts s^{-1}) being high enough to ensure both distributions become essentially identical [101, 104].

To evaluate the precision of each PMT, the system is set to sample 'zero air', generating signal to noise statistics for each channel. Zero air is defined as air containing zero NO_x or at a concentration well below the detection limit of the system. For high accuracy detection of low NO_x mixing ratios ($<$ 50 pptv), such as in remote environments, high purity zero air is essential. Figure 2.15 shows measured NO and NO_2 mixing ratios from 'zero air' over a two-hour period. Average measured NO is 25.13 ppt and NO_2 is -12.67 ppt, which suggests that the NO_2 in the 'zero air' is below the instruments limit of detection and so generates negative values.

Figure 2.16 shows the normalised frequency distribution of the 'zero air' mixing ratio data for both measurement rates. The reduction in the data scatter is equal to 2σ divided by the square root of 9.2, so indicating the instrument is measuring at approximately 9 Hz. For 1 Hz data, the 2σ for NO was found to be 22.19 ppt and for NO_2 41.53 ppt. For 9 Hz data, the 2σ for NO was found to be 67.32 ppt and for NO_2 125.96 ppt.

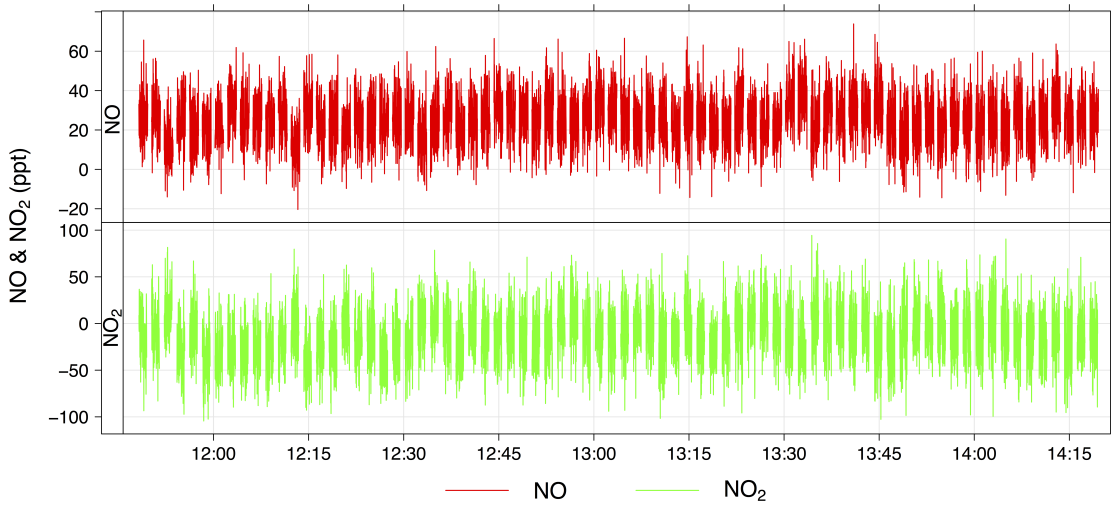

Figure 2.15: NO and NO_2 'zero air' data from a two hour period. Average NO of 25.13 ppt and NO_2 of -12.67 ppt, suggesting the NO_2 is below the instruments limit of detection.

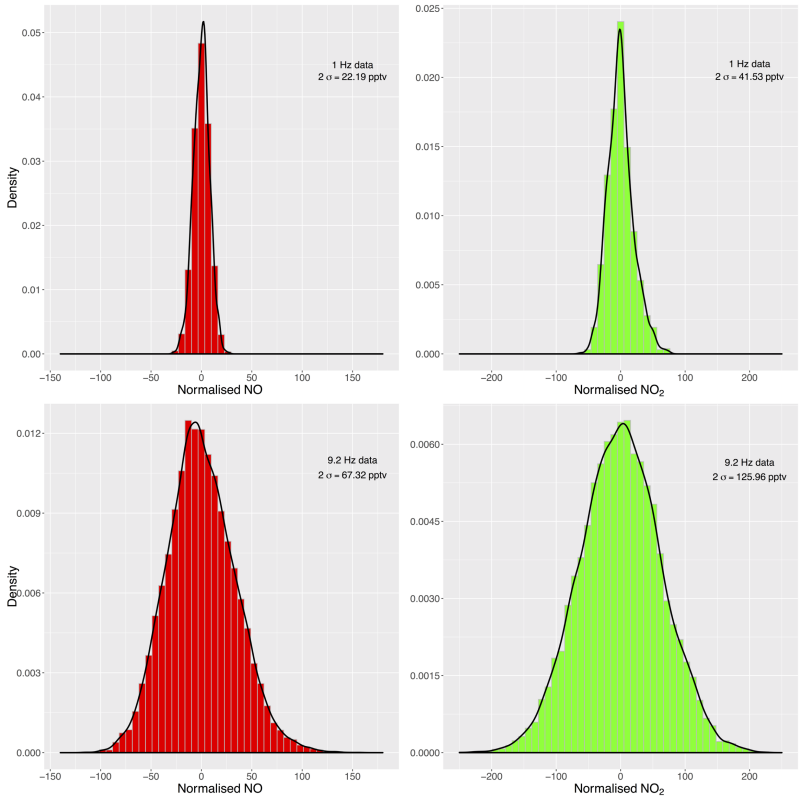

Figure 2.16: Top) Frequency distributions for 1 Hz NO and NO_2 [ppt] 'zero air' data over a two hour period. Bottom) Frequency distributions for 9 Hz NO and NO_2 [pptv] 'zero air' data over the same period.

Along with precision, the accuracy of the NO/ NO_2 measurement is also vital in understanding the total error. The accuracy of a measurement describes the systematic error associated with the instrument. To calculate the accuracy on the measurements, three types of uncertainty were assessed [101]:

(i) The sample and calibration mass−flow controller accuracies.

(ii) The accuracy of the NO concentration in the calibration standard.

(iii) The accuracy in determining the artefact ('fake NO' signal [105]) on each channel.

The uncertainty on the mass-flow controllers for each channel and also addition of the 5 sccm of NO/N_2 calibration standard is ±1%. To ensure the accuracy of the mass-flow controllers, they are calibrated before and after a field campaign using a gilibrator. Another important uncertainty is the accuracy of the NO/N_2 standard used during calibrations. As quoted by BOC who supplied the cylinder, the standard is accurate to ±1%. BOC quote calibration gas stability for 5 years, after which time variability maybe seen in the standard's NO concentration. The overall accuracy is calculated to be 4% from the; calibration standard, mass−flow controller accuracy and CE accuracy of the blue−light converter. By taking the root sum of the squares of the accuracy and precision errors, the overall uncertainty associated with each measurement can be calculated. Tables 2.1 to 2.4 gives example NO and NO_2 mixing ratio values for both data acquisition rates, and the overall uncertainty for each measurement.

Table 2.1: Errors associated with 1 Hz measurements of NO.

NO / pptv	Accuracy/ %	Precision/ %	Total error/ %
10,000	4.00	0.22	4.00
5,000	4.00	0.44	4.02
2,000	4.00	1.11	4.15
1,000	4.00	2.22	4.75
500	4.00	4.44	5.97
100	4.00	22.19	22.55

Table 2.2: Errors associated with 1 Hz measurements of NO_2.

NO_2 / pptv	Accuracy/ %	Precision/ %	Total error/ %
10,000	4.00	0.42	4.02
5,000	4.00	0.83	4.09
2,000	4.00	2.10	4.15
1,000	4.00	4.15	5.77
500	4.00	8.31	9.22
100	4.00	41.52	41.72

Table 2.3: Errors associated with 9 Hz measurements of NO.

NO/ pptv	Accuracy/ %	Precision/ %	Total error/ %
10,000	4.00	0.67	4.06
5,000	4.00	1.35	4.22
2,000	4.00	3.37	5.23
1,000	4.00	6.73	7.83
500	4.00	13.46	14.05
100	4.00	67.32	67.44

Table 2.4: Errors associated with 9 Hz measurements of NO_2.

NO_2/ pptv	Accuracy/ %	Precision/ %	Total error/ %
10,000	4.00	1.25	4.19
5,000	4.00	2.52	4.73
2,000	4.00	6.30	7.46
1,000	4.00	12.59	13.22
500	4.00	25.19	25.51

2.8 Conclusions

A chemiluminescence system has been specifically designed to operate on−board the NERC Dornier 228 Aircraft. The system is a dual channel instrument and can quantify NO and NO_2 in parallel. Housed in a flight rack, the system can quantify mixing ratios of NO_x up to an altitude of 23,000 ft via pressure controlling the system at a constant low pressure. NO is quantified through ozone chemiluminescence showing linear response to measure photon count rates. NO_2 is quantified through indirect ozone chemiluminescence reaction. NO_2 is converted to NO using a blue−light photolytic light converter at 395 nm. At 395 nm NO_2 is converted to NO at an efficiency of above 85%, with ozone chemiluminescence then used to quantify the NO + converted NO_2 fraction in the sample.

The system is calibrated using a 5 ppm NO/N_2 standard before, during and at the end each flight, ensuring channel sensitives and conversion efficiency of NO_2 blue−light PLC are fully captured throughout a flight. During field campaigns, the calibration standard needs to be constantly assessed to ensure the concentration within the standard stays constant by comparison to a higher accuracy standard before and after the campaign has been completed. Overall the instrument is perfectly suited for emission analysis studies, as discussed in Chapter 4. It is a fast time resolution instrument which can measure NO and NO_2 mixing ratios at 9 Hz. Having a fast responding instrument is vital for eddy covariance calculations, as turbulent changes in concentration must be captured.

Chapter 3

Methodology for Airborne Flux Calculation and Surface Layer Interaction

This chapter discusses airborne eddy−covariance theory and the specifications required for calculating high spatiality fluxes over a large city such as London. The described technique couples airborne eddy−covariance with a footprint model allowing for top−down comparison of emission inventories, with specific parameterisation for NO_x and VOCs.

3.1 Introduction

The emission of trace gases into the atmosphere is an important process, driving air quality on both regional and global scales. Emissions can stem from anthropogenic sources such as vehicles and biological processes such as isoprene emissions from woodland [106, 107]. Both sources have the potential to affect air quality considerably within the local region. Understanding global emission sources is vital for constraining emission models and helping continued improvement in global air quality.

Assessment of emissions via scientific measurement classically has followed an eddy-covariance approach, from tower sites. Eddy−covariance (EC) quantifies the correlation between atmospheric eddy movement and changes of an atmospheric component, such as trace gas concentration or temperature on an instantaneous time scale. Equation 3.1 defines the eddy−flux (F). P_d is the density of air, w' is the instantaneous change of the vertical wind component and c' is the instantaneous change in the concentration component [108]. The overline represents the mean of each variable.

$$F = \overline{P_d w' c'} \tag{3.1}$$

Atmospheric transport is a chaotic process, with non−linear flows generating turbulent structure. This non−uniformity of the atmosphere leads to the formation of eddies as highlighted in Figure 3.1. Atmospheric eddies found in the lower troposphere range in size, shape and direction of rotation. It is this dynamic process that drives the emission/ deposition of atmosphere tracers in the troposphere. Figure 3.2 shows a schematic representation of two eddies, with one rotating clockwise representing in the negative removal of concentration to the surface (deposition) and the other in a clockwise fashion leading to the positive removal of concentration from the surface (emission).

Figure 3.1: Atmospheric transport eddies moving across a vegetated region, varying in size and direction of rotation. Taken from Burba. (2013) [108].

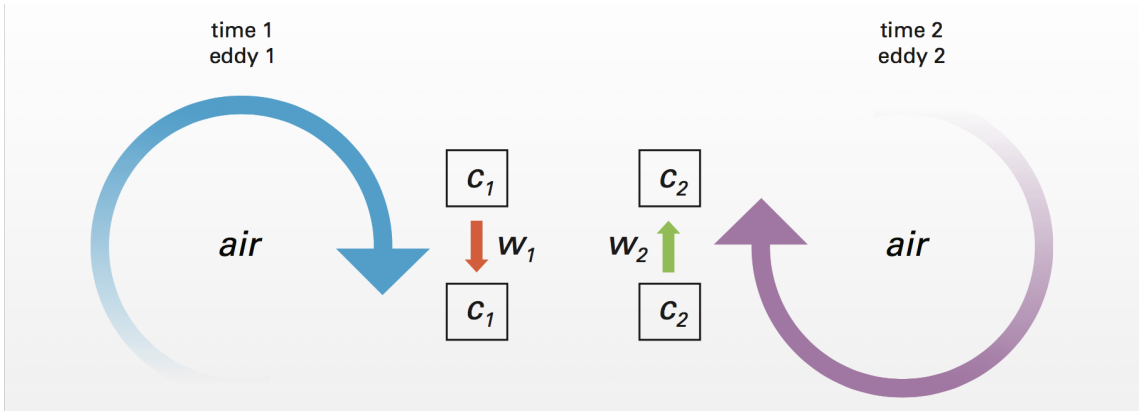

Figure 3.2: Representation of emission and deposition via eddy−movement. Eddy 1 shows the movement of concentration 1 (C_1) downwards, and eddy 2 the movement of concentration 2 (C_2) upwards. Taken from Burba. (2013) [108].

The ground work for EC was first laid out by the work of Reynolds (1894) and Scrase (1930) [109, 110]. However, due to limitations in technology at the time, the now standard EC approach was first described by Swinbank (1951) for the evaluation of heat and water vapour transport by eddies in the lower atmosphere [111]. Swinbank was able to measure these fluxes using a fast responding hot−wire which generated fluctuating vertical wind data. The rise of EC has been driven by the technological improvements over the last 60 years, allowing analysis of micro−scale meteorological changes in real time. EC has become a standard tool for evaluating transport within the lower atmosphere. Original studies focusing on ecosystem exchange. Baldocchi et al. (1988) discussed the applicability

of EC in helping advance the measurement and understanding of biosphere/ atmosphere exchange, and the improvement such an approach would bring over more classical chamber techniques [112]. EC is now a key approach used in assessing carbon dioxide (CO_2) exchanges rate from ecosystem, allowing for real time evaluation over long time periods. As discussed by Baldocchi et al. (2003) the technique has replaced traditional tools such as leaf cuvettes and soil chamber experiments, all of which have known artefacts [113, 114, 115].

Previous work has shown the advantages of using EC at tower measurement site towards evaluating surface emissions. Studies have investigated emissions stemming from biological sources such as vegetation and forestry [116, 117], and urban emissions [106, 118, 119, 120]. The mentioned studies are just a fraction of the total published work on tower site EC. However, they all share a common disadvantage. Tower sites are highly localised, which means that any measurements made will be strongly influenced by the meteorological conditions. In densely populated regions such as major cities, areas where measurements sites can be set up maybe very restrictive and not always at the point of most interest.

Due to the limited spatiality of a tower, moving platforms such as an aircraft would be more beneficial when assessing emissions of an entire city. Measurements from aircraft allow assessment of the atmosphere over large distances and at a range of altitudes. Improvements in instrument design over last 20 years has allowed eddy-covariance to be possible on−board aircraft. Previous studies have used AEC for assessing volatile organic carbons (VOCs) emissions over major cities such as Mexico City [121] and biogenic sources of isoprene in California [107]. Building upon previous work [107, 121], this Chapter discusses the methodologies for calculating and evaluating anthropogenic and biogenic fluxes from an aircraft.

3.2 Airborne Eddy-Covariance

Airborne eddy−covariance (AEC) is a developing field, with growing numbers of studies proving its applicability towards assessing surface layer emissions for a wide range of atmospheric tracers [107, 121, 122, 123, 124, 125]. To date, the core technique used for calculated fluxes via EC from aircraft has been continuous wavelet transform (CWT). CWT uses a wavelet waveform to extract frequency and time information from a data signal. For AEC, CWT is used to quantify frequency and time information from instantaneous vertical wind speed and concentration signals, which can then be used to calculate flux in accordance with Equation 3.1.

Wavelets being used for signal analysis started in seismology, where they are now commonly used to assess earthquake data [126]. Recently, wavelets have found new application in the field of atmospheric science, analysing turbulence data signals. Due to the uniqueness of wavelet waveforms, they are perfectly suited for analysing instantaneous turbulent changes on micro−timescales.

3.2.1 Introduction to Wavelets

A wavelet, unlike a normal sine waves used in Fast Fourier Transform (FFT), is a localised signal with a defined start and end point, averaging to 0. The shape of a wavelet's waveform can be tailored to suit the application, giving them a unique strength over conventional methods. The tropospheric mixing layer is in a constant state of flux, highly turbulent and chaotic in nature. This structure is highly non−uniform, with atmospheric eddies of ranging sizes and directions of rotation. This non−uniformity makes wavelet use perfectly aligned to generate useful information about micro−scale changes occurring within the mixing layer. Figure 3.3 depicts 4 typical wavelet waveforms all showing unique characteristics.

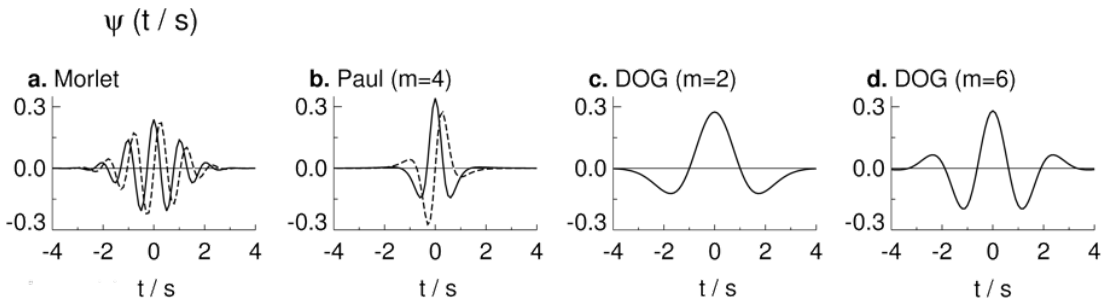

Figure 3.3: Wavelet waveforms in the time domain. a) Morlet wavelet, b) Paul wavelet, c) DOG wavelet m=2, d) DOG wavelet m=6. m represents the wavelet function parameter. The solid line shows the real part of the wavelet and the dotted the imaginary. Adapted from Torrence & Compo. (1998) [127].

The Morlet wavelet has been used in previous studies for calculating AEC fluxes [107, 121, 124]. The Morlet waveform has a main Gaussian peak at time 0, with symmetrically degrading signal oscillations in both time directions. The Morlet is a complex waveform, with real and imaginary parts, as shown in Figure 3.3a. Mathematically, Equation 3.2 describes the Morlet waveform. ω_0 represents the non-dimensional frequency and η the non-dimensional time. Equation 3.3 denotes localisation of the original mother wavelet in the frequency and time domains, known as the daughter wavelet. The mother wavelet is denoted by ψ, parameters a & b act to scale and localise the wavelet in the frequency and time domains.

$$\psi_0(\eta) = \pi^{-\frac{1}{4}} \exp^{i\omega_0\eta} \exp^{-\eta^2/2} \tag{3.2}$$

$$\psi_{a,b}(t) = \frac{1}{\sqrt{a}}\psi\left(\frac{t-b}{a}\right) \tag{3.3}$$

3.2.2 Eddy-Covariance Continuous Wavelet Transform

CWT compares a discrete data signal to a wavelet waveform over defined frequency and time intervals. The convolution of a signal through CWT can be defined as the following, where signal *x(n)* of N data points is transformed by the daughter wavelet, which has been scaled (a), spaced (b) and had a normalization factor (p) specific to that wavelet applied to it, as defined in Equation 3.4 [122].

$$w_x(a,b) = \sum_{n=0}^{N} x(n)\, \psi^*_{p,a,b}(n) \tag{3.4}$$

CWT generates coefficients dependent on the values chosen for the wavelet scaling parameters (a & b). A 2−dimensional picture can be generated of the signal in terms of frequency and time, by plotting the group of coefficients generated from the CWT as a scalogram. The scalogram represents all possible coefficients from all variations of a & b, as a matrix which is defined in Equation 3.5. The matrix is defined along the x axis in the time domain and y axis in the frequency domain [123]. As for any flux calculation, two variables of interest are being compared to each other, requiring 2−dimensional CWT. The mathematics involved are identical, the only difference being the matrix produced is of a complex nature due to the Morlet waveform being complex (Equation 3.6). This is described in Equation 3.6 as the star (*).

$$Coefficient_{matrix} = |w_x(a,b)|^2 \tag{3.5}$$

$$Coefficient_{matrix} = w_x(a,b)\, w_y(a,b)^* \tag{3.6}$$

Taking the transformation further, the complete covariance between two signals (x & y) can be deduced by looking at global covariance across all possible frequency scales as shown in Equation 3.7. The average frequency resolved coefficients for a chosen segment of time gives a real covariance for the two signals, which can then be used to calculate for the chosen segment of time a true eddy−flux value [123].

During 2−dimensional CWT, the wavelet is scaled in both frequency and time domains (Equations 3.8 & 3.9). Frequency domain scales (a_j) are increased exponentially, $j = 0$ to J, with J being the largest frequency scale. The extreme frequency scale used is equal to the Nyquist frequency, and represents 2 times the sample period of the tracer instrument. Time domain scales (b_n) are increased linearly, from $n = 0$ to N-1, with N being length of data series. δj sets the frequency increments, with previous studies using a δj value of 0.25 [107, 123]. δt is the sampling period of the data series. $\delta t = 0.1$ s for NO/NO_2 and 0.5 s for VOCs. Overall this method allows for the calculation of local fluxes, including all eddy transport scales.

$$COV_{a,b} = \frac{\delta j \delta t}{C_\delta N} \sum_{j=0}^{J} \sum_{n=0}^{N-1} \frac{w_x\left(a_j, b_n\right) w_y\left(a_j, b_n\right)^*}{a_j} \tag{3.7}$$

$$a_j = a_0 2^{j\delta j} \tag{3.8}$$

$$b_n = n\delta t \tag{3.9}$$

3.3 Eddy-Covariance Algorithm

Using the CWT principles outlined above, it has been possible to calculate localised fluxes from an aircraft via disjunct eddy−covariance using an algorithm adapted from work by Karl et al. (2013) and Misztal et al. (2014) [107, 124]. The algorithm is coded in the Matlab^{TM} coding language, and has been specifically adapted under the guidance of Dr. Misztal for calculating fluxes over London and Southern England, as discussed in Chapter's 4 and 5.

3.3.1 Data Section and Resampling

The algorithm conducts CWT analysis over several stages. The first stage involves resampling fast meteorology data at 20 Hz to the time stamp of either NO/NO_2 mixing ratios at 9 Hz or VOC mixing ratios at 2 Hz through interpolation, giving an uniform dataset of micrometeorology and concentration data. Mixing ratio data is converted from ppbv to mg m^{-3} using known temperature, pressure and molecular weight. The user defines the section of flight data for which to conduct AEC. The selected region appears highlighted in red on the flight track (Figure 3.4 lower). Areas containing high bank angles, such as the region next to the start of the selected region (Figure 3.4 Upper), are not used for calculated eddy−fluxes. High bank angles from sharp aircraft turning affects AIMMS−20 measured wind vectors.

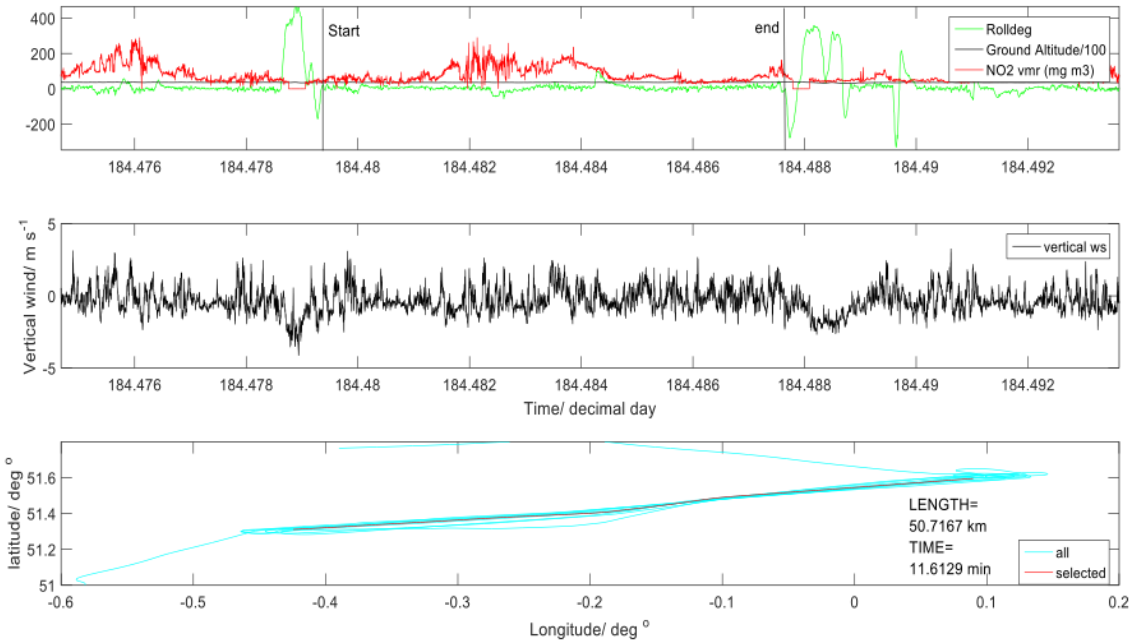

Figure 3.4: Top) roll degree of the aircraft (green), ground altitude/100 (black) at 360 m and NO_2 concentration in mg m^3. The selected region for AEC is shown in the box. Middle) vertical wind speed in m s^{-1}. Bottom) flight track with selected region highlighted in red.

3.3.2 De−Trending and Lag−Time Correction

The next stage involves the de−trending of vertical wind speed and concentration data. Reynolds decomposition is used to evaluate the degree of variation of a data series from its mean. During Reynolds decomposition, the mean of the data series is subtracted from each individually data point along the time series, giving instantaneous change from the mean.

Measurements of meteorology and concentration were obtained at different positions on−board the aircraft. Meteorology was obtained using a AIMMS−20 probe [128] mounted under the left wing, and trace gases were sampled out of a forward−facing steel inlet. The difference in sampling region and the time taken for samples to reach the instrument results in the two data series having a lag time, and so requires correction to align the data sets.

To assess and correct for the lag time, the correlation coefficient between the vertical wind speed and the concentration is calculated. Figure 3.5, shows the normalised correlation coefficients for a C_2 alkyl−benzenes flight leg over London, after the lag time has been corrected. Calculated lag times ranges between 2−10 s. Only flight legs which showed clear covariance peaks were used. This shifted the calculated fluxes to the positive end; however, flight legs without a clear peak could not be accurately corrected. Clear covariance peaks may not occur if bidirectional flux occurs. If a positive and negative flux occur in a short time period, the overall emission will be zero.

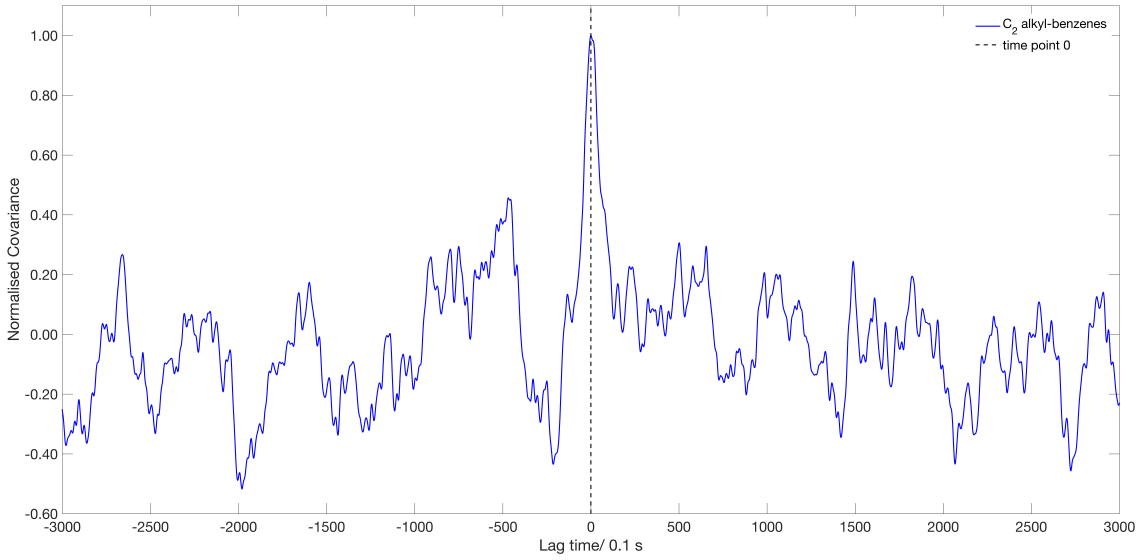

Figure 3.5: Normalised correlation coefficient between vertical wind speed and instantaneous concentration, showing no lag between the two variables and maximum correlation at time 0.

3.3.3 CWT Parameterisation

CWT is parameterised to consider all possible eddy period contributions to the observed flux. Conducting wavelet transformation in Matlab^{TM} takes on the following form, with the user defining the following parameters (Equation 3.10) [129]. The chosen mother wavelet is the Morlet, and δt is set to either 0.1 s for NO/ NO_2 or 0.5 s for VOCs. Pad allows the user to pad the data series with enough zeros to allow the value of N to increase to the next power of 2. This speeds up the transform process; however, does increase error at the start and end of the time series, and so these regions are ignored. S_0 defines the smallest frequency scale which is set normally to 2 x the sample rate. The final parameter J_1 defines the number of frequency scale the wavelet transform is conducted over. A full list of each parameter and value used is shown in Table 3.1.

$$[WAVE, Period, Scale, COI] = wavelet\,(data, \delta t, Pad, \delta_j, S_0, J_1, MOTHER) \quad (3.10)$$

Table 3.1: Matlab^{TM} CWT analysis parameters

CWT Parameter	Values
data	c′ / w′
δt	0.1
Pad	TRUE
δj	0.25
S_0	0.05
J_1	128
MOTHER	Morlet

Using the CWT parameterisation above, the global scalogram is calculated for the covariance between instantaneous variations in vertical wind speed and concentration. Figure 3.6a), represents the de−trended data for both the vertical wind and the C_2 alkyl−benzenes concentration, after the lag time has been corrected for. Figure 3.6b), depicts the wavelet power spectrum for the flight section. The distance travelled is displayed on the x−axis (time domain) and the y−axis giving the eddy contributions integrated over all periods (frequency domain). The cone of influence is also plotted as a dotted black line. The cross−scalogram is colour scaled in terms of the calculated coefficient generated for each wavelet transform, with the higher the colour value the more correlated the vertical wind with an increase in measured analyte concentration. Figure 3.6c) shows the average cross−variance for all the influencing eddy contributions along the flight leg, which is used to calculate flux along the flight track.

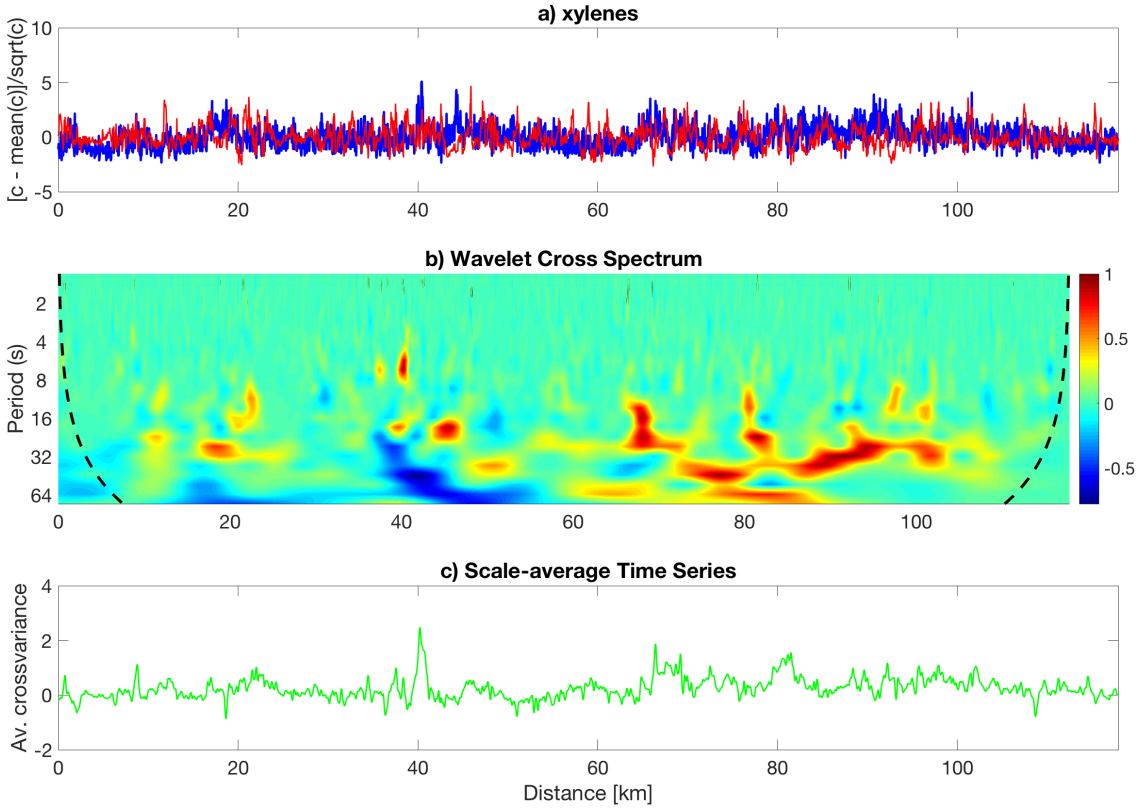

Figure 3.6: a) Variance of C_2 alkyl−benzenes and vertical wind speed, b) time resolved wavelet power spectrum with cone of influence shown as black dotted line, c) the average cross−variance between C_2 alkyl−benzenes and vertical wind.

3.3.4 Frequency Analysis

As with all EC analysis, stringent data quality is essential. Analysis of CWT frequency spectra is done to ensure the process has generated high quality fluxes. FFT is conducted alongside CWT to obtain a reference spectrum. Both CWT and FFT generate signal frequency information, showing similar frequency spectra; although, it should be noted that whilst FFT is affect by non-stationary and non-homogeneity, it allows for a good reference point.

Figure 3.7 depicts normalised power spectra for both temperature flux and VOC flux using both EC methods plotted in terms of frequency contributions. The co−spectra (Figure 3.7a)) shows the normalised flux frequency distribution of CWT and FFT. The cumulative co-spectra (Figure 3.7b)) shows the cumulative sum of all influencing frequencies up to a value of 1. Both CWT and FFT show similar low frequency structure. The analysis is limited to frequencies below the disjunct sampling time 0.2 Hz for VOCs and 9 Hz for NO/NO_2. The temperature and VOC flux power spectra show similar structure across all frequencies for both methods, giving high confidence for CWT calculated fluxes. Any major frequency deviation structure of either temperature or $NO/\ NO_2$/VOC flux is considered bad data, resulting in that leg being discarded. The majority of spectral contributions occur at low frequencies between 0 and 0.01 Hz, corresponding to spatial scales of 0.05 to 7.00 km.

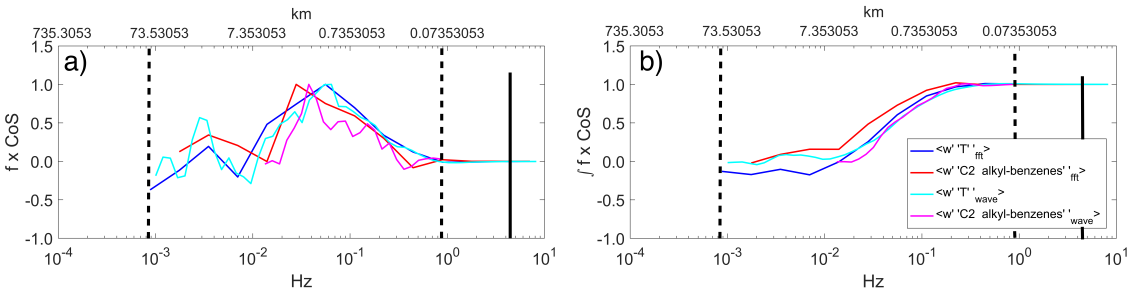

Figure 3.7: a) co−spectra of C_2 alkyl-benzenes and temperature flux using CWT and FFT methods, b) cumulative co−spectra for C_2 alkyl−benzenes and temperature flux using CWT and FFT methods. Black line represents Nyquist frequency and dotted lines being the contributing frequency boundaries.

High and low frequencies must be fully captured for a correct calculation of the flux. The spectral structure observed for NO/NO_2 and VOC CWT fluxes, as shown in Figure 3.7, shows no requirement for high frequency correction due to all flux contributions occurring at low frequencies. Low frequency contributions occur at wavelet periods ranging up to 128 s, which was chosen as the largest scale as highlighted in other published

studies [107, 121]. Karl et al. (2009a) investigated the effect of bandwidth ranges on total toluene flux contributions [121]. Bandwidths from 0.1−32 s accounted for the majority of the toluene flux, whereas a smaller bandwidth range of 32−64 s accounted for a limited proportion.

The calculated NO/ NO_2 fluxes showed low frequency contributions for bandwidth frequencies between 0.1−128 Hz, requiring no low frequency correction. Most of the flux contributions occurred in a bandwidth period range of 4−64 s. Bandwidth frequencies for VOCs were also 0.1−128 Hz showing that all low frequencies are being capture. Figure 3.8 shows C_2 alkyl−benzenes flux contributions for 0−32, 0−64 and 0−128 s bandwidth frequency ranges. Increasing frequency periods to include scales up to 128 s accounted for 7.76% more flux contribution due to low frequencies, with 5% being from scales between 64−128 s. Accounting for scales above approximately 128 s resulted in fluxes increasing y < 1%. Scales about 128 s represent eddy transport scale greater than 12 km and are larger than most transport scales found in lower mixing boundary layer.

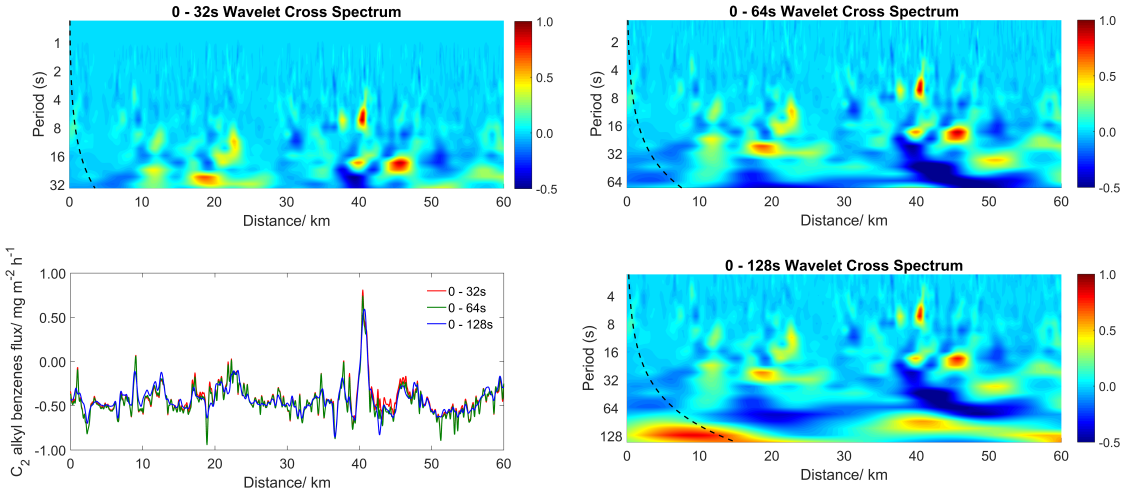

Figure 3.8: Wavelet cross−spectrum for 0−32, 0−64 and 0−128 s frequency period bandwidths. Average flux contributions along total flight track for each frequency period bandwidths.

3.3.5 Cone of Influence

As discussed, the majority of flux contributions occur at low frequencies. A downside of high low frequency contributions is that the start and end of the CWT wavelet power spectrum is affected most by edge effects. As discussed by Torrence and Compo. (1998), CWT edge effects are greatest at the beginning and end due to the data series being of finite−length in time [127]. A technique commonly used in CWT is to pad the time series with zeros at the start and end, ensuring the highest edge effects are concentrated on the zero padded regions and less on the actual data series [123].

The Cone of Influence (COI) is the region of the wavelet power spectrum where the influence of edge effects is greatest, resulting in calculated coefficients in this area being prone to higher uncertainties. Mauder et al., highlighted the effect of considering flux contributions from areas of the wavelet power spectrum above the cone of influence [122]. Calculated fluxes of CO_2 showed lower values when frequency contributions above the COI were considered. Flux contributions above the COI had opposite signs to those within the COI, resulting in underestimation of the total flux.

Figure 3.6b shows the COI as a black dotted line on the wavelet cross spectrum, with COI found at lower period frequencies at the start and end of the wavelet power spectrum. To remove influence of flux data which falls outside of the COI, we only consider data inside of the cone and pad the beginning and end with zeros to help remove the highest effect from edge effects [107].

3.3.6 Flux Errors

As with all flux measurements, high data quality is paramount and understanding the uncertainty associated with such a measurement is vital. As discussed by Vickers et al., there are two main types of error associated with flux measurements. The first, systematic error (se), is due to the incomplete capture of the largest transport scales, resulting in the calculated flux being an underestimate. The second, random error (re), is caused by incomplete capturing of the main transport eddies due to the flux time averaging being too short [130]. Due to the reduced time scales at which airborne fluxes are measured at compared to ground fluxes, their uncertainties can be significant. A detailed study into the effect re and se have on airborne fluxes can be found in Mann & Lenschow. (1994) [131]. They found a direct link between the chosen flux averaging timescales (τ_F), perturbation timescale (τ) and both error types. The scale of both errors is dependant on $\tau_F > \tau$.

Error quantification for the instantaneous fluxes was conducted as previously described by Karl et al. (2009a), with the total error being due to both random (re) and systematic (se) errors as defined in Equation 3.11 and 3.12 [121]. l denotes the flight leg length, Z_M the flight altitude and Z_i the height of the boundary layer. Boundary layer heights were obtained at the beginning and end of each flight via atmospheric soundings (Li−DAR) from Heathrow Airport, West London. Wolf et al. discussed the effect both types of error have on measured atmospheric flux, with the flight altitude being proportional to the error. The length of the flight transection or time period of the flux measured is inversely proportional to both types of error [125].

$$re \leq 1.75 \left(\frac{Z_m}{Z_i}\right)^{0.25} \left(\frac{Z_i}{l}\right)^{0.50} \tag{3.11}$$

$$se \leq \frac{2.2 Z_i \left(\frac{Z_m}{Z_i}\right)^{0.50}}{l} \tag{3.12}$$

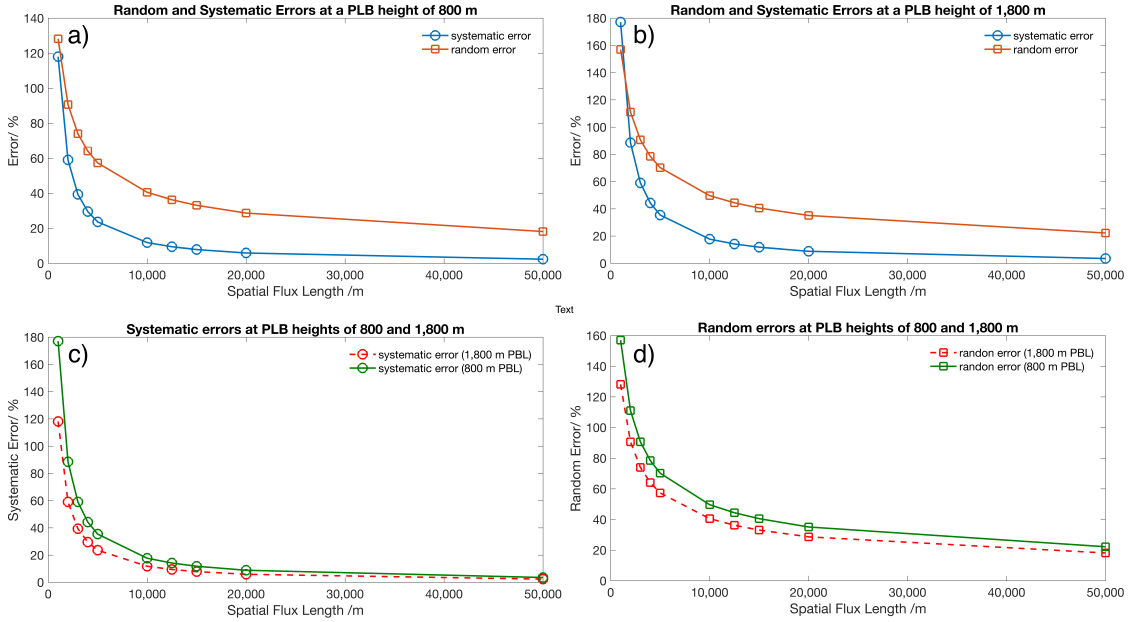

Figure 3.9: a & b) Calculated random and systematic errors for two PBL heights as a function of flux averaging scales, c) systematic error at two PBL heights as a function of flux averaging scales, d) random error at two PBL heights as a function of flux averaging scales.

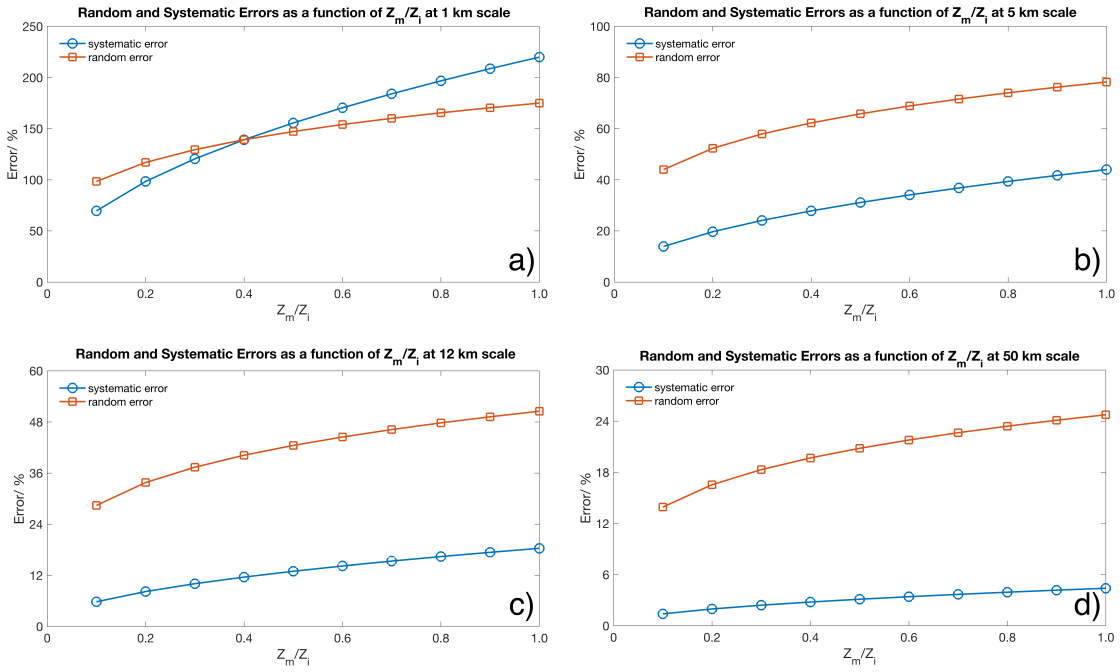

Figure 3.10: Random and systematic errors as a function of Z_M/Z_i for a range of flux averaging scales (1, 5, 12 and 50 km).

For 1 km resolved fluxes (e.g. Z_M = 360 m, Z_i = 800 m, Z_M/Z_i = 0.45 and l = 1000 m) the *re* is approximately 130% and the *se* 120%. This a relatively high error compared to instrument uncertainties; although, higher spatial information can be gained from 1 km fluxes. As flux averaging scales increase, associated error decreases non linearly. Figure 3.9 shows the effect of increasing flux spatial scales has on both *re* and *se* for two PLB conditions. Figure 3.9 highlights that both error types decrease as flux averaging increase from 1 to 50 km.

During flights over London the altitude was kept constant at 360 m. The PBL height increasing from approximately 800 m in the morning up to 1800 m during the afternoon. This gives a Z_M/Z_i ratio range of 0.20 to 0.45. As shown in Figure 3.10, increasing the ratio of Z_M/Z_i leads to larger values of *re* and *se*. This is due to eddy transport structure in the lowest part of the mixing layer not being captured, when the flight altitude approaches the PBL. Keeping the altitude constant helps reduce major variances in both errors. Flights with lower PBL heights (during the mornings) have lower errors as more of the eddy transport scales are captured, compared to an elevated PBL (during the afternoons) when larger transport scales have developed.

Overall the *re* and *se* associated with 1 km resolved fluxes is very large and requires the flux averaging window to be increased. As discussed in Chapters 4 and 5, analysis of London's emissions in regards to UK emission inventories is done using a minimum flux averaging window greater than 15 km, which will keep the overall uncertainty below 50%. If an averaging scales of 50 km is used, which represents an entire run over London, the uncertainty on the flux measurement will be approximately 20%. Figure 3.11 highlights the overall flux uncertainty decreasing to 20% as the averaging scales increase to 50km.

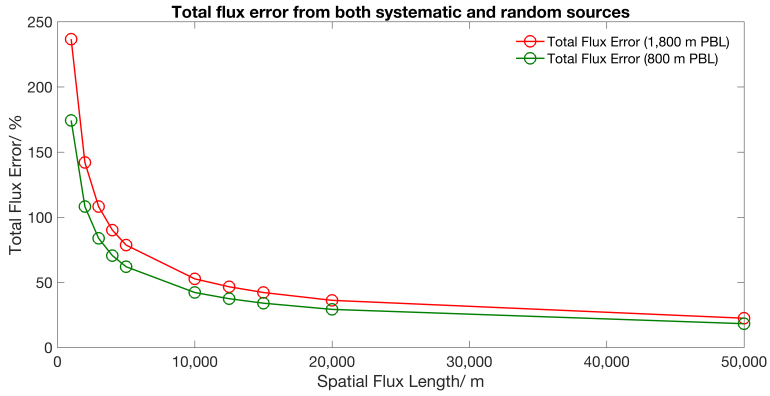

Figure 3.11: Total flux error accounting for random and systematic errors as a function of averaging scales, at two PLB heights and a fixed flight altitude (360 m).

3.4 Footprint Model

Understanding the spatial origin of a measurement is vital if context is to be drawn from the measurement. The term footprint model, first coined by Schuepp et al. and Leclerc & Thurtell. [132, 133], describes the upwind source area responsible for a scientific measurement. The influence area of a flux is two dimensional with contributions stemming from both unwind and crosswind regions. Schmid. (1994) depicts the source area of a flux function in x and y as a weighting function in the f plane, Figure 3.12 [134].

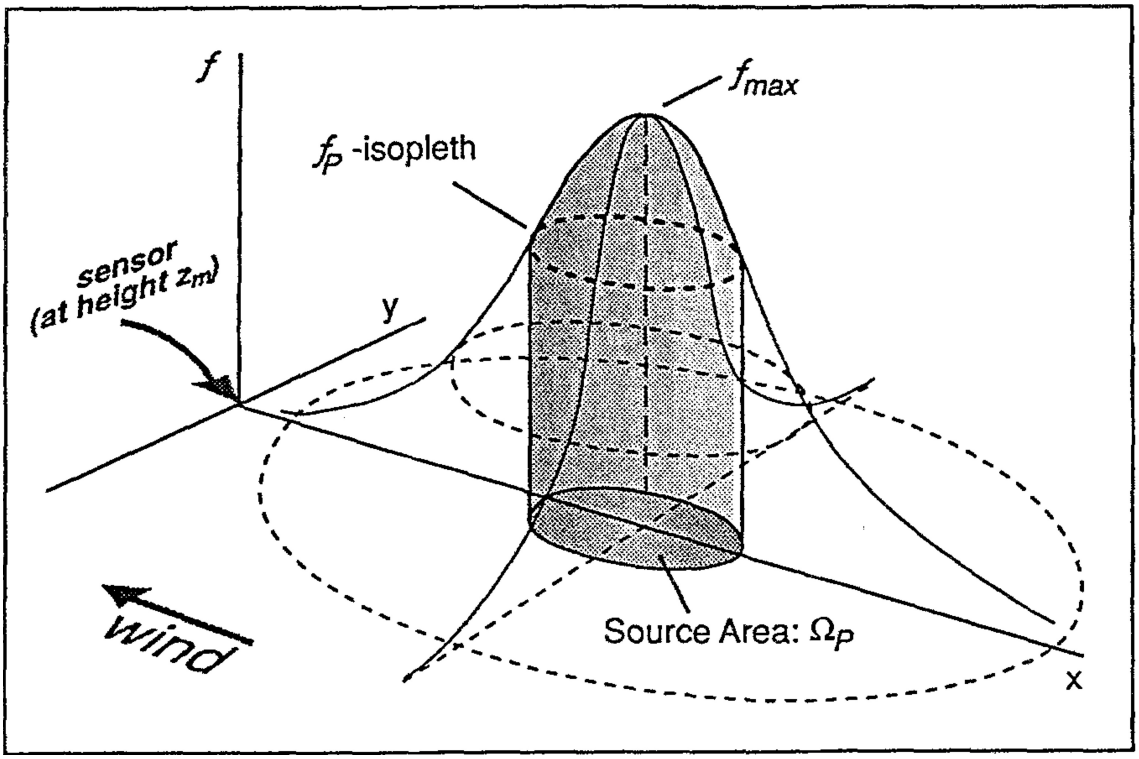

Figure 3.12: Footprint influence area in x and y directions from point of measurement, grey shaded area showing region of highest source influence. Taken from Schmid. (1994) [134].

Footprint models have developed greatly over the last 30 years allowing for more accurate prediction as to the exact influence area a measurement is stemming from. Footprint models have classically taken several different approaches. Analytical models aim to solve the advection-diffusion equation from which the vertical transportation of material from the surface to the point of measurement can be resolved [135]. These models have previously been shown to be able to give footprint approximations depending on the model used in either 1, 2 or 3−dimensions. Run time of these models is normally relatively fast and non−computer intensive.

One of the most well−known analytical model approaches is the Horst & Weil. model which was developed to overcome some of the limitations these kinds of models had shown [136, 137]. Previously, whilst analytical models exhibited ease of use, these were bound to limited atmospheric conditions and neutral stability. The Horst & Weil. (1992, 1994) approach added non−passive scalar transfer and parameterisation for non−stable atmospheric conditions, normally found in the surface mixing layer [136, 137]. The model can predict for known surface roughness and atmospheric stability, a normalised footprint which is integrated to include crosswind influences. Other notable footprint models employing an analytical approach include: Schmid. (1997), Kaharabata et al. (1997), Kormann & Meixner. (2001) and Neftel et al. (2008) [138, 139, 140, 141].

Lagrangian models use a stochastic Langevin equation to assess diffusion of a scalar [142]. The models assess atmospheric turbulent diffusion to calculate footprint and source area of a measurement. As depicted by Flesch. (1996), Lagrangian models work backwards assessing the movement of a large number particles measured at point P, and calculate all possible particle trajectories, based on measured meteorology and fluid dynamics (Figure 3.13) [143]. Using all the predicted particle trajectories, a 2−dimensional footprint can be constructed. Notable models which employ a Lagrangian approach are: Leclerc & Thurtell. (1990), Sabelfeld & Kurbanmuradov. (1998) and Kljun et al. (2002) [133, 144, 145].

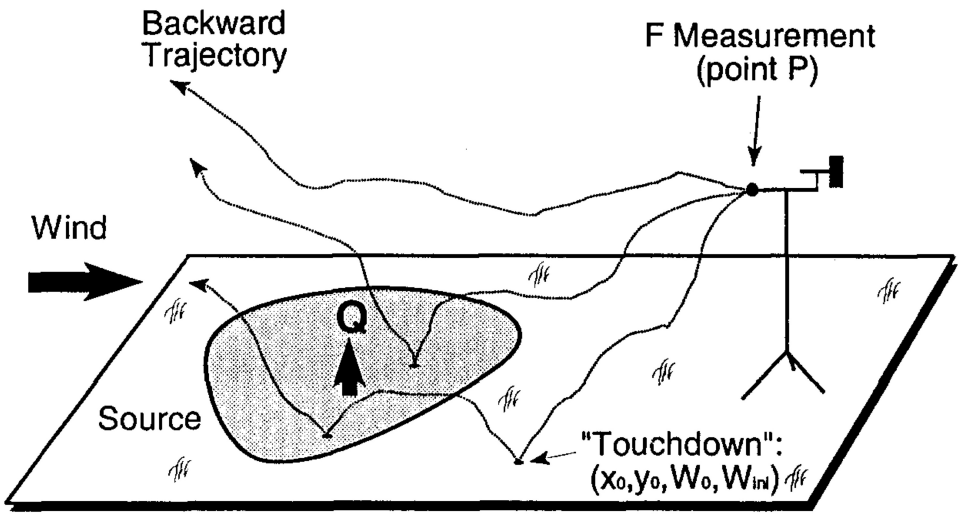

Figure 3.13: Footprint based on a backwards Lagrangian simulation using particle release ideology. Taken from Flesch. (1996) [143].

Higher−order closure models differ from conversional analytical and Lagrangian models. They can assess scalar flux when parameters such as aerodynamic properties differ for two adjoining fields [135]. An example of such a model, SCADIS, is described by Sogachev et al. (2002, 2005) [146, 147]. The model assesses conditions both within a canopy and planetary boundary layer, allowing for footprint assessment in both types of conditions.

In addition to the discussed model types, large−eddy simulation (LES) models also show promise for complex footprint calculation. Models following this approach can determine a large array of parameters ranging from turbulent statistics, scalar fluxes and other important meteorological conditions all without the need for external data input. Prabha et al. combined a LES approach to run a Lagrangian footprint model [148]. The model employed LES to calculate flow statistics, ultimately driving the Lagrangian stochastic model. A combination of approaches can be advantageous over classic methods, where calculated turbulent statics driving the footprint model maybe be more representative of real world conditions. The Cai & Leclerc. (2007) study employed a LES powered Lagrangian model allowing for footprint calculation at four different levels within the convective boundary layer [149].

3.5 Aircraft Footprint Model

In this study, we follow the same approach as Metzger et al. (2012), in using a footprint model cable of assessing influence from prevailing and perpendicular wind directions [150]. Metzger et al. uses the Kljun et al. (2004) model (KL04), which is a parametrised version of the Kljun et al. (2002) backwards Lagrangian model [145, 151].

The model can investigate stable and strongly convective conditions for footprint estimates using Buckingham's−Theorem [152]. The model is parameterised using measurement height (Z_m), friction velocity (u_*), standard deviation of vertical wind (σ_w), standard deviation of horizontal wind (σ_v), boundary layer depth (Z_i) and aerodynamic roughness length (Z_0). $\alpha 1$ and $\alpha 2$ are free parameters.

$$X_* = \left(\frac{\sigma_w}{u_*}\right)^{\alpha_1} \frac{x}{Z_m} \tag{3.13}$$

$$F_* = \left(\frac{\sigma_w}{u_*}\right)^{\alpha_2} \left(1 - \frac{Z_m}{Z_i}\right)^{-1} Z_m \overline{f^y} \tag{3.14}$$

$$\widehat{F_*} = a \left(\frac{\widehat{X}_* + d}{c}\right)^b \exp\left\{b\left(1 - \frac{\widehat{X}_* + d}{c}\right)\right\} \tag{3.15}$$

Equations 3.13 & 3.14 define the crosswind−integrated footprint F^* and alongwind distance X^* in a non−dimensional state. Under the one roughness length regime, Equation 3.15 was defined by Kljun et al. (2004), giving a scaled footprint estimate as a functional relationship between F^* and X^*. Parameters a, b, c and d act as fitting parameters during the footprint calculation through stepwise regression. The fitting parameters allow the footprint model to be valid for a wide range of Z_0 values.

$$a \approx \frac{A_f}{(B - \ln Z_0)} \tag{3.16}$$

$$b \approx \frac{1}{(A_f A_c)} \tag{3.17}$$

$$c \approx A_c \, (B - \ln Z_0) \tag{3.18}$$

$$d \approx A_d \, (B - \ln Z_0) \tag{3.19}$$

Parameter a defines the maximum value of the flux distribution, and parameter d the maximum upwind extend in a non−dimensional state. All parameters except b are proportional to Z_0, Equations 3.16-3.19. Kljun et al. deduced optimal values of: $A_c = 4.28$, $A_d = 1.68$, $A_f = 0.18$, $A_x = 2.59$, $B = 3.42$ and $b = 3.70$ [151]. Figure 3.14 shows the dependency of the fitting parameters in relation to surface aerodynamic roughness length for a range of atmospheric conditions [151]. Under all conditions (highly−stable, stable, neutral, unstable and highly−unstable), the parameters follow similar trends against $Ln(Z_0)$. From the chosen values, the non−dimensional and dimensional maximum alongwind footprint extent can be calculated as described in Equations 3.20 and 3.21.

$$\widehat{X_{*,max}} \approx A_x \left(b - \ln Z_0\right) \tag{3.20}$$

$$X_{max} \approx \widehat{X_{*,max}} Z_m \left(\frac{\sigma_w}{u_*}\right)^{-\alpha_1} \tag{3.21}$$

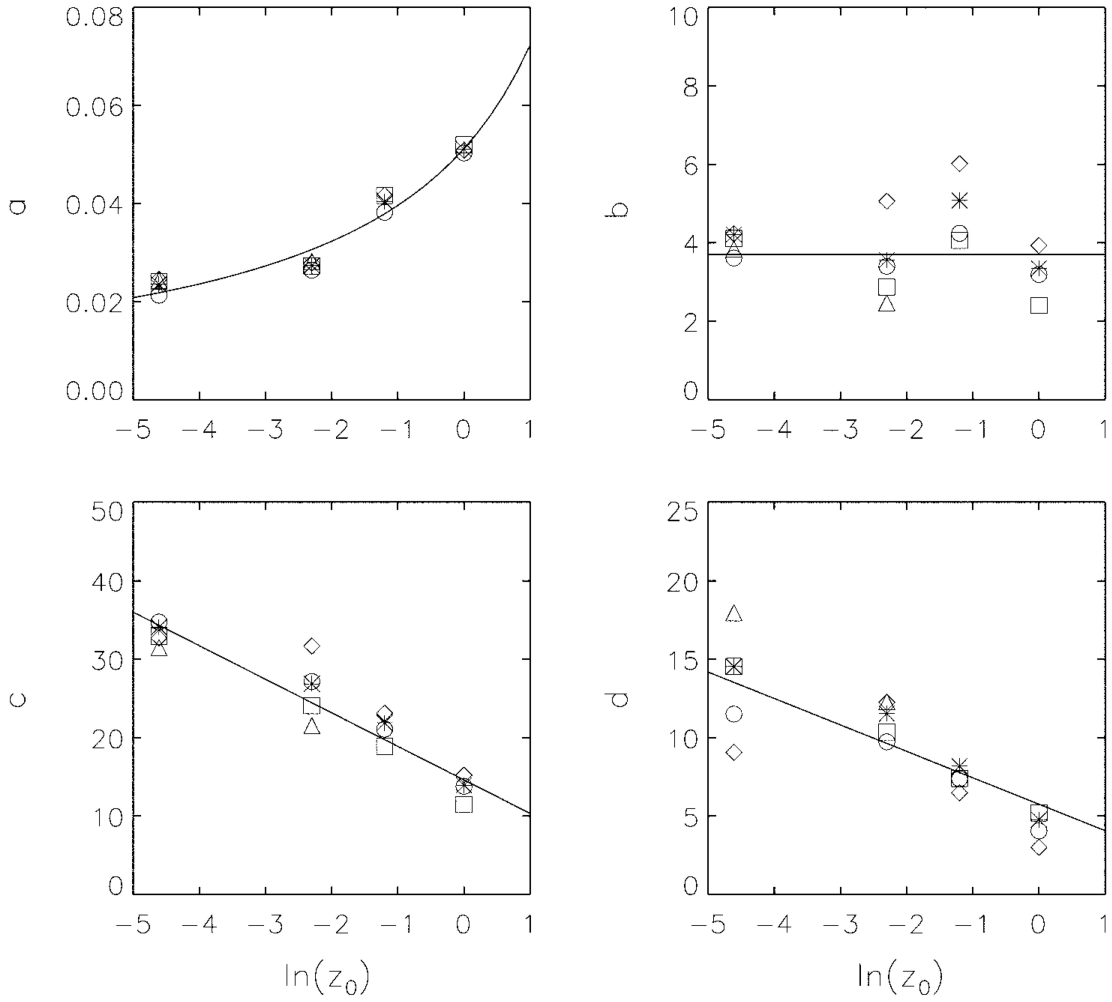

Figure 3.14: Dependence of fitting parameters a, b, c, d on aerodynamic surface roughness length at different atmospheric conditions. Z_0 range from 0.007 to 2.72 m. Taken from Kljun et al. (2004) [151].

3.6 Footprint Calculation

As previously employed in the Metzger et al. (2013) study, the same footprint model was used to assess the spatial influence on flight tracks during 2013 and 2014 over Greater London and Southern England [123]. The model was run in RStudio GUI, using R programming language version 2.15.3, and was coded by Dr. Mezger at the National Ecological Observatory Network (NEON). The footprint model resolution chosen was 1 km, to mirror that of UK emission inventories, for high spatial assessment.

The model generates an individual weighting matrix every 1 km along the flight track of identical grid size (1 km^2) and extent to the inventory matrix being assessed. An example of a calculated weighting matrix is shown in Figure 3.15. The sum of the weighting matrix equates to 1. The matrix weights every inventory cell individually and by summing all weighted cells an individual emission estimate at that point along the flight track is calculated, as defined in Equation 3.22. W_{xy} defines the individual cells of the weighting matrix and $Inventory_{xy}$ the corresponding cells of the inventory.

$$Footprint = \sum_{x} \sum_{y} w_{xy} Inventory_{xy} \tag{3.22}$$

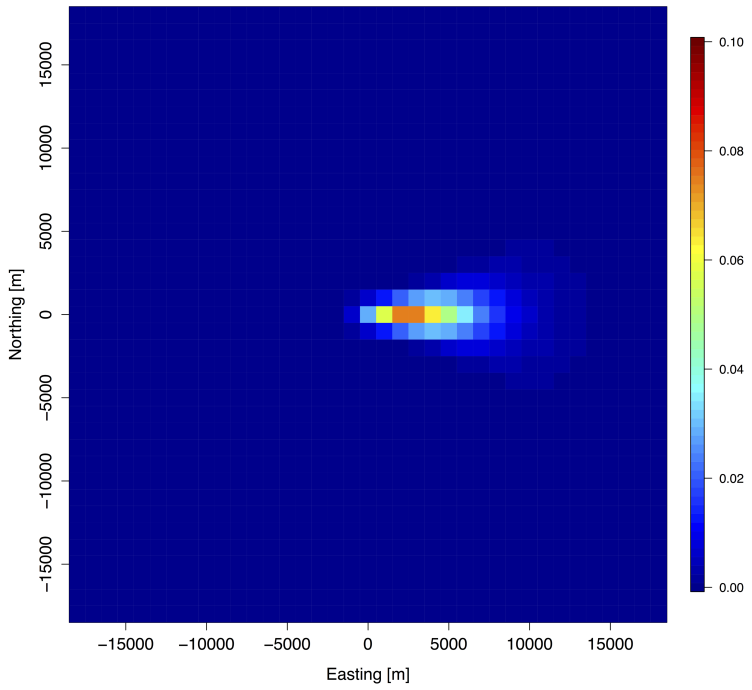

Figure 3.15: Footprint weighting matrix of 1 km^2 cell size, equal to a unity value of 1. Position of flux measurement at the centre of the grid (Northing 0, Easting 0).

3.6.1 Model Parameterisation

The model procedure for calculating footprint estimates is broken down into four key steps. Firstly, input variables are imported into the footprint function. Parameters u_*, σ_w, Z_m and σ_v are calculated for each km section along the flight track, from the measured meteorology. Parameters Z_0 and Z_i are inputted by the user. For most flights, all the variables were known; however, Z_i and Z_0 are not always known. Model variability towards both is discussed later.

From the inputted variables and fitting parameters (a, b, c and d) as discussed earlier, the size of the footprint matrix contribution can be calculated. Footprint matrix is estimated accounting for influences from alongwind and crosswind. The position of maximum footprint influence alongwind equates to fitting parameter a, at a spatial distance defined in Equations 3.20 and 3.21. From the maximum influence point, the negative influence up to the measurement point is calculated from the known matrix cell size and fitting parameter d and scale. Positive influence alongwind is calculated up to 1% influence from the point of maximum. For crosswind contributions, the extent to the left and right of primary wind direction is calculated as a density distribution until the extent again falls to below 1%, accounting for transport velocity and travel time of the air particles.

Using both alongwind and crosswind distributions, a $2-$dimensional matrix is formed. Cells are allocated at the defined size (e.g. 1,000 m) in both x and y directions, forming a weighting matrix equal to a unity value of 1. The matrix; however, at this stage is not of equal size to the inventory. To correct for this, zeros are padded around the matrix to being the number of rows and columns equal to that of the inventory. The center cell of the matrix is equal to the aircraft coordinates. The final stage rotates the calculated matrix 180 degrees minus the prevailing wind direction angle. This is to aligning the matrix clockwise into the mean wind direction.

3.7 Footprint Parameter Analysis

The described footprint model depends on 6 key parameters for calculating the 2−dimensional spatial area responsible for measured flux. Understanding the importance of each parameter is key if correct footprints are to be calculated. All parameters affect the extent and localisation of the calculated footprint. The following sections will discuss the effect of each parameter has on the alongwind footprint extent. Calculated footprint weighting matrices from the following parameter evaluations can be found in Appendix A.

3.7.1 Aerodynamic Roughness Length

Z_0 can vary greatly due to the non-homogeneity of the landscape over London and Southern England. The structural properties of a surface directly influence the path and speed which a gaseous medium flows. The Z_0 of a surface denotes the relative effect it has towards allowing the gaseous medium to flow over it without affecting its flow properties. An increase in roughness length can be thought of as a direct effect from an increase in surface altitude. The larger the surface roughness length, the longer the gas will take to travel over the surface due to increased wind shear generated from the higher altitude.

Values of Z_0 can be indirectly calculated from measured wind profile, as defined by Graf et al. (2014) [153]. Equation 3.23 defines averaged wind speed over a period, Ψ_m as the momentum function, k the von Karmon Constant, L the Obukhov length, u_* the friction velocity, Z_m the height and Z_0 as aerodynamic roughness length. By rearranging Equation 3.23, aerodynamic roughness length can be extracted as a factor of the measured surface wind profile Equation 3.24.

Footprints calculated for Southern England transects as discussed in Chapter 5, used calculated Z_0 values in accordance to Equation 3.24 from measured micrometeorology. Values of Z_0 for London were taken from the Drew et al. (2013) study which gives 1 km^2 resolution estimates of Z_0 for westerly and easterly wind directions [154]. Figure 3.16 shows aerodynamic roughness lengths for Greater London under the influence of a westerly wind direction [154].

$$\bar{u} = \frac{u_*}{k}\left(\ln\frac{Z_m}{Z_0} - \Psi_m\left(\frac{Z_m}{L}\right)\right) \tag{3.23}$$

$$Z_0 = \frac{Z_m}{\exp\left(\frac{\bar{u}k}{u_*} + \Psi_m\left(\frac{Z_m}{L}\right)\right)} \tag{3.24}$$

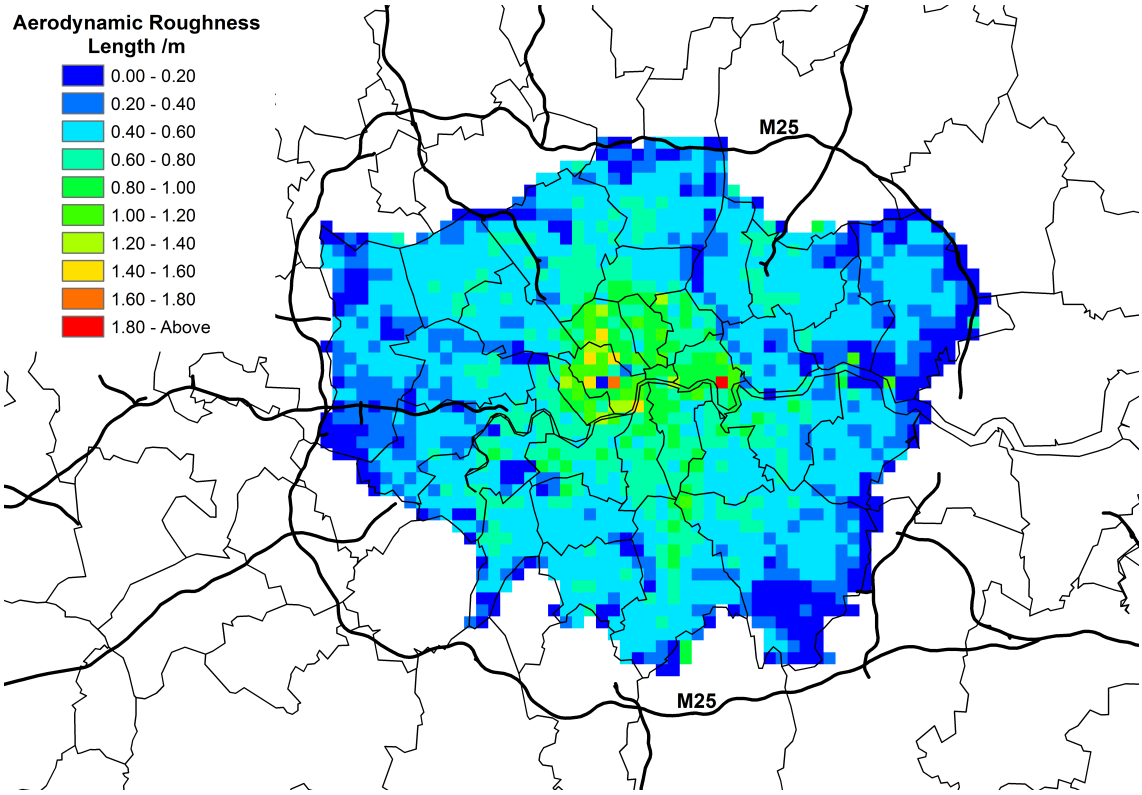

Figure 3.16: Aerodynamic roughness lengths for greater London, accounting for easterly and westerly wind directions [154].

For flight transects over London, the only parameter defined by the user is the aerodynamic roughness length of the surface below. London is highly heterogeneous with suburban areas having relatively low Z_0 values compared to most central areas which have been shown to have Z_0 above 1.8 m due to the high density of skyscrapers within the city of London and Canary Warf.

The dependency of Z_0 towards the calculated footprint was investigated. Only Z_0 was varied, with other parameters set to the following $u_* = 0.2$, $\sigma_w = 0.2$, $\sigma_v = 0.2$, $Z_i = 1000$, $Z_m = 360$ and wind angle $= 90^o$. An altitude of 360 m is representative of flight legs over both London and Southern England. Increments for Z_0 were chosen to account for smooth surfaces in the lower range of 0.1 m to extreme rough surfaces at 6.4 m for high rise buildings.

Figure 3.17 shows calculated footprint influence to a cumulative sum of 100% as a function of alongwind distance from measurement point 0, for 7 Z_0 values. The lowest value for Z_0 shows a large footprint extent ranging up to 28 km alongwind from the point of measurement. The main influence region of the calculated footprint was found within the region of $1-10$ km upwind. As Z_0 values are increased, the upwind footprint extent

decreases rapidly with influence from negative distances reducing to 0 at extreme Z_0 values. For Z_0 values above 1.0, the majority of the footprint influence is highly compressed within 5 km of the measurement point. Z_0 values in the region of 0.4 to 0.8 are representative of suburban and Greater London regions where there is not a dense region of high−rise buildings. Overall values of Z_0 are the only parameter to be not calculated from measured micrometeorology such as over London. Due to this Z_0 is the defining parameter which could affect calculated footprint accuracy. Table 3.2 gives detailed statistics for each Z_0 parameterisation of the footprint model.

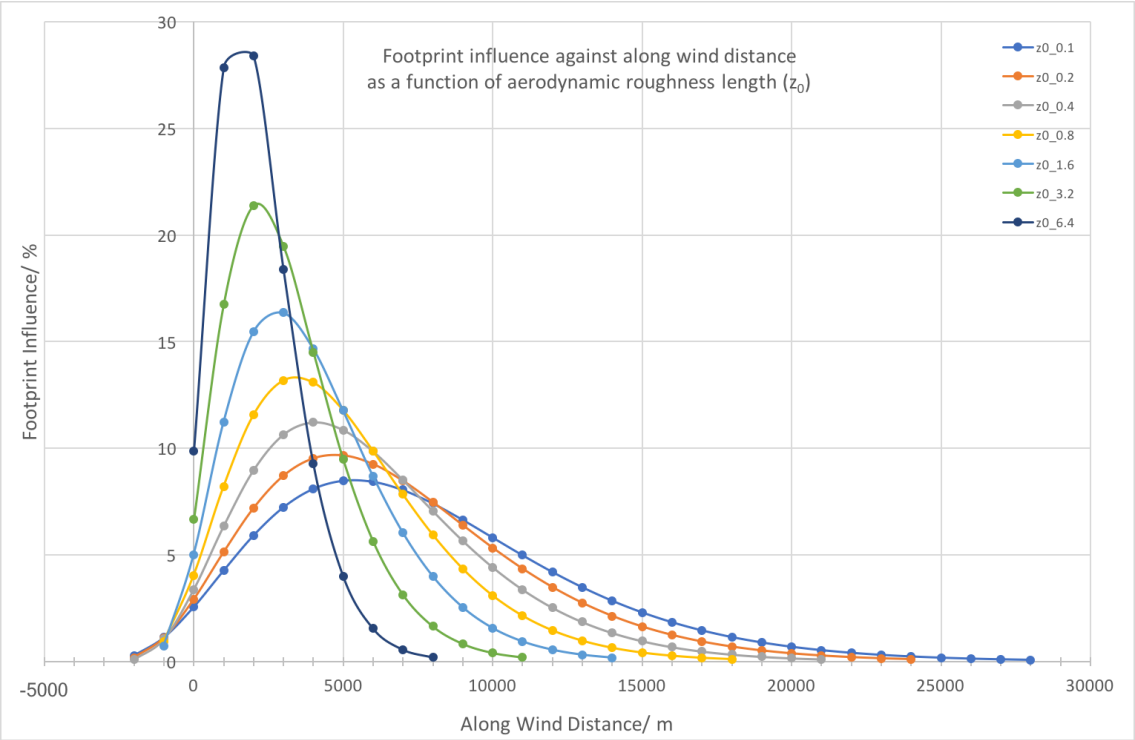

Figure 3.17: Effect of aerodynamic roughness length on alongwind footprint influence up to 100% influence.

Table 3.2: Aerodynamic roughness length statistics of maximum flux influence distance and percentage, 80 and 100% footprint influence distance.

Z_0/ m	X_{max}/ m	F_{max}/ %	f_{80}/ m	X_{tot} /m
0.1	5,335.74	8.48	14,000	28,000
0.2	4,689.45	9.66	12,000	24,000
0.4	4,043.16	11.21	11,000	21,000
0.8	3,396.87	13.18	9,000	18,000
1.6	2,750.58	16.35	8,000	14,000
3.2	2,104.29	21.37	7,000	13,000
6.4	1,458	28.39	5,000	11,000

3.7.2 Friction Velocity

Friction velocity accounts for shear stress in the turbulent boundary layer, and can be calculated from the instantaneous wind vectors u', v' and w' [155, 156]. Equation 3.25 defines friction velocity. The effect of friction velocity towards the calculated footprint was investigated. Only u_* was varied, with other parameters set to the following: $Z_0 = 1$, $\sigma_w = 0.2$, $\sigma_v = 0.2$, $Z_i = 1000$, $Z_m = 360$ and wind angle = 90^o.

$$u_* = \left[\overline{(u'w')}^2 + \overline{(v'w')}^2\right]^{0.25} \tag{3.25}$$

Metzger et al. (2012) previously limited values of friction velocity to stay above 0.2 m s^{-1} in accordance with Kljun et al. (2004), and so we here will use the same assumption [150, 151]. Lee et al. measuring fluxes from the BT tower in London also set their u_* threshold to 0.2 m s^{-1}, which is indicative other eddy−covariance studies as discussed by Aubinet et al., (2012) [106, 157]. Velocities below 0.2 m s^{-1} highlight inadequate vertical turbulence and can result in the horizontal flux term being more important which brakes down the principles of eddy−covariance [157]. As depicted in Figure 3.18, increasing the friction velocity expands the overall footprint extent up to a maximum of 69 km, as calculated for $u_* = 1.2$ m s^{-1}. Alongwind footprint influence also become less concentrated as u_* is increased, as shown in Table 3.3. Influence decreased from a maximum of 14% at 3.2 km, to ≈3% at 13.3 km up wind from the point of measurement. For a typical flight transect over London values of u_* ranged from 0.05 to 0.70 m s^{-1} giving a maximum alongwind influence distance range of between 3−8 km. For flight transects over Southern England, u_* values observed ranges from 0.2 to 1.0 m s^{-1} putting maximum alongwind influence distance at between ≈3 to 11.5 km under the set parameterisation.

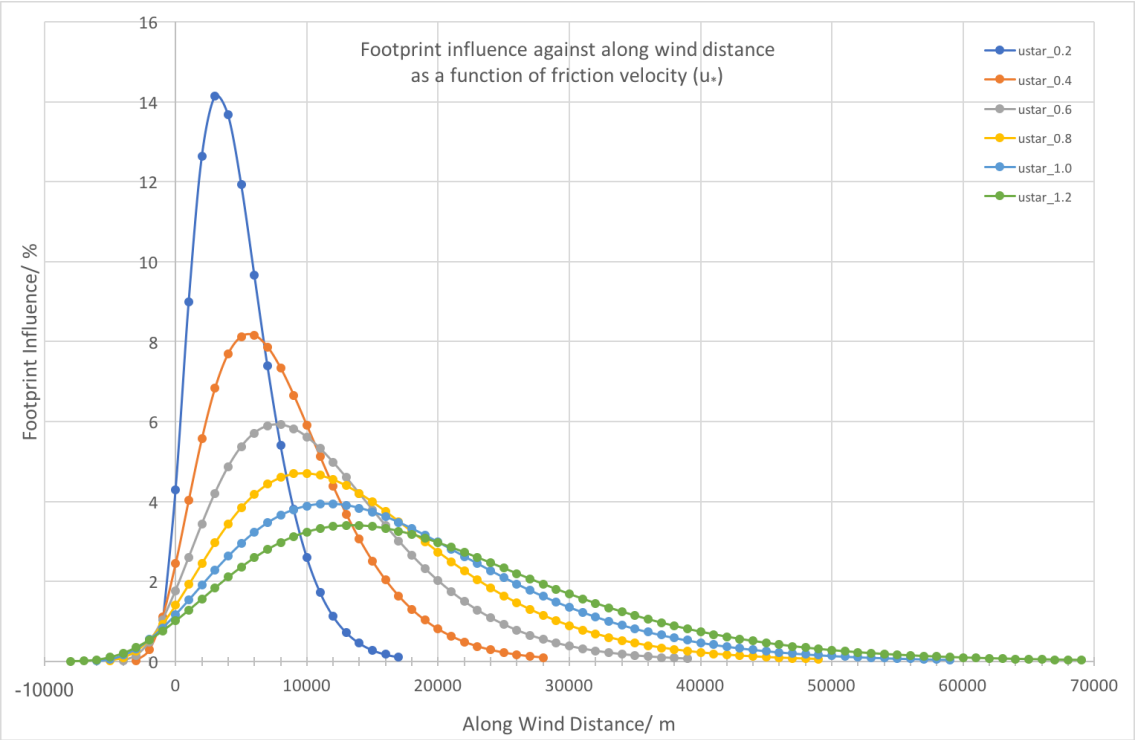

Figure 3.18: Effect of friction velocity on alongwind footprint influence up to 100% influence.

Table 3.3: Friction velocity statistics of maximum flux influence distance and percentage, 80 and 100% footprint influence distance.

u_*/ m s^{-1}	X_{max}/ m	F_{max}/ %	f_{80}/ m	X_{tot} /m
0.2	3,188.81	14.14	9,000	17,000
0.4	5,552.04	8.15	14,000	28,000
0.6	7,679.37	5.92	19,000	39,000
0.8	9,666.66	4.7	23,000	49,000
1.0	11,555.93	3.94	27,000	59,000
1.2	13,370.56	3.4	31,000	69,000

3.7.3 Planetary Boundary Layer

The planetary boundary layer (PBL) is the lowest layer in the troposphere. It's structure is highly turbulent and is influenced by the surface layers' shape. Above the PBL the troposphere's structure is more uniform and decoupled from surface influence. Coupling emissions from the surface layer can be achieved through footprint models such as this one, where the point at which measurement occurs is lower than the top of the PBL.

To investigate the footprint model's dependence on PBL height, a range of different heights were used. Whilst keeping all parameters constant, 4 PBL heights were inputted into the model (500, 1,000, 1,500 and 2,000 m). Figure 3.19 shows for each of the 4 PBL's, the footprint influence as a function of along wind distance. All 4 PBL heights show identical results with the maximum influence within the first 7 km. The model is unaffected by changes in the PBL height as long as it remains higher than the flight altitude.

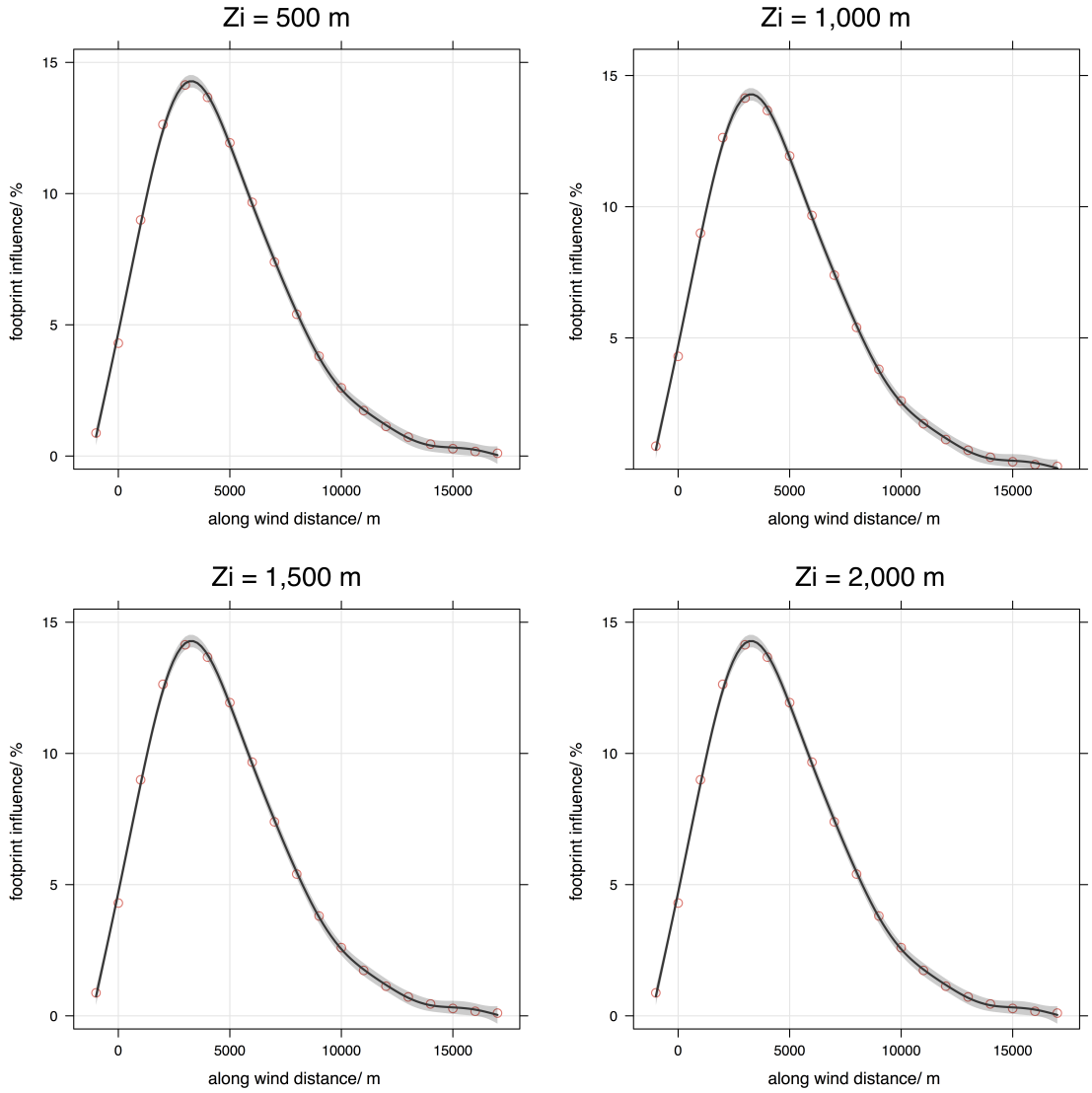

Figure 3.19: Effect of PBL height (500, 1,000, 1,500 and 2,000 m) on alongwind footprint influence up to 100% influence.

3.7.4 Measurement Height

The altitude at which measurements are conducted is not always a parameter which can be controlled freely due to strict air traffic control regulations, especially over Greater London which is home to Heathrow, one of the busiest airports in the world. Keeping all other parameters constant, altitude was varied from 100 to 450 m at 50 m intervals as shown in Figure 3.20. Below altitudes of 250 m, all influence from the main wind direction is positive into the alongwind plane.

At altitudes below 100 m at a footprint model cell size of 1 km, the footprint model extent falls below 1 km, so setting a lower limit for the model at 100 m. Higher flight altitudes increase alongwind footprint extent whilst decreasing localisation of influence area. At the highest altitude (450 m), footprint extent was highly non localised, with 80% influence being 20 km away from the measurement point. The footprint extent will continue to increase whilst the flight altitude is below the PBL height, after which point, the footprint model breaks down due to disentanglement from the surface layer above the PBL. Overall flight altitude is not a parameter which will affect calculated footprint accuracy, due to it being measured inflight.

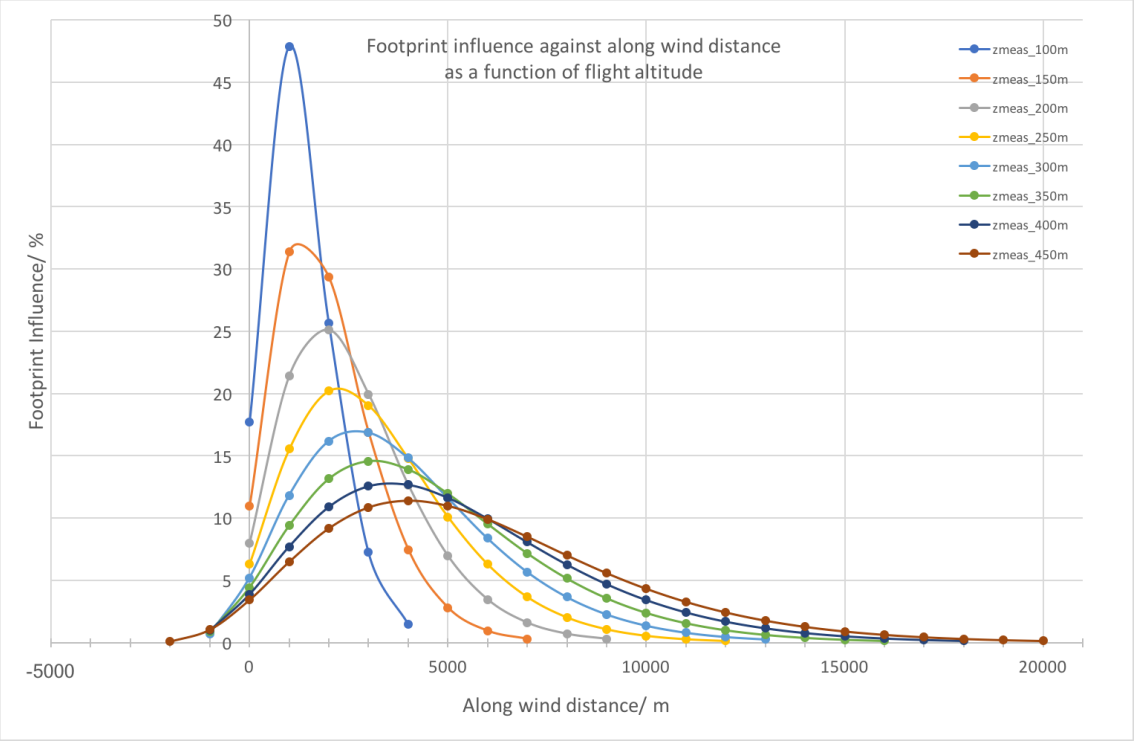

Figure 3.20: Effect of measurement height on alongwind distance footprint influence up to 100% influence.

Table 3.4: Measurement height statistics of maximum flux influence distance and percentage, 80% and 100% footprint influence distance.

Z_m/ m	X_{max}/ m	F_{max}/ %	f_{80}/ m	X_{tot} /m
100	885.78	47.85	4,000	4,000
150	1,328.67	31.36	5,000	7,000
200	1,771.56	25.1	6,000	9,000
250	2,214.45	20.22	7,000	12,000
300	2,657.35	16.85	8,000	13,000
350	3,100.23	14.57	9,000	16,000
400	3,543.12	12.67	10,000	18,000
450	3,986.01	11.38	11,000	20,000

3.7.5 Standard Deviation of Horizontal and Vertical wind

The standard deviation of horizontal σ_v and vertical wind σ_w is calculated for each footprint using measured micrometeorology by the AIMMs−20 turbulence probe. Ranging values of σ_v from 0.2−1.2 m s^{-1} showed no effect on the calculated alongwind footprint extent and density distributions. This is due to horizontal wind deviations accounting for non−perpendicular footprint influences only. As shown in Figure 3.21 the footprint is stretched in the y−axis (Northing plane) by increasing the value of σ_v, which highlights enhanced contribution from perpendicular wind directions.

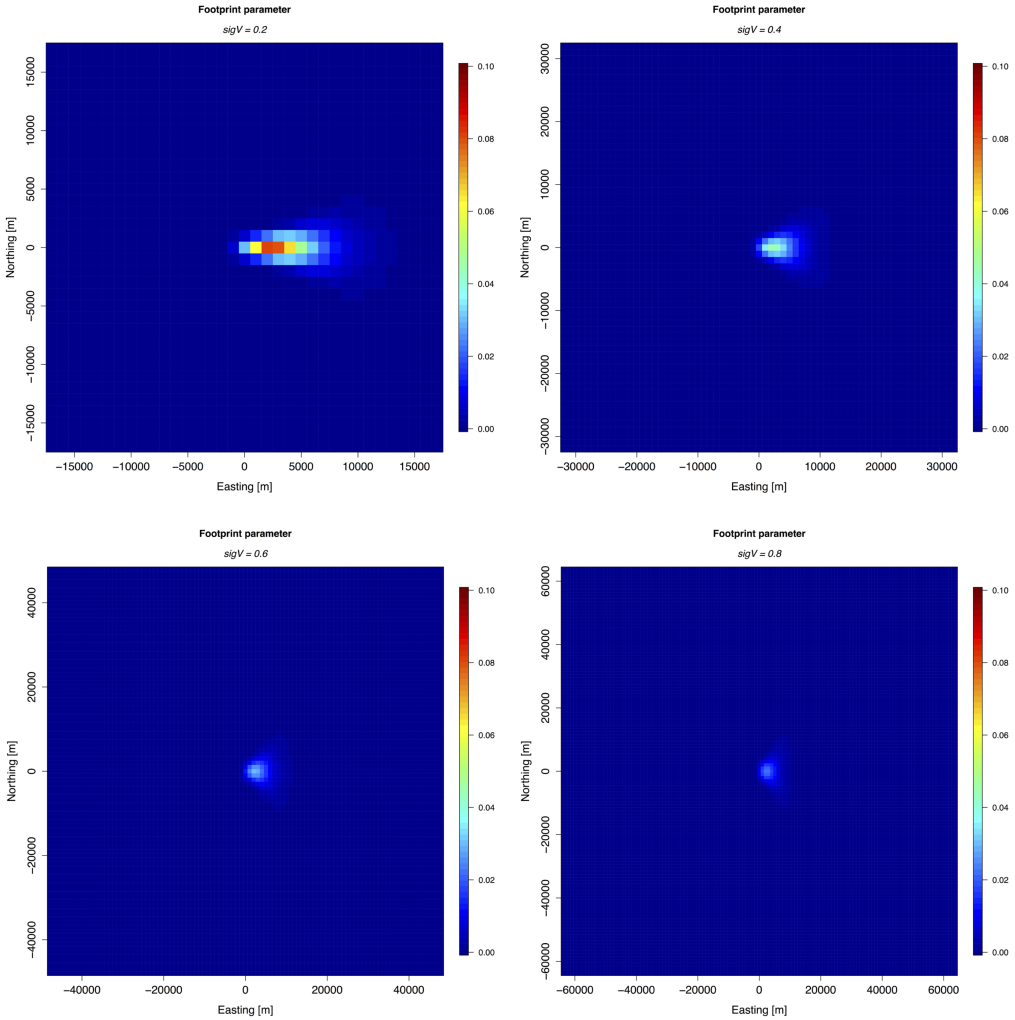

Figure 3.21: Effect of σ_v on horizontal and perpendicular wind direction footprint influence. Increasing σ_v acts to stretch the footprint along the y−axis (Northing plane).

Standard deviations of vertical wind do play a significant part in localising alongwind footprint extent, compared to the horizontal wind. Figure 3.22 shows the effect of increasing σ_w up to a maximum value of 1.0. Increases in σ_w act to localise alongwind footprint extent dramatically as found for a value of 1.0, where 100% footprint influence decreased by a factor of 4 from 17 km to 4 km. Observed values of σ_w during OPFUE flight ranges from 0.3−1.2 m s^{-1}, so potentially localising footprint extent in a range 17 to 4 km. Due to σ_v and σ_w being calculated from measurement meteorology, they will not affect calculated footprint accuracy.

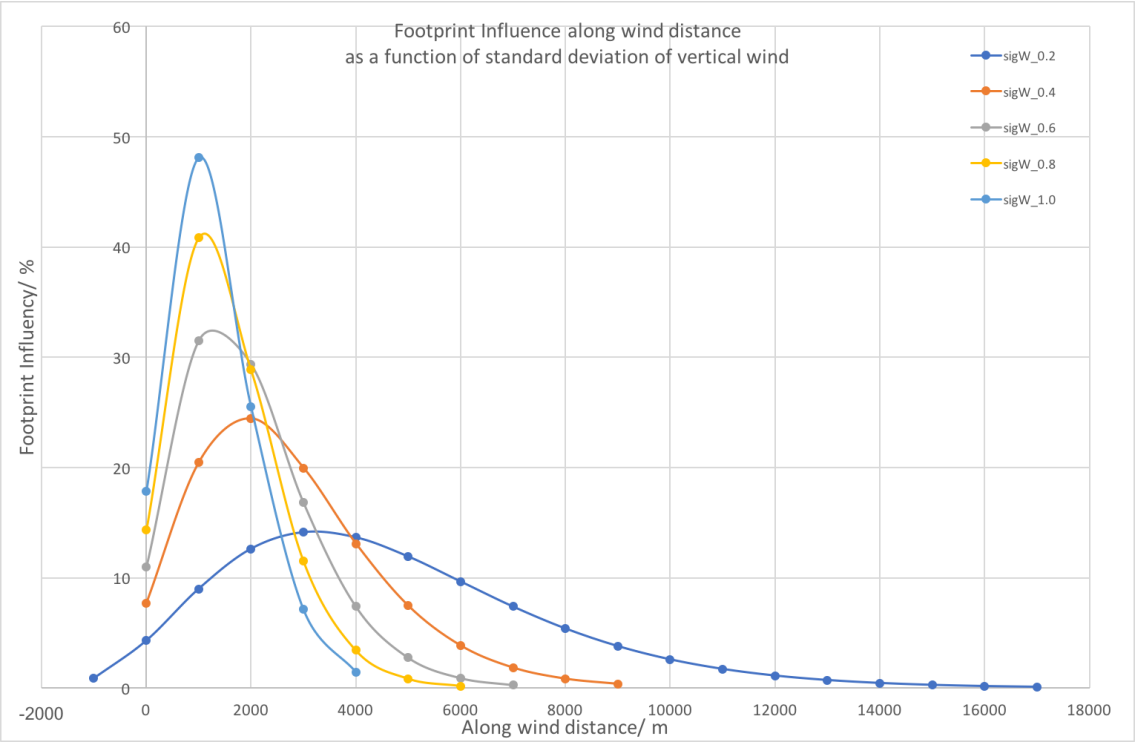

Figure 3.22: Effect of σ_w on alongwind footprint influence up to 100% influence.

3.8 Conclusions

Aircraft measurements allow for high spatial assessment of pollutants over large distances. Eddy−covariance measurements, classically, have been performed from tower sites, allowing for specific spatial assessment of the nearby region. Aircraft eddy-covariance is becoming a more commonly used technique for assessing surface emissions and micrometeorology. It overcomes the stationary problem of a tower site, whilst still being able to generate high time resolution flux data.

Continuous wavelet transform (CWT) has been used to calculate eddy−covariance fluxes from an aircraft due to their ability to extract frequency and time information from analyte signals. This study has assessed the applicability of using CWT for calculating fluxes from an aircraft, whilst employing a footprint model to identify the surface spatial influence responsible for the measured flux. Using high time resolution data from flights over London and Southern England, continuous wavelet transform was used to calculate 1 km resolved emissions for a range of anthropogenic and biogenic pollutants. For all compounds, spectral assessment, highlighted all high and low frequency eddy-flux contributions were captured in the frequency range of 0−128 s. High spatiality fluxes below 1,500 m resolution had high associated errors mainly due to random flux error, which decreases when averaged across the entire of London.

A footprint model was used to couple calculated fluxes to the surface layer. Using the model described by Kljun et al. (2004) and Metzger et al. (2012, 2013), footprint estimates for every km along the flight path as a weighing function could be calculated from measured meteorology. The model is parameterised by measurement height, friction velocity, standard deviation of vertical and horizontal wind, boundary layer height and aerodynamic roughness length. All parameters, except boundary layer height and standard deviations in horizontal wind affect the alongwind extent of the calculated footprint. Aerodynamic roughness length is a particularly important parameter localising the maximum footprint influence under extreme lengths, such as in cities, close to the flight track. Aerodynamic roughness length is the main source of footprint uncertainty, as all other parameters are derived from either measured meteorology and Li-DAR observations.

The two techniques coupled together offer unique insight into emissions from areas which under normal measurement strategies would be impossible. Chapters 4 and 5 give in−depth details of the specific applications this technique has been employed for.

Chapter 4

Airborne Eddy-Covariance Measurements of NO_x Fluxes over London during 2013 and 2014

This Chapter discusses calculated NO_x fluxes during the 2013 and 2014 OPFUE campaigns with direct comparison to the National and London Atmospheric Emissions Inventories (NAEI and LAEI).

A.R. Vaughan, J.D. Lee, P.K. Misztal, S. Metzger, M.D. Shaw, A.C. Lewis, R.M. Purvis, D.C. Carslaw, A.H. Goldstein, and C.N. Hewitt. Spatially resolved flux measurements of NO_x from London suggest significantly higher emissions than predicted by inventories. Faraday discussions, 189:455−472, 2016. ISSN 1364-5498.

4.1 Introduction

Due to its adverse effects on human health [158, 159, 160, 161], nitrogen dioxide (NO_2) concentrations are regulated by the EU Air Quality Directive which sets limit values for hourly and annual mean ambient concentrations. The annual mean limit value of 40 μg m^{-3} is exceeded in many urban centres throughout the UK, including London. In addition to its direct health effects, NO_x (the sum of NO + NO_2) contributes to the formation of ozone and secondary particles through a series of photochemical reactions [162] and hence reductions in NO_x emissions are necessary to control the regional-scale ground level concentrations of ozone, which is itself a regulated pollutant under the Air Quality Directive.

Concentrations of carbon monoxide (CO) and hydrocarbons in urban centers in the UK have decreased by around an order of magnitude over the past 20 years, providing clear evidence of the effectiveness of both the legislative framework and the emission control technologies employed for these pollutants. However, whilst trends in ambient concentrations of NO_x and NO_2 in the UK generally showed a decrease in concentration from 1996 to 2002, this has been followed by a period of more stable concentrations from 2004 to 2014. This is not in line with the expected decrease suggested by the UK emission inventories [45], as shown in Figure 4.1.

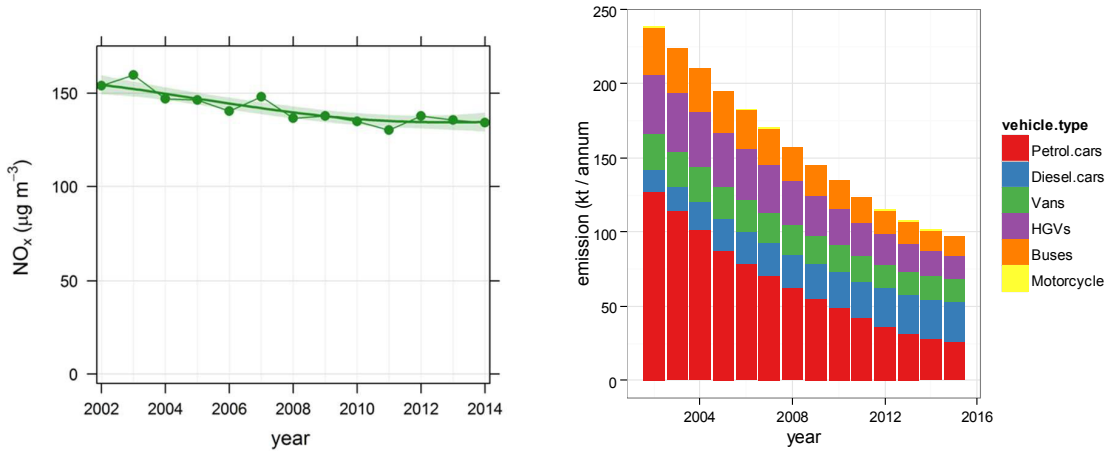

Figure 4.1: left) Trends in the mean concentration of NO_x across 35 roadside sites in Greater London with at least 10 years of data capture, right) projected change in urban road transport emissions split by main vehicle type from the NAEI using 2002 as a base year.

It is known that ambient NO_2 has not respond linearly to reductions in the concentration of NO_x, in part due to changes in diesel emission control technology leading to increases in directly emitted NO_2 [42], and partly due to the complexities of atmospheric chemistry. This may partially explain why ambient concentrations of NO_x have not declined as rapidly as expected. Although it has been known for some time that on-road emissions of NO_x from diesel passenger cars are often higher than those measured during test cycles [163], it has very recently emerged that this may be due to deliberate action by some manufacturers. The issues surrounding NO_x emission from diesel vehicles are exacerbated in Europe by the high proportion of diesel engine vehicles in the passenger car fleet [164]. Hence, not surprisingly, there remain considerable difficulties in reconciling predictions of changes in NO_x concentrations arrived at using emission inventories with actual measurements of ambient concentrations.

Air pollutant emission inventories provide input data for air pollution models, which in turn are used for predicting current and future air pollution and in developing strategies for improving air quality. One approach uses the so called 'bottom up' approach involving estimating emissions from different individual sources (e.g. emissions from a particular type of vehicle per km driven) and activity factors (e.g. number of vehicle km driven on a particular road) to produce annual emission estimate [165]. Therefore errors in the emissions from a large source sector (such as passenger cars) can lead to significant inaccuracies in the inventories, which then further propagate into forecasts of air pollutant levels. Evaluation of emission inventories can be carried out by comparing air quality model predictions (using inputs from the inventory) to observed concentrations. However this method does not provide a direct comparison with the emission rate as it requires knowledge of other parameters such as chemistry and meteorology, as well as the inherent uncertainty in the models themselves. In contrast, the eddy-covariance technique provides a direct measurement of an atmospheric pollutant flux from a particular 'footprint', providing a 'top down' approach for quantifying emissions [166].

A recent study from a tall tower site in central London [106] directly compared the measured NO_x emission rate with estimates from UK emissions inventories [165, 167]. The study found observed emissions of NO_x were on average 80% higher than standard inventory estimates for central London, suggesting the inventory was poor at estimating NO_x where traffic is the dominant source. Agreement was found to be better when an inventory with more explicit treatment of traffic emissions was used, so showing the importance of correctly accounting for the traffic source in London. While this tower-based study well represents the vicinity of the measurement location, it cannot reveal spatial patterning across Greater London.

Measurements of NO_x fluxes were taken from a low flying aircraft over London. Full details of the 2013 flight tracks, as well as measurement concentrations of NO_x and volatile organic carbons (VOCs) from the aircraft (including a comparison to various ground based measurements in London) can be found in Shaw et al. 2015 [168]. This study will focus exclusively on flux measurements. Spatially resolved data is compared to emissions inventories, providing a measure of how well the inventories reproduce measured emissions over a wide area of central and suburban London.

4.2 Overview

Research flights during the Ozone Precursor Fluxes in an Urban Environment (OPFUE) campaign 2013 and 2014, were conducted using the Natural Environment Research Council's (NERC) Dornier 228 aircraft based at the Airborne Research and Survey Facility (ARSF) at Gloucester Airport. The Dornier 228 has a maximum flight range of 24,000 km, maximum science operation altitude of 4,500 m due to an unpressurised cabin. Every flight conducted had a crew consisting of two pilots, one mission scientist, and up to three instrument scientists. A schematic of the aircraft is shown in Figure 4.2.

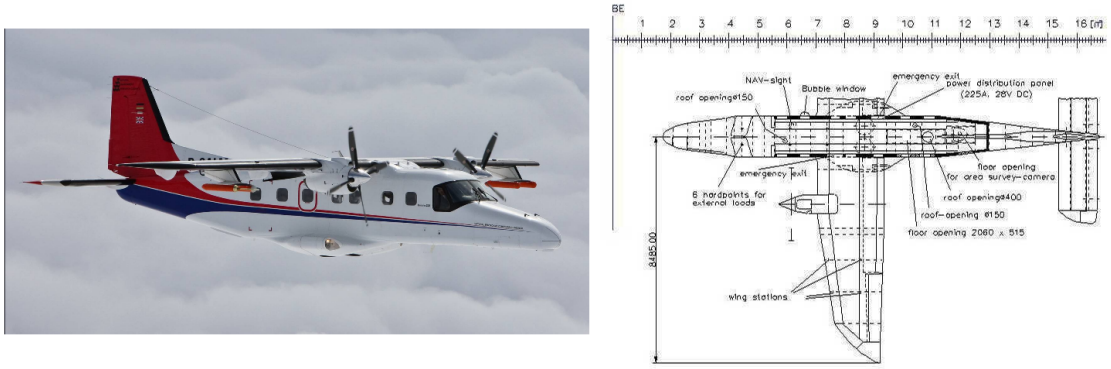

Figure 4.2: left) NERC Dornier 228 aircraft in−flight, right) schematic of aircraft. Taken from NERC Airborne Research and Survey Facility's Website [169].

The on−board science payload during the 2013 campaign consisted of: a fast chemiluminescence instrument for NO_x analysis (AQD-Fast-NO_x) for which a detailed description can be found in Chapter 2, a Proton-Transfer-Reaction Mass-Spectrometer (PTR-MS) which is described in Chapter 5 [168] and a Aircraft Integrated Meteorological Measurement System (AIMMS-20) [128].

The AIMMS−20 probe gives highly accurate measurements of atmospheric pressure; temperature, humidity, aircraft altitude and three-dimensional wind vectors at 20 Hz. Aircraft location was recorded using an Inertial−Position and Altitude System (IPAS 20), which had an accuracy during all flights of 0.05−0.30 m. The 2014 campaign instrument configuration was identical to 2013, with the added addition of a PICARRO gas analyser, giving 1 second resolved Carbon Dioxide (CO_2) and Methane (CH_4) mixing ratio data. The AIMMS−20 probe was mounted under the left wing, and calibrated via a calibration flight before OPFUE flights began. All on−board instruments sampled off a main front facing manifold pipe, located on the top of the aircraft.

4.2.1 Research Flights

OPFUE campaign during 2013 consisted of 12 research flights from Gloucester Airport to Greater London. Each flight would takeoff from Gloucester profiling up to high altitude (≈5,000 ft), for calibrations in clean air above the boundary layer. After transiting towards the London, a spiral descent around the Goodwood gave boundary layer height. Descending to an altitude off approximately 1,000 ft, replicate transects were made around the South Sussex area and then over Greater London starting at the southwest corner of the M25 and ending at the northeast corner of London. Each research flight contained 5+ transects over London. Replicate transects were conducted to assess the temporal variability of measured fluxes. Figure 4.3 left, shows all flight transects across Greater London during July 2013.

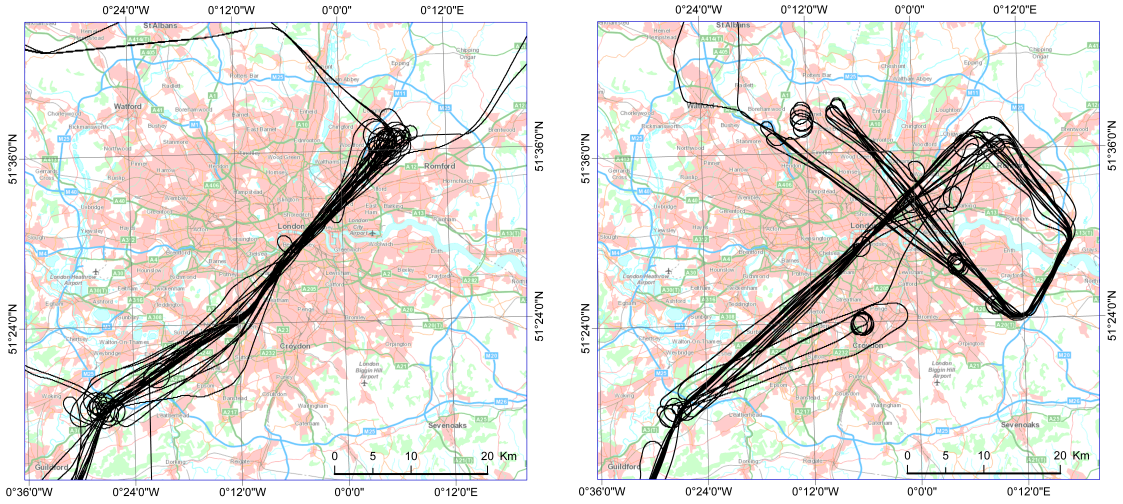

Figure 4.3: OPFUE 2013 flight transects over the Greater London region, right) OPFUE 2014 flight transects over the Greater London region.

The OPFUE campaign during 2014 consisted of 7 research flights again from Gloucester Airport to London. Flight structure used was the same with high altitude calibrations conducted on the transit from Gloucester to Southern England. A profile descent was again done over Goodwood to evaluate boundary layer height. Profiles over London were slightly changed from the originals. Straight leg transects were conducted from the southwest M25 to the northeast of London. The fight track then took a sharp right turn towards the more industrial areas of London, and then towards the Dartford tunnel. The transect then ran perpendicular to the original ending at the northwest corner of London completing a figure of 8 shape. The additions legs allowed for greater evaluation of London's emission profile.

Figure 4.3 right shows all flight transects across Greater London during July 2014 with the new figure of 8 flight path.

4.3 Experimental

4.3.1 Eddy-Covariance Fluxes

This study builds upon the previous work described by Torrence & Compo. (1998) and Thomas & Foken. (2007) [127, 170] and uses continuous wavelet transform (CWT) methodology for quantifying eddy−covariance fluxes from an aircraft. A full in-depth description of CWT flux methodology can be found in Chapter 3, only specific parameterisation is listed here. CWT is conducted via Equation 4.1, defining the transform of the discrete data sequence *x(n)* via complex conjugate of the Morlet wavelet $\psi^*_{p,a,b}$, for N data points [171].

$$w_x(a,b) = \sum_{n=0}^{N} x(n)\,\psi^*_{p,a,b}(n) \tag{4.1}$$

ψ denotes the mother wavelet, with a and b acting as parameters to scale and localise the wavelet in frequency and time respectively, and p as the normalised factor. The base equation for a wavelet is coined by the mother wavelet after localisation has occurred. This is defined in Equation 4.2 [123].

$$\psi_{a,b}(t) = \frac{1}{\sqrt{a}}\psi\left(\frac{t-b}{a}\right) \tag{4.2}$$

Wavelets are localised both in the frequency domain as for Fast Fourier Transform (FFT) but also in the time domain [172]. This allows for a signal's properties to be explored in both domains. Another added strength of the method is the ability to tailor the wavelet's properties to suit the application. As described in-depth in Chapter 3, the complex Morlet wavelet is used in this study as expressed in Equation 4.3, [127].

$$\psi_0(\eta) = \pi^{-\frac{1}{4}} e^{i\omega_0\eta} e^{-\frac{\eta^2}{2}} \tag{4.3}$$

ω_0 represents the frequency and η the time parameter in non−dimensional state. A more in-depth description for wavelet principles and the Morlet wavelet can be found in Torrence & Compo. (1998) [127]. The Morlet wavelet has been implemented in a number of previous studies specifically for analysing airborne measurements [107, 121, 123, 124, 171].

4.3.2 Flux Calculation

Flux is the measure of the rate of change of a quantity moving through an area per unit time, in this case, the amount of a chemical species (NO and/or NO_2) being uplifted at a point in space per unit time. In order to quantify this, the flux calculation algorithm as discussed in Chapter 3 is used. Using CWT, the covariance between vertical wind and species of interest is evaluated.

Lag time difference was calculated between vertical wind speed (w') and analyte concentration (c'), where w' represents the difference of the instantaneous vertical wind measurement to the mean vertical wind and c' is the difference of the instantaneous concentration to the mean concentration value. This allows the two data sets to be aligned, giving normalised covariance. Only flight legs showing a clear covariance peak were analysed. This was due to the lag−time not being constant between legs and so it could not be ensured that legs without a clear peak were being corrected properly.

The lag time between the two data sets was found to be in the range of 4−7 s. Due to the observed non−stationarity of the lag difference, each flight leg was analysed separately ensuring no additional bias. Before CWT fluxes were calculated, de−spiking of the data was conducted. The CWT calculates the global cross-spectrum between analyte concentration and vertical wind speed.

Figure 4.4b, depicts an example of the global cross−spectrum for a flight leg of NO_2 concentration data, with the y−axis giving the eddy contributions integrated over all frequency periods in seconds and the x−axis being the distance travelled along the flight leg. For each individual flight leg, co and cumulative co-spectra were compared across all frequencies for both the CWT and a standard Fast Fourier Transform (FFT). For all the flight legs, the majority of the flux contributions were found to be below 0.1 Hz. A more in-depth discussion of flux frequency contributions is discussed in Chapter 3.

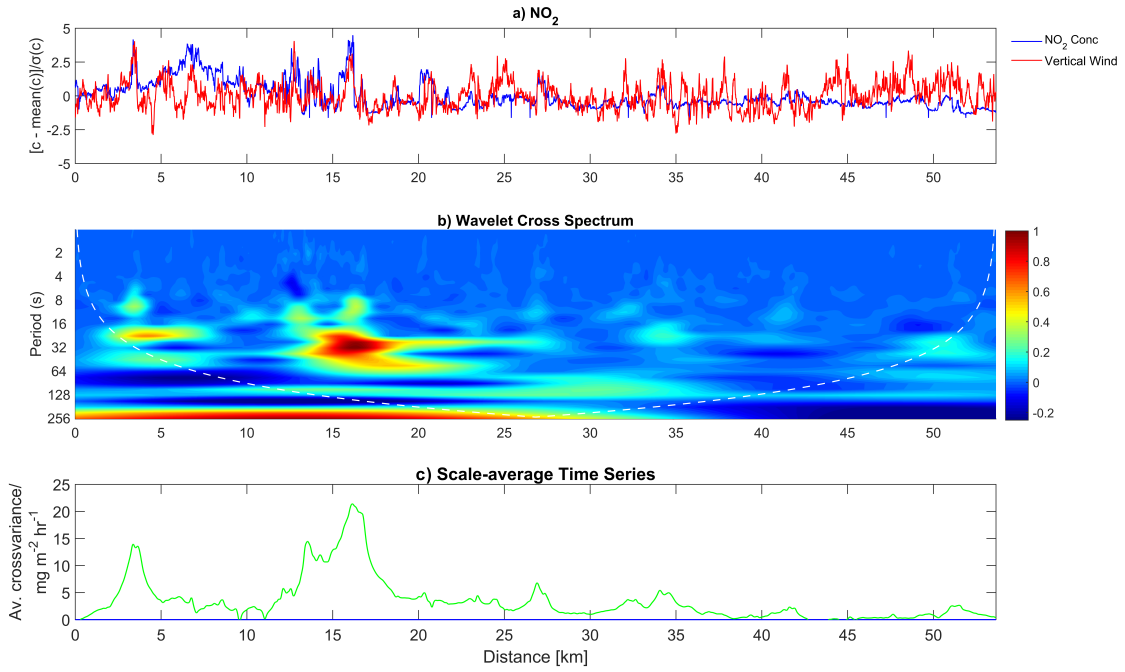

Figure 4.4: (a) Variation of NO_2 concentration from the mean and variance of vertical wind speed from the mean, (b) time resolved wavelet cross-spectrum, (c) the average cross−covariance between NO_2 concentration and vertical wind, for a typical NE to SW run across London.

4.3.3 Footprint model

In order to carry out interpretation of the data and compare to emissions inventories, it is necessary to calculate a flux footprint for each measurement. For this a footprint model was used which quantifies the spatial area from which the emission originates from [173, 174, 175]. An in−depth review into footprint models and their continued development can be found in Lenclerc et al. (2014).[135] Chapter 3 discusses in−depth the footprint model used in this study, and so only specific model parameterisation is discussed.

The footprint model described by Metzger et al. (2012) was used due to its similar application [150]. The model builds upon a cross−wind integrated model, which quantifies the flux contribution relative to the distance away from the measurement position, into the prevailing wind direction. This approach alone still leaves uncertainty due to the analysis being only in 1−dimensional space. For this purpose Metzger et al. (2012) coupled the model with a cross−wind function, allowing for non−perpendicular wind direction influences to be accounted for [150].

The model was parameterised using friction velocity (u_*), measurement height (Z_M), standard deviation of the vertical and horizontal wind (σ_w & σ_v) and roughness length (Z_0). Turbulence statistics for the footprint model are calculated at 1 km intervals from the wavelet cross−scalogram, with movement in both the x and y direction being 1 km for each new footprint. The Drew et al. (2013) study data was used to estimate expected roughness lengths for the London area [154]. For suburban area roughness lengths, values generally range from 0.4−0.6 m but up to 2.0 m for central London. The model evaluates the maximum influence distances in all directions, with the measurement point at its centre. From this it is possible to create a weighing matrix at the same temporal resolution as the inventories being quantified. The matrix when summed up gives a value of 1. This weighting matrix predicts, for every overflown 1,000 m cell, the ground influence contributing to the observed emission flux. The matrix is set to the same coordinate system as the inventory. A separate weighting matrix is calculated for every measurement point along the flight track.

For each point along the flight track, the emission inventory value for every cell within the footprint matrix is weighted accordingly and summed up to give a single emission estimate. All estimates from all source sectors are summed to give a total emission estimate every 1 km. Figure 4.5 depicts an example of the area which is predicted to be spatially representative for the flux measurements. The footprint area ranges in distance from the flight track anywhere from 5 to 12 km into the prevailing westerly wind direction. Part of the footprint area includes part of the London Low Emissions Zone (LEZ) which was introduced in 2008 to help improve air quality in central London.

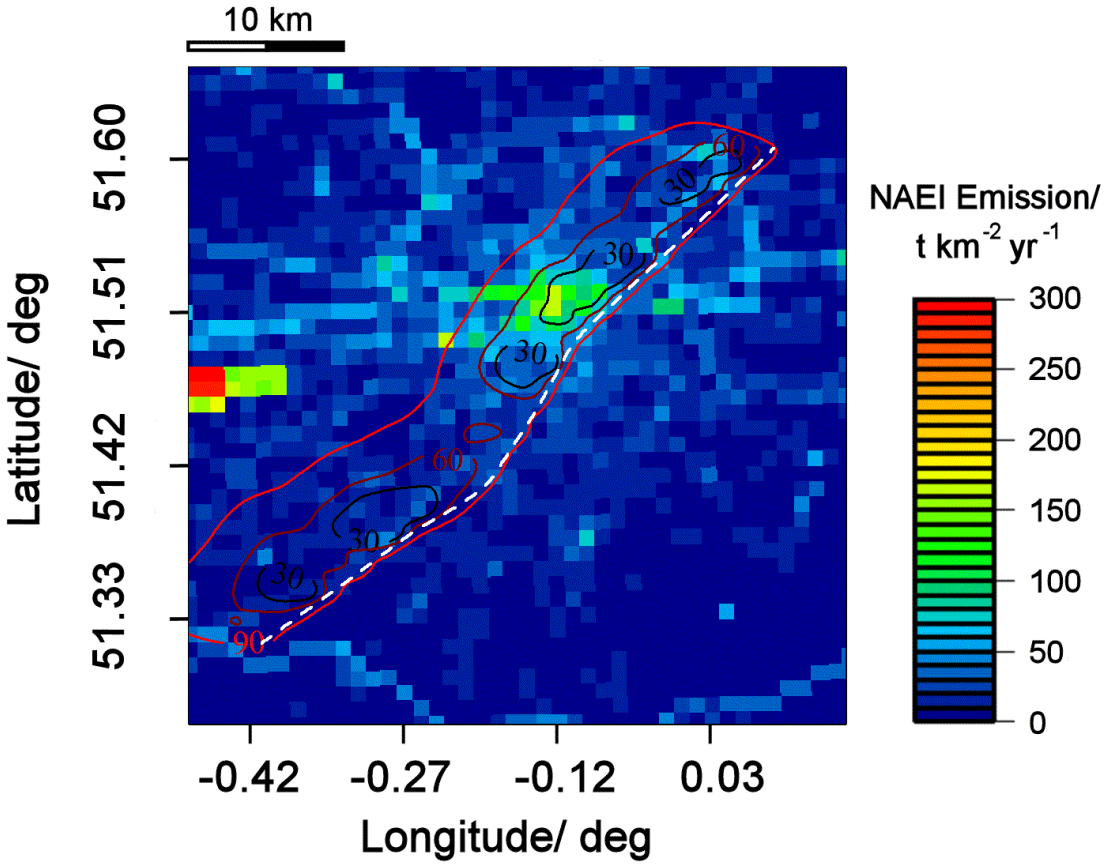

Figure 4.5: The contributing footprint area to a typical flight track, dependent on the prevailing wind direction and altitude of flight. The footprint is overlaid onto the NAEI at 1 km^2 grid resolution, coloured to annual NO_x tonnage emission estimates.

4.4 Results and Discussion

4.4.1 Spatially Resolved Flux Observations

Due to problems with the AIMMS−20 probe, NO_x fluxes were only calculated from data collected on three 2013 flights (research flights 5, 7 and 12), from 3^{rd} to 9^{th} July. Flight 5 was conducted during the morning rush hour from 08:00 until 10:00 am. Flights 7 and 12 were performed during the afternoon (12:00 to 16:00), thus providing some diurnal information of the emissions. Flights 5 and 7 had wind directions from the West giving information about the emissions coming from Central London. Flight 12 had wind directions prevailing from the NE giving emission information from more easterly areas of London. All the flights were performed during clear sunny days with the highest air temperatures observed (>23 ^{o}C) during flight 12.

Calculated fluxes during 2013 flights showed significant variability along the flight track. Figure 4.6 shows instantaneous flux across London as an average of flights 5, 7 and 12 (total of 17 legs) using inverse distance weighting (IDW) in ArcGIS. Highest observed fluxes consistently coincided within the same spatial area of Central London. This area is known to contain high traffic density, high−rise buildings and London Bridge Railway Station, from which a high number of diesel trains operate. Measured NO flux during 2013 flights displayed high localisation. NO_2 fluxes showed more consistent elevation throughout the whole of Central London, compared to the sharp NO emission peak (Figure 4.6a & b).

Measured NO_x flux over central areas ranged from 30−90 mg m^{-2} h^{-1}, with the high observed during flight 5. This corresponded to the morning rush hour period from 08:00 to 10:00 with high traffic densities in Central London [176]. Fluxes measured on the other flights over Central London during the afternoon showed consistently lower NO_x flux compared to the morning, in the range of 30−40 mg m^{-2} h^{-1}, with no clearly definable evening rush hour period obvious. For all flights, measured NO_x flux outside of Central London (both in the SW and NE directions) was significantly lower, typically in the range 5−10 mg m^{-2} h^{-1}, corresponding to lower traffic densities in these parts of the city. Some spikes in NO_x fluxes, up to 20 mg m^{-2} h^{-1}, were observed on some legs, which seem to correspond with major roads (e.g. the M25 ring road).

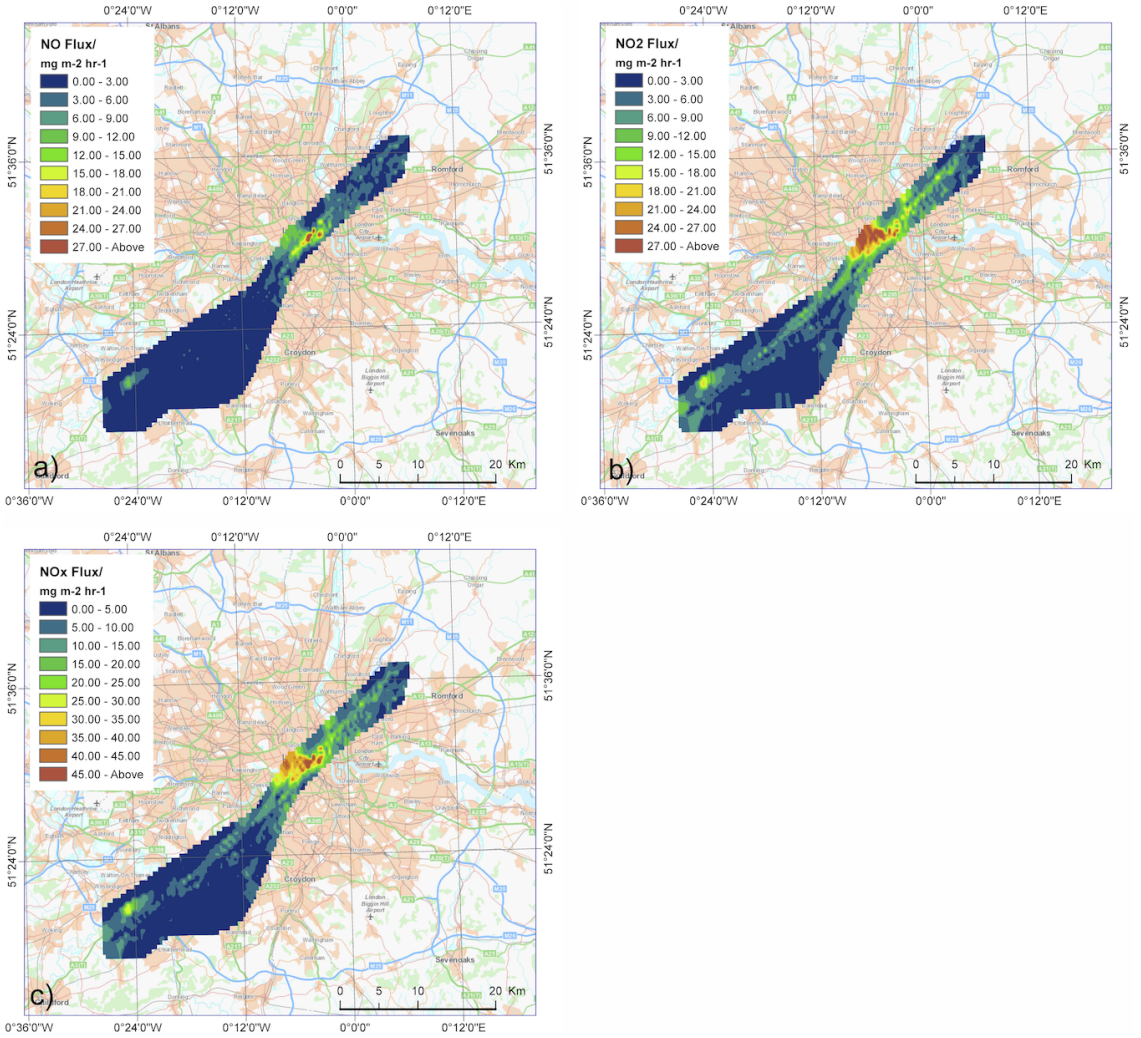

Figure 4.6: 500 m fluxes calculated from all 2013 flight transects using inverse distance weighting (IDW) in ArcGIS. a) average instantaneous NO flux at 500 m resolution, b) average instantaneous NO_2 flux at 500 m resolution, c) average instantaneous NO_x flux at 500 m resolution.

From 5 RF's during the OPFUE 2014 campaign, 25 flight transects over London gave good flux data from a possible total of 28. Using the enhanced flight path discussed in Section 4.2.1, the temporal−variability of NO_x emissions over London were again investigated for a second successive year. Figure 4.7 shows the spatial variability of NO/ NO_2/ NO_x emissions over a large area of London, at 500 m using IDW from all 2014 flight transects. NO flux showed again a strong emission point for Central London >27 mg m^{-2} h^{-1}, with Greater−London areas also showing enhancement up to 15 mg m^{-2} h^{-1}. Outer regions showed lower NO enhancement, with no apparent influence observed from the M25 motorway, where road transport will be the dominant source of NO emission.

Quantified NO_2 emissions during 2014 displayed more varied structure, with central areas showing highest emissions up to 27 mg m^{-2} h^{-1}. Greater London showed stronger NO_2 emission characteristics than for NO, which could be attributed to the major road network along the flight path. Overall, maximum measured NO_x emission from all 2014 flights was found to be >30 mg m^{-2} h^{-1}. The enhancement is lower than observed previously during 2013, where NO_x elevation at times reached >60 mg m^{-2} h^{-1}. This may be due to meteorological conditions being different, and also the revised flight path giving a lower number of flight transects over the original area, thus meaning the full emission profile over that area was not fully captured during 2014.

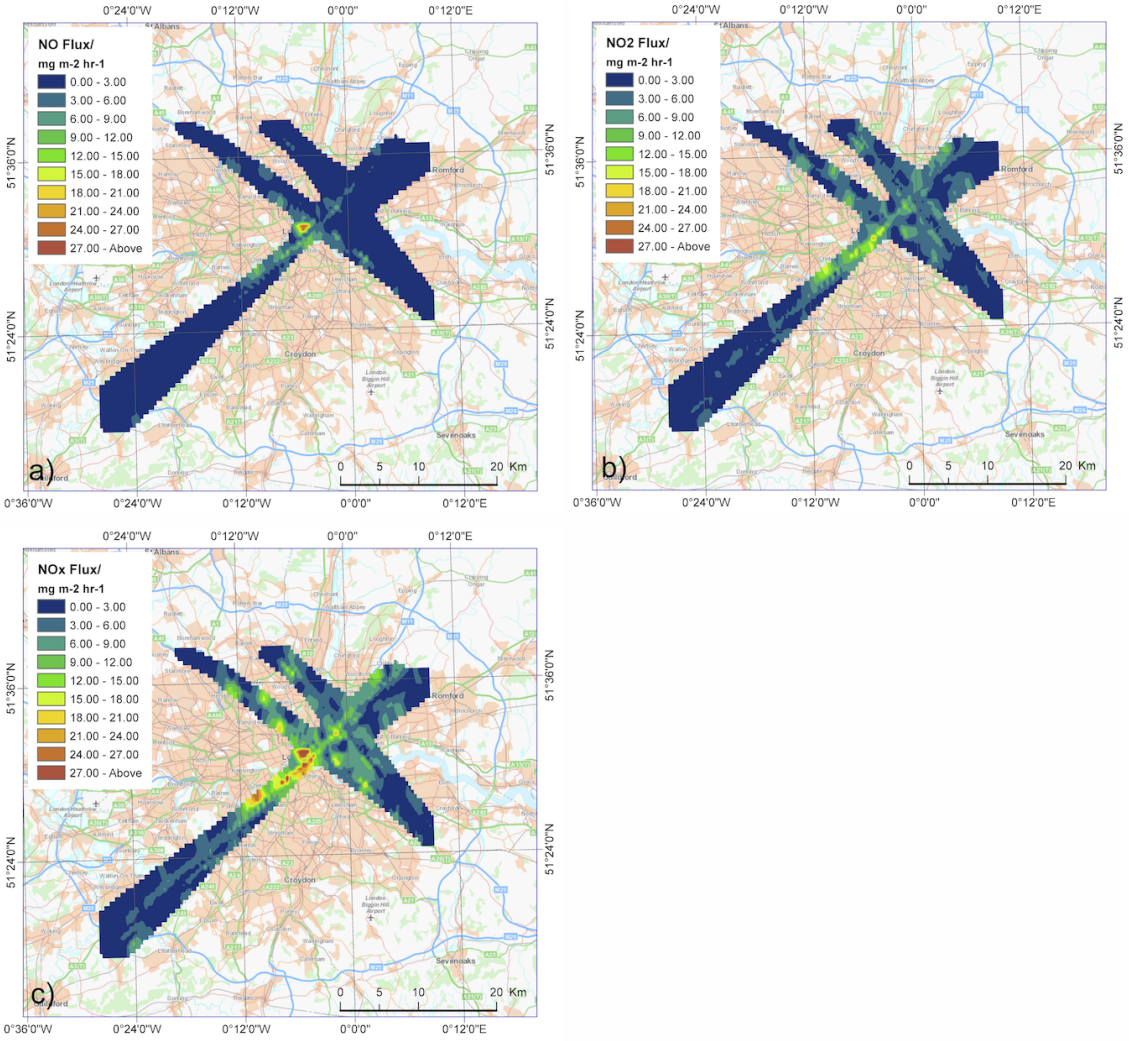

Figure 4.7: 500 m fluxes calculated from all 2014 flight transects using inverse distance weighting (IDW) in ArcGIS. a) average instantaneous NO flux at 500 m resolution, b) average instantaneous NO_2 flux at 500 m resolution, c) average instantaneous NO_x flux at 500 m resolution.

4.4.2 Comparison to the National Atmospheric Emissions Inventory

The UK's National Atmospheric Emissions Inventory (NAEI) is the standard tool for both reporting and understanding the emissions for a range of pollutants in the UK. For each pollutant the inventory is broken down into a series of source types which, when grouped and summed together, give an annual emission estimate at 1 km^2 resolution across the entire country. Emission source types include road transport, rail and aviation, domestic and industrial combustion, energy generation and other sources such as waste production [177]. In common with many other emission inventories in Europe, the traffic source in the NAEI is mainly based on the (Calculation of Emissions from Road Transport) COPERT 4 emission factor model for road vehicle emissions. The COPERT 4 methodology is part of the European Monitoring and Evaluation Programme/European Economic Area (EMEP/EEA) air pollutant emission inventory guidebook for the calculation of air pollutant emissions [178].

To allow for real time comparison between airborne flux measurements and the inventory, the footprint methodology outlined in Section 4.3.4 was used. Each inventory source sector is assessed individually, giving an emission contribution. The emission inventories used here only provide annual emission estimates for each grid square from the wide range of source sectors, they do not directly provide temporally−resolved hour of the day or day of the year estimates. Therefore, each source sector is scaled separately, using scaling factors [177] that take into account the temporal variation in emissions for any given month, day and hour. By scaling each source sector individually, more realistic emission estimates were generated for the specific time of day and day of the year of the flux measurements. Scaled estimates for each source sector are then summed up at each point along the flight track, to give 1 km resolution estimates for NO_x emission. Nevertheless, such temporal profiles represent the typical average profiles expected for different emission sources. Uncertainty will be introduced when comparing estimates obtained over short periods of time with the mean profiles used in atmospheric emission inventories.

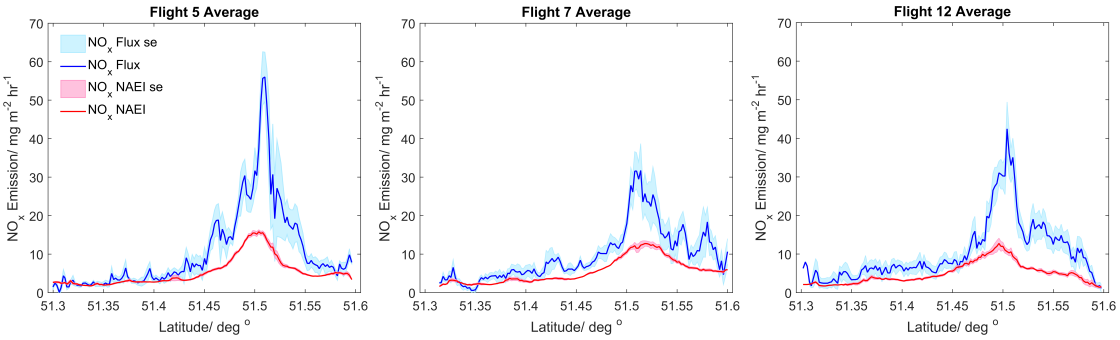

Figure 4.8: Average for Flights 5, 7 and 12 (2013), measured NO_x flux plotted in blue with standard error shown as the shaded blue area. Calculated NAEI estimates using the described footprint methodology for NO_x are plotted in red, with standard error shown as the shaded red area. NAEI estimates have been scaled to account for month, day and hour temporality.

Figure 4.8 depicts spatially resolved NO_x flux observations averaged for three 2013 flights in blue and the 2013 NAEI emission estimates plotted in red, all against the flight track latitude. All flights showed relatively good agreement between the NAEI estimates and the measurements in suburban London; however, there appears to be a significant underestimation in the inventory compared with the measurements, by a factor of 2−4, in Central London (latitude 51.43−51.52). The data interpretation is complicated by the significant uncertainty (60−250%) of 1 km spatially−resolved flux measurements. Therefore, in order to further reduce these uncertainties, each flight track is divided into four parts, each approximately 15 km in length. The first two segments represent outer regions of SW London (zones 1 and 2) and the second set (zones 3 and 4) for Central and Greater NE London. The flux data is then averaged for each segment to give a single NO_x emission value. The uncertainty associated for these fluxes is greatly reduced compared to the more spatially resolved flux data, as shown in Figure 4.8, now being in the range 30−45%.

Clearly, the NAEI is unable to accurately represent emissions of NO_x from Central London. One possible explanation for this is in the way in which the inventory accounts for road transport emissions. Figure 4.9 shows that across the whole of the area surveyed road transport is the dominant source of NO_x. Traffic contributes up to 90% of NO_x emissions in outer London (zones 1 and 2), strongly suggesting that significant error in the road traffic source in the inventory is responsible for the underestimation of NO_x emissions by the inventory relative to the flux observations. In Central and Greater NE London (zones 3 and 4), where the underestimation of the inventory is highest, road transport, while still the largest source, is responsible for 65−70% of the total NO_x emissions in the inventory, with most of the remainder due to domestic and commercial combustion

of gas for space and water heating. The relatively low use of gas for heating during July is taken into account via the emission scaling factors applied to the NAEI, but the large underestimation in the inventory in the Central London area suggests that as well as underestimation of traffic−derived NO_x, there is also some error in the NAEI treatment of domestic and commercial combustion, or there is a major missing source of NO_x in the inventory.

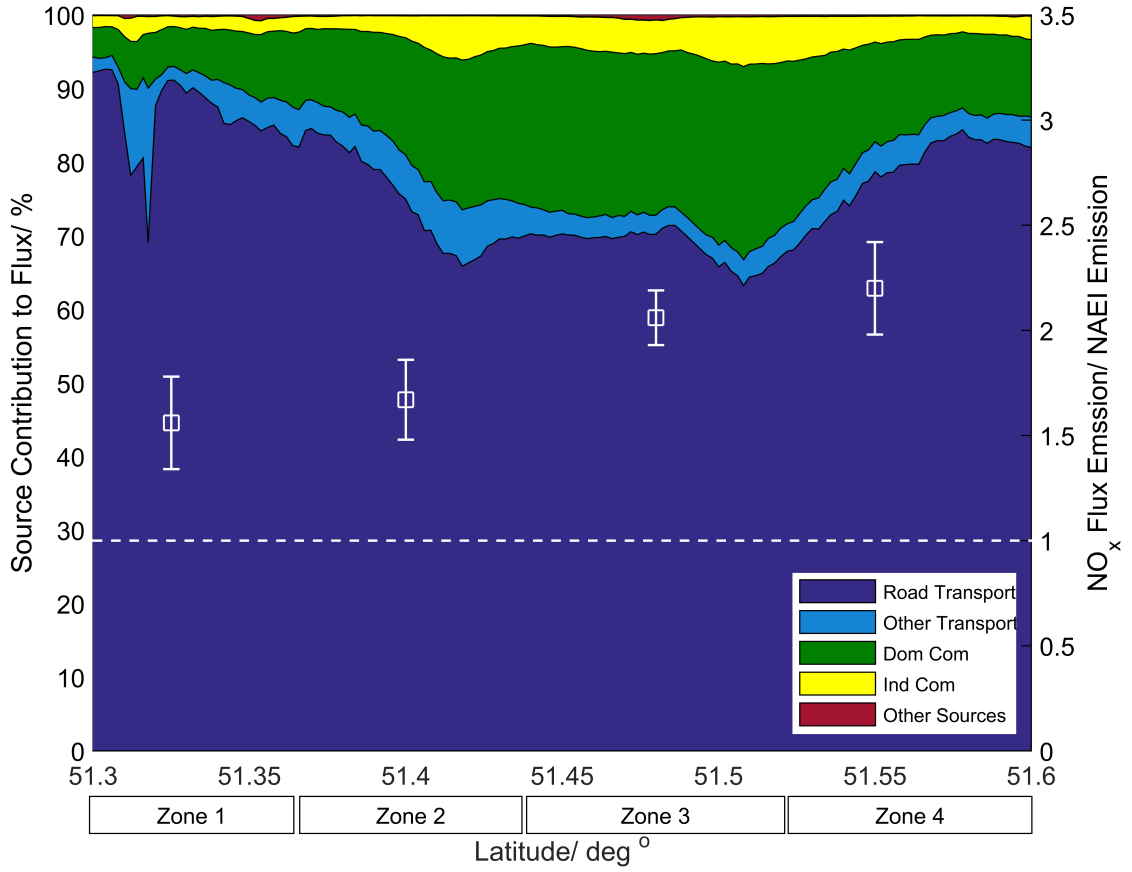

Figure 4.9: Calculated emission source contributions from the NAEI plotted on the first y axis, with sources being broken down into road transport; other transport (such as rail), domestic and commercial combustion, industrial combustion and other sources. Also plotted on the second y axis as white squares is the ratio of measured to NAEI estimated NO_x flux, with the error bars denoting the standard error of all points included. The flight is broken into 4 zones, with 1 and 2 being SW outer London, 3 central London and 4 NE outer London.

Calculated 2014 NO_x fluxes show similar emission structure to those observed during 2013. Highest emissions of NO_x are again found within most central latitudes of London. Comparing measured flux to the 2014 NAEI for NO_x as shown in Figure 4.10, again highlights underestimation by the inventory. Suburban and Greater London regions show relative agreement as previously discussed during the 2013 comparison. For the Central London; however, underestimation is more prevalent. Although not as large as observed during 2013, the NAEI is shown to underestimate by up to a factor of 2. On average for Central London, the NAEI underestimates NO_x emission by 70% which is an improvement when compared the 2013 underestimation for the same region, showing >100%. The improvement by the inventory maybe due to the reduced number of flight transects over the region, causing the full emission structure of Central London to be only partially captured.

Table 4.1, gives detailed statistics for each of the four zones as discussed earlier in terms of: average measured flux, time−of−day NAEI emission estimates and the ratio between measurement and inventory. Across the four zones, improvement is observed by the NAEI in relation to measured NO_x flux duing 2014. More comparable measurements are needed to better understand the improvement. Overall, the results described are potentially important as the NAEI is used to provide emissions for air quality forecasting models, which inform potential future air quality abatement strategies. The following sections will discuss potential reasons for the discrepancy, including measurement errors, and investigate the advantages of using a more London−specific emissions inventory with a more explicit treatment of the road traffic source.

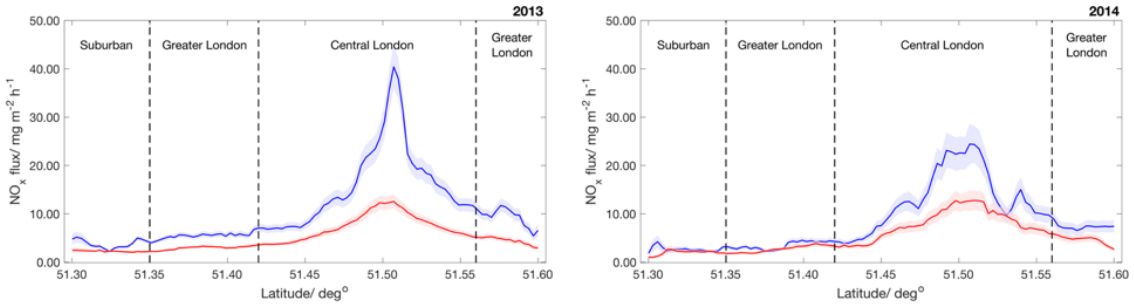

Figure 4.10: Average measured NO_x flux (blue) and time−of−day scaled NAEI estimates (red) for 2013 and 2014 flights against latitude with standard error shown as shaded area.

Table 4.1: Upper) Average measured NO_x flux and time−of−day NAEI estimate during 2013 and 2014 flights with subsequent breakdown into four regions of London. Lower) Average ratio of measured flux to NAEI estimate with breakdown of four regions of London

	Average Flux/ mg m $^{-2}$ h^{-1}	Suburban London/ mg m $^{-2}$ h^{-1}	Northwest Greater London/ mg m $^{-2}$ h^{-1}	Central London/ mg m $^{-2}$ h^{-1}	Northeast Greater London/ mg m $^{-2}$ h^{-1}
NO_x (2013)	10.51	3.79	5.51	16.04	12.09
NO_x NAEI (2013)	5.09	2.28	3.22	8.08	5.62
NO_x (2014)	8.26	2.69	3.47	13.42	9.40
NO_x NAEI (2014)	5.36	1.88	2.83	6.97	6.95

	Average Flux to NAEI/ ratio	Suburban London/ ratio	Northwest Greater London/ ratio	Central London/ ratio	Northeast Greater London/ ratio
NO_x (2013) NO_x NAEI (2013)	2.06	1.66	1.71	1.99	2.15
NO_x (2014) NO_x NAEI (2014)	1.54	1.43	1.23	1.93	1.35

4.4.3 Measurement Uncertaines

The uncertainty of the calculated flux is dependent on both the random and systematic errors. A detailed description of both error types can be found in Chapter 3 (Section 3.3.6). Karl et al., defines the random (re) and systematic (se) error for the airborne flux as shown in Equations 4.4 and 4.5 [121]. l denotes the flight leg length, Z_M the flight altitude and Z_i the height of the boundary layer. Boundary layer heights were obtained at the beginning and end of each flight via atmospheric soundings (Li-DAR) from Heathrow Airport, West London. A more detailed study into the relative effects of errors for calculated flux measures can be found in Mann & Lenschow. (1994) [131].

$$re \leq 1.75 \left(\frac{Z_M}{Z_i}\right)^{0.25} \left(\frac{Z_i}{l}\right)^{0.50} \tag{4.4}$$

$$se \leq \frac{2.2 z_i \left(\frac{Z_M}{Z_i}\right)^{0.50}}{l} \tag{4.5}$$

For 1 km resolved fluxes, the overall error is significant and can be over 200%, which is discussed in greater detail in Section 3.3.6. To reduce this high uncertainty, flux scales scan be increased. As discussed in Table 4.1, the four London regions which are compared to the NAEI are about 15 km long. By averaging over this larger spatial scale, the flux uncertainty improves to approximately 40%. Also by averaging across the entire flight path, the uncertainty will greatly improve to approximately 20%.

In addition to the flux uncertainties, the flux limit of detection (LoD) was calculated from the covariance function, above which measured flux can be distinguished from the combined effects of instrument noise [124, 179]. The flux LoD was calculated for each flight leg and was found to vary from flight to flight. Over all the flux LoD was found to be in the range 0.075−0.180 mg m^{-2} h^{-1}. Some NO_x emitted at the ground surface may be lost before it is detected at the flight altitude, causing an error in the flux estimates. Using measured meteorological parameters and the wavelet transform, Deardorff velocities (w^*) for each flight were calculated. w^* gives a turn−over time for all the influencing eddies which account for the measured flux. w^* was found to be in the range of 0.5−3.0 m s^{-1}, which gives a vertical ascent time of 2−8 minutes from the surface to the measurement altitude of 300 m.

Loss of emitted substances can occur via three mechanisms: chemical reaction, weakening vertical transport and storage. To account for chemical losses in the atmosphere,

the vertical flux profiles obtained in the Karl et al. (2009b) study was used [180]. They calculated the loss of isoprene emission during transport through the boundary layer. To use this method, NO_x chemistry was fed into the model in place of isoprene, taking into account the lifetime of NO_x in the troposphere with respect to chemical reaction of NO_x with the hydroxyl radical (OH). Middle−of−the−day OH abundances measured in London during summer 2012 were used, as reported in the Lee et al. (2015) study [106], of 2.0 x 10^6 molecule per cm^3. This gives a lifetime of NO_x above London of ≈11 hours. Using this calculated NO_x lifetime, it is estimated that the loss of NO_x flux between the ground surface and the flight altitude is only between 1 and 2%.

Not all chemical NO_x loss processes have been considered (e.g. PAN formation) as these will be small compared to the reaction of NO_2 with OH. Loss due to weakening vertical transport accounts for vertical momentum decreasing as altitude increases and is estimated to be 25−30%. The final loss process involves storage of some of the emission within the urban structure, such as street canyons [181, 182]. However, this is not considered to be an important loss process. Significant storage of NO_x within the street canyon in London would result in a steady buildup of concentrations, something that is not typically observed. Thus, if deposition is ignored, the transfer of NO_x out of the street canyon is essentially equal to the emissions, with the only result being a potential time lag from emission to measurement. Future work in this area could gain from using the Lenschow et al. (2016) study to account for all three loss terms in unison [183]. All these loss processes have the potential to increase measured fluxes, which would further increase the discrepancy between measured and inventory−estimated emissions.

As discussed above, the study shows that, even in outer London where traffic sources are estimated to contribute 90% of the emitted NO_x, there is observed inventory underestimation by a factor of around 150%, adding further evidence that it is the traffic source sector that contains the major error. There are several sources of disagreement between the flux emission estimates and those from the emission inventories. The emission inventories focus on longer term (annual) emission totals rather than providing estimates by hour of the year. For this, reason the emissions for a particular hour of the year need to be estimated through the scaling factors described in the previous section. It is; however, difficult to quantify the additional uncertainties introduced when scaling factors are used in emission inventories in this way.

4.4.4 The London Atmospheric Emissions Inventory

The London Atmospheric Emissions Inventory (LAEI) provides emission estimates for eight key air pollutants (including NO_x) at 1 km^2 resolution across all London boroughs, to the outer M25 motorway boundary that encompasses Greater London. The inventory reflects the geography of the roads in London, enabling an accurate assessment of population exposure and health impacts. The inventory is broken down into source sectors, contributing to the total annual estimates. Sources within the LAEI include: road transport (exhaust and non−exhaust), large regulated industrial processes, small regulated industrial processes, large boiler plants, gas heating (domestic and industrial-commercial), oil combustion sources (domestic and commercial), coal combustion sources (domestic and commercial), agricultural and natural sources, rail, ships, airports and others such as sewage plants. The LAEI also contains a non−road mobile machinery source (e.g. cranes, small electricity generators and other construction machinery), which has been shown previously to be a significant source of NO_x in central London [167].

The LAEI uses a 'bottom up' road traffic inventory taking vehicle flow and speed on each road and combining these with national and London−specific vehicle stock data (including buses and taxis) to calculate emissions for each of the 11 vehicle types and combining these to create emissions at 1 km^2 resolution. The data used here benefits from roadside emissions measurements, obtained using the University of Denver Fuel Efficiency Automobile Test (FEAT) system (IR/UV absorption spectroscopy), deployed for a 6 week campaign and taking measurements from 70,000 vehicles, including cars, buses and taxis, at four locations across London [184]. Vehicle number plates were recorded for each vehicle and these were cross−referenced against vehicle databases to obtain relevant vehicle details including their Euro emissions classification. The roadside emissions measurements quantified exhaust emissions of both total NO_x and NO_2 as a ratio to carbon dioxide (CO_2), with the results then combined with CO_2 estimates from the LAEI to create NO_x and NO_2 emissions in g km^{-1}. The emissions from vehicle types that were not measured during the campaign, most notably articulated heavy goods vehicles, were taken from the published LAEI results [167].

In order to try to produce an improved agreement between the inventory and measured emissions an 'enhanced' version of the NAEI was produced. All NAEI sources except road transport were used to form the base of the inventory. To account for road transport emissions, the LAEI's road emission estimates were scaled using the described roadside

measurements, increasing the road traffic source by an average of ≈50% across London. Currently the NAEI does not include specific emissions from non−road mobile machinery (NRMM), so the LAEI's NRMM source was also added to the inventory. Collectively the 'enhanced' NAEI is formed of a base NAEI model with scaled road transport emissions and NMRR estimates from the LAEI.

Comparing the 'enhanced' NAEI with the measured fluxes has allowed for a better assessment of using a more explicit treatment of traffic emissions in the national inventory. The same methodologies, as used for NAEI comparison, were used in analysis of the enhanced NAEI. Each enhanced NAEI source sectors was analysed to give emission estimates along the flight track at 1 km resolution. Each sector was scaled individually to allow for time of day comparison using the scaling factors described earlier, then added together to give overall NO_x emission estimates.

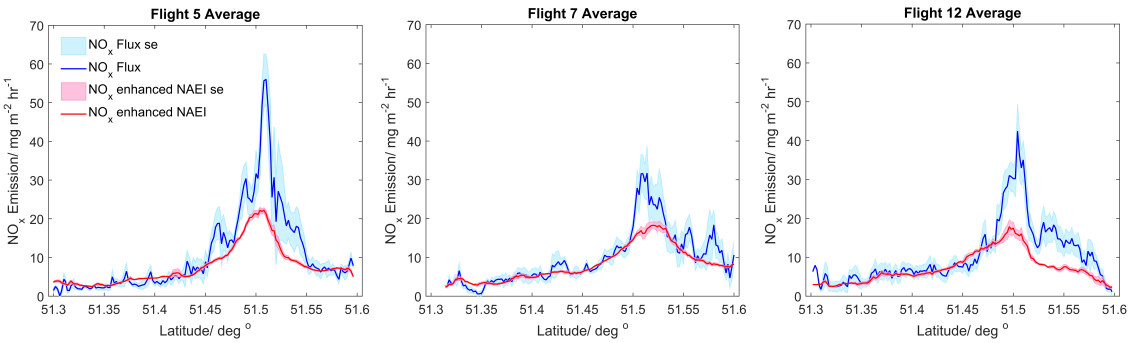

Figure 4.11: Average for Flights 5, 7 and 12 (2013), measured NO_x flux plotted in blue with standard error shown as the shaded blue area. Calculated and scaled 'enhanced' NAEI estimates of NO_x emission are plotted in red, with standard error shown as the shaded red area.

Figure 4.11 shows how 'enhanced' NAEI emission estimates in red (standard error as light red shading) compare with the measured NO_x fluxes (2013 flights) in blue (standard error as light blue shading) for each flight average. It is apparent that the agreement between the measurement and the inventory is better than for the standard NAEI. Outer regions of London seem to compare very well, with all flight legs showing only a small degree of discrepancy. However, despite the agreement being improved and almost always falling within the error of the 1 km spatially resolved flux measurement, there is still a significant discrepancy observed in central London. As with the standard NAEI data, the flight track was also divided into four parts, each approximately 15 km in length, with the flux data then averaged for each segment to give a single NO_x emission flux with reduced error (again in the range 30−45%).

Figure 4.12 depicts the average ratio of the measured to 'enhanced' emission inventory flux from all the flight legs, with the error bars denoting the standard error of the 17 legs included, along with the source sector contribution as before. The contribution from the different source sectors is similar for the enhanced NAEI as for the standard inventory. The main difference is the addition of the NRMM source, which now contributes up to 9% of total NO_x emissions in central London. The ratio of measurement to enhanced emissions inventory for all zones shows considerable improvement compared to the standard NAEI. For the SW outer London zones, the ratio is close to one (average of 1.1), which is within the standard error of the measurements. However, in central and NE London, there is still some significant underestimation (average measurement to inventory ratio of 1.48), which is outside the (30−45%) flux measurement uncertainty. The observed improvements in the enhanced emission inventory estimation of NO_x can be directly related to the improved road transport source increasing the magnitude of the road transport emissions and the addition of the NRMM as a key source not currently accounted for in the standard NAEI.

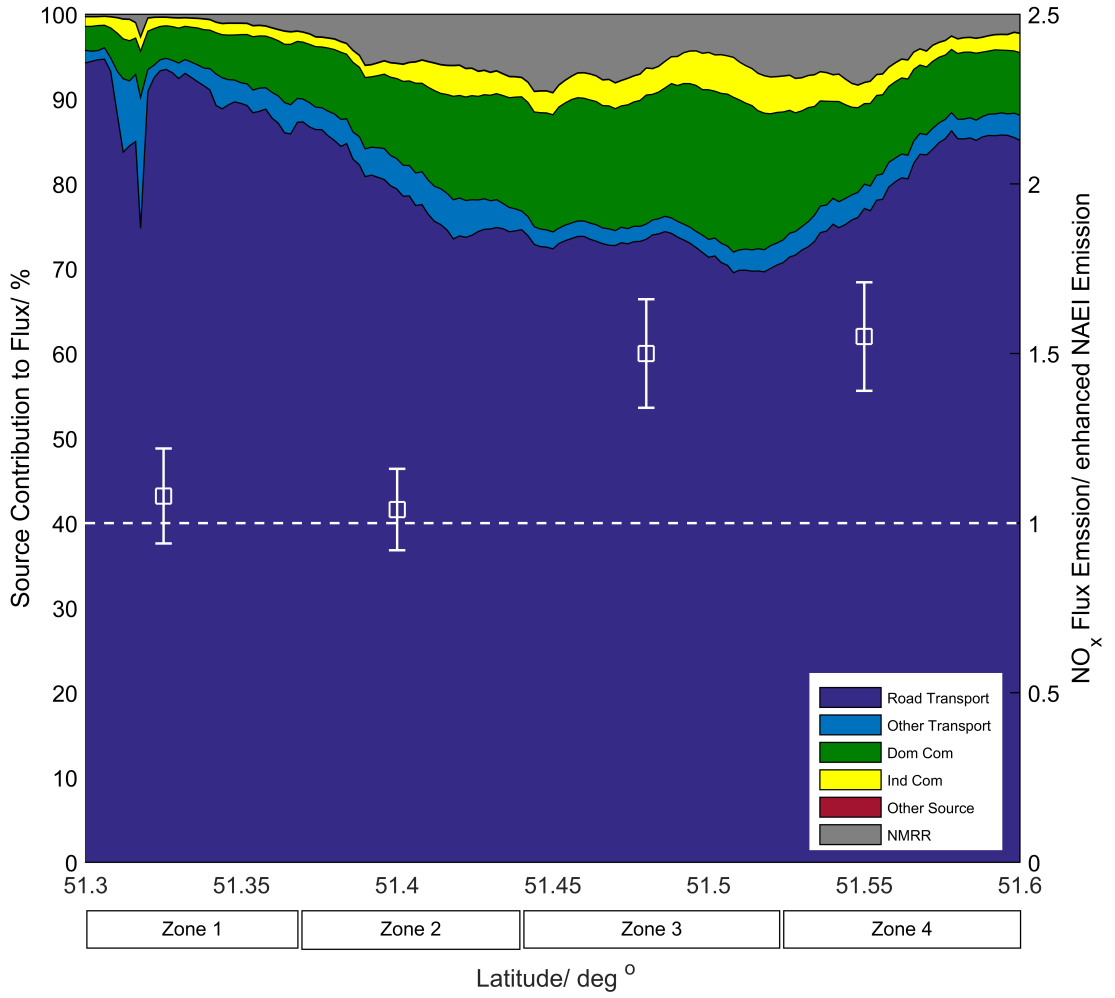

Figure 4.12: Calculated emission source contributions from the 'enhanced' NAEI (see text for details) plotted on the first y axis, with sources being broken down into road transport; other transport (such as rail), domestic combustion, industrial combustion, other sources and non−road mobile machinery (NRMM). Also plotted on the second y axis as white squares is the ratio of measured to enhanced NAEI estimated NO_x flux, with the error bars denoting the standard error of all points included. The flight is broken into 4 zones, with 1 and 2 being SW outer London, 3 central London and 4 NE outer London.

Comparison of measured 2014 fluxes to the enhanced NAEI showed good agreement across the entire flight track. Figure 4.13 shows latitude average of measured flux and the enhanced NAEI for both years flights. Suburban and Greater London regions compared well, with Central London showing good improvement compared to the standard NAEI. The addition of the LAEI's road transport and NRMM source sectors greatly improved the reliability of the inventory. Splitting the flight track into the previously discussed 4 zones, the agreement between measurement and inventory can be further classified, with overall error on each flux measurement greatly reduced.

Table 4.2 gives detailed statistics of measured flux and footprint calculated time−of−day 'enhanced' NAEI emission estimates for each of the four London zones. Overall, the agreement between measurement and 'enhanced' NAEI is good. For 2013 the ratio between measurement and inventory was found to be 1.4, which subsequently improves to a value of ≈1.2 for 2014. The agreement for Suburban and Greater London was within standard error for both years. Slight overestimation by the enhanced NAEI was found for certain regions of Greater London during 2014; however, due to the low levels of NO_x emitted at these latitudes the overall impact is negligible. Central London still showed a slight underestimation, up to 45% during 2013 and 30% during 2014. On average, the 'enhanced' NAEI is better able to predict time−of−day NO_x emissions than the standard NAEI. The vast improvement shown here further strengthens the need for refined road transport emission estimates in the NAEI.

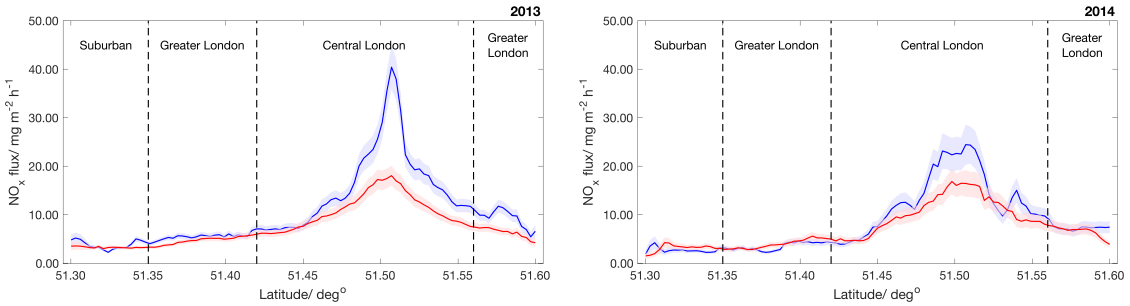

Figure 4.13: Average measured NO_x flux (blue) and time−of−day scaled enhanced NAEI estimates (red) against latitude with shaded area as standard error, for 2013 and 2014 flights.

Table 4.2: Upper) Average measured NO_x flux and time−of−day enhanced NAEI estimate during 2013 and 2014 flights with subsequent breakdown into four regions of London. Lower) Average ratio of measured flux to enhanced NAEI estimate with breakdown of four regions of London

	Average Flux/ mg m $^{-2}$ h^{-1}	Suburban London/ mg m $^{-2}$ h^{-1}	Northwest Greater London/ mg m $^{-2}$ h^{-1}	Central London/ mg m $^{-2}$ h^{-1}	Northeast Greater London/ mg m $^{-2}$ h^{-1}
NO_x (2013)	10.51	3.79	5.51	16.04	12.09
NO_x en−NAEI (2013)	7.50	3.28	4.70	11.06	8.10
NO_x (2014)	8.26	2.69	3.47	13.42	9.40
NO_x en−NAEI (2014)	7.08	3.11	3.96	10.25	8.28

	Average Flux to NAEI/ ratio	Suburban London/ ratio	Northwest Greater London/ ratio	Central London/ ratio	Northeast Greater London/ ratio
NO_x (2013) / NO_x en−NAEI (2013)	1.40	1.16	1.17	1.45	1.62
NO_x (2014) / NO_x en−NAEI (2014)	1.16	0.86	0.88	1.31	1.14

4.4.5 Breakdown of London's Road Transport Emissions

As previously discussed the main source of London's NO_x is from road transport. Any error in this emission source sector could have major implications towards the NAEI being able to accurately predict London's emissions. The 'enhanced' NAEI has been successfully shown to reduce observed underestimation by using a refined road traffic source. As discussed, remote sensing detection (RSD) measurements are used to constrain London's road transport emissions through analysis of individual vehicles [45]. Collectively, this analysis gives a far more detailed breakdown into individual vehicle types and their emission characteristics.

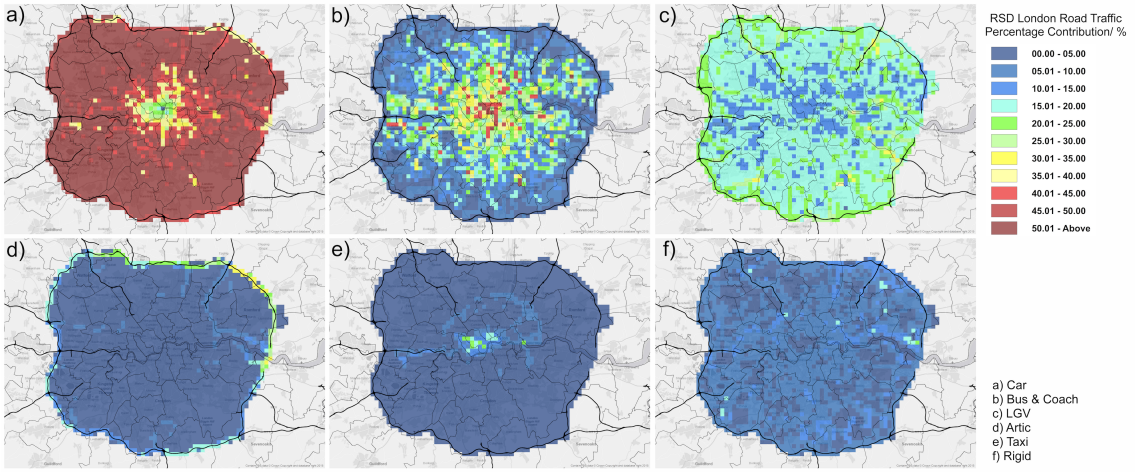

Figure 4.14: RSD percentage contribution of each vehicle type to road transport emissions at 1 km^2 resolution for the whole of greater London.

The 'enhanced' NAEI's road transport source sector can be broken down into 7 vehicle types: car, bus, LGV, taxi, rigid, artic and motorbike. LGV accounts for large goods vehicles weighing no more than 3.5 Tons. Rigid vehicles, also known as HGVs, are heavier goods vehicles that are not articulated in design. Articulated vehicles are the largest class of goods vehicle and can carry loads of up to 40 Tons. Figure 4.14 shows the emission contribution for each vehicle type at 1 km^2 resolution for London's total road transport emissions. Cars are the dominant source for Suburban London making up more than 50% of road transport NO_x emissions. LGV are a steady contributor across London, ranging from 15−20%. For Greater and Central London, the contribution of buses increases from 5% to 30%. This increase can be attributed to the higher usage of public transport. In Central London, buses and cars show nearly equal emission characteristics. Due to this, both vehicle types need to be at the centre of any emission control strategies if

improvements in NO_x emissions is to be achieved. Currently, London's low emission zone targets private cars and other high emitting diesel vehicles. This strategy is not specifically aimed at buses being one of the main emission sources, and so may benefit from future refinement. Figure 4.15 shows the latitude average percentage contribution of each vehicle type for the whole of Greater London, further clarifing the large emission contribution buses have in Central London.

The remaining vehicle types are: taxis, rigid, motorbikes and articulated lorries. The contribution of motorbikes is very small, <1%. Articulated lorries show significant contribution around London's major road network and the M25. Other lorry types that fall under the rigid classification give a steady emission contribution of ≈10%. Both lorry types (artic and rigid) are considered in the low emission zone strategy for NO_x reduction. The final vehicle type is taxis, which shows increased contribution for Central London up to ≈10%.

Using footprint method previously described, the emission contribution for each of the 7 vehicle types was assessed with respect to London's overall NO_x emissions. An 'enhanced' NAEI model was run containing road transport emissions broken down into the individual vehicle types. As shown in Figure 4.16 car emissions are the dominant source for Suburban London, forming a steady 50%. LGVs are also an important contributor at ≈20% in Suburban London. In more central regions car contribution drops to below 40%, with buses and LGVs becoming higher emitters at ≈30%. The enhanced contribution of both vehicle types clearly shows the need to include them into any future emission strategy along with cars.

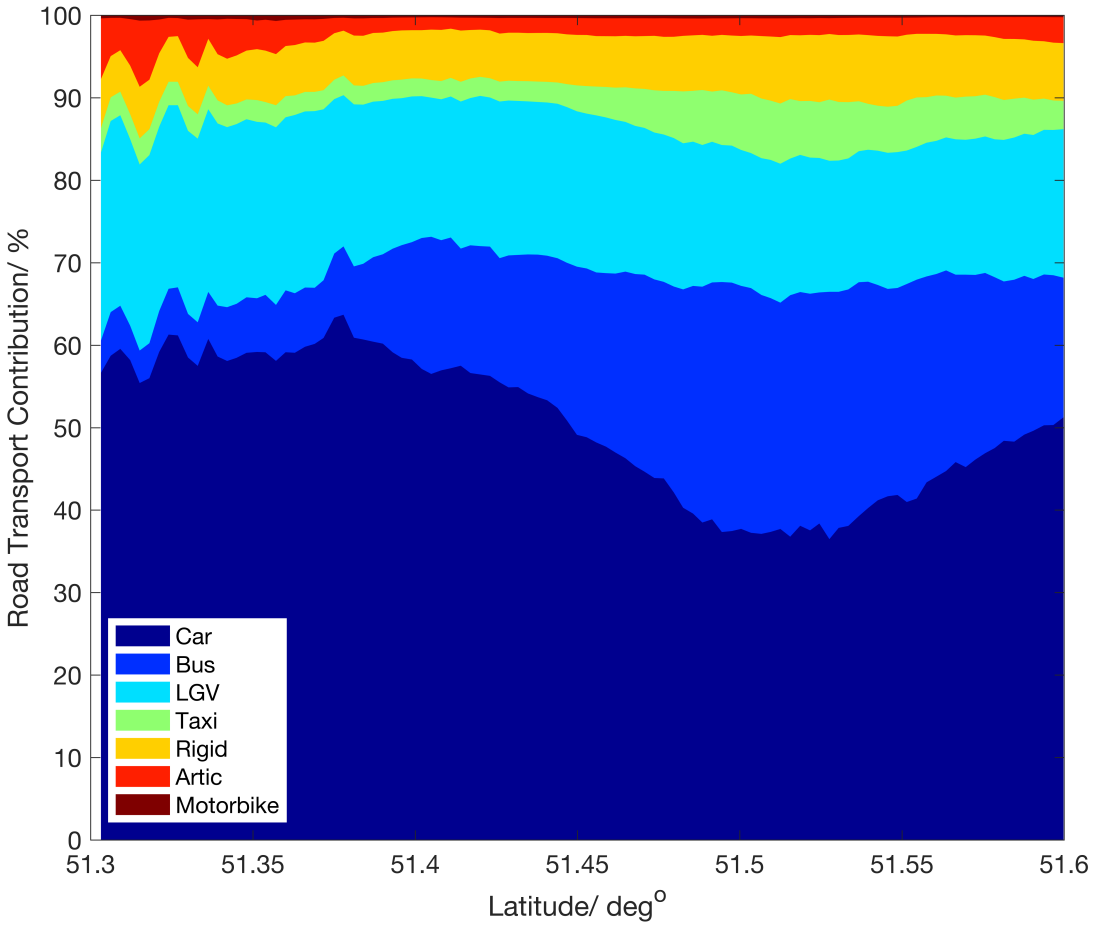

Figure 4.15: 'enhanced' NAEI road transport emission contribution for each vehicle type across London.

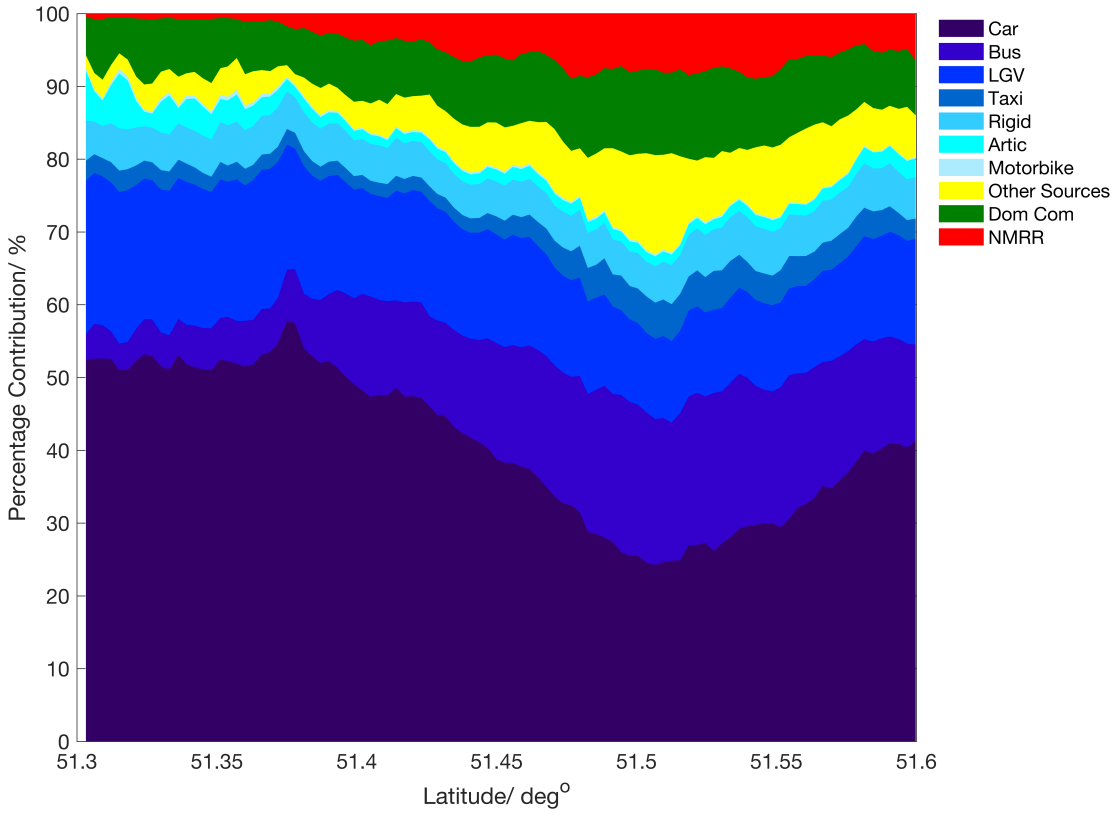

Figure 4.16: Percentage contribution of each 'enhanced' NAEI emission source sector, with specific breakdown of road transport into individual vehicle types.

4.5 Conclusions

In this study, NO_x fluxes have been measured from an aircraft flying low over London using continuous wavelet transform, allowing for spatial analysis of NO_x emissions. NO_x fluxes were observed to be largest in Central London, with maximum emissions of 80 mg m^{-2} h^{-1} observed during 2013 flights at the morning rush hour. After calculating flux footprints along the flight tracks, measurements were compared to scaled NAEI estimates providing a top−down analysis of the inventory. A significant discrepancy was identified between NAEI emission estimates and actual flux measurements, with the highest underestimation being a factor of two in Central London. In outer London, where the source of NO_x is almost exclusively from road transport (90%), there is an underestimation in the inventory of around a factor of 1.5, indicative of the poor treatment of the road traffic source in the NAEI. Due to the potential loss of some NO_x emitted at ground level during its transport to the measurement altitude, the calculated inventory underestimation can be considered as conservative.

Measurements were compared to an enhanced version of the NAEI, containing both non−road mobile machinery emission sources from the LAEI and real world traffic emissions from the enhanced LAEI, which provides a much better treatment of NO_x coming from these sources. The comparison yielded better agreement between the two, especially in outer London, where the measured to inventory ratio was found to be around 1.1. In Central London; however, there is still an average underestimation of around a factor of 1.5 compared to the measurements.

The current work has provided important information on the spatial variation in NO_x emissions over a large and complex urban environment. There are several areas where further research would be beneficial. First, the inhomogeneous terrain in London presents a challenge for flux measurements, both in terms of the inhomogeneous nature of the roughness and distributions of emissions (horizontally and vertically). Further measurements over different city areas would help better understand these effects. For example, measurements over a city such as Paris that has fewer high−rise buildings than London would provide a useful contrast. Second, the measurement of the fluxes of other species such as CO and CO_2 would help provide more comprehensive analysis of the NO_x flux emission estimates. More work is also required on understanding and quantifying the short−term accuracy of emission inventories. Emission inventories tend to focus on providing longer term (annual) emission estimates and are less able to provide information

on the temporal nature of emissions. Improved information on the temporal characteristics of emissions would improve the reliability of short−term flux measurements when compared with emission inventories. In particular, the measurements highlighted the critical importance of obtaining independent measurements of pollutant emission rates from vehicles during on−road driving conditions and using such data in emission inventories, rather than relying on emissions data obtained during artificial test driving conditions or provided by vehicle manufacturers.

Chapter 5

Airborne Eddy-Covariance Measurements of VOC Fluxes over London and Southern England during 2013 and 2014

This Chapter discusses calculated VOC fluxes during the 2013 and 2014 OPFUE campaigns over Southern England and London, with footprint model comparison to the NAEI and EMEP4UK inventory.

A.R. Vaughan, J.D. Lee, M.D. Shaw, P. Misztal, S. Metzger, M. Vieno, B. Davison, T. Karl, L.J. Carpenter, A.C. Lewis, R. Purvis, A. Goldstein, and C.N. Hewitt. VOC emission rates over London and South East England obtained by airborne eddy covariance. Faraday Discussions, 2017. ISSN 1359-6640.

5.1 Introduction

Non-methane volatile organic compounds (VOCs) are a class of organic molecules that are sufficiently volatile to enter the atmosphere. Some, including benzene, are directly toxic to humans, while others are reactive in the atmosphere producing secondary pollutants such as ozone and particles, and hence impact air quality [185]. Globally, most VOCs originate from the terrestrial biosphere, but in cities and other areas of high anthropogenic emissions, pollution sources usually dominate.

Emissions of VOCs in cities such as London have been well studied, with vehicles recognised as a significant source [120, 186, 187], either via emission in the exhaust gas or by the evaporation of unburnt or partially burnt fuel [188, 189, 190]. Na et al. found that 58% of aromatic VOC emissions in Seoul, Korea, originated from vehicle exhausts [189]. Measurements made during summer 2001 in Sacramento by Rubin et al. found fuel evaporative emissions could contribute up to 29% of total vehicular VOC emissions [190]. Quantifying the emission rates of individual VOCs is a prerequisite to their cost−effective and successful control and this is routinely attempted by the construction of bottom−up emission inventories such as the UK's National Atmospheric Emissions Inventory (NAEI) [165]. In the case of VOCs of biogenic origin, the most widely used models of emissions are derived from that of Guenther et al. (1995) [191].

The validation of emission inventory estimates is difficult as they are built up from many emission factors and activity rates. Measurements of atmospheric volume mixing ratios do not allow their direct validation but require a model of atmospheric chemistry and transport to infer emission rates. Micrometeorologically based surface to atmosphere flux measurements can allow direct validation, but normally only at one point on the surface, which is not representative of an entire city. For example, Langford assessed VOC emission fluxes from central London by making flux measurements at the BT Tower [120]. They found good agreement for benzene, toluene and C_2 alkyl−benzenes fluxes with NAEI emission estimates generated using a spatial footprint model but the study was limited by confined spatiality [120].

Measurements from aircraft allow for a larger spatial assessment compared with tower measurements. Due to the high speed at which aircraft move, coupling aircraft measurements to surface fluxes has different challenges to those from tower site. Small aircraft that can fly low and slow have previously been used to study atmospheric turbulent structure through airborne eddy-covariance [122, 192]. One such approach employs disjunct eddy-

covariance (DEC), as first described by Karl et al. (2002) [116]. DEC allows for sample processing time to be slower than the air sampling rate (<1 s) causing data to become discontinuous, while still being able to fully capture the turbulent statistics required for eddy-covariance [116, 119, 121]. DEC was implimented on−board an aircraft, to assess city−wide emissions of toluene and benzene from Mexico City, and found that sampling rates above 2 Hz captured the majority of the eddy flux [121]. Misztal also investigated VOC emissions from an aircraft via DEC [107]. Isoprene fluxes were quantified over a large region of California, at high spatial resolution. The study gave direct assessment of a statewide emission inventory used in predicting ozone concentrations, which previously, had not been possible on such a large spatial scale [107].

Shaw et al. 2015 assessed the temporo−spatial distributions of benzene, toluene and NO_x mixing ratios over London using an aircraft in 2013. The strong correlation between aircraft and ground site measurements highlighted the applicability of using aircraft to assess ground level pollution sources. Vehicles were predicted to be a major source of VOCs over central London [168]. During the same flights, Vaughan et al. measured fluxes of nitrogen oxides (NO_x) over London and found that the NAEI greatly underestimated NO_x fluxes, mainly because road vehicle sources were under predicted by the NAEI [193]. This was the first attempt to validate the NAEI at the city scale. This Chapter continues the study by directly assessing the NAEI, and an inventory of biogenic VOC emissions, to provide a direct validation of the current ability of emissions inventories to predict VOC emissions in SE England. The work has important policy implications as it highlights current weaknesses in the ability to estimate VOC emission rates to the atmosphere.

5.2 Methodology

The Ozone Precursor Fluxes in an Urban Environment (OPFUE) campaigns ran during July 2013 and July 2014. The strategy for both campaigns was to determine the highly spatially resolved emissions of a range of ozone precursor species from both anthropogenic and biogenic sources, over Greater London and SE England [168].

5.2.1 Flight Strategy

The OPFUE campaign (24^{th} June – 9^{th} July 2013) consisted of 12 research flights aboard the Natural Environment Research Council's Airborne Research and Survey Facility (ARSF) Dornier−228 aircraft, based at Gloucestershire Airport. Each flight involved replicated legs across Greater London and the rural area to its south (described as South Sussex below). Figure 5.1a, shows all flight transects across greater London (∼50 km length). Figure 5.1c, shows all flight transects across the rural South Sussex region (∼50 km length). At the end of every flight a profile ascent was conducted to high−altitude (2,400 m) allowing an assessment of the boundary layer height and for instrument calibrations to be conducted.

In July 2014 (9^{th} – 16^{th} July), similar fight paths were used over London, with extra legs added to form an incomplete figure of 8 (Figure 5.1b) with each transect ∼120 km long. The expanded flight path allowed for greater spatially coverage, passing over important emission areas, including the industrialised area around the Dartford crossing over the River Thames. Flights over the South Sussex region followed the same flight path as used in July 2013, shown in Figure 5.1d.

In summary, a total of ∼2,150 km of data was collected over Greater London during 2013 and ∼1,500 km during 2014. Over rural South Sussex ∼500 km of data was collected during 2013 and ∼700 km during 2014. Table 5.1 outlines the meteorology during each flight over London and Southern England.

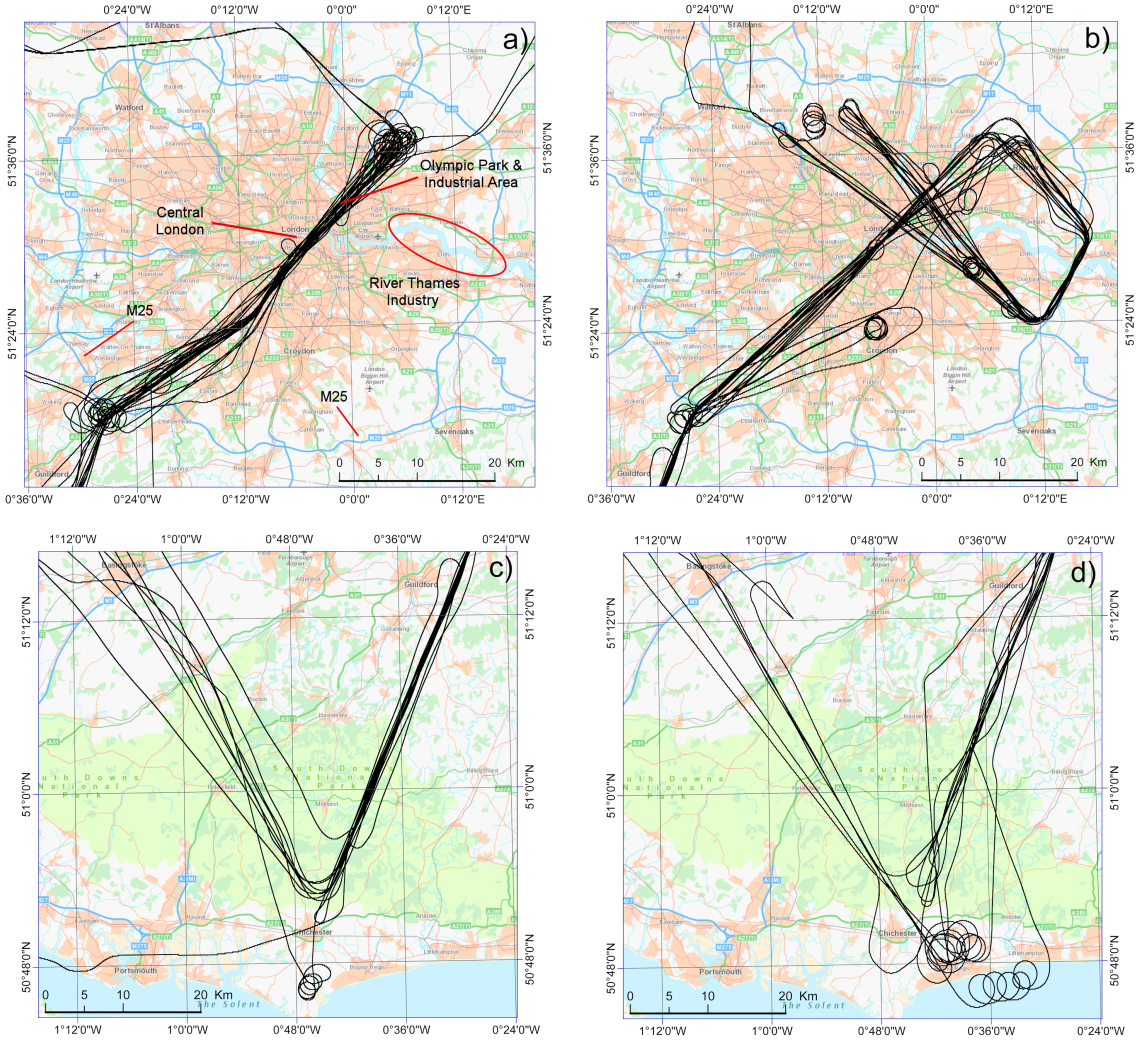

Figure 5.1: a) Research flight (RF) transects over London during July 2013, and b) July 2014. c) RF biogenic transects over South Sussex region during July 2013, d) July 2014.

5.2.2 Flight Meteorology

Table 5.1: Top) Meteorological conditions during all biogenic RF's over Southern Sussex (July 2013 & 2014). Bottom) Meteorological conditions during anthropogenic RF's over greater London (July 2013 & 2014).

South Sussex	Date/ ToD	Temp/ ^{o}C	Humidity/ %	Wind Speed/ m s^{-1}	Wind direction/ deg
8 (2013)	07/07/2013 (PM)	25.40 +/- 0.70	53.35 +/- 6.11	4.95 +/- 1.62	76.02 +/- 54.87
9 (2013)	08/07/2013 (AM)	21.22 +/- 0.25	50.76 +/- 9.75	7.99 +/- 1.37	48.49 +/- 12.92
10 (2013)	08/07/2013 (PM)	24.20 +/- 0.47	47.37 +/- 5.63	7.28 +/- 1.70	58.13 +/- 42.01
3 (2014)	12/07/2014 (PM)	18.71 +/- 6.13	68.81 +/- 8.88	4.58 +/- 2.50	224.77 +/- 60.09
4 (2014)	14/07/2014 (PM)	14.78 +/- 3.79	66.59 +/- 11.22	7.95 +/- 1.92	250.74 +/- 26.55
5 (2014)	15/07/2014 (AM)	14.95 +/- 4.29	53.85 +/- 21.93	5.73 +/- 3.20	279.02 +/- 24.81
7 (2014)	16/07/2014 (PM)	18.57 +/- 3.73	63.73 +/- 11.97	4.95 +/- 0.96	249.95 +/- 23.77

London	Time−of−Day	Temp/ ^{o}C	Humidity/ %	Wind speed/ m s^{-1}	Wind Direction/ deg
5 (2013)	03/07/2013 (AM)	15.41 +/- 0.71	84.89 +/- 20.34	6.31 +/- 1.29	281.09 +/- 11.22
7 (2013)	04/07/2013 (PM)	20.00 +/- 0.54	74.92 +/- 9.79	7.53 +/- 1.41	241.29 +/- 11.37
8 (2013)	07/07/2013 (PM)	24.15 +/- 0.78	55.08 +/- 3.03	5.48 +/- 1.49	80.44 +/- 33.23
9 (2013)	08/07/2013 (AM)	21.70 +/- 0.54	49.78 +/- 13.23	7.23 +/- 1.30	57.79 +/- 13.42
10 (2013)	08/07/2013 (PM)	23.49 +/- 0.48	55.87 +/- 3.52	7.26 +/- 1.36	56.99 +/- 15.62
11 (2013)	09/07/2013 (AM)	15.92 +/- 1.77	41.78 +/- 25.83	6.87 +/- 4.75	50.83 +/- 42.85
12 (2013)	09/07/2013 (PM)	22.87 +/- 0.49	33.21 +/- 3.42	5.54 +/- 1.28	53.64 +/- 40.08
3 (2014)	12/07/2014 (PM)	17.88 +/- 8.52	59.76 +/- 6.64	2.54 +/- 1.52	197.60 +/- 83.61
4 (2014)	14/07/2014 (PM)	19.05 +/- 3.44	47.66 +/- 7.93	7.55 +/- 1.81	245.05 +/- 17.29
5 (2014)	15/07/2014 (AM)	17.09 +/- 3.66	57.39 +/- 14.56	5.06 +/- 2.79	283.48 +/- 30.97
6 (2014)	16/07/2014 (AM)	16.17 +/- 3.27	66.62 +/- 3.77	2.84 +/- 2.16	239.16 +/- 81.64
7 (2014)	16/07/2014 (PM)	21.81 +/- 0.83	47.84 +/- 3.75	4.21 +/- 1.49	233.78 +/- 27.69

5.2.3 Scientific Payload

5.2.3.1 Scientific Payload

Meteorological measurements were made using an Aircraft-Integrated Meteorological Measurement System (AIMMS−20) turbulence probe, mounted under the aircraft's left wing. The AIMMS−20 measures 3−dimensional wind vectors, atmospheric temperature, pressure and humidity at 20 Hz [128]. Accurate aircraft position data were obtained using an Inertial−Position and Altitude System (IPAS 20), which generates aircraft coordinates and altitude data at the same rate as the AIMMS−20.

5.2.3.2 Volatile Organic Compound Measurements

Measurements of VOC mixing ratios were made using a high sensitivity proton transfer reaction - mass spectrometer (PTR−MS, Ionicon, Innsbruck, Austria). Dr. M. Shaw operated the PTR−MS during all OPFUE flights. Measurement and calibration strategies are described below [168]. The measured VOCs were then used in this study to calculate instantaneous fluxes for a range of VOCs.

In−depth theory and design of PTR−MS have been well documented in previous studies [107, 121, 194, 195, 196]. The instrument used in the OPFUE study has been described in detail by Shaw et al. (2015) [168], therefore only instrument set up, operation and flight modifications are outlined here. A pressure controller (Bronkhorst) was added to the instrument to regulate the inlet flow (50−500 STP sccm), such that pressure upstream of the controller was maintained at a constant value. Thus, the PTR−MS drift tube pressure was independent of fluctuations in ambient pressure caused by varying flight altitude. Ambient air was only exposed to heated (70^{o}C) Teflon and stainless steel tubing before entry into the instrument, minimising memory effects, inlet losses and the build−up of impurities in the inlet system. Considerable efforts were made to prevent VOC contamination of the PTR−MS inlet during operation on the ground and during take−off. On the ground, the PTR−MS inlet remained closed (and all sample tubing capped).

VOC measurements were obtained at a sampling rate of 2 Hz. The target protonated masses and likely contributing compounds were m/z 57 (methyl tert−butyl ether, MTBE), m/z 69 (isoprene), m/z 71 (methyl vinyl ketone/methacrolein, MVK/MACR), m/z 79 (benzene), m/z 93 (toluene), m/z 107 (C_2 alkyl−benzenes ethylbenzene/benzaldehyde/xylene isomers) and m/z 121 (C_3 alkyl−benzene isomers). Additionally, both the primary ion

m/z 21 ($H_3O_{18}^+$), its first water cluster (H_3O_{18} $H_2O_{16}^+$) at m/z 39 and O_2^+ at m/z 32 were determined. PTR−MS drift tube pressure, temperature and voltage were held constant at 2.0 mbar, 40^{o}C and 480 V respectively, maintaining an E/N ratio of approximately 110 Townsend's (Td). For flights at ∼360 m a.g.l, the m/z 21 primary ion count ranged between (4−7) x 10^7 ion counts per second (cps) with a mean of 6 x 10^7 cps. Ion counts of m/z 32 ranged between (0.8−3) x 10^6 cps, with an average of 2 x 10^6 cps, which represented 3% of the primary ion signal. Ion counts of m/z 39 ranged between (1−5) x 10^6 cps with an average of 3 x 10^6 cps, which represented 6% of the primary ion signal. Due to O_2^+ and NO^+ impurities in PTR−MS (≈1−5%), elevated concentrations of butane and higher alkanes are going to be detected at the most abundant ion fragments such as at m/z 57 and 71, which will contribute to the ion signals of MTBE and MVK/MACR [197].

Several major vehicle exhaust emission components are expected to contribute to the ion signal at m/z 57, including MTBE and C_4H_8 (butene) isomers. The butenes react to form protonated molecular ions at this mass. Greater than 95% of the MTBE proton transfer reaction products fragment to the mass 57 ion [198]. It is now recognised that the concentrations derived from ion intensity measurements at m/z 57 are due to petroleum vehicular emissions predominately reflect the sum of the butene isomers and MTBE. However, Rogers et al. (2006) concluded that m/z 57 ion receives significant intensity from a wide variety of neutral components including the isomeric butenes, acrolein, higher order alkenes and alkanes particularly those abundant in vehicular diesel exhaust [198, 199]. The ion signal at m/z 57 (MTBE*) was therefore assumed to represent the vehicular emission source across Greater London with mixing ratios calculated assuming a rate constant k_cMTBE* of 2 x 10^{-9} cm^3 s^{-1}. MTBE* represents MTBE with contribution from butene isomers, C_4 and higher alkenes and alkanes.

5.2.3.3 PTR−MS Calibration

Toluene and benzene calibrations were carried out approximately 2 hours prior to each flight using an in−house built dynamic dilution calibration system. This involved the dynamic dilution of a 500 ppbv certified gas standard (Apel−Riemer) with humidity controlled zero grade air (BOC Gases) to mixing ratios near those typically observed in urban air. Typical instrument sensitivities observed during the campaign ranged between 250−350 icps $ppbv^{-1}$, 4−5 normalised counts per second (ncps), 220−300 icps $ppbv^{-1}$ (3−4 ncps), 380−480 icps $ppbv^{-1}$ (6−8 ncps), 400− 550 icps $ppbv^{-1}$ (6−9 ncps), 370−520 icps $ppbv^{-1}$ (5−6 ncps), 170−240 icps $ppbv^{-1}$, (≈3 ncps), 1000−1200 icps $ppbv^{-1}$ (16−18 ncps) for C_2 alkyl-benzenes, C_3 alkyl−benzenes, benzene, toluene, isoprene, total monoterpenes and MVK/MACR respectively. Instrument uncertainties were 19 ± 5 %, 17± 5 %, 16 ± 5%, 21 ± 9 %, 6 ± 8 %, 16 ± 4 % and 7 ± 9 % for C_2 alkyl-benzenes, C_3 alkyl benzenes, benzene, toluene, isoprene, MVK/MACR and total monoterpenes respectively, calculated using the standard deviation of linear regression (Sm) of pre- flight calibrations. Instrument limits of detection (LoDs) were determined by the method outlined by Taipale et al. and were 23±7 pptv, 20±9 pptv, 13±8 pptv, 18±11 pptv, 18±5 pptv, 19±7 pptv and 39±6 pptv for C_2 alkyl-benzenes, C_3 alkyl benzenes, benzene and toluene, isoprene, MVK/MACR and total monoterpenes respectively [200].

During flights, ambient air was sampled from the forward facing isokinetic inlet along a heated (70 ^oC) 5 m 1/4" Teflon (PFA) tube pumped by a stainless−steel diaphragm pump (Millipore) at a flow−rate of 22 L min^{-1}. A portion of this ambient air (∼300 sccm) was diverted into the pressure controlled inlet of the PTR−MS instrument such that the overall delay time was <3 s. To determine blank VOC mixing ratios, the remaining ambient air was purged into a custom built zero air generator, which consisted of a 3/8" stainless steel tube packed with 1 g of platinum coated quartz wool (Elemental Microanalysis) which efficiently removes VOCs [201]. The zero−air generator was operated at 350 ^oC and 30 psi for the duration of the flights to maintain optimal operating conditions. The catalytic converter does not remove water vapour from the sample stream, which is of importance as background impurities may depend upon sample air humidity. Zero air was periodically back−flushed through the inlet system to determine the instrument background signal.

5.2.4 Disjunct Eddy-Covariance

Eddy covariance is a well−defined technique for quantifying trace gases emissions from the surface to the atmosphere. Here we use a moving aircraft to gain greater spatial coverage than possible from a tower, hence continuous wavelet transform (CWT) was chosen to generate fluxes with high time (and hence spatial) resolution. Chapter 3 gives in-depth methodology for CWT eddy-covariance, and so only specific parameterisation will be listed in this chapter. CWT gives both frequency and time−resolved flux information, compared to frequency only from the more conventional Fast Fourier Transform (FFT) approach. CWT gives advantages over conventional FFT, with stationarity not needing to be conserved and time resolved spectral contributions quantified. All calculated mixing ratios from the PTR−MS are dry mixing ratios, with fluxes calculated using this methodology not requiring water vapour content correction.

Using identical methodology as proven successful in previous studies [107, 121, 124, 193], CWT was conducted via Equation 5.1, which defines the transformation of the discrete sequence of data *x(n)* (being either the instantaneous change of concentration or vertical wind speed data from its mean), using the daughter scaled Morlet wavelet [171]:

$$w_x(a,b) = \sum_{n=0}^{N} x(n)\, \psi^*_{p,a,b}(n) \tag{5.1}$$

ψ denotes the mother wavelet, with a and b acting as parameters to scale and localise the wavelet in frequency and time respectively, and p as the normalised factor. Due to differences in sample location and time taken for sample to react the PTR−MS, lag−time correction was conducted. Through cross−correlation analysis, correlation coefficient between instantaneous vertical wind and concentration was quantified as a function of lag time. After correction, maximum correlation between the two would be at time 0. Each VOC species showed different lag−times, requiring individual RF transects to be corrected independently. CWT calculates eddy contributions over all frequency periods with respect to the distance along the flight path, which is shown as a global cross−spectrum. Spatial scales used were long enough to capture all flux frequencies (0−128 s), with no loss of low frequency flux contributions. Average flux is then calculated across all frequency periods. Figure 5.2b shows the global cross−spectrum for a C_2 alkyl−benzenes flight leg over Greater London, with the 'hotter' coloured regions showing positive fluxes and 'cooler' colours showing deposition (negative fluxes). Example global cross-spectrums for each

VOC are given in Appendix B.

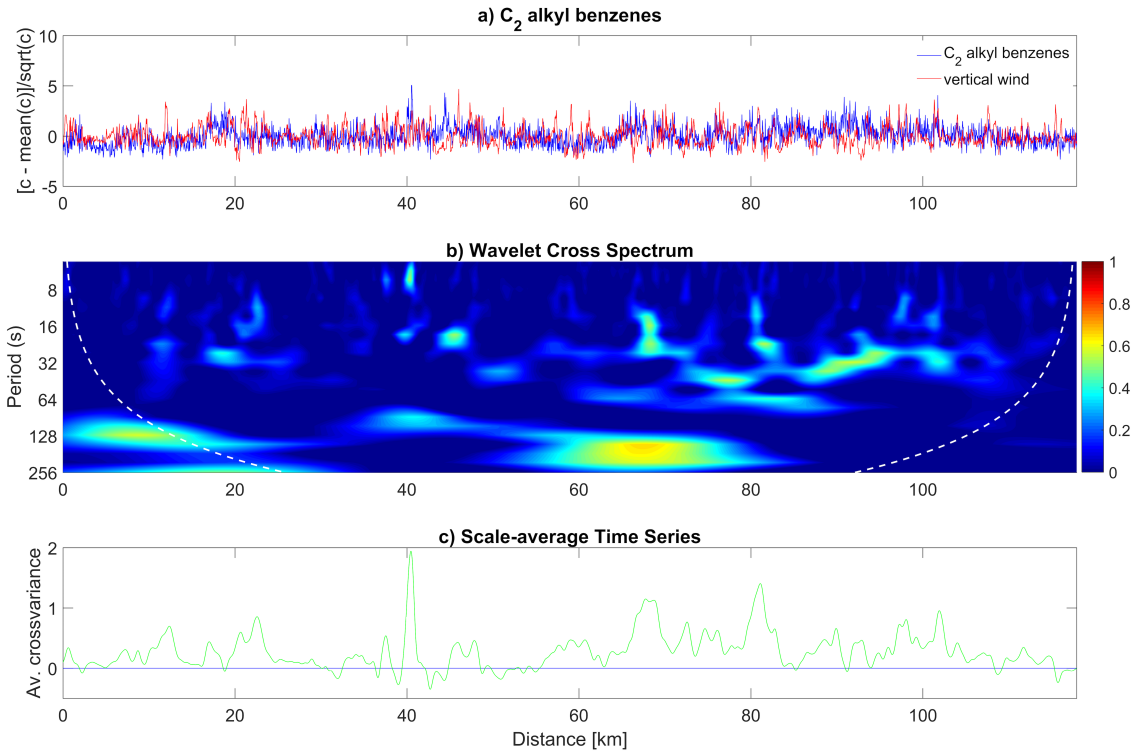

Figure 5.2: a) instantaneous changes of vertical wind and C_2 alkyl-benzenes concentration from their respective means, b) global cross−spectrum of eddy contributions integrated over all frequency periods along flight track, c) average cross variance along flight track.

For flux data quality control, conventional FFT flux analysis was run at the same time as the CWT analysis [107]. A comparison was then made between the two. By analysing both the co−spectra and cumulative co−spectra, an assessment was made as to whether any frequency correction was needed. Figure 5.3 shows the CWT and FFT flux spectra across all frequencies for heat and C_2 alkyl−benzenes flux for one run over London. For all analysed runs, the spectra followed the general trend shown in Figure 5.3, with all major flux contributions below 0.1 Hz, inferring that high frequency correction for flux loss was not needed. Any major deviations found between FFT and CWT spectras would result in data being discarded. Good fluxes were deemed to displayed similar spectra to that of the standard FFT, showing no high frequency loss, and a ratio of FFT:CWT flux of 0.7−1.3. The calculated FFT flux data would still be affected by non-stationary and inhomogeneity [107]. However, this comparison still points to whether the CWT flux analysis had been successful. Example co and cumulative co-spectra for each VOC are shown in Appendix C.

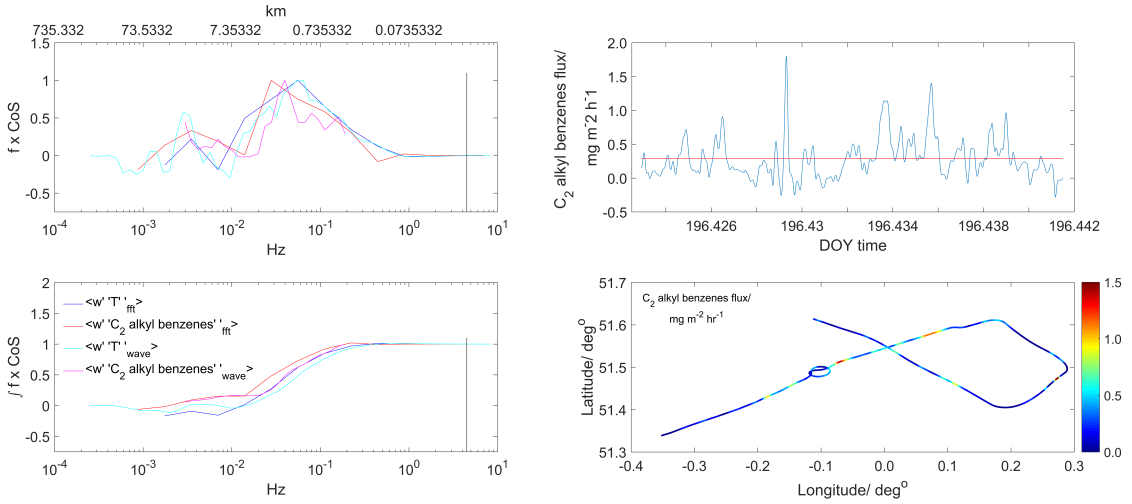

Figure 5.3: Top left) co-spectra of temperature and C_2 alkyl-benzenes flux across all frequencies using CWT and FFT methods. Top right) measured CWT flux in blue and FFT flux in red against day of year time (DOY). Bottom left) cumulative co-spectra of temperature and C_2 alkyl-benzenes flux across all frequencies using CWT and FFT methods. Bottom right) flight path over London coloured by measured C_2 alkyl-benzenes flux.

A final data quality process involved the removal of any flux contributions which sat outside of the cone of influence (COI). The COI is the area of the wavelet cross-spectrum which is free from edge effects, with the area outside it being of lower flux quality [127]. Figure 5.2b shows the COI as a white dotted line on the global cross-spectrum. Edge effects were found to be greatest at the beginning and end of each flight run. To help reduce this, the beginning and end of each run was padded with instrument zeros before conducting CWT analysis; however, fluxes calculated at the beginning and end of each run will still be prone to greater uncertainties than fluxes from more central parts of each run.

5.2.5 Isoprene Loss Correction

Emissions of isoprene were measured during both campaigns over SE England (Section 5.3.3). Isoprene reacts about ten times faster with hydroxyl (OH) radicals than benzene does, hence reactive losses of isoprene during the time taken to reach the flight level from the surface require correction. Karl et al. quantified the vertical flux loss of isoprene through oxidation with the hydroxyl radical [180]. For the 2013 flight data, the same methodology was used as Karl et al. with an estimated OH concentrations (2.0 x 10^6 molecules per cm^3) [180] and boundary layer height during each flight used to estimate flux loss correction factor estimates. Vertical flux divergence was calculated to be 7.15 x 10^{-5} mg m^{-2} h^{-1} per vertical meter. Overall, measured isoprene flux during 2013 flights were to increase by 33% at an altitude of 360 m.

For the 2014 flights, loss of isoprene due to oxidation was corrected using the measured methyl vinyl ketone / methacrolein (MVK/MACR) flux. MVK and MACR are direct oxidation products of isoprene, and hence this flux ratio gives a direct estimate of isoprene flux loss. Under high NO conditions (>100 ppt) MACR formation accounts for ≈23% of isoprene oxidation products, with ≈34% contribution from MVK [202]. At lower NO conditions (<100 ppt) molar yield of both products increases, with MVK contribution increasing up to ≈49% and ≈27% for MACR. Figure 5.4 shows oxidation paths ways for isoprene and the formation of MACR and MKV from the intermediates. At measured NO concentrations of <1 ppbv, MVK/MACR formation from isoprene oxidation was calculated to be ∼48%, using the Master Chemical Mechanism v 3.3.1 which was then used to correct the isoprene fluxes [202]. Figure 5.5 shows uncorrected and corrected isoprene flux along the flight track at 500 m averages.

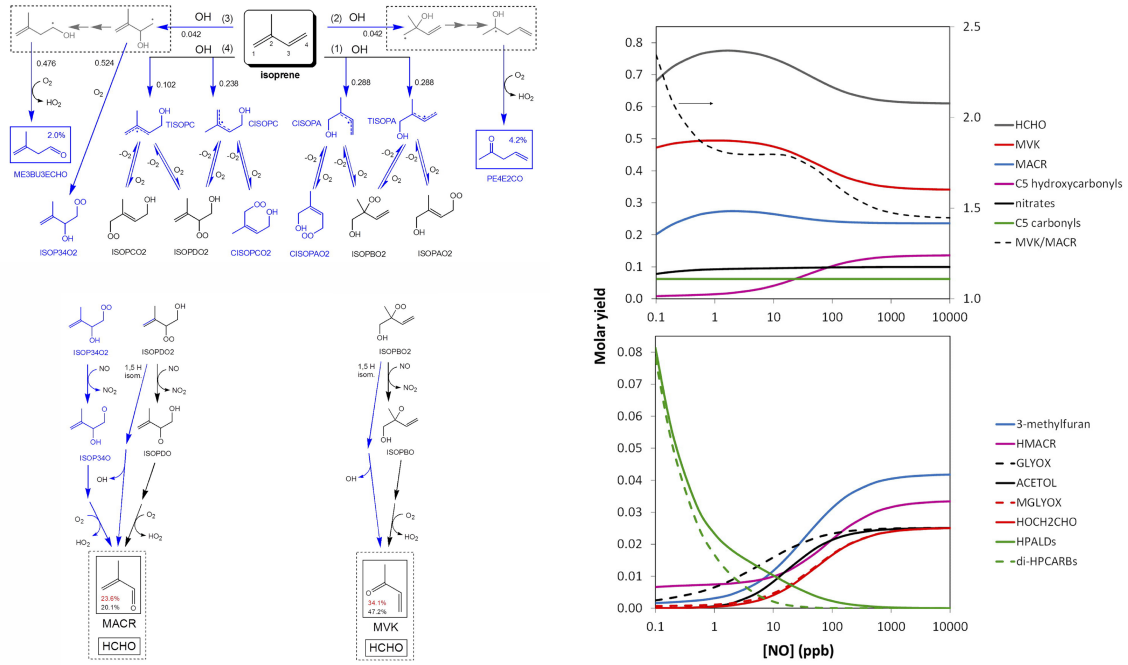

Figure 5.4: Left) isoprene oxidation pathways showing intermediates and the formation of MACR and MVK. Right) Molar yield of isoprene oxidation products as a function of NO mixing ratio. Adapted from Jenkin et al. (2015) [202].

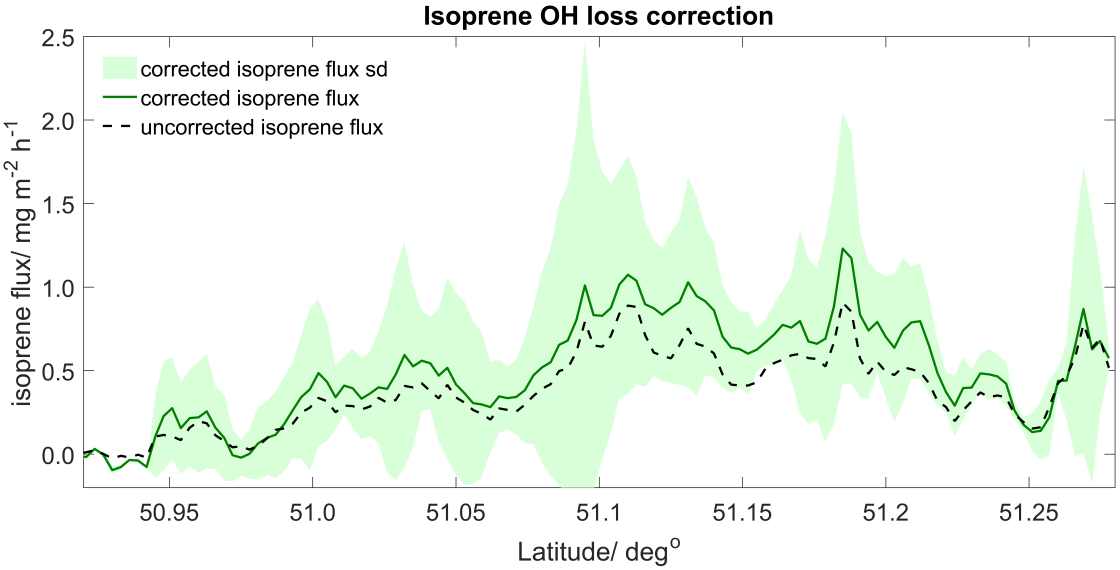

Figure 5.5: Correction of isoprene flux due to chemical loss via OH oxidation.

5.2.6 Footprint Calculation

A lagrangian footprint model was used to calculate the origin of the emissions as measured by the aircraft: The scalars of interest are mixed and transported downwind between the time of emission from the surface and their measurement at the aircraft position. Chapter 3 gives an in-depth description of the footprint model used, with only specific parameterisation listed here. The footprint model permits calculating an ensemble trajectory for each aircraft observation, and thus to spatially attribute the measured emissions to surface sources in a probabilistic framework. Metzger et al. provide an in−depth description of the model along with comparisons to alternative footprint models [150].

The parameterisation depends upon friction velocity u_*, measurement height Z_m, standard deviation of the vertical wind velocity σ_w, standard deviation of the crosswind wind velocity σ_v, aerodynamic roughness length Z_0, and the boundary layer depth Z_i, and is valid in the range -200 $\leq Z_m/L \leq$ 1, $u_* \geq$ 0.2 m s^{-1}, and 1 m $\leq Z_m \leq Z_i$. As previously used in Vaughan et al. (2016), Z_0 values for London were taken from the Drew et al. (2013) study at 1 km^2 resolution [154, 193]. Z_i estimates for London were obtained via Li−DAR sounding from Heathrow. For flight transects over the South Sussex region of England, Z_i estimates were obtained from vertical profiles at the beginning and end of each RF. Z_0 values for the South Sussex region were calculated according to Monin−Obukhov theory [154, 203, 204]. Remaining variable are directly used from the aircraft measurements.

For each 1 km flux observation, the model calculates a surface weighting matrix at 1 km resolution, i.e. identical to the emission inventory grid resolution. The surface weights for each observation sum to unity, which permits cell−wise multiplication of the surface weights with the emission inventory, and subsequent aggregation over the entire grid extent. This results in the estimate of the emission strength that should be detected by the aircraft, based on the emission inventory [150]. Additional methodological detail is provided in Metzger et al. (2013) [123]. Figure 5.6 shows an example calculated footprint over London, overlaid onto 1 km^2 NAEI total NMHC emission estimates.

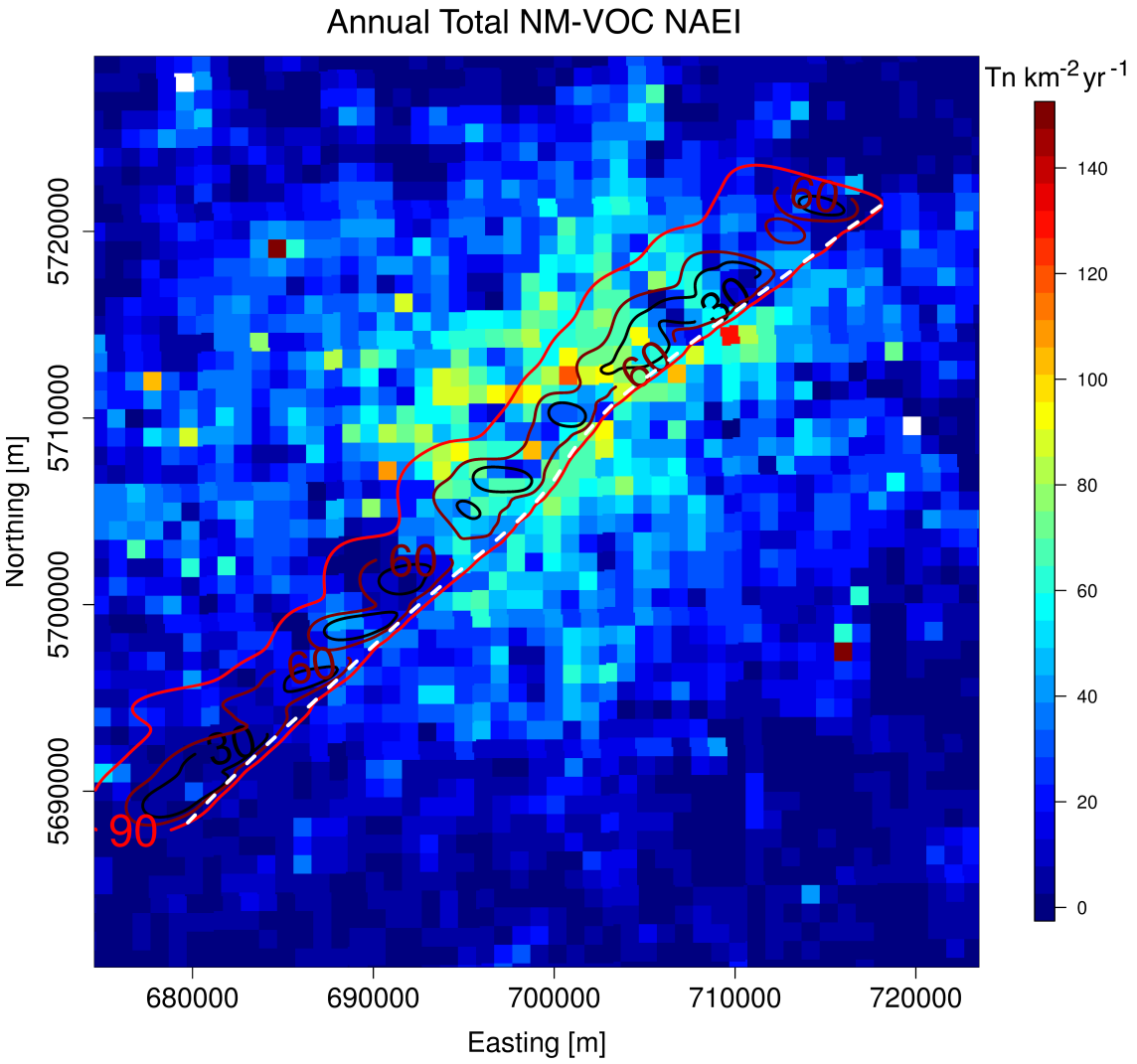

Figure 5.6: Example footprint for 2014 RF transect over London showing the 30, 60, 90% footprint influence areas from flight track (white), overlaid onto 1 km^2 NAEI total NMHC emission estimates.

5.2.7 NAEI Comparison

Measured anthropogenic fluxes (benzene, toluene and C_2 alkyl-benzenes) were compared to emission estimates of benzene and total non-methane hydrocarbons (NMHCs) from 11 source sectors made by the UK's National Atmospheric Emissions Inventory at 1 km^2 spatial resolution [177]. The source sectors include solvent use, road transport, agriculture and industrial processes. NAEI road transport estimates follow the COPERT 4 emission factor model, which can be found in the European Monitoring and Evaluation Programme/European Economic Area (EMEP/EEA) air pollutant emission inventory guidebook [178]. A full description of NAEI model methodology can be found in Bush et al. (2008) [165]. Comparison to measured fluxes using the NAEI was done using year-specific inventory data for either 2013 or 2014.

Emission estimates at 1 km^2 resolution from each source sector were quantified using the footprint model described above. As NAEI emission estimates are annual averages, month−of−the−year, day−of−the−week and time−of−day scaling is required to produce hourly average emission estimates for the specific days of the year on which flux measurements were made. Each source sector was scaled separately, with each scaling factor accounting for temporal variation in emissions for each month, day and hour [177]. Scaled estimates for each source sector were then summed up for every 1 km along the flight track, giving time−of−day emission estimates along the flight track.

Measured fluxes of toluene and C_2 alkyl−benzenes were compared to NMHCs estimates from the NAEI. As before, annual estimates were scaled to time−of−day using the described scaling factors, giving temporally-resolved hour of the day estimates. To extract specific VOC emission estimates from the inventory, the Passant et al. (2002) study was used [205]. The study gives detailed characterisation for each NAEI source sector, with percentage contribution of each VOC quantified. Each source sector was scaled using the relevant percentage contribution, with all sectors summed up every 1 km along the flight track, giving time−of−day emission estimates for toluene and C_2 alkyl−benzenes.

5.2.8 EMEP Comparison

Emission measurements of biogenically−derived isoprene were compared with emission estimates made using the European Monitoring and Evaluation Programme model (EMEP MSc−W) for the United Kingdom (EMEP4UK). The model gives 5 km^2 emission estimates of isoprene for the whole of the UK at hourly resolution using near−surface air temperature and photosynthetically active radiation (PAR) flux [206, 207, 208, 209]. A detailed description of EMEP4UK biogenic isoprene emissions can be found in Simpson et al. (2012) [210]. Figure 5.7 shows EMEP4UK isoprene emission estimates for the entire UK and Southern England. Using the described footprint model, time−of−day estimates of isoprene emission rates were quantified using interpolated 1 km^2 EMEP4UK estimates. Comparison using the EMEP4UK model to measured isoprene fluxes was done using year-specific inventory data either 2013 or 2014.

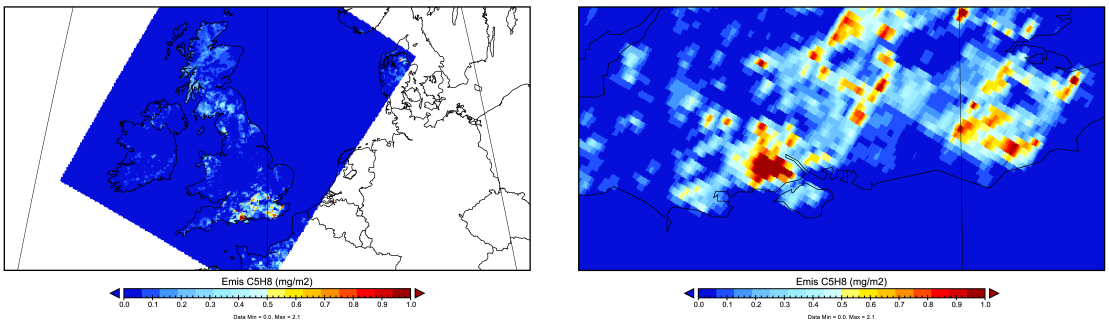

Figure 5.7: Left) EMEP4UK isoprene emission estimates at 5 km^2 resolution for entire of the UK. Right) South Sussex region EMEP4UK Isoprene emission estimates showing a maximum of 2.1 mg m^{-2} h^{-1}.

5.3 Results and Discussion

5.3.1 Anthropogenic VOC fluxes over London

Measurements conducted during the 2013 flights over London focused on two anthropogenic VOCs, benzene and toluene. Both compounds are highly volatile with a wide range of previously identified emission sources in London [120, 168]. Meteorological conditions during the flights are summarised in Table 5.1, with prevailing wind directions predominately from the SW and temperatures above 20 ^{o}C. Inverse distance weighing (obtained using ArcGIS) at 500 m, was used to interpolate all measured fluxes from all RF transects, generating spatially averaged benzene and toluene fluxes, as shown in Figure 5.8. Approximately 4 hours of benzene fluxes were obtained from 5 RFs, covering a total area of ∼400 km^2 over London. These fluxes highlight the spatial heterogeneity of VOC emission over central London, with maximum emission rates of 0.20 mg m^{-2} h^{-1}. Higher benzene fluxes were also observed around the M25 region and industrial areas of London, as shown in Figure 5.8a. The mean benzene flux from all RFs was 0.051±1 mg m^{-2} h^{-1}.

Toluene fluxes were quantified during 33 transects over 6 RFs, giving ∼5.5 hours of flux data with total coverage over London ∼400 km^2. The observed structure of London's toluene emissions was comparable to that of benzene, with highest averaged emissions of 0.30±1 mg m^{-2} h^{-1} found over central London. Toluene emissions across London were always higher than those of benzene, with a mean toluene flux from all RFs of 0.18±1 mg m^{-2} h^{-1}. Emission rates exceeding 1.0 mg m^{-2} h^{-1} of toluene were observed in central London (Figure 5.8b). In 2014, toluene fluxes where obtained from 5 RFs, with >75% of transects generating fluxes. A total of ∼3 hours of toluene fluxes with coverage of ∼700 km^2 over London were obtained. The emissions profile was comparable to the previous year's data, with the highest measure toluene flux of 0.30 mg m^{-2} h^{-1}. Figure 5.8d shows interpolated toluene fluxes from all transects across London. No benzene flux data were available from the 2014 flights due to reduced instrument performance.

As discussed by Langford et al. benzene/toluene ratios can help evaluate the emission source of measured fluxes [120]. Flux ratios in the range of 0.41−0.83 indicate vehicle exhaust emissions as the dominant source [119, 211]. To investigate the spatial emission distribution over London, the flight path was split into 4 zones: Suburban London latitudes of 51.30−51.35^{o}; Southwest Greater London with latitudes of 51.35−51.42^{o} con-

taining mainly residential areas; Central London latitudes of $51.42-51.56^o$ containing the most densely populated areas of London; and Northeast Greater London, at latitudes of $51.56-51.60^o$, containing a mix of residential and industrial areas.

Suburban London showed an average benzene/toluene ratio of 0.43 indicating vehicular exhaust emissions as the main VOC source. Within the suburban region of London is the M25 motorway ring road, which encompasses the entire Greater London area. The highest benzene/toluene ratio observed, 0.82, was measured over the area indicating direct VOC emissions coming from the motorway. As discussed by Rogers, higher benzene/toluene ratios can also be attributed to correct operation of vehicle emission control systems, i.e. the catalytic converter. Ratios will however depend on the performance of the converter and the fuel used [198].

For Southwest Greater London, the average benzene/toluene ratio was lower at 0.28. Ratios below 0.41 are indicative of other sources being dominant [121, 198]. The average benzene/toluene ratio for central London was also 0.28, suggesting similar sources are responsible for these two regions VOC emissions. Northeast Greater London showed the lowest average benzene/toluene ratio of 0.20, which as discussed by Karl et al. (2009a) [121], is indicative of more industrial processes and evaporation. Karl et al. observed a ratio of 0.13 over Mexico City, with a multitude of emission sources predicted to be responsible [121]. Langford et al. observed similar benzene/toluene flux ratios from the BT tower in central London of 0.21 [120]. The similarities between their findings and aircraft calculated ratios indicate the measured flux in this study can capture ground level emission sources successfully.

Measurements made during 2014 flights over the London focused on a wider range of VOCs. Meteorological conditions during all 2014 flights (RFs 3−7) are shown in Table 5.1. Flux measurements were not possible during RFs 1 and 2 due to adverse weather conditions and instrument problems. Prevailing wind directions during many of the RFs over London were from the SW, with high summer air temperatures. The higher order benzenoid compounds, C_2 alkyl-benzenes and C_3 alkyl-benzenes, were measured during the 2014 flights. Fluxes of C_2 alkyl-benzenes were measured during 5 RFs, giving 1.5 hours of flux data and a total spatial coverage of $\sim$450 km^2. High emissions were observed over central London and industrial areas of Greater London region (Figure 5.8c), with a maximum flux of 1.00 mg m^{-2} h^{-1}. Measurements of C_3 alkyl-benzenes fluxes were obtained during 2 RFs, giving $\sim$30 mins of data, over a total area of 150 km^2. C_3 alkyl-

benzenes such as 1,2,4-trimethylbenzenes are a product of petroleum refining and have industrial applications, including as a blending additive in petroleum fuels [212, 213]. Maximum observed emissions of C_3 alkyl-benzenes were found to be 1.00 mg m^{-2} h^{-1}, observed over central London. Figure 5.8e shows interpolated instantaneous C_3 alkyl-benzenes fluxes from all RFs transects.

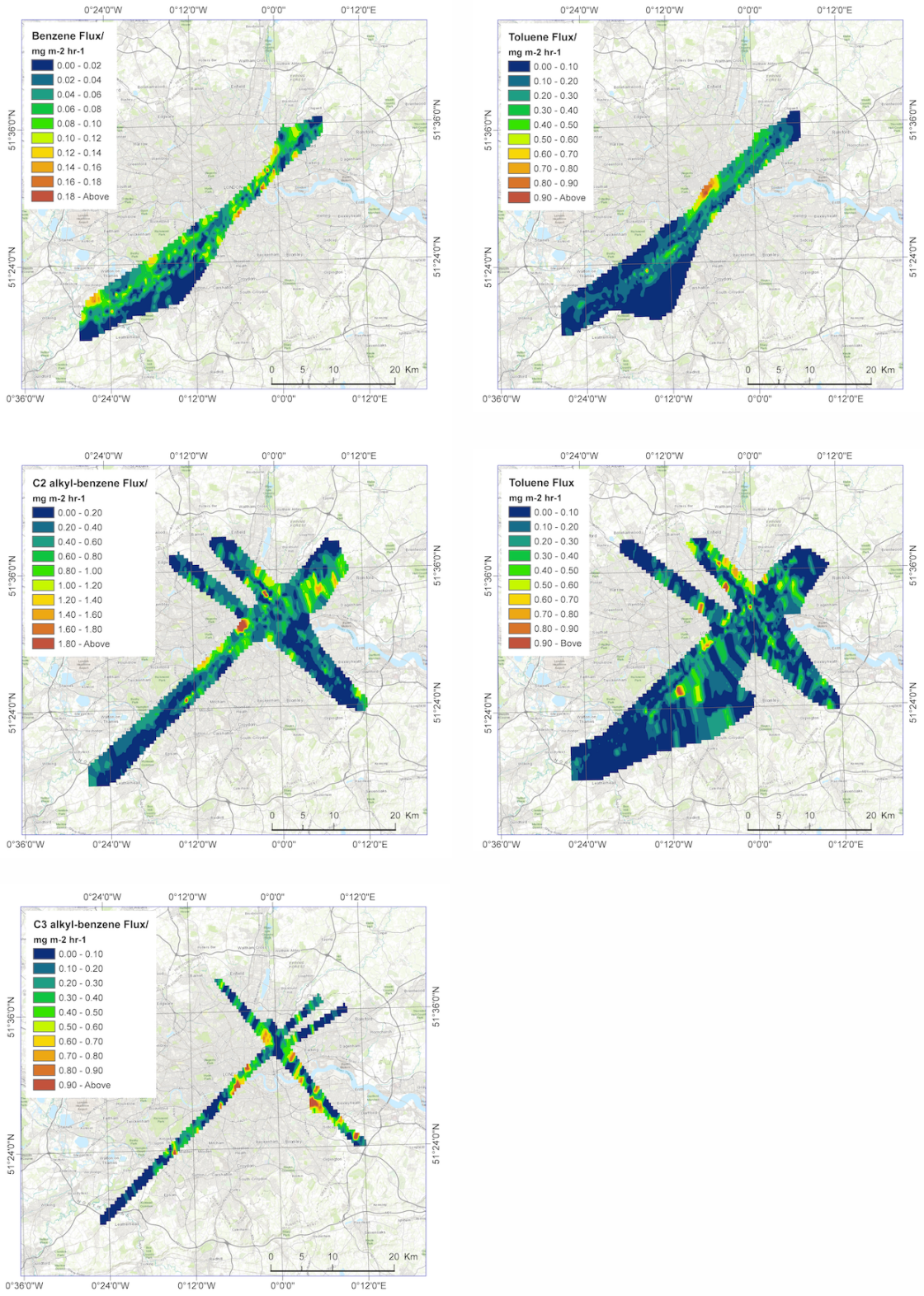

Figure 5.8: Measured instantaneous anthropogenic fluxes of a) benzene (2013), b) toluene (2013), c) C_2 alkyl-benzenes (2014), d) toluene (2014) and e) C_3 alkyl-benzenes (2014), interpolated at 500 m using inverse distance weighting from all RF transects..

MTBE* fluxes were measured during two (2014) RFs, giving total spatial coverage of ≈100 km^2. Methyl tert−butyl ether (MTBE) is a key additive in petrol fuel, acting as an anti-knocking agent [213]. The highest measured emissions of MTBE* were observed over areas with similarly high toluene emissions, with up to 1.00 mg m^{-2} h^{-1} of MTBE* observed. Figure 5.9, shows a latitude averages of all flight transects (1 km resolved) of MTBE and toluene emission, with both in good agreement. The average MTBE* flux for Central London was calculated to be 0.21 mg m^{-2} h^{-1}, compared to 0.20 mg m^{-2} h^{-1} for toluene, suggesting an approximate 1:1 ratio. In 2008 in the UK, the average MTBE concentration in petroleum was 3.4% (v/v) [214]. As MTBE* is a good indicator of vehicular emissions, the observed toluene emissions from central London can be attributed mainly due to vehicle emissions.

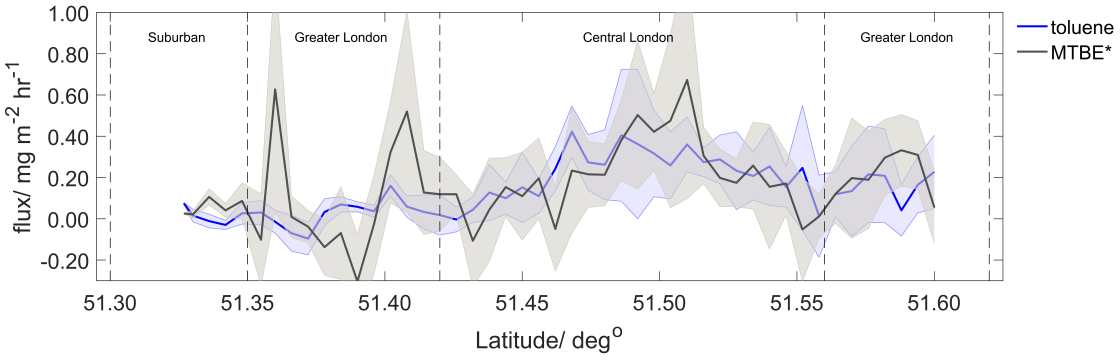

Figure 5.9: Latitude averaged (1 km) MTBE* (grey) and toluene flux (blue) with standard deviation (shaded area).

5.3.2 NAEI Comparison

Benzene fluxes quantified for all RFs during 2013 were compared to 1 km^2 footprint estimates of benzene from the NAEI, scaled to time−of−day as described above. The lateral displacement of the footprint from the flight track due to the horizontal boundary layer wind extended 4−12 km upwind (Figure 5.6). Figure 5.10a, shows 1 km latitude averages of measured benzene fluxes and NAEI benzene emission estimates with the standard deviation shaded. Good agreement between measurements and NAEI emission estimates was found for across most of London. Due to the significant uncertainty of benzene flux at 1 km^2 resolution (100−300%), benzene flux and NAEI estimates were averaged across the entire flight path, reducing uncertainty. The average measured benzene flux (0.051 mg m^{-2} h^{-1}) and the average NAEI estimate (0.037 mg m^{-2} h^{-1}) agree within the bounds of measurement uncertainty, with a ratio of 1.40. To investigate the spatial emission distri-

bution over London, the flight path was split into 4 zones as previously discussed, reducing the overall error associated with 1 km flux averages. The suburban London region was found to have the largest difference between averaged benzene flux and NAEI. The average flux was found to be 3 times higher than predicted NAEI estimates. Greater and Central London areas showed better agreement, with ratios of average flux/NAEI below 1.70.

Toluene fluxes measured in 2013 were also compared to NAEI emission estimates. Figure 5.10c shows 1 km^2 latitude averages of toluene flux and NAEI estimates with standard deviation shaded. In suburban areas of London, measured fluxes are a factor of 1.4 higher than NAEI estimates. In the other zones, measured fluxes are 30 to 50% lower than estimates. When averaged across the whole of London, the NAEI emission estimates for toluene were a factor of two higher than the average measured flux (0.39 mg m^{-2} h^{-1} from the NAEI compared with 0.18 mg m^{-2} h^{-1}).

Comparison of 1 km^2 latitude average toluene flux (2014) and NAEI estimates are shown in Figure 5.10d, with good agreement for outer London. Again, higher NAEI emission estimates are observed for most of London. Average NAEI toluene estimates are a factor of 2 higher compared to measured fluxes, with average NAEI estimate of 0.28 mg m^{-2} h^{-1}, compared to the average measure value of 0.14 mg m^{-2} h^{-1}). With stricter legislation now restricting emissions from sources such as road transport, solvent emissions are now predicted to be the main source for NMHCs in London [215]. As observed in 2013, Greater and Central areas show measured fluxes to be 50% less than predicted by the NAEI, further implying the need for refinement of emission sources for toluene within the NAEI.

Comparison between C_2 alkyl−benzenes fluxes to 1 km^2 NAEI estimates (Figure 5.10b) show good agreement across London. Average NAEI estimates for C_2 alkyl−benzenes are higher than the average measured C_2 alkyl−benzenes flux. This overestimation is likely due to errors in the source sector factors for C_2 alkyl−benzenes emissions. Average suburban measured C_2 alkyl−benzenes flux agreed well with the NAEI estimates, compared to the average South−westerly Greater London average flux which was 70% lower than NAEI estimates. Table 5.2 and 5.3 gives an in−depth review into measured fluxes and NAEI footprint estimates for both years' flights, giving averages and ratios for each of the 4 defined London zones.

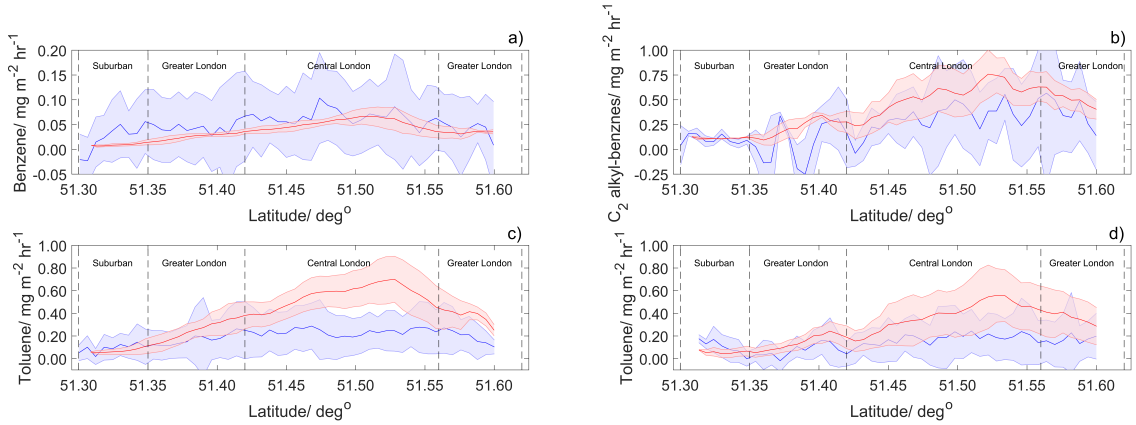

Figure 5.10: Latitude averages (1 km) for: a) benzene flux (2013), b) C_2 alkyl−benzenes flux (2014), c) toluene flux (2013) and d) toluene flux (2014) shown in blue, with footprint NAEI estimates in red. Shaded areas being calculated standard deviation of all RF transects.

Table 5.2: Averaged flux and footprint estimates during 2013 and 2014 for each London zone. Suburban London latitudes (51.30−51.35^o), Southwest Greater London latitudes (51.35−51.42^o), Central London latitudes (51.42−51.56^o), Northeast Greater London latitudes (51.56−51.60^o).

	Average Flux/ mg m^{-2} h^{-1}	Suburban London/ mg m^{-2} h^{-1}	Northwest Greater London/ mg m^{-2} h^{-1}	Central London/ mg m^{-2} h^{-1}	Northeast Greater London/ mg m^{-2} h^{-1}
benzene (2013)	0.052	0.035	0.044	0.065	0.039
benzene NAEI (2013)	0.037	0.009	0.026	0.052	0.034
toluene (2013)	0.18	0.098	0.18	0.24	0.19
toluene NAEI (2013)	0.39	0.069	0.26	0.56	0.38
toluene (2014)	0.14	0.104	0.076	0.17	0.16
toluene NAEI (2014)	0.28	0.058	0.14	0.38	0.37
C_2 alkyl−benzene (2014)	0.32	0.107	0.064	0.32	0.38
C_2 alkyl−benzene NAEI (2014)	0.49	0.11	0.22	0.54	0.51

Table 5.3: Average flux/NAEI ratio for each London zone. Suburban London latitudes (51.30−51.35^o), Southwest Greater London latitudes (51.35−51.42^o), Central London latitudes (51.42−51.56^o), Northeast Greater London latitudes (51.56−51.60^o).

	Flux to NAEI/ ratio	Suburban London/ ratio	Northwest Greater London/ ratio	Central London/ ratio	Northeast Greater London/ ratio
benzene (2013) benzene NAEI (2013)	1.4	3.7	1.7	1.3	1.1
toluene (2013) toluene NAEI (2013)	0.46	1.4	0.7	0.4	0.5
toluene (2014) toluene NAEI (2014)	0.5	1.8	0.5	0.5	0.4
C_2 alkyl−benzenes (2014) C_2 alkyl−benzenes NAEI (2014)	0.64	0.9	0.3	0.6	0.7

5.3.2.1 Eddy-Covariance Flux Errors

A specific error which affects measured fluxes by PTR-MS is disjunct sampling. This error occurs when the quadrupole detector analyzes sequentially at 10 Hz but is separated by longer sample gaps of 0.5 s. To reduce this error the flight tracks where kept relatively long (∼50 km) and the frequency of VOC sampling greater than 2 Hz. Due to flight restrictions over London, stacked altitude flight legs were not possible, hence it was not possible to quantify chemical losses occurring between the surface and the point of measurement by directly observing the flux gradient. The vertical divergence of NO_x fluxes over London due to reaction of NO_2 with the hydroxyl radical has previously been assessed and found to be in the region of 1−2% (Chapter 4) [193]. Some of the reported VOC fluxes in this study are more reactive than NO_x, therefore the underestimation is by at least the same amount [124].

The calculated error associated for each flux transect considers the random, systematic and disjunct errors as an average across the transect, using the methods of Lenschow et al. and Karl et al. [124, 216]. It should be noted that the error associated with 1 km resolved fluxes was much greater than the average error across each flight track, with calculated errors increasing to 200 %, suggesting the need to average the fluxes to larger scales. As discussed in Table 5.3, the four London regions which are compared to the NAEI are approximately 15 km in length, and each regions flux estimate as an uncertainty of approximately 40%. Chapter 3 (Section 3.3.6) gives an in-depth discussion of the flux error types and how averaging decreases the overall uncertainty. A summary of calculated flux errors as an average over each flight transect is shown in Table 5.4.

Table 5.4: Calculated flux errors for each VOC compound for systematic, random and disjunct error as an average for each flight transect (50 km resolved fluxes).

Compound	Systematic Error/ %	Random Error/ %	Disjunct Error/ %
C_2 alkyl-benzenes	7.1	25.1	0.8
toluene	19.1	35.0	1.0
benzene	25.3	47.0	1.1
C_3 alkyl-benzenes	5.0	12.0	0.7
MTBE	2.4	18.0	1.3
isoprene	9.5	30.1	2.2
MVK/MACR	2.1	16.6	1.6
monoterpenes	2.3	17.7	1.9

5.3.3 Biogenic VOC Fluxes

Measurements of several VOCs of predominantly biogenic origin were made over the South Sussex region of Southern England. Figure 5.1c and d show all flight transects conducted during the two campaign periods. Figure 5.11 shows the calculated footprint extent from the flight track overlaid onto the UK's National Land Classification map at 25 m^2 resolution. This demonstrates that for a typical flight over the region, areas of mixed broadleaved woodland containing Quercus and other tree species known to emit isoprene occur within the measurement footprint [217, 218, 219].

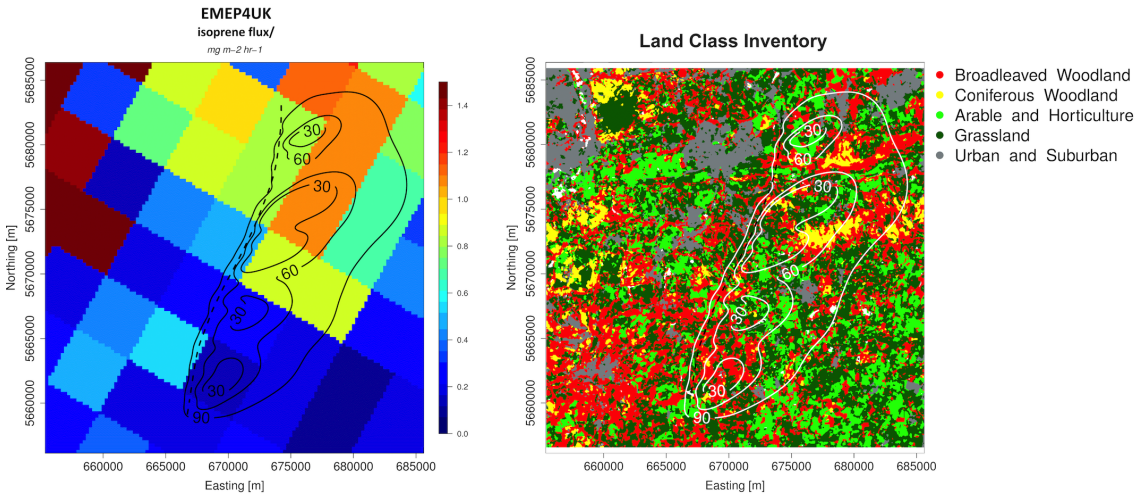

Figure 5.11: RF flight track during 2013 flight over South Sussex region. Left) Calculated footprint extent 30, 60, 90% from flight track, overlaid onto EMEP4UK isoprene emission grid. Right) footprint extent 30, 60, 90% from flight track, overlaid onto UK National Land Class Inventory 2012 at 25 m^2 resolution.

Measured isoprene fluxes varied from 0.20 to 2.00 mg m^{-2} h^{-1} (Figure 5.12 a−b). In general, temperature and the flux of photosynthetically active radiation (PAR) were higher during the 2013 flights than during the 2014 flights. Figure 5.13 shows mean isoprene emissions from identical flight transects conducted on three consecutive days ($7-9^{th}$ July 2013), each flight consisting of 1.5 hours and ∼40 km repeated flight legs. Mean measured isoprene emission rates in areas of broadleaved woodland displayed a dependence on both PAR and ground temperature. Maximum isoprene emissions measured during both campaigns were found to be 2.0 mg m^{-2} h^{-1} and 1.0 mg m^{-2} h^{-1} for July 2013 and July 2014 respectively.

MVK/MACR fluxes were quantified during two RFs in 2014. Overall, one hour of flux data was obtained, giving spatial coverage of ∼180 km^2. Maximum fluxes of ∼0.20 mg m^{-2} h^{-1} were observed between latitude of 51.10−51.20^o, with high isoprene fluxes observed over the same area. Measured NO mixing ratios during all flights were found to be <1 ppbv. Under these conditions the MCM 3.1.1 predicts that 70% of the measured flux will be MVK and 30 % MACR.

Emissions of monoterpenes were also quantified during both campaigns. PTR−MS intensities at m/z 137 where assumed to give a measure of the total monoterpene flux, since no separation of individual species was possible. In 2013, 1 hour of data monoterpene flux data was obtained from 2 RFs and ∼160 km^2 of spatial coverage. Monoterpenes measured during 2014 generated 1.25 hours of flux data, with overall spatial cover of 180 km^2. Both campaigns showed similar emission characteristics, with highest emissions found at latitudes 51.00−50.90^o. Maximum emissions were found to be 1.00 mg m^{-2} h^{-1} during 2013 and 0.80 mg m^{-2} h^{-1} during 2014. Figure 5.12 c−d show interpolated monoterpene fluxes during both years. Table 5.5 gives a full statistical breakdown of all measured biogenic VOCs during 2013 and 2014.

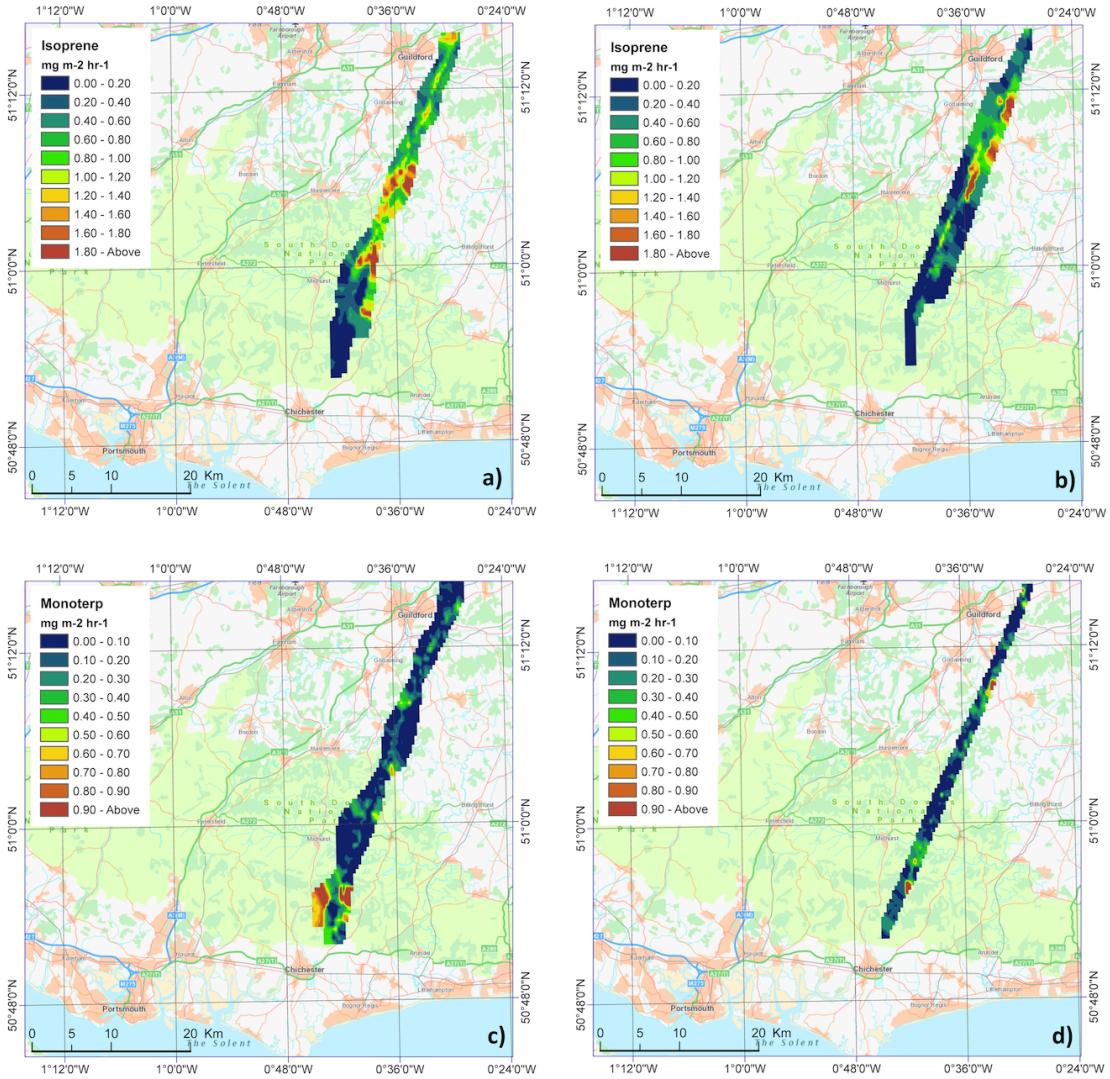

Figure 5.12: Measured biogenic instantaneous fluxes of a) isoprene (2013), b) isoprene (2014), c) monoterpenes (2013) and d) monoterpenes (2014), interpolated at 500 m using inverse distance weighting from all RF transects.

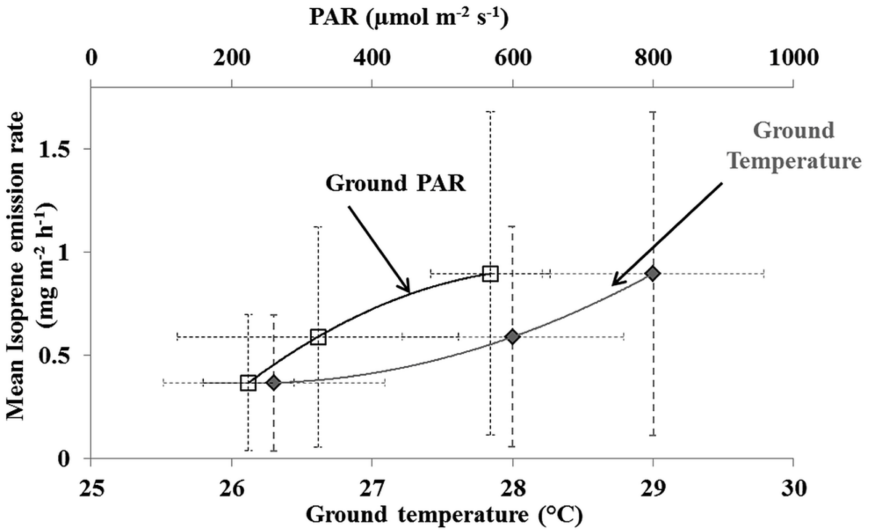

Figure 5.13: Mean isoprene emissions from 3 OPFUE (July 2013) identical flight transects conducted on 3 consecutive days (7/7/13−9/7/13), each flight consisting of 1.5 hours of data and ∼40 km repeated flight legs. Mean isoprene emission in the dense broadleaved woodland area displayed a dependence on photo−synthetically active radiation (PAR) (black) and ground temperature (grey). Ground PAR and temperature data is from the Goodwood AURN site.

Table 5.5: Measured biogenic flux statistics during both campaigns for isoprene, total monoterpenes and MVK/MACR.

	Flux mean/ mg m^{-2} h^{-1}	Flux median/ mg m^{-2} h^{-1}	Standard Deviation	Standard Error	95th Percentile
isoprene (2013)	0.74	0.72	0.45	0.021	1.60
isoprene (2014)	0.48	0.47	0.32	0.025	0.96
Total monoterpenes (2013)	0.16	0.11	0.21	0.01	0.54
Total monoterpenes (2014)	0.12	0.1	0.19	0.01	0.45
MVK/MARC (2014)	0.056	0.054	0.047	0.003	0.13

5.3.4 EMEP model comparison

The measured isoprene fluxes from 2013 and 2014 were compared to hourly−average EMEP4UK isoprene estimates at 5 km^2 resolution. Due to EMEP4UK estimates only account for biogenic sources of isoprene, the NMHCs NAEI was used to account for any anthropogenic contribution. Isoprene contribution for each of the 11 source sectors within the NAEI was accounted for in remaining unspeciated contributions, with no seperation [205]. Total anthropogenic contributions of isoprene for the region was found to be less than 1% of EMEP4UK estimates, highlighting biogenic sources as dominant.

The flux footprint represented an area 5−10 km upwind from the flight tracks (Figure 5.11 left). Latitude averages of isoprene flux and EMEP4UK time−of−day estimates for 2013 (Figure 5.14 left) show good agreement from latitudes of 51.15−51.30^o. The EMEP4UK model however fails to capture the high isoprene fluxes observed at latitudes between 51.05−51.15^o. The model predicts isoprene emissions of <0.20 mg m^{-2} h^{-1}, with measured isoprene fluxes ranging from 1.00−2.00 mg m^{-2} h^{-1}. This discrepancy maybe be due to the relatively coarse (5 km^2) land classification used by the emission model (Figure 5.11 left) or too low normalised ('base') emission rates.

Figure 5.14 right shows latitude−averaged isoprene fluxes compared to the EMEP4UK estimates for 2014. The degree of agreement between the measurement and the inventory is poor, with measured flux consistently higher than EMEP4UK estimate. Measured isoprene fluxes range from 0.10−1.00 mg m^{-2} h^{-1}, compared to the EMEP4UK estimates of ≤0.40 mg m^{-2} h^{-1}. Again, the discrepancy may be due to land classification resolution or unrealistic normalised emission rates.

The highly spatially resolved (1 km^2) flux measurements have significant uncertainty (100−300 %), so to overcome this, overall average fluxes obtained from all the measurement data were compared with the corresponding EMEP4UK emissions estimate. A full statistical description is given in Table 5.6, for average comparison between measured isoprene flux and EMEP4UK estimates. In 2013, average measured isoprene flux was 60% higher than the EMEP4UK estimate. In 2014, the average measured isoprene flux was 140% higher than the EMEP4UK estimate.

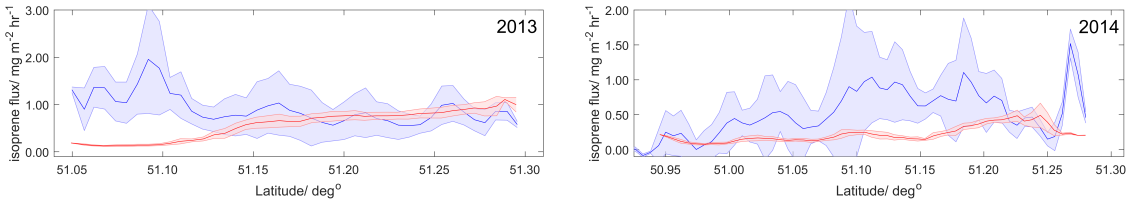

Figure 5.14: Latitude averaged (1 km) of measured isoprene flux (blue) and EMEP4UK isoprene emission (red) with shaded standard deviation for 2013 and 2014.

Table 5.6: Statistics for measured flux and footprint model generated EMEP4UK emission estimates of isoprene during both field campaigns.

	Flux to EMEP/ ratio	Flux mean/ mg m^{-2} h^{-1}	Flux median/ mg m^{-2} h^{-1}	Standard Deviation	Standard Error	95th Percentile
isoprene (2013)	1.6	0.902	0.82	0.32	0.032	1.50
EMEP4UK (2013)		0.57	0.65	0.301	0.03	0.95
isoprene (2014)	2.4	0.48	0.47	0.31	0.025	0.96
EMEP4UK (2014)		0.201	0.17	0.10	0.008	0.402

5.4 Conclusions

This study has allowed the first direct measurements of VOC emission rates over Greater London and SE England. A total of 11 flights during July 2013 and 2014 gave 16 hours of high spatial resolution flux measurements over London for a range of anthropogenic NMHCs, corresponding to emission measurements from ≈4,500 grid cells of 1 km^2 each. Measured benzene fluxes over London displayed high spatial heterogeneity and compared relatively well to NAEI estimates. Measured toluene and C_2 alkyl−benzenes fluxes showed high emissions emanating from central and industrial regions of London, although these were overestimated by the NAEI. It is clear that further refinement of the NAEI, both in terms of the speciation of its NMHC inventory and in terms of individual VOC emission rates, is required.

Isoprene and monoterpene fluxes, presumably predominantly from biogenic sources, were measured over SE England. A total of 5 flights over SE England gave 6.5 hours of highly spatially resolved fluxes covering ∼800 km^2. Measured isoprene fluxes showed relatively higher emissions over areas containing Quercus and other broadleaf tree species known to emit isoprene. The EMEP4UK inventory significantly underestimated the measured isoprene fluxes. This may be due in part to the failure of the model to capture regions of elevated isoprene flux due to its use of land classification at 5 km^2 resolution when much of the woodland in SE England is smaller than this. Improvements in the spatial resolution of land use classification could help improve model performance with respect to isoprene and monoterpene emissions. This is important as it is possible that biogenic VOCs (especially isoprene) could become of increasing importance to secondary pollutant formation in the UK and Northern Europe in a future warming climate, with increased prevalence of high temperature events, and as anthropogenic VOC emissions continue to decline with improved regulation and control technologies.

Overall this work demonstrates the suitability of using a low-flying aircraft to determine anthropogenic and biogenic VOC fluxes by eddy covariance and the possibility of validating emission inventories with these measurements. Further evaluation and improvements to the emission inventories of anthropogenic and biogenic VOCs used for regulatory, policy and research purposes is clearly an urgent requirement.

Chapter 6

Conclusions and Future work

6.1 Conclusions

Poor air quality is a major global problem and has been linked to respiratory and cardiovascular disease, which can ultimately increase the risk of premature mortality. In the UK, high emissions of nitrogen oxides ($NO + NO_2 = NO_x$) is a major concern and is a result of increased diesel vehicle usage. Diesel vehicles emit higher proportions of NO_x as NO_2, which can perturb the NO_x photochemical cycle with O_3. Higher NO_2 emissions have led to NO_x concentrations plateauing over the last 15 years, which has not been in line with predicted emission reductions. The governmental department charged with overseeing the UK's air quality is the Department of Environment, Food and Rural Affairs (DEFRA). DEFRA assesses UK emissions and reports them to EU, in order to meet strict air quality legislation. NO_x emissions from cities such as London, regularly exceed safe EU limits, posing a direct threat to human health.

A key tool used by DEFRA towards meeting air quality legislation is the National Atmospheric Emissions Inventory (NAEI). This inventory gives detailed annual emission estimates for pollutants such as NO_x and VOCs, for the entire UK at 1 km^2 resolution. The accuracy of these emission estimates will directly impact whether the UK is able to meet EU air quality regulations. Previous work assessing the reliability of the NAEI has been conducted from tower sites, including the BT tower in London. By making eddy−covariance measurements over a period of months, emission rates can be compared to annual NAEI estimates. The main disadvantage of this approach is that it is particularly area specific therefore it cannot be extrapolated over an entire city. More recently, eddy-covariance from an aircraft has been used to measure emissions from entire cities, such as Mexico City. In terms of the UK, this strategy allows for cities such as London to be assessed on a resolution note previously possible using classical eddy-covariance approaches.

Airborne eddy-covariance was used to calculate emission rates for NO_x and a number of different VOCs over London and Southern England at low altitude (360 m). The technique uses wavelets to calculate an eddy-flux, whilst ensuring all frequency contributions are accounted for. Wavelets also allow each flux measurement to be conducted at spatial scales below 1 km giving highly detailed emission structure for the area being flown over. As each flight leg took approximately 20 minutes to complete, multiple passes were done to reduce the temporal variability of the eddy−fluxes. Flights were conducted in the summer of 2013 and 2014, running for two two week periods. This gave a total of 32 hours' worth

of flight data from which fluxes could be calculated from. Measured NO_x fluxes from both years flights highlighted very high emissions emanating from central London. The emission signature was very similar for both years, with high emissions observed concurrently over the same areas. Calculated VOC fluxes showed interesting structure depending on the species. Toluene's emission structure over London followed that of NO_x with highest emission over central London. Benzene fluxes showed higher temporal−variability and no clear emission maximum over London. Flux ratios of benzene to toluene for central areas were indicative of multiple emission sources, rather than from road vehicles alone.

To give context to the measured eddy-fluxes, comparison to the NAEI was conducted using a footprint model. The footprint model assesses the contributing 2−dimensional area responsible for the measured flux in the form of a weighting matrix. The calculated matrix is the same size as the emissions inventory and weights each 1 km emission cell individually up to a cumulative sum of 1. Each matrix is calculated using measured meteorology during each flight. In order to scale footprint NAEI emission estimates to the time−of−day at which the eddy−flux measurements were made, scaling factors were used. Each factor is unique depending on the pollutant (NO_x, VOCs) and accounts for changes in emission rate for each month, day and hour. Cumulatively this approach allows for direct time-of-day comparison between aircraft measurements and scaled NAEI estimates.

A significant discrepancy was identified between NAEI emission estimates and actual NO_x flux measurements, with the highest underestimation being a factor of two in Central London. In outer London, where the source of NO_x is almost exclusively from road transport (90%), there is an underestimation in the inventory of around a factor of 1.5, indicative of the poor treatment of the road traffic source in the NAEI. Due to the potential loss of some NO_x emitted at ground level during its transport to the measurement altitude, the calculated inventory underestimation can be considered as conservative. When measurements were compared to an enhanced version of the NAEI, containing both non-road mobile machinery emission sources from the LAEI and real-world traffic emissions from the enhanced LAEI, a better agreement was found. This highlights the need for better traffic emission estimates in NAEI.

In addition to NO_x, VOCs were compared to the NAEI. Measured benzene fluxes over London displayed high spatial heterogeneity and compared relatively well to NAEI estimates. Measured toluene and C_2 alkyl−benzenes fluxes showed high emissions emanating from central and industrial regions of London, although these were overestimated by the

NAEI. It is clear that further refinement of the NAEI, both in terms of the speciation of its NMHC inventory and in terms of individual VOC emission rates, is required.

More work is needed to better understand and quantify the short−term accuracy of emission inventories. Emission inventories tend to focus on providing longer term (annual) emission estimates and are ill equipped to provide information on the temporal nature of emissions. Improved information on the temporal characteristics of emissions would improve the reliability of short−term flux measurements when compared with emission inventories. In particular, NO_x measurements highlight the critical importance of obtaining independent pollutant emission rates from vehicles during on−road driving conditions and using such data in emission inventories, rather than relying on emissions data obtained during artificial test driving conditions or provided by vehicle manufacturers.

In conclusion, the combination of real−time emission measurements and spatial comparison to emission inventories using the discussed methodology is a powerful tool. It has allowed for spatial assessment on a scale not previously possible in the UK. Due to the importance such inventories like the NAEI play, direct assessment of their accuracy is highly important with this technique giving a reliable way of doing just that.

6.2 Uncertainties in Airborne Flux Measurements

A key area which underpins the work presented in this thesis, is the relative uncertainties of the airborne flux measurements made. These measurements have multiple sources of uncertainty which together can be significant if not properly understood. Firstly, NO_x measurements made by the Fast−AQD−NO_x instrument have uncertainties related to the precision and accuracy of the instrument. The overall uncertainty of the measurements at 9 Hz was low, with mixing ratios of NO_x typically above 1 ppb giving an error of $< 15\%$.

The second uncertainty which affects the flux measurements is the eddy−covariance calculation. Classical eddy-covariance gives a single flux estimate over a 30−minute period, compared to wavelets which generate fluxes at far greater time resolution. The finer time scales at which these fluxes are made increases the uncertainty. This increase in uncertainty is due to both systematic and random errors, which stem from the meteorological probe not being able to capture all the contributing eddies to the flux and also the largest transport eddies due to the reduced time scales. In relation to how these uncertainties affect the measured fluxes, 1 km resolved fluxes can have an uncertainty above 250% which is highly significant.

Classical eddy-covariance gets around the high uncertainty problem by averaging the data over longer time periods (30 minute intervals) which allows the sensor capture more of the contributing eddies. For aircraft measurements, averaging over longer distances helps reduces the overall uncertainty. Averaging airborne fluxes to 15 km scales reduces the overall uncertainty for this study $< 50\%$, and $< 25\%$ for 50 km scale fluxes which represent an average flight leg over London.

Another important uncertainty is in the emission inventory and footprint model comparison. The footprint model is dependent most on the surface roughness length used. For homogenous terrain finding the correct roughness is simple; however, London is highly heterogeneous, represents a real challenge when trying to account for large degrees of change. Going forward this is an area which needs better understanding as to what uncertainty highly heterogeneous terrain has on the model and in turn emission estimates generated by it.

Overall the main source of uncertainty is down to the eddy-covariance methodology. When accounting for only the eddy−covariance calculation and NO_x measurement uncertainties (square root of the summed squared individual errors), 15 km scale fluxes have an overall uncertainty of 52%. 50 km scale fluxes an overall uncertainty of 32%. At both these

flux scales, the uncertainty is less significant than for 1 km scales and does not impact on the conclusions drawn in Chapter 4 and 5 towards the emission inventory assessment. In future, it is an area of the technique which requires greater attention as there are only a limited number of studies which investigate these flux uncertainties.

6.3 Future work

Classical ground based eddy-covariance gives a single flux estimate over a 30−minute to 1 hour period, compared to wavelets which are able to generate fluxes at far greater time resolution. Future studies may want to assess whether ground based eddy−covariance could follow a wavelet approach to generate higher time resolution fluxes, whilst still meeting the same robustness as the current classical methodology.

Another aspect of the presented work which will need continued development is the footprint model. Footprint models have classically been applied to homogeneous terrains with small changes in surface roughness. The work discussed here applies the model to a highly heterogeneous surface with high variability of surface roughness. Understanding the effect large buildings have on surface roughness is complex, requiring highly resolution measurements of both surface structure and wind profiles. The surface roughness estimates used here were not able to fully capture the effect a single skyscraper would have on the footprint model, and so requires future studies to better elaborate on this. Overall, by better understanding the two highlighted areas, the robustness and applicability of the wavelet based flux methodology would be greatly increased.

Appendix A

Footprint Weighting Matrices

Shown here are calculated footprint weighting matrices from the footprint parameterisation as discussed in Chapter 3.

The following Figures show calculated footprint weighting matrices for varying PBL heights (Z_i). Other footprint parameters were set at constant values: $\sigma_v = 0.2$, $\sigma_w = 0.2$, $u_* = 0.2$, $Z_M = 360$, $Z_0 = 1.0$.

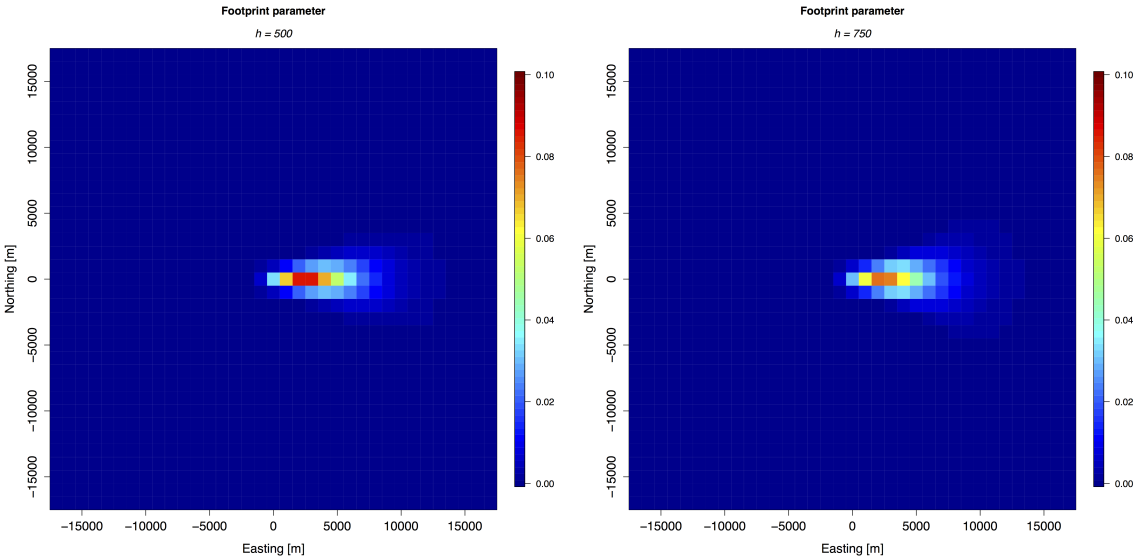

Figure A.1: Footprint weighting matrix for set Z_i of 500 and 750 m. All other footprint parameters set constant.

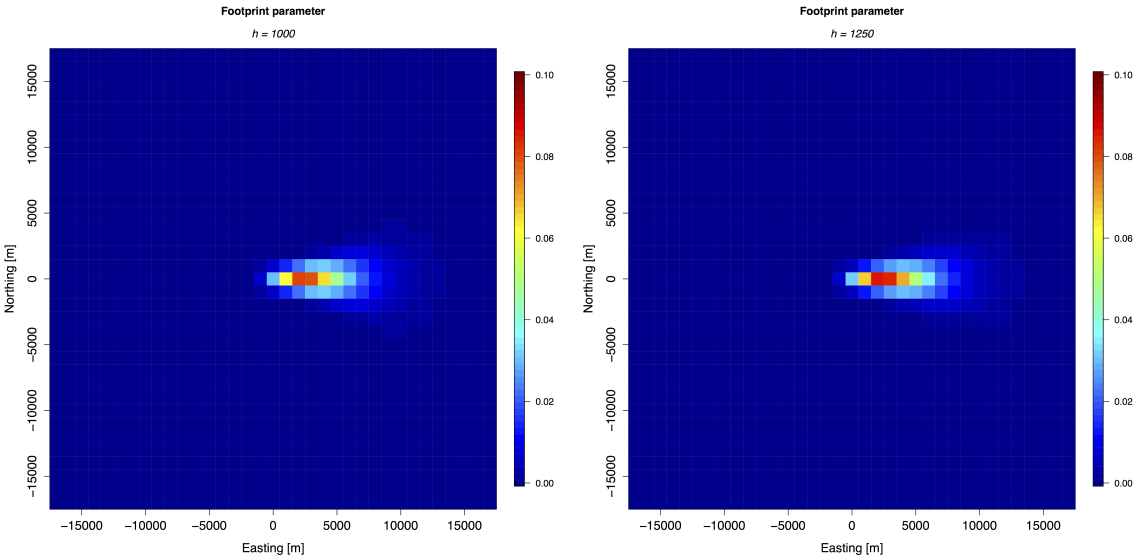

Figure A.2: Footprint weighting matrix for set Z_i of 1,000 and 1,250 m. All other footprint parameters set constant.

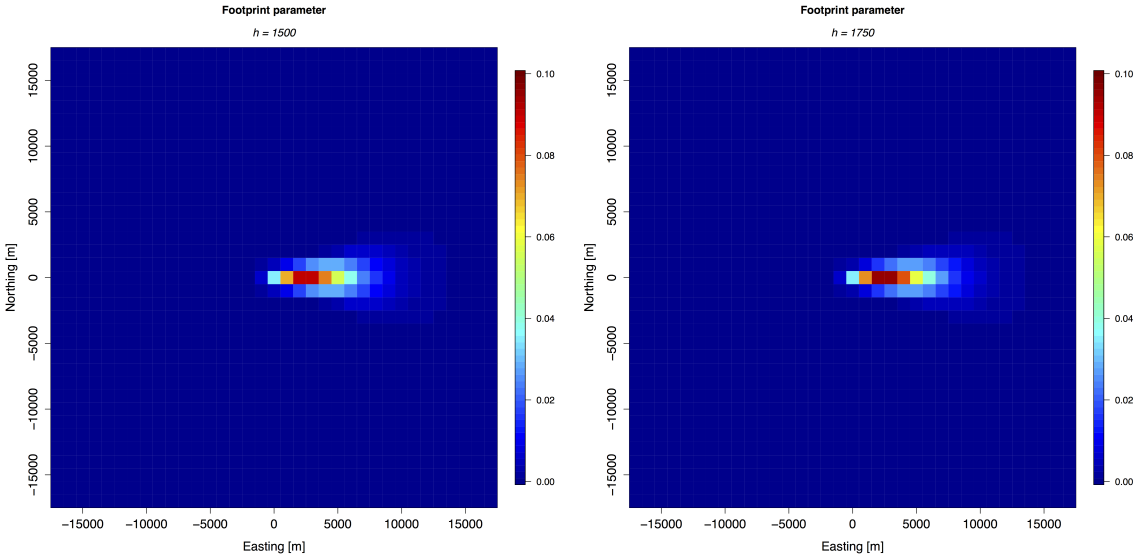

Figure A.3: Footprint weighting matrix for set Z_i of 1,500 and 1,750 m. All other footprint parameters set constant.

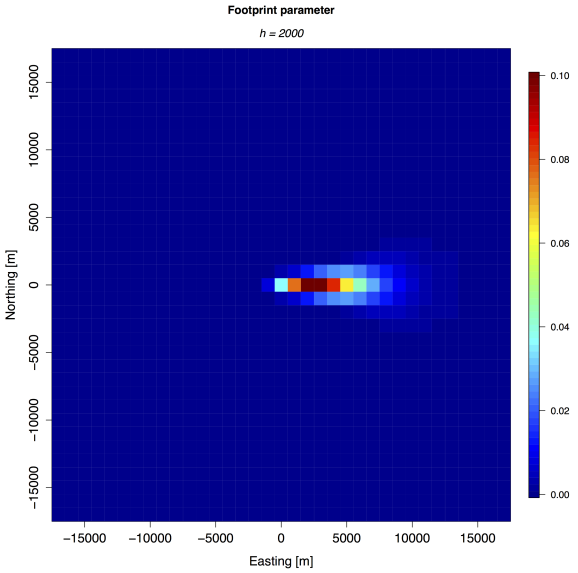

Figure A.4: Footprint weighting matrix for set Z_i of 2,000 m. All other footprint parameters set constant.

The following Figures show calculated footprint weighting matrices for varying standard deviation of horizontal wind (σ_v). Other footprint parameters were set at constant values: $\sigma_w = 0.2$, $u_* = 0.2$, $Z_M = 360$, $Z_0 = 1.0$, $Z_i = 1{,}000$.

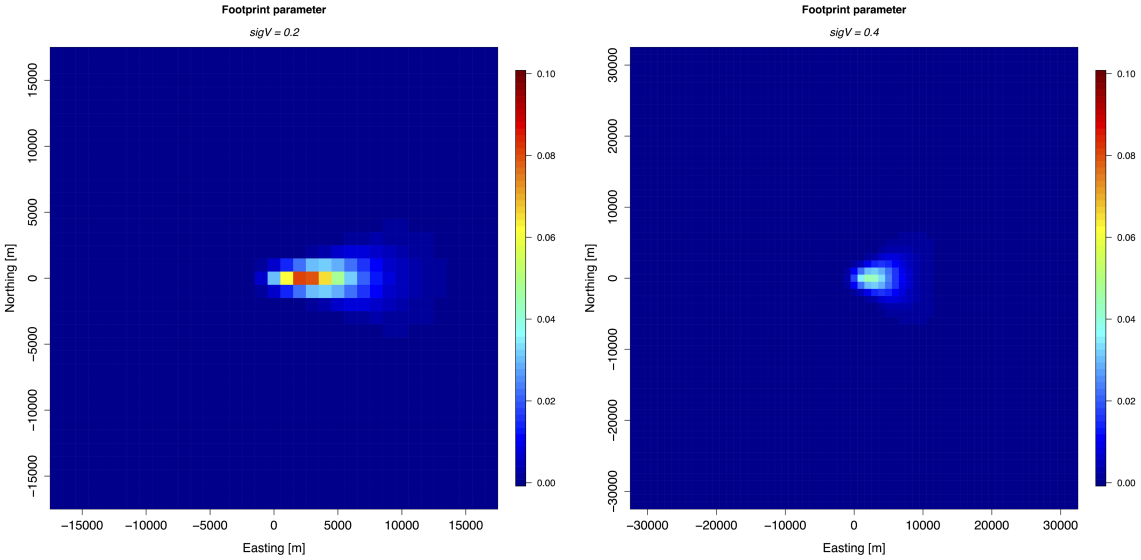

Figure A.5: Footprint weighting matrix for set σ_v of 0.2 and 0.4 m s^{-1}. All other footprint parameters set constant.

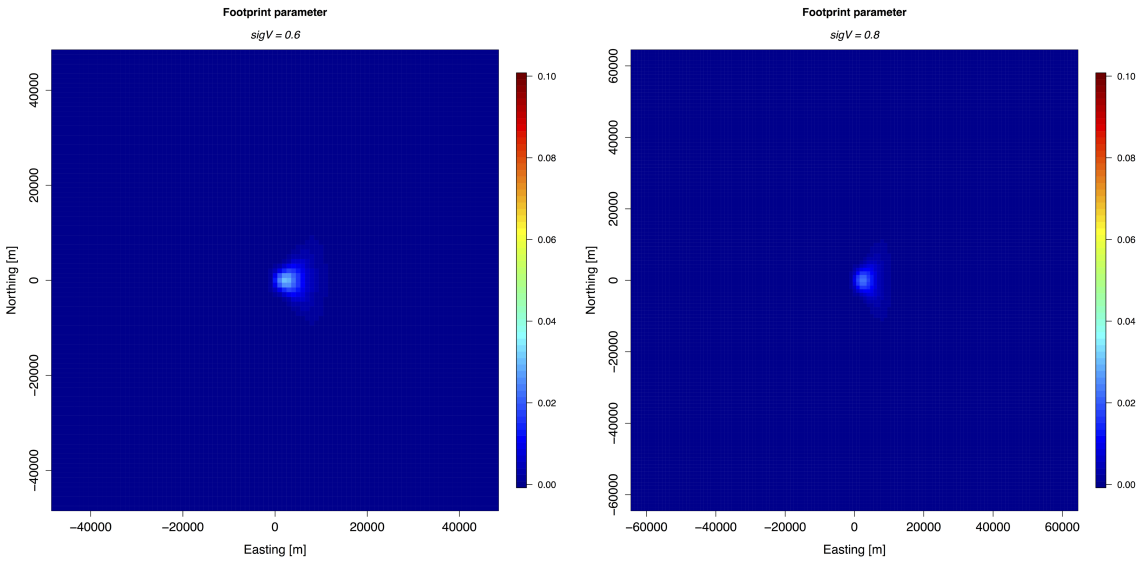

Figure A.6: Footprint weighting matrix for set σ_v of 0.6 and 0.8 m s^{-1}. All other footprint parameters set constant.

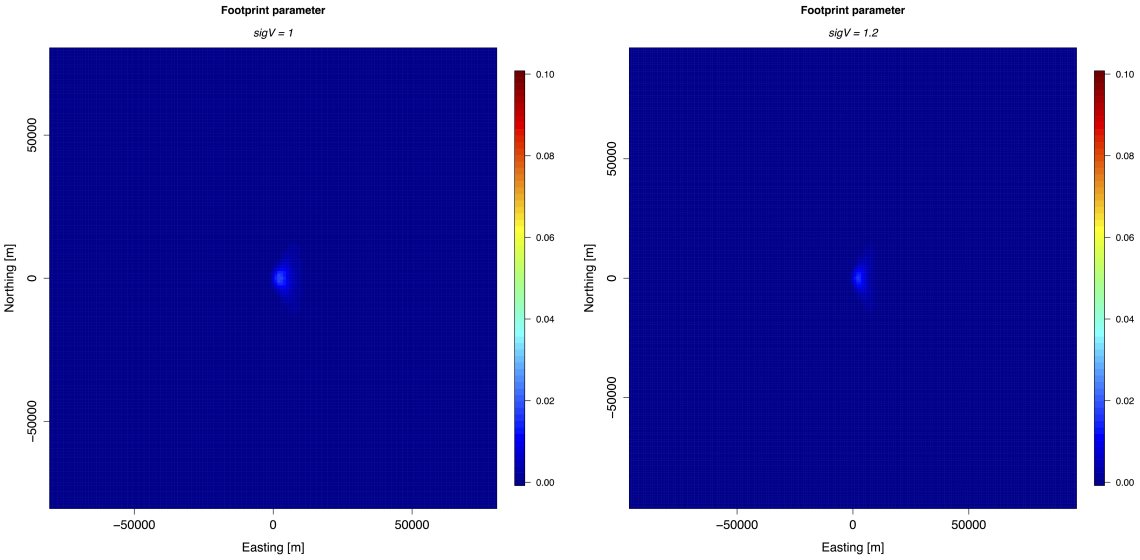

Figure A.7: Footprint weighting matrix for set σ_v of 1.0 and 1.2 m s^{-1}. All other footprint parameters set constant.

The following Figures show calculated footprint weighting matrices for varying standard deviation of vertical wind (σ_w). Other footprint parameters were set at constant values: $\sigma_v = 0.2$, $u_* = 0.2$, $Z_M = 360$, $Z_0 = 1.0$, $Z_i = 1{,}000$.

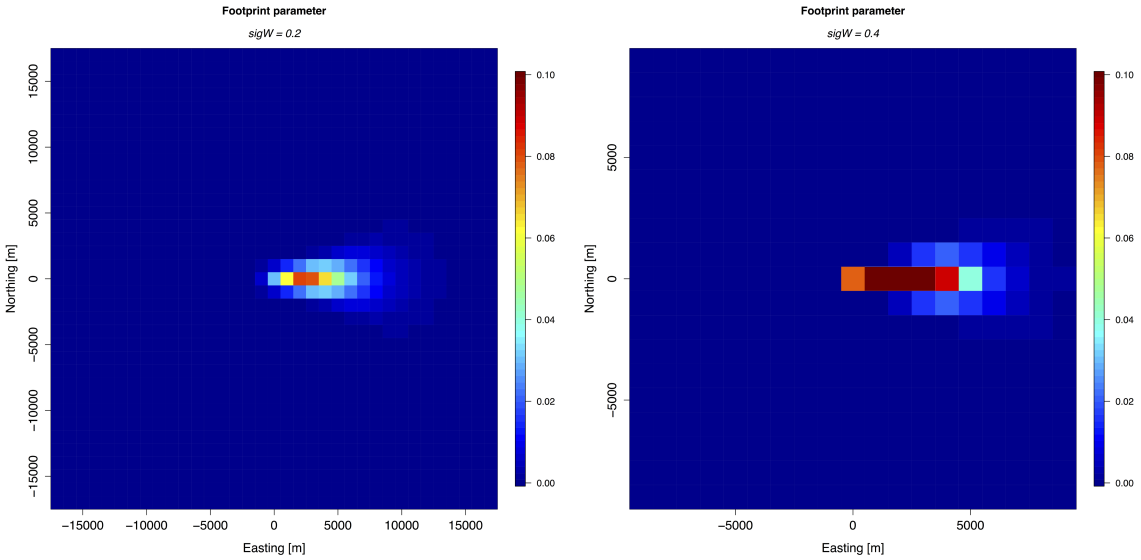

Figure A.8: Footprint weighting matrix for set σ_w of 0.2 and 0.4 m s^{-1}. All other footprint parameters set constant.

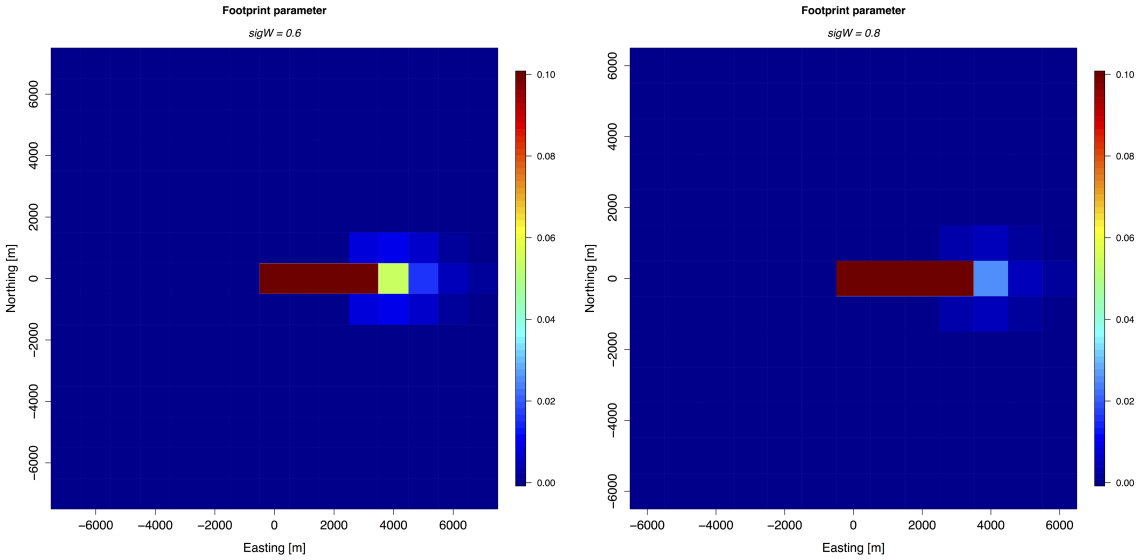

Figure A.9: Footprint weighting matrix for set σ_w of 0.6 and 0.8 m s^{-1}. All other footprint parameters set constant.

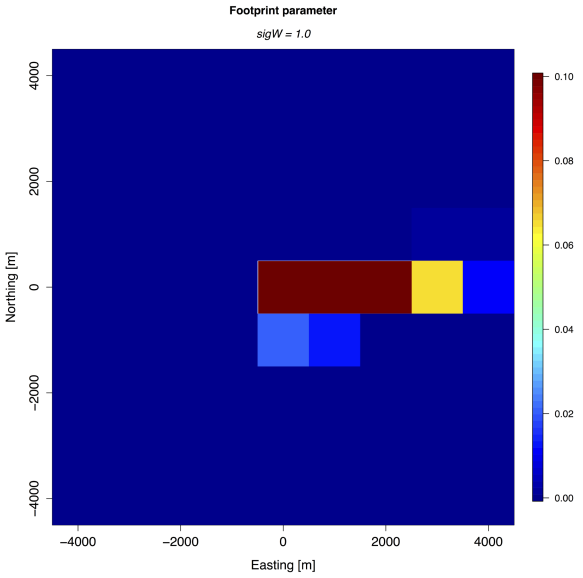

Figure A.10: Footprint weighting matrix for set σ_w of 1.0 m s^{-1}. All other footprint parameters set constant.

The following Figures show calculated footprint weighting matrices for varying friction velocity (u_*). Other footprint parameters were set at constant values: $\sigma_w = 0.2$, $\sigma_v = 0.2$, $Z_M = 360$, $Z_0 = 1.0$, $Z_i = 1{,}000$.

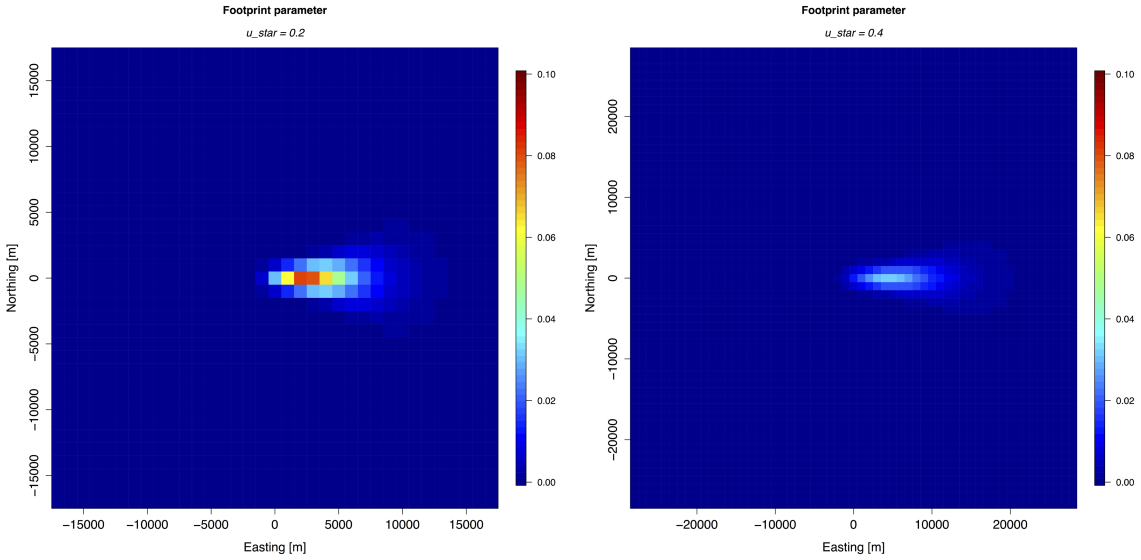

Figure A.11: Footprint weighting matrix at set u_* of 0.2 and 0.4 m s^{-1}. All other footprint parameters set constant.

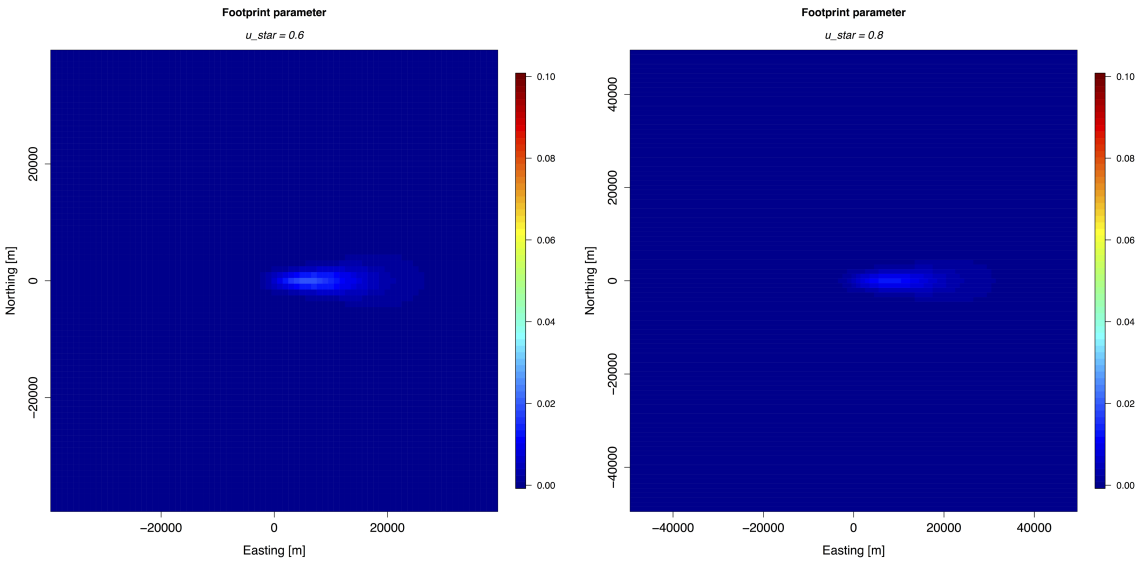

Figure A.12: Footprint weighting matrix at set u_* of 0.6 and 0.8 m s^{-1}. All other footprint parameters set constant.

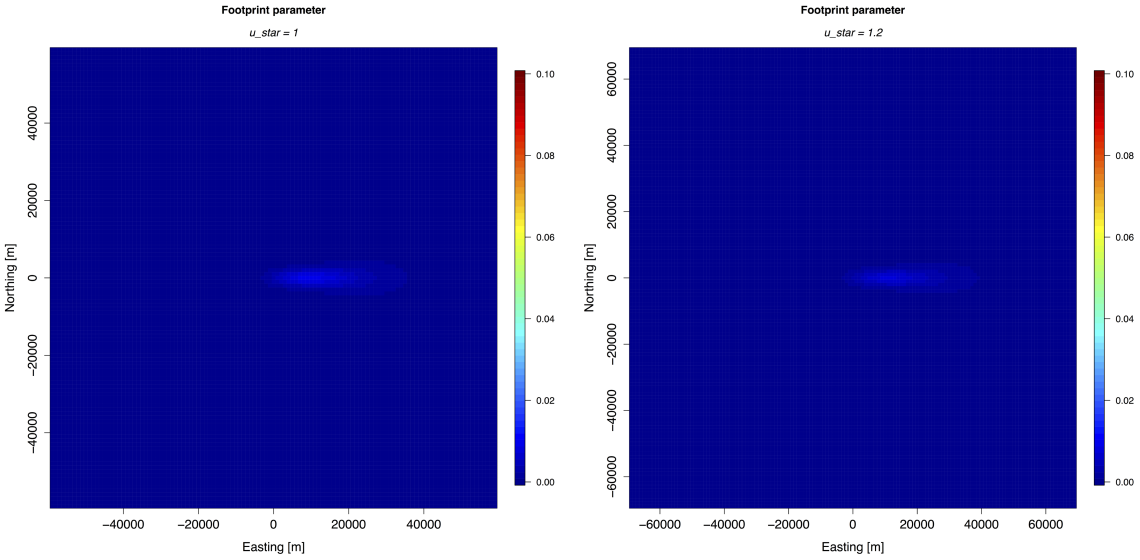

Figure A.13: Footprint weighting matrix at set u_* of 1.0 and 1.2 m s^{-1}. All other footprint parameters set constant.

The following Figures show calculated footprint weighting matrices for varying aerodynamic roughness length (Z_0). Other footprint parameters were set at constant value: $\sigma_w = 0.2$, $\sigma_v = 0.2$, $u_* = 0.2$, $Z_M = 360$, $Z_i = 1{,}000$.

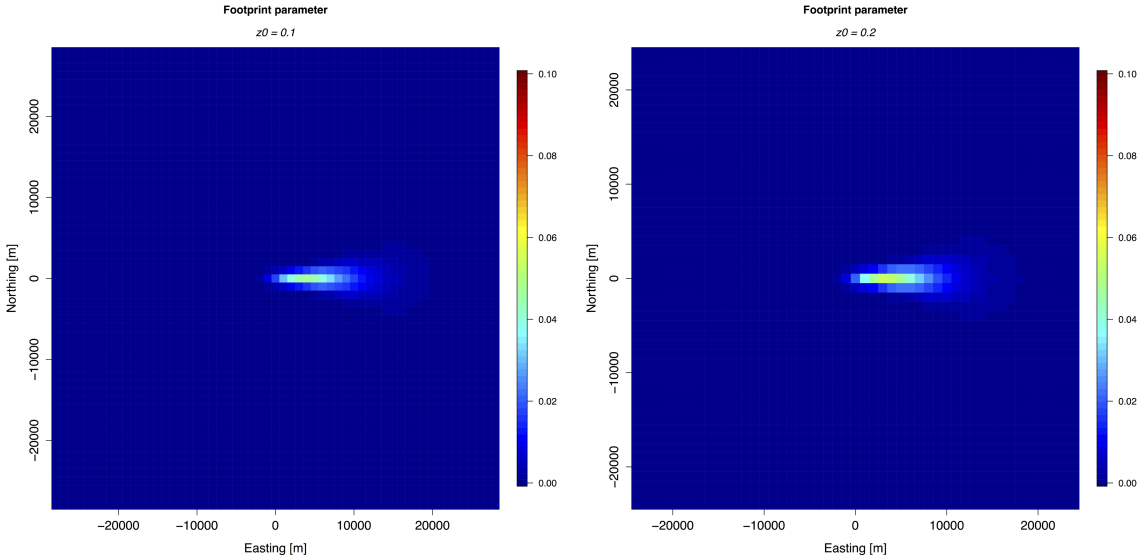

Figure A.14: Footprint weighting matrix at set Z_0 of 0.1 and 0.2 m. All other footprint parameters set constant.

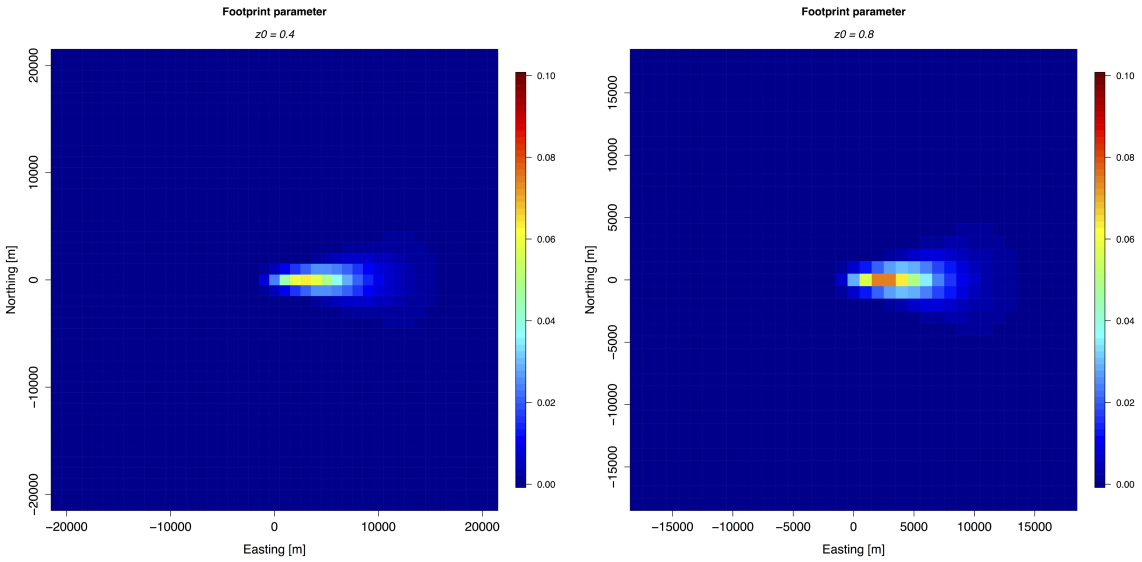

Figure A.15: Footprint weighting matrix at set Z_0 of 0.4 and 0.8 m. All other footprint parameters set constant.

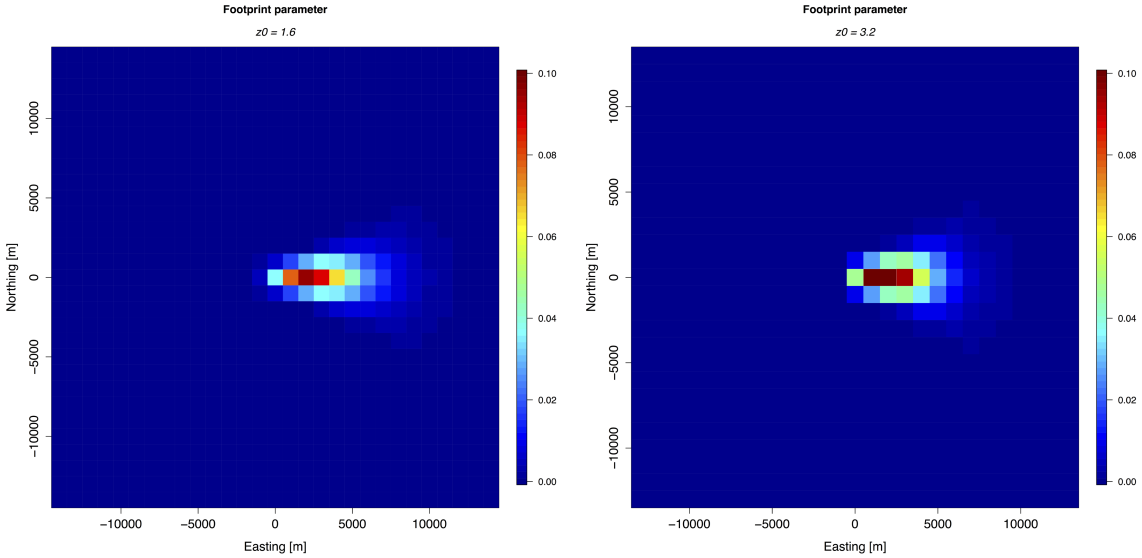

Figure A.16: Footprint weighting matrix at set Z_0 of 1.6 and 3.2 m. All other footprint parameters set constant.

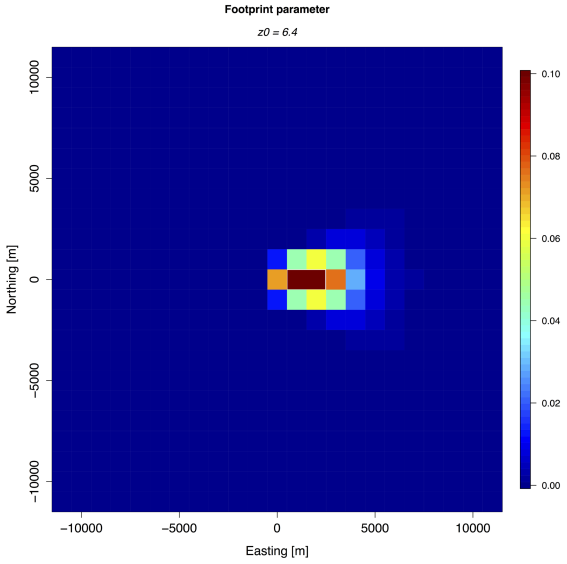

Figure A.17: Footprint weighting matrix at set Z_0 of 6.4 m. All other footprint parameters set constant.

The following Figures show calculated footprint weighting matrices for varying measurement height (Z_M). Other footprint parameters were set at constant values: $\sigma_w = 0.2$, $\sigma_v = 0.2$, $u_* = 0.2$, $Z_0 = 1.0$, $Z_i = 1{,}000$.

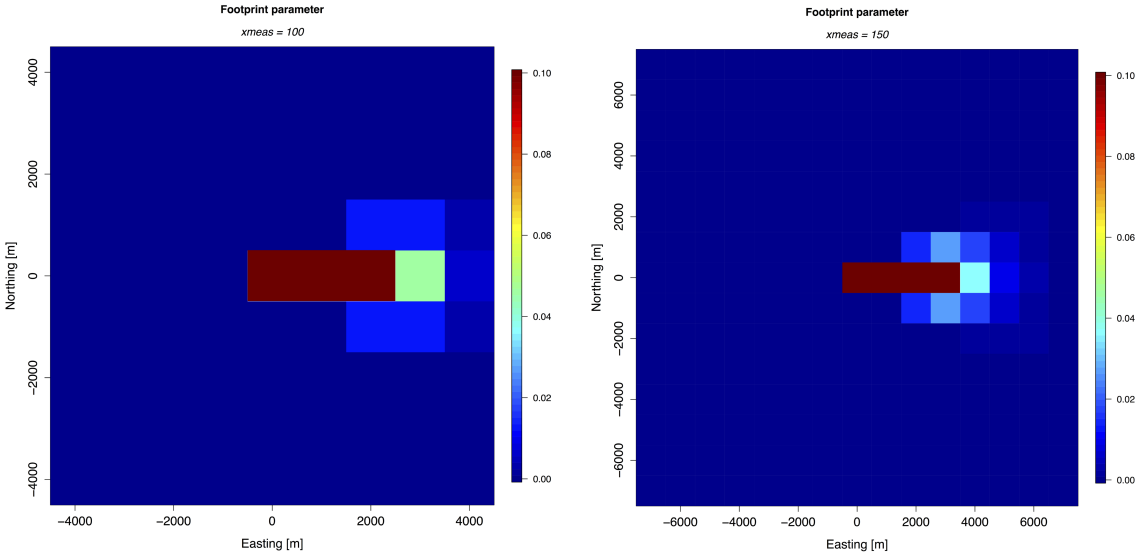

Figure A.18: Footprint weighting matrix at set Z_M of 100 and 150 m. All other footprint parameters set constant.

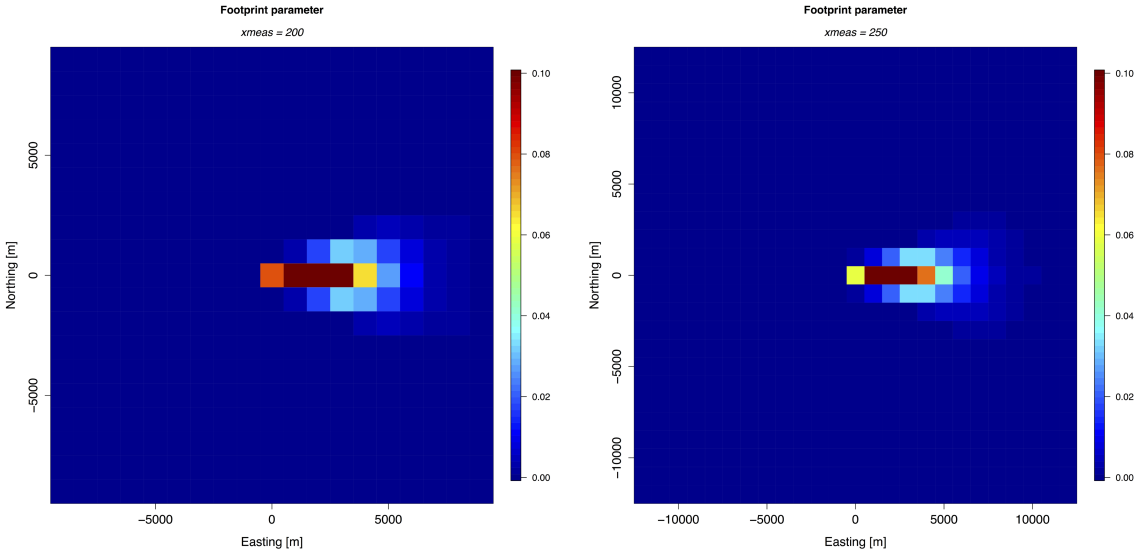

Figure A.19: Footprint weighting matrix at set Z_M of 200 and 250 m. All other footprint parameters set constant.

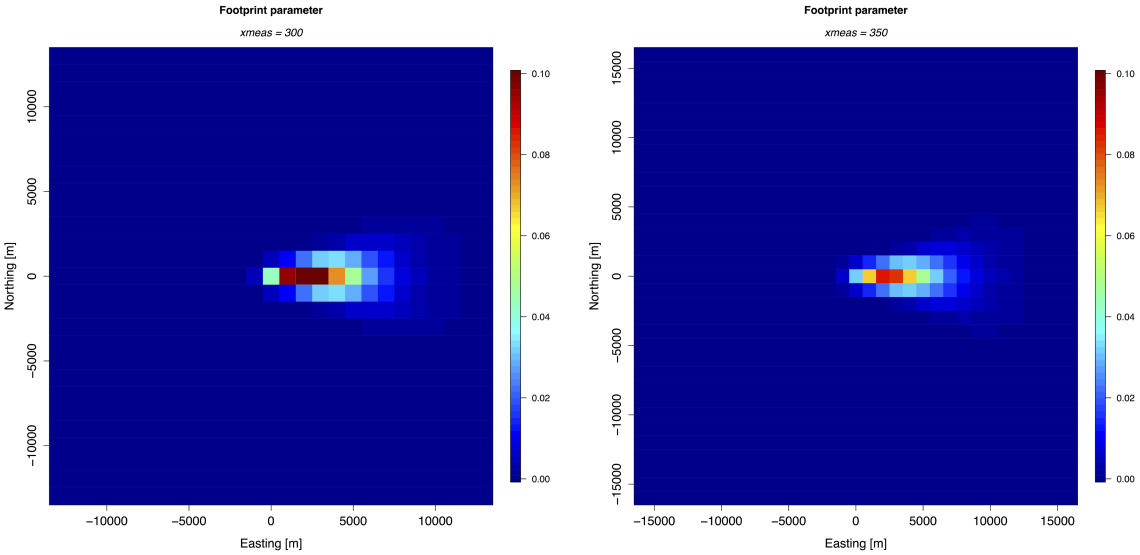

Figure A.20: Footprint weighting matrix at set Z_M of 300 and 350 m. All other footprint parameters set constant.

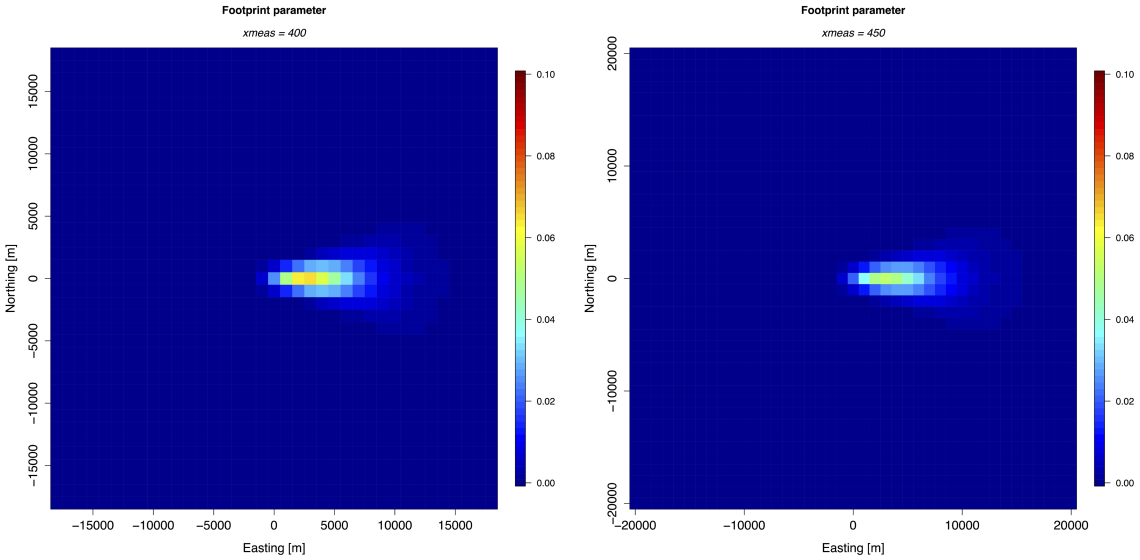

Figure A.21: Footprint weighting matrix at set Z_M of 400 and 450 m. All other footprint parameters set constant.

Appendix B

Continuous Wavelet Transform Cross−Spectrums

Shown here an examples of calculated CWT Cross−Spectrums for NO_x and VOC fluxes, as described in Chapters 4 and 5.

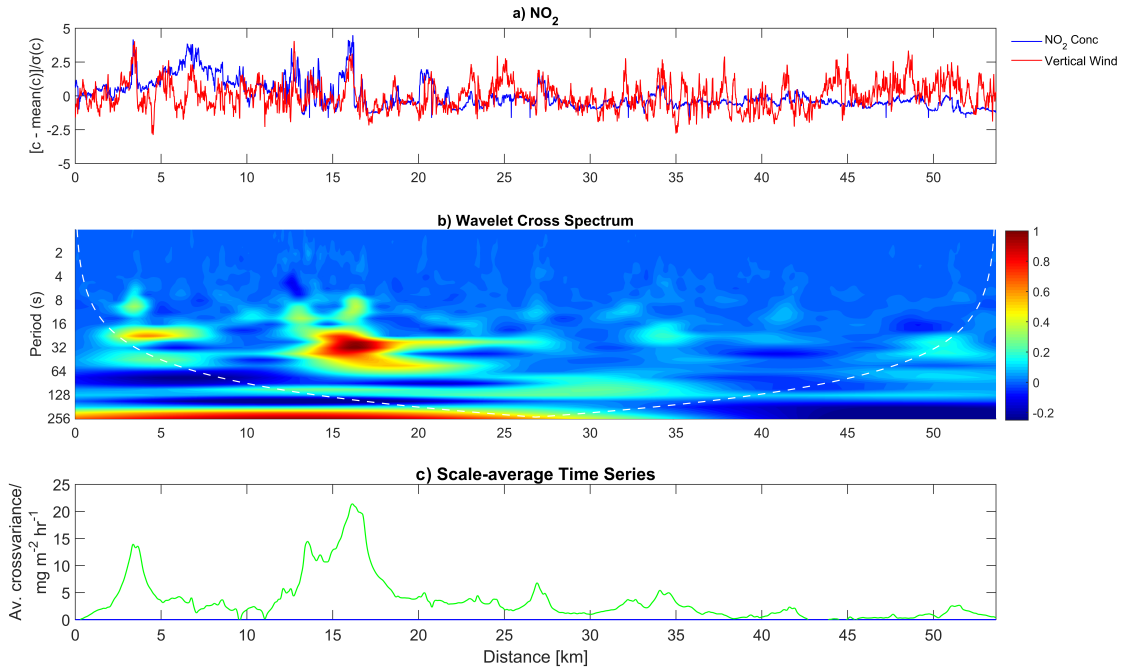

Figure B.1: (a) Variation of NO_2 concentration from the mean and variance of vertical wind speed from the mean, (b) time resolved wavelet cross spectrum, (c) the average cross−covariance between NO_2 concentration and vertical wind, for a typical NE to SW run across London.

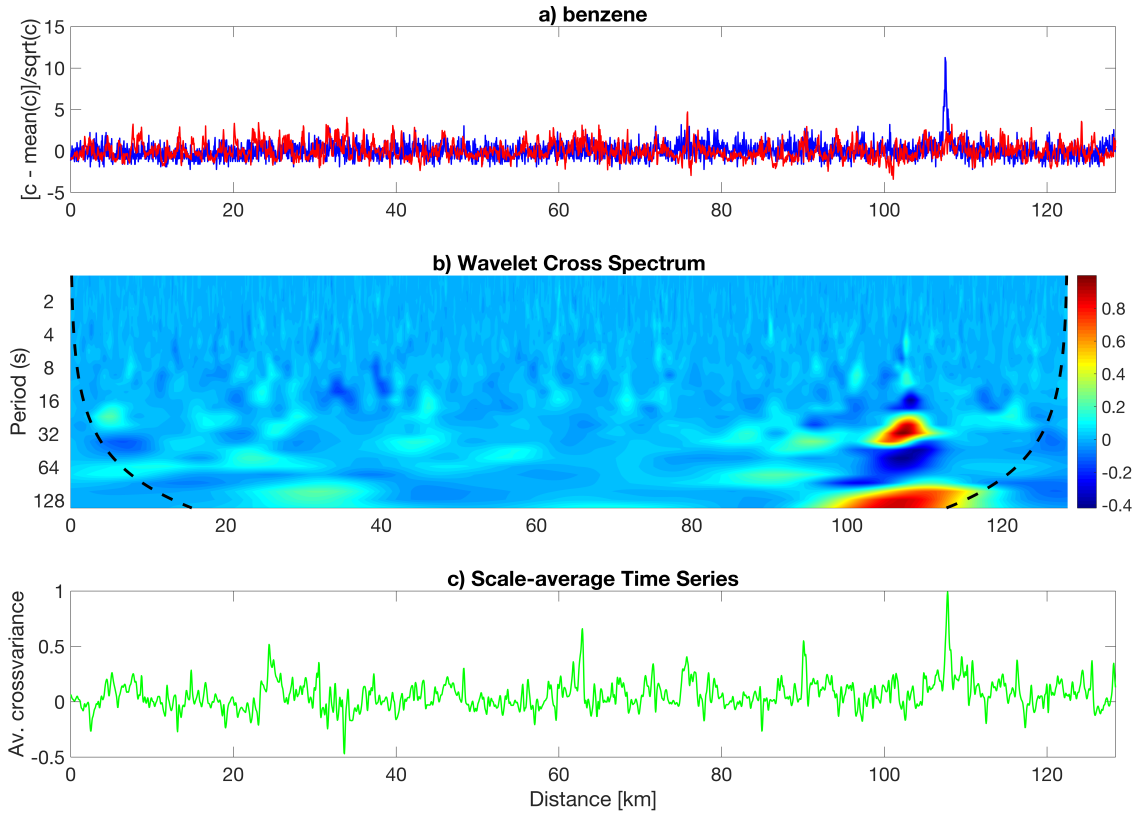

Figure B.2: (a) Variation of benzene concentration from the mean and variance of vertical wind speed from the mean, (b) time resolved wavelet cross spectrum, (c) the average cross−covariance between benzene concentration and vertical wind, for a typical NE to SW run across London.

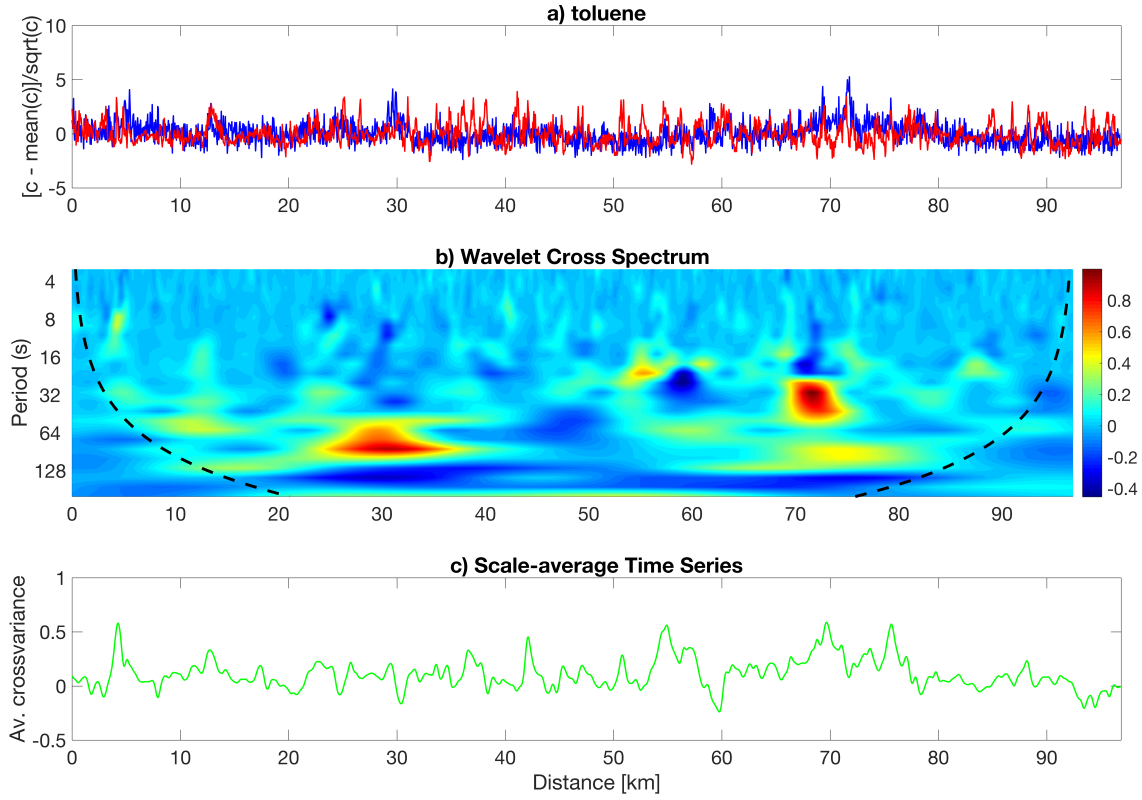

Figure B.3: (a) Variation of toluene concentration from the mean and variance of vertical wind speed from the mean, (b) time resolved wavelet cross spectrum, (c) the average cross−covariance between toluene concentration mixing ratio and vertical wind, for a typical NE to SW run across London.

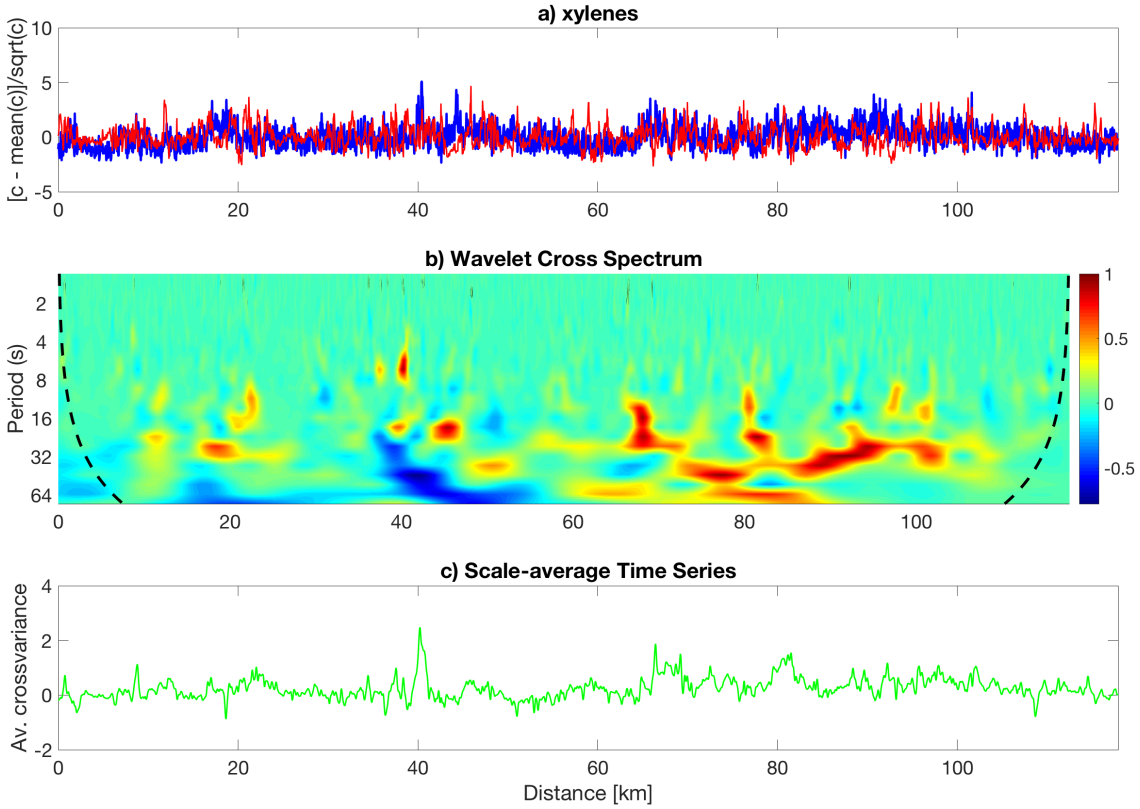

Figure B.4: (a) Variation of C_2 alkyl−benzenes concentration from the mean and variance of vertical wind speed from the mean, (b) time resolved wavelet cross spectrum, (c) the average cross−covariance between C_2 alkyl−benzenes concentration and vertical wind, for a typical NE to SW run across London.

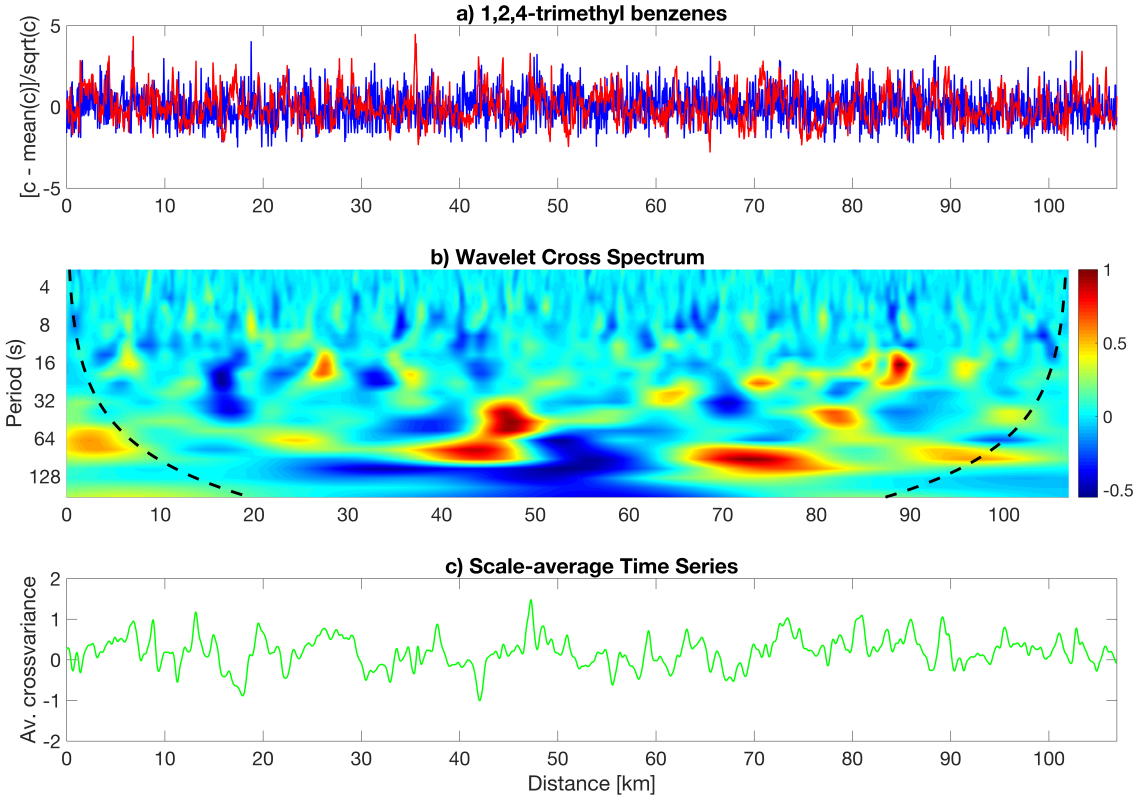

Figure B.5: (a) Variation of C_3 alkyl−benzenes concentration from the mean and variance of vertical wind speed from the mean, (b) time resolved wavelet cross spectrum, (c) the average cross−covariance between C_3 alkyl−benzenes concentration and vertical wind, for a typical NE to SW run across London.

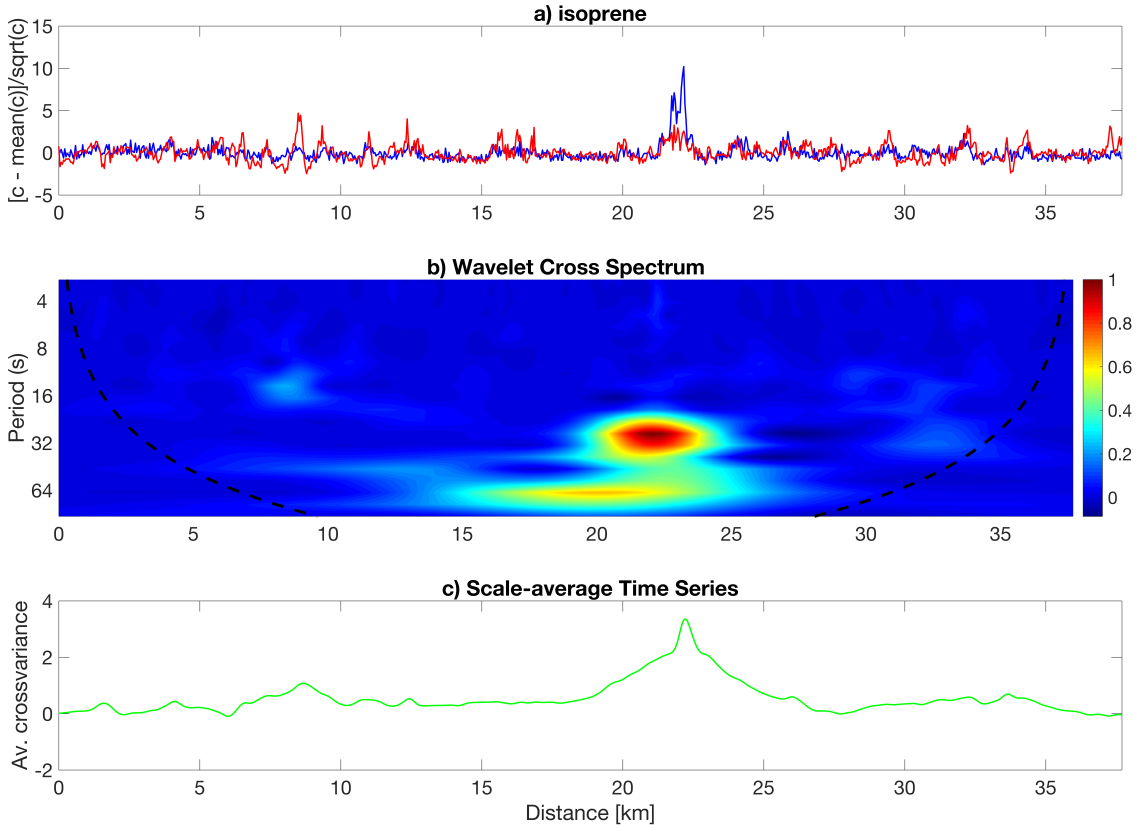

Figure B.6: (a) Variation of isoprene concentration from the mean and variance of vertical wind speed from the mean, (b) time resolved wavelet cross spectrum, (c) the average cross−covariance between isoprene concentration and vertical wind, for a typical run across Southern England.

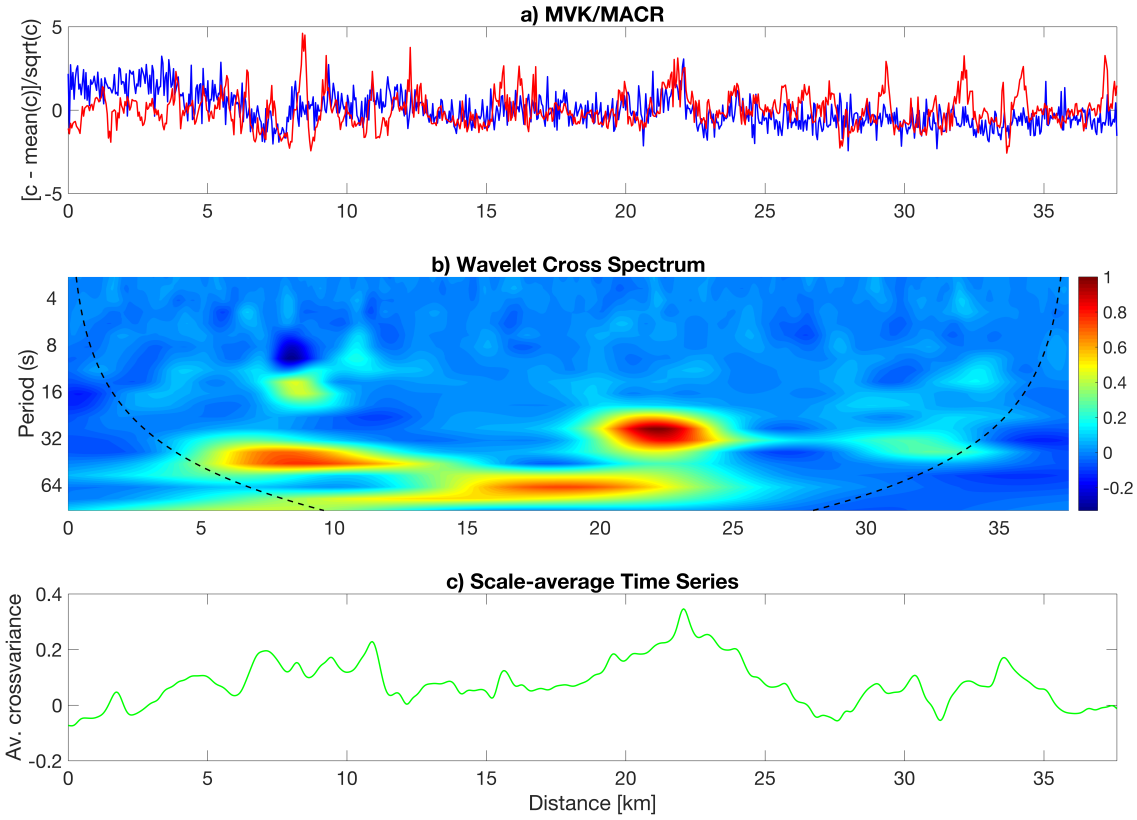

Figure B.7: (a) Variation of MVK/MACR concentration from the mean and variance of vertical wind speed from the mean, (b) time resolved wavelet cross spectrum, (c) the average cross−covariance between MVK/MACR concentration and vertical wind, for a typical run across Southern England.

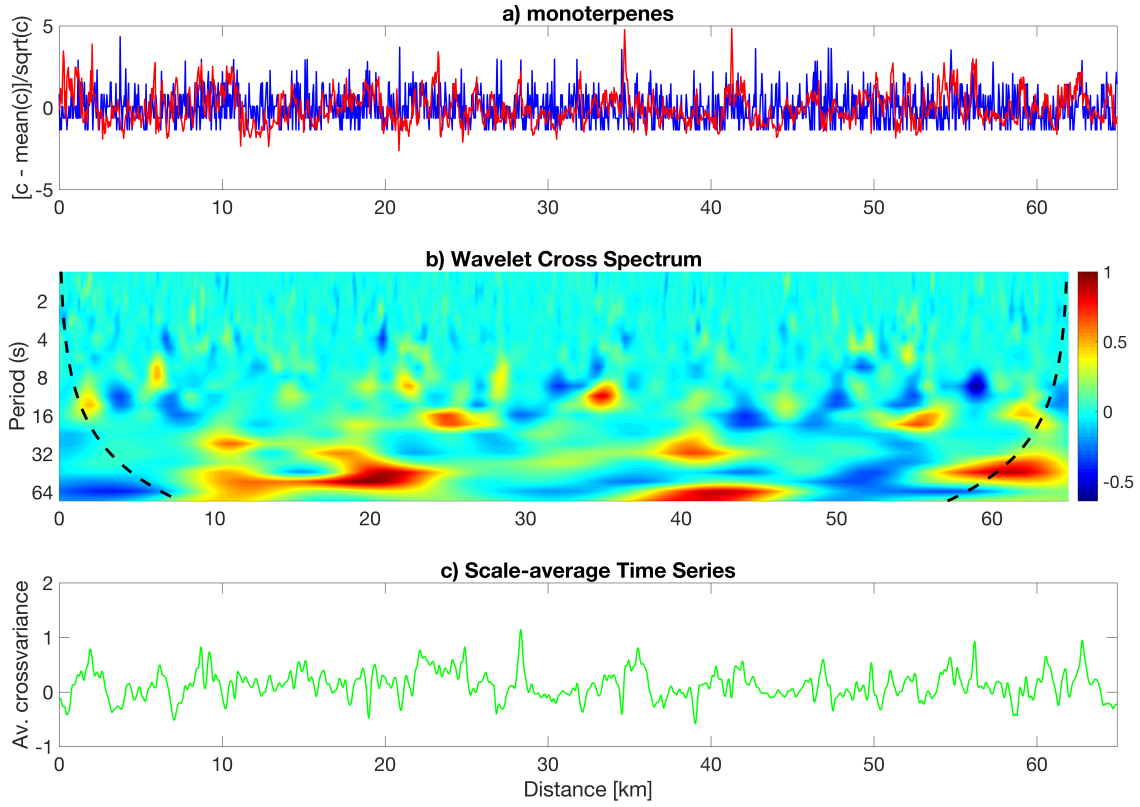

Figure B.8: (a) Variation of monoterpenes concentration from the mean and variance of vertical wind speed from the mean, (b) time resolved wavelet cross spectrum, (c) the average cross−covariance between monoterpenes concentration and vertical wind, for a typical run across Southern England.

Appendix C

Continuous Wavelet Transform Co and Cumulative Co-Spectra

Shown here an examples of calculated CWT Co and cumulative Co−Spectra for NO_x and VOC fluxes, as described in Chapters 4 and 5.

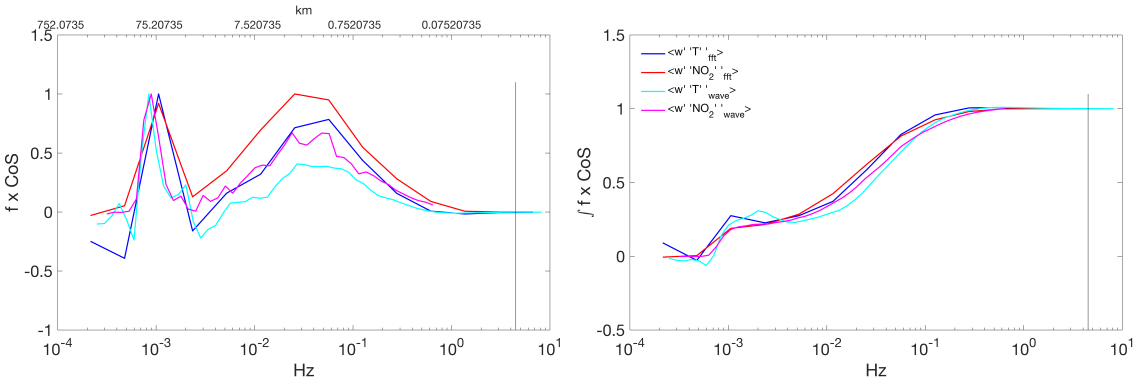

Figure C.1: left) co−spectra of NO_2 and temperature flux using CWT and FFT methods. Right) cumulative co−spectra for NO_2 and temperature flux using CWT and FFT methods.

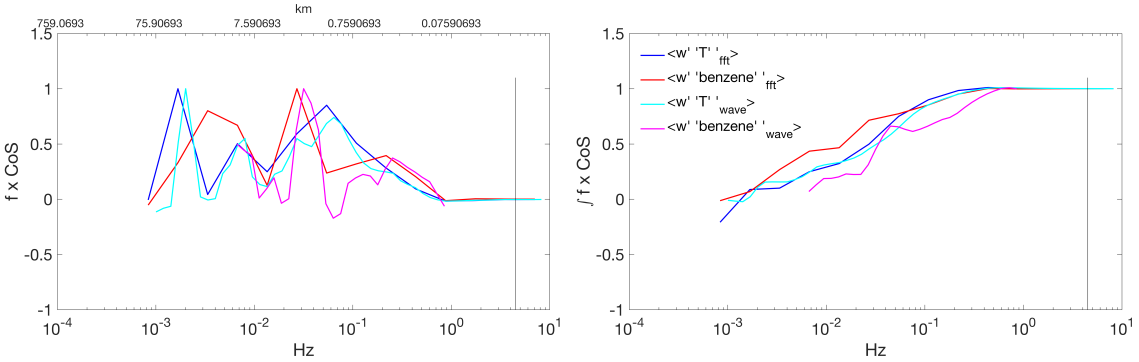

Figure C.2: left) co−spectra of benzene and temperature flux using CWT and FFT methods. Right) cumulative co−spectra for benzene and temperature flux using CWT and FFT methods.

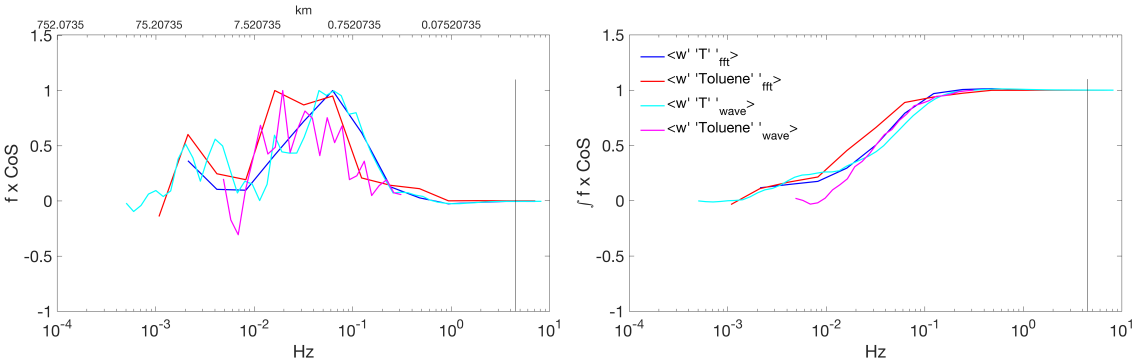

Figure C.3: left) co−spectra of toluene and temperature flux using CWT and FFT methods. Right) cumulative co−spectra for toluene and temperature flux using CWT and FFT methods.

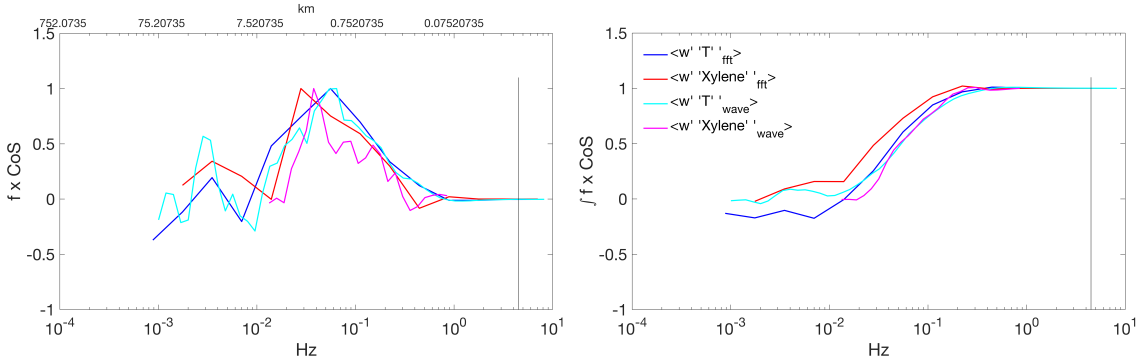

Figure C.4: left) co−spectra of C_2 alkyl-benzenes and temperature flux using CWT and FFT methods. Right) cumulative co−spectra for C_2 alkyl-benzenes and temperature flux using CWT and FFT methods.

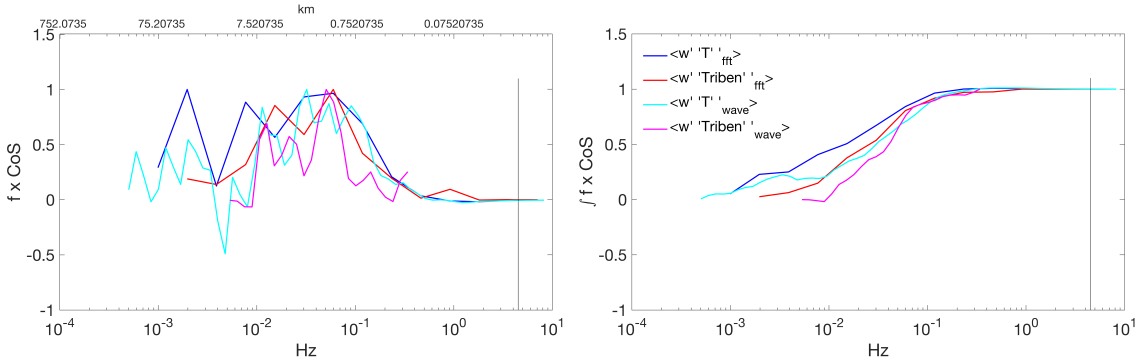

Figure C.5: left) co−spectra of C_3 alkyl-benzenes and temperature flux using CWT and FFT methods. Right) cumulative co−spectra for C_3 alkyl-benzenes and temperature flux using CWT and FFT methods.

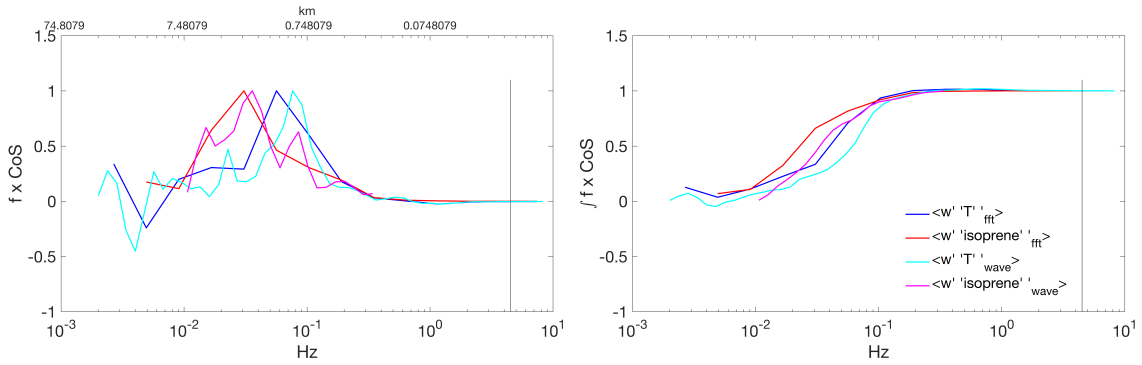

Figure C.6: left) co−spectra of isoprene and temperature flux using CWT and FFT methods. Right) cumulative co−spectra for isoprene and temperature flux using CWT and FFT methods.

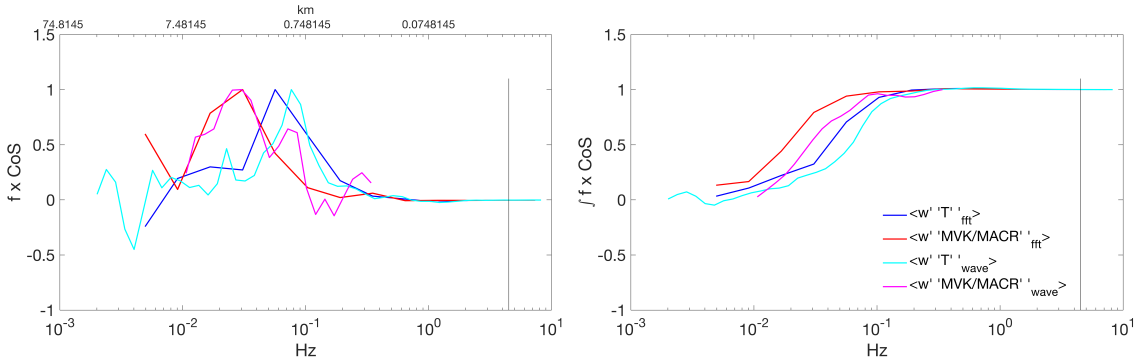

Figure C.7: left) co−spectra of MVK/MACR and temperature flux using CWT and FFT methods. Right) cumulative co−spectra for MVK/MACR and temperature flux using CWT and FFT methods.

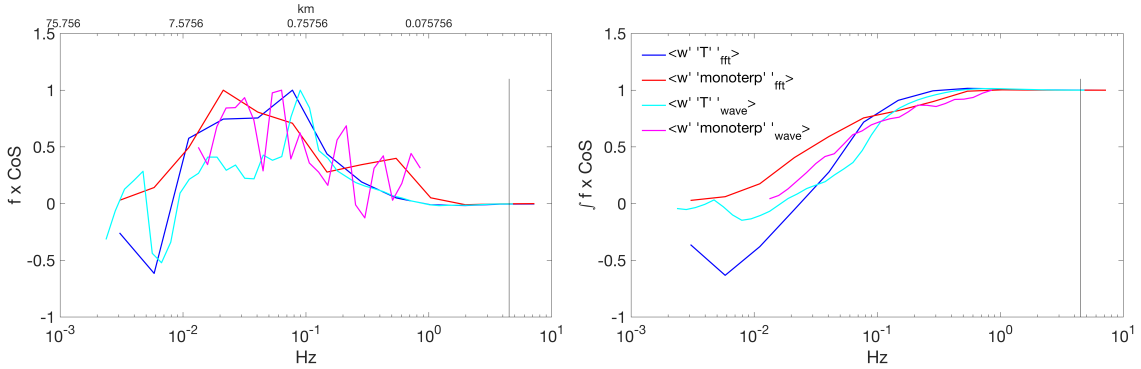

Figure C.8: left) co−spectra of monoterpenes and temperature flux using CWT and FFT methods. Right) cumulative co−spectra for monoterpenes and temperature flux using CWT and FFT methods.

Abbreviations

$\mathbf{a}_j$	Continuous Wavelet Transform frequency domain scales
AIMMS−20	Aircraft−Integrated Meteorological Measurement System
AQD	Air Quality Design Inc.
$\mathbf{b}_n$	Continuous Wavelet Transform time domain scales
blue−light PLC	Blue−Light Photolytic Converter
BOC	British Oxygen Company
$BrONO_2$	bromine nitrate
c'	Instantaneous deviations of concentration from its mean
CD	Corona Discharge
CE	Conversion Efficiency of blue−light PLC
$CH1_{nom}$	Channel 1 nominal sensitivity
$CH2_{nom}$	Channel 2 nominal sensitivity
CL	Chemiluminescence
CO	carbon monoxide
CO_2	carbon dioxide
COI	Cone of Influence
CWT	Continuous Wavelet Transform

de	Disjunct Error
DEFRA	Department of Environmental, Food and Rural Affairs
EC	Eddy−Covariance
EEA	European Economic Area
EMEP	European Monitoring and Evaluation Programme
EMEP4UK	European Monitoring and Evaluation Programme model (EMEP MScW) for the United Kingdom
Fast−AQD−NO_x	Fast NO_x Chemiluminescence Instrument
FC	Flow−Controllers
FFT	Fast Fourier Transform
HONO	nitrous acid
IDW	Inverse Distance Weighting
k	von Karmon Constant
L	Obukhov length
LAEI	London Atmospheric Emissions Inventory
LEDs	Light Emitting Diodes
LEZ	Low Emission Zone
LoD	Limit of Detection
MACR	methacrolein
MFC	Mass−Flow Controllers
MTBE	methyl tert−butyl ether
MVK	methyl vinyl ketone
NAEI	National Atmospheric Emissions Inventory
NERC	Natural Environment Research Council

NMHCs	non-methane hydrocarbons
N_2	nitrogen
NO	nitrogen monoxide
NO_2	nitrogen dioxide
NPL	UK National Physical Laboratory
NRMM	Non-Road Mobile Machinery
O_3	ozone
O_3−CLD	Ozone Chemiluminescence Detection
OPFUE	Ozone Precursor Fluxes in Urban Environments
p	Continuous Wavelet Transform normalisation factor
PC	Pressure−Controller
P_d	Density of Air
PLC	Photolytic Converter
PLC−O_3−CLD	Photolytic Ozone Chemiluminescence Detection
PM	Particulate Matter
$PM_{2.5}$	Particulate Matter sized $\leq$2.5 micrometers
PM_{10}	Particulate Matter sized $\leq$10 micrometers
PMT	Photomultiplier Tube
PTR−MS	Proton−Transfer−Reaction Mass−Spectrometry
re	Random Error
RF	Research Flight
RSD	Remote Sensing Detector
RV	Reaction−Vessel
se	Systematic Error

u*	Friction Velocity
UK	United Kingdom
UV	Ultra−Violet light
VOC	Volatile Organic Carbon
w'	Instantaneous deviations of vertical wind from its mean
$\mathbf{Z}_0$	Aerodynamic Roughness Length
$\mathbf{Z}_i$	Planetary Boundary Layer
$\mathbf{Z}_m$	Measurement Height
$\mathbf{Z}_V$	Zero−Volume

References

[1] BBC. How bad is air pollution in the UK?, 2017. URL http://www.bbc.co.uk/news/science-environment-38979754.

[2] BBC. Beijing: The city where you can't escape smog, 2017. URL http://www.bbc.co.uk/news/magazine-38587580.

[3] Sky UK. Pollution study: Tens of thousands of children breathing in toxic air, 2017. URL http://news.sky.com/story/pollution-study-tens-of-thousands-of-children-breathing-in-toxic-air-10780834.

[4] Guardian News and Media Limited. Traffic pollution must be fixed: our children's lungs demand it, 2017. URL https://www.theguardian.com/commentisfree/2017/mar/03/children-lungs-air-pollution-diesel.

[5] World Health Organization. The cost of a polluted environment: 1.7 million child deaths a year, says WHO, 2017. URL http://www.who.int/mediacentre/news/releases/2017/pollution-child-death/en/.

[6] J.H. Seinfeld and S.N. Pandis. Atmospheric chemistry and physics: from air pollution to climate change. 2006. ISSN 0471720178.

[7] G. Tang, P. Zhao, Y. Wang, W. Gao, M. Cheng, J. Xin, X. Li, and Y. Wang. Mortality and air pollution in Beijing: The long-term relationship. *Atmospheric Environment*, 150:238–243, 2017. ISSN 1352-2310.

[8] Royal College of Physicians. Every breath we take: the lifelong impact of air pollution. Report of a working party. Technical report, London, 2016.

[9] M.L. Bell and D.L. Davis. Reassessment of the lethal London fog of 1952: novel indicators of acute and chronic consequences of acute exposure to air pollution. *Environmental health perspectives*, 109(Suppl 3):389, 2001.

[10] P. Brimblecombe. The clean air act after 50 years. *Weather*, 61(11):311–314, 2006. ISSN 1477-8696.

[11] V.M. Thomas. The elimination of lead in gasoline. *Annual Review of Energy and the Environment*, 20(1):301–324, 1995. ISSN 1056-3466.

[12] U. Strömberg, A. Schütz, and S. Skerfving. Substantial decrease of blood lead in Swedish children, 1978-94, associated with petrol lead. *Occupational and environmental medicine*, 52(11):764–769, 1995. ISSN 1470-7926.

[13] P.J. Landrigan. The worldwide problem of lead in petrol. *Bulletin of the World Health Organization*, 80(10):768, 2002. ISSN 0042-9686.

[14] W.M. Foster, R.H. Brown, K. Macri, and C.S. Mitchell. Bronchial reactivity of healthy subjects: 1820 h postexposure to ozone. *Journal of Applied Physiology*, 89 (5):1804–1810, 2000. ISSN 8750-7587.

[15] S.M. Oh, H.R. Kim, Y.J. Park, S.Y. Lee, and K.H. Chung. Organic extracts of urban air pollution particulate matter (PM2.5)-induced genotoxicity and oxidative stress in human lung bronchial epithelial cells (BEAS-2B cells). *Mutation Research/Genetic Toxicology and Environmental Mutagenesis*, 723(2):142–151, 2011. ISSN 1383-5718.

[16] G.R.S. Budinger, J.L. McKell, D. Urich, N. Foiles, I. Weiss, S.E. Chiarella, A. Gonzalez, S. Soberanes, A.J. Ghio, and R. Nigdelioglu. Particulate matter-induced lung inflammation increases systemic levels of PAI-1 and activates coagulation through distinct mechanisms. *PloS one*, 6(4):e18525, 2011. ISSN 1932-6203.

[17] W.J. Gauderman, E. Avol, F. Gilliland, H. Vora, D. Thomas, K. Berhane, R. McConnell, N. Kuenzli, F. Lurmann, and E. Rappaport. The effect of air pollution on lung development from 10 to 18 years of age. *New England Journal of Medicine*, 351(11):1057–1067, 2004. ISSN 0028-4793.

[18] T. Götschi, J. Heinrich, J. Sunyer, and N. Künzli. Long-term effects of ambient air pollution on lung function: a review. *Epidemiology*, 19(5):690–701, 2008. ISSN 1044-3983.

[19] C. Chang, S. Tsai, S. Ho, and C. Yang. Air pollution and hospital admissions for cardiovascular disease in Taipei, Taiwan. *Environmental Research*, 98(1):114–119, 2005. ISSN 0013-9351.

[20] T.W. Wong, W.S. Tam, T.S. Yu, and A.H.S. Wong. Associations between daily mortalities from respiratory and cardiovascular diseases and air pollution in Hong Kong, China. *Occupational and environmental medicine*, 59(1):30–35, 2002. ISSN 1470-7926.

[21] T.E. O'toole, Y. Zheng, J. Hellmann, D.J. Conklin, O. Barski, and A. Bhatnagar. Acrolein activates matrix metalloproteinases by increasing reactive oxygen species in macrophages. *Toxicology and applied pharmacology*, 236(2):194–201, 2009. ISSN 0041-008X.

[22] J.C. Uzoigwe, T. Prum, E. Bresnahan, and M. Garelnabi. The emerging role of outdoor and indoor air pollution in cardiovascular disease. *North American journal of medical sciences*, 5(8):445, 2013. ISSN 1947-2714.

[23] T.W. Wong, T.S. Lau, T.S. Yu, A. Neller, S.L. Wong, W. Tam, and S.W. Pang. Air pollution and hospital admissions for respiratory and cardiovascular diseases in Hong Kong. *Occupational and environmental medicine*, 56(10):679–683, 1999. ISSN 1470-7926.

[24] L. Yu, G. Wang, R. Zhang, L. Zhang, Y. Song, B. Wu, X. Li, K. An, and J. Chu. Characterization and source apportionment of PM2.5 in an urban environment in Beijing. *Aerosol and air quality research*, 13(2):574–583, 2013.

[25] United States Environmental Protection Agency. Particulate Matter (PM) Basics, 2016. URL `https://www.epa.gov/pm-pollution/particulate-matter-pm-basics`.

[26] COMEAP UK. Long-term exposure to air pollution: effect on mortality. *Committee on the Medical Effects of Air Pollutants (COMEAP), UK Health Protection Agency, London, UK*, 2009.

[27] EC Directive. Council Directive 2008/50/EC on ambient air quality and cleaner air for Europe. *Official Journal of the European Communities, L*, 151:1–44, 2008.

[28] The Air Quality Expert Group. Fine Particulate Matter (PM2.5) in the United Kingdom. Technical report, 2012.

[29] DEFRA. The Air Quality Strategy for England, Scotland, Wales and Northern Ireland. Technical report, 2007. URL `https://www.gov.uk/government/`

publications/the-air-quality-strategy-for-england-scotland-wales-and-northern-ireland-volume-1.

[30] DEFRA. 2010 to 2015 government policy: environmental quality. Technical report, 2015.

[31] NAEI. NAEI UK Emissions Interactive Map, 2017. URL http://naei.defra.gov.uk/data/gis-mapping.

[32] DEFRA. Emissions of Air Quality Pollutants 1990-2014. Technical report, 2016.

[33] I. Tsagatakis, S. Brace, C. Jephcote, N. Passant, B. Pearson, B. Kiff, and A. Fraser. UK Emission Mapping Methodology 2014. Technical report, 2016.

[34] X. Tie, R. Zhang, G. Brasseur, and W. Lei. Global NOx production by lightning. *Journal of Atmospheric Chemistry*, 43(1):61–74, 2002. ISSN 0167-7764.

[35] K. Miyazaki, H.J. Eskes, K. Sudo, and C. Zhang. Global lightning NOx production estimated by an assimilation of multiple satellite data sets. *Atmospheric Chemistry and Physics*, 14(7):3277–3305, 2014. ISSN 1680-7316.

[36] R. Conrad. Soil microorganisms as controllers of atmospheric trace gases (H2, CO, CH4, OCS, N2O, and NO). *Microbiological reviews*, 60(4):609–640, 1996. ISSN 1092-2172.

[37] G.C.M. Vinken, K.F. Boersma, J.D. Maasakkers, M. Adon, and R.V. Martin. Worldwide biogenic soil NOx emissions inferred from OMI NO2 observations. *Atmospheric Chemistry and Physics*, 14(18):10363–10381, 2014. ISSN 1680-7316.

[38] K.L. Denman, G.P. Brasseur, A. Chidthaisong, P. Ciais, P.M. Cox, R.E. Dickinson, D.A. Hauglustaine, C. Heinze, E.A. Holland, and D.J. Jacob. Couplings between changes in the climate system and biogeochemistry. In *Climate change 2007: The physical science basis*. Cambridge University Press, 2007.

[39] P. Schneider, W.A. Lahoz, and R. van der A. Recent satellite-based trends of tropospheric nitrogen dioxide over large urban agglomerations worldwide. *Atmospheric Chemistry and Physics*, 15(3):1205–1220, 2015. ISSN 1680-7316.

[40] European Environment Agency. Nitrogen oxides (NOx) emissions. Technical report, 2010. URL http://www.eea.europa.eu/data-and-maps/indicators/eea-32-nitrogen-oxides-nox-emissions-1/assessment.2010-08-19.0140149032-3.

[41] D. Carslaw, S. Beevers, E. Westmoreland, M. Williams, J. Tate, T. Murrells, J. Stedman, Y. Li, S. Grice, and A. Kent. Trends in NOx and NO2 emissions and ambient measurements in the UK. *Defra, London*, 2011.

[42] D.C. Carslaw. Evidence of an increasing NO2/NOX emissions ratio from road traffic emissions. *Atmospheric Environment*, 39(26):4793–4802, 2005. doi: 10.1016/j.atmosenv.2005.06.023.

[43] D.C. Carslaw, T.P. Murrells, J. Andersson, and M. Keenan. Have vehicle emissions of primary NO2 peaked? *Faraday discussions*, 189:439–454, 2016. ISSN 1364-5498.

[44] ERG King's College London. London Atmospheric Emissions Inventory, 2016. URL https://www.londonair.org.uk/london/asp/annualmaps.asp.

[45] D.C. Carslaw, S.D. Beevers, J.E. Tate, E.J. Westmoreland, and M.L. Williams. Recent evidence concerning higher NOx emissions from passenger cars and light duty vehicles. *Atmospheric Environment*, 45(39):7053–7063, 2011. doi: 10.1016/j.atmosenv.2011.09.063.

[46] N.A. Chigier. *Energy and Combustion Science*. Pergamon international library of science, technology, engineering, and social studies. Elsevier Science, 2013. ISBN 9781483182247. URL https://books.google.co.uk/books?id=7Lu2AgAAQBAJ.

[47] R.J. Farrauto and R.M. Heck. Catalytic converters: state of the art and perspectives. *Catalysis Today*, 51(3):351–360, 1999. ISSN 0920-5861.

[48] S. Grice, J. Stedman, A. Kent, M. Hobson, J. Norris, J. Abbott, and S. Cooke. Recent trends and projections of primary NO2 emissions in Europe. *Atmospheric Environment*, 43(13):2154–2167, 2009. ISSN 1352-2310.

[49] J.A. Sullivan and O. Keane. A combination of NOx trapping materials and urea-SCR catalysts for use in the removal of NOx from mobile diesel engines. *Applied Catalysis B: Environmental*, 70(1):205–214, 2007. ISSN 0926-3373.

[50] T. Johnson. Diesel engine emissions and their control. *Platinum Metals Review*, 52 (1):23–37, 2008. ISSN 0032-1400.

[51] W.S. Epling, L.E. Campbell, A. Yezerets, N.W. Currier, and J.E. Parks. Overview of the fundamental reactions and degradation mechanisms of NOx storage/reduction catalysts. *Catalysis Reviews*, 46(2):163–245, 2004. ISSN 0161-4940.

[52] J. Valentine. EPA, California notify Volkswagen of clean air act violations/carmaker allegedly used software that circumvents emissions testing for certain air pollutants, 2015. URL `http://yosemite.epa.gov/opa/admpress.nsf/bd4379a92ceceeac8525735900400c27/dfc8e33b5ab162b985257ec40057813b!OpenDocument`.

[53] Environmental Protection Agency. Volkswagen Clean Air Act Civil Settlement, 2017. URL `https://www.epa.gov/enforcement/volkswagen-clean-air-act-civil-settlement`.

[54] Guardian News and Media Limited. Volkswagen under investigation over illegal software that masks emissions, 2015. URL `https://www.theguardian.com/business/2015/sep/18/epa-california-investigate-volkswagen-clean-air-violations`.

[55] BBC. VW emissions scandal hits 11m vehicles, 2015. URL `http://www.bbc.co.uk/news/business-34325005`.

[56] House of Commons Transport Committee. Volkswagen emissions scandal and vehicle type approval, Third Report of Session 201617. Technical report, 2016. URL `https://www.publications.parliament.uk/pa/cm201617/cmselect/cmtrans/69/69.pdf`.

[57] L.J. Carpenter, K.C. Clemitshaw, R.A. Burgess, S.A. Penkett, J.N. Cape, and G.G. McFadyen. Investigation and evaluation of the NOx/O3 photochemical steady state. *Atmospheric Environment*, 32(19):3353–3365, 1998. ISSN 1352-2310.

[58] R. Atkinson. Atmospheric chemistry of VOCs and NOx. *Atmospheric environment*, 34(12):2063–2101, 2000. ISSN 1352-2310.

[59] MCMv3.3.1. URL `http://mcm.leeds.ac.uk/MCM`.

[60] S.S. Brown and J. Stutz. Nighttime radical observations and chemistry. *Chemical Society Reviews*, 41(19):6405–6447, 2012.

[61] A.K. Benton, J.M. Langridge, S.M. Ball, W.J. Bloss, M. Dall'Osto, E. Nemitz, R.M. Harrison, and R.L. Jones. Night-time chemistry above London: measurements of NO3 and N2O5 from the BT Tower. *Atmospheric Chemistry and Physics*, 10(20): 9781, 2010. ISSN 1680-7324.

[62] J. Matsumoto, K. Imagawa, H. Imai, N. Kosugi, M. Ideguchi, S. Kato, and Y. Kajii. Nocturnal sink of NOx via NO 3 and N 2 O 5 in the outflow from a source area in Japan. *Atmospheric Environment*, 40(33):6294–6302, 2006. ISSN 1352-2310.

[63] S.R. Aliwell and R.L. Jones. Measurements of tropospheric NO3 at midlatitude. *Journal of Geophysical Research: Atmospheres*, 103(D5):5719–5727, 1998. ISSN 2156-2202.

[64] A. Wahner, T.F. Mentel, and M. Sohn. Gasphase reaction of N2O5 with water vapor: Importance of heterogeneous hydrolysis of N2O5 and surface desorption of HNO3 in a large Teflon chamber. *Geophysical Research Letters*, 25(12):2169–2172, 1998. ISSN 1944-8007.

[65] N.L. Wagner, T.P. Riedel, C.J. Young, R. Bahreini, C.A. Brock, W.P. Dubé, S. Kim, A.M. Middlebrook, F. Öztürk, and J.M. Roberts. N2O5 uptake coefficients and nocturnal NO2 removal rates determined from ambient wintertime measurements. *Journal of Geophysical Research: Atmospheres*, 118(16):9331–9350, 2013. ISSN 2169-8996.

[66] D.J. Jacob. Heterogeneous chemistry and tropospheric ozone. *Atmospheric Environment*, 34(12):2131–2159, 2000. ISSN 1352-2310.

[67] C.L. Badger, P.T. Griffiths, I. George, J.P.D. Abbatt, and R.A. Cox. Reactive uptake of N2O5 by aerosol particles containing mixtures of humic acid and ammonium sulfate. *The Journal of Physical Chemistry A*, 110(21):6986–6994, 2006. ISSN 1089-5639.

[68] J.D. Lee, L.K. Whalley, D.E. Heard, D. Stone, R.E. Dunmore, J.F. Hamilton, D.E. Young, J.D. Allan, S. Laufs, and J. Kleffmann. Detailed budget analysis of HONO in central London reveals a missing daytime source. *Atmospheric Chemistry and Physics*, 16(5):2747–2764, 2016. ISSN 1680-7316.

[69] G.J. Phillips, N. Pouvesle, J. Thieser, G. Schuster, R. Axinte, H. Fischer, J. Williams, J. Lelieveld, and J.N. Crowley. Peroxyacetyl nitrate (PAN) and peroxyacetic acid (PAA) measurements by iodide chemical ionisation mass spectrometry: first analysis of results in the boreal forest and implications for the measurement of PAN fluxes. *Atmospheric Chemistry and Physics*, 13(3):1129–1139, 2013. ISSN 1680-7316.

[70] Karim Movassaghi, Mario Vincenzo Russo, and Pasquale Avino. The determination and role of peroxyacetil nitrate in photochemical processes in atmosphere. *Chemistry Central Journal*, 6(S2):S8, 2012. ISSN 1752-153X.

[71] S. Penkett, S. Gilge, C. Plass-Duelmer, I. Galbally, N. Brough, J.W. Bottenheim, F.M. Flocke, H. Gerwig, J.D. Lee, and M. Milton. WMO/GAW Expert Workshop on Global Long-term Measurements of Nitrogen Oxides and Recommendations for GAW Nitrogen Oxides Network. *WMO, Geneva*, (WMO/TD-No. 1570), 2011.

[72] D. Krochmal and L. Gorski. Determination of nitrogen dioxide in ambient air by use of a passive sampling technique and triethanolamine as absorbent. *Environmental science & technology*, 25(3):531–535, 1991. ISSN 0013-936X.

[73] D. Krochmal and A. Kalina. A method of nitrogen dioxide and sulphur dioxide determination in ambient air by use of passive samplers and ion chromatography. *Atmospheric Environment*, 31(20):3473–3479, 1997. ISSN 1352-2310.

[74] H. Plaisance, I. Sagnier, J.Y. Saison, J.C. Galloo, and R. Guillermo. Performances and application of a passive sampling method for the simultaneous determination of nitrogen dioxide and sulfur dioxide in ambient air. *Environmental monitoring and assessment*, 79(3):301–315, 2002. ISSN 0167-6369.

[75] G.J.M. Velders, C. Granier, R.W. Portmann, K. Pfeilsticker, M. Wenig, T. Wagner, U. Platt, A. Richter, and J.P. Burrows. Global tropospheric NO2 column distributions: Comparing threedimensional model calculations with GOME measurements. *Journal of Geophysical Research: Atmospheres*, 106(D12):12643–12660, 2001. ISSN 2156-2202.

[76] A. Richter, J.P. Burrows, H. Nüß, C. Granier, and U. Niemeier. Increase in tropospheric nitrogen dioxide over China observed from space. *Nature*, 437(7055):129–132, 2005. ISSN 0028-0836.

[77] I. Ortega, T. Koenig, R. Sinreich, D. Thomson, and R. Volkamer. The CU 2-D-MAX-DOAS instrumentPart 1: Retrieval of 3-D distributions of NO2 and azimuth-dependent OVOC ratios. *Atmospheric Measurement Techniques*, 8(6):2371–2395, 2015. ISSN 1867-1381.

[78] F. Wittrock, H. Oetjen, A. Richter, S. Fietkau, T. Medeke, A. Rozanov, and J.P. Burrows. MAX-DOAS measurements of atmospheric trace gases in Ny-Ålesund-Radiative transfer studies and their application. *Atmospheric Chemistry and Physics*, 4(4):955–966, 2004. ISSN 1680-7316.

[79] R. Sinreich, U. Frieß, T. Wagner, and U. Platt. Multi axis differential optical absorption spectroscopy (MAX-DOAS) of gas and aerosol distributions. *Faraday discussions*, 130:153–164, 2005.

[80] B. Dix, T.K. Koenig, and R. Volkamer. Parameterization retrieval of trace gas volume mixing ratios from Airborne MAX-DOAS. *Atmospheric Measurement Techniques*, 9(11):5655, 2016. ISSN 1867-8548.

[81] H.D. Osthoff, S.S. Brown, T.B. Ryerson, T.J. Fortin, B.M. Lerner, E.J. Williams, A. Pettersson, T. Baynard, W.P. Dube, and S.J. Ciciora. Measurement of atmospheric NO2 by pulsed cavity ringdown spectroscopy. *Journal of Geophysical Research: Atmospheres*, 111(D12), 2006. ISSN 2156-2202.

[82] U. Platt, D. Perner, and H.W. Pätz. Simultaneous measurement of atmospheric CH2O, O3, and NO2 by differential optical absorption. *Journal of Geophysical Research: Oceans*, 84(C10):6329–6335, 1979. ISSN 2156-2202.

[83] A. Fried, R. Sams, W. Dorko, J.W. Elkins, and Z. Cai. Determination of nitrogen dioxide in air-compressed gas mixtures by quantitative tunable diode laser absorption spectrometry and chemiluminescence detection. *Analytical Chemistry*, 60(5): 394–403, 1988. ISSN 0003-2700.

[84] J. Matsumoto and Y. Kajii. Improved analyzer for nitrogen dioxide by laser-induced fluorescence technique. *Atmospheric Environment*, 37(34):4847–4851, 2003. ISSN 1352-2310.

[85] H. Fuchs, S.M. Ball, B. Bohn, T. Brauers, R.C. Cohen, H.P. Dorn, W.P. Dubé, J.L. Fry, R. Häseler, and U.M. Heitmann. Intercomparison of measurements of NO2 con-

centrations in the atmosphere simulation chamber SAPHIR during the NO3Comp campaign. 2010. ISSN 1867-1381.

[86] B.A. Ridley and F.E. Grahek. A small, low flow, high sensitivity reaction vessel for NO chemiluminescence detectors. *Journal of Atmospheric and Oceanic Technology*, 7(2):307–311, 1990. ISSN 1520-0426.

[87] D. Kley and M. McFarland. Chemiluminescence detector for NO and NO2. *Atmos. Technol.;(United States)*, 12, 1980.

[88] G. Villena, I. Bejan, R. Kurtenbach, P. Wiesen, and J. Kleffmann. Interferences of commercial NO2 instruments in the urban atmosphere and in a smog chamber. *Atmospheric Measurement Techniques*, 5(1):149, 2012. ISSN 1867-8548.

[89] E.J. Dunlea, S.C. Herndon, D.D. Nelson, R.M. Volkamer, F. San Martini, P.M. Sheehy, M.S. Zahniser, J.H. Shorter, J.C. Wormhoudt, and B.K. Lamb. Evaluation of nitrogen dioxide chemiluminescence monitors in a polluted urban environment. *Atmospheric Chemistry and Physics*, 7(10):2691–2704, 2007. ISSN 1680-7316.

[90] D.D. Parrish, C.H. Hahn, D.W. Fahey, E.J. Williams, M.J. Bollinger, G. Hübler, M.P. Buhr, P.C. Murphy, M. Trainer, and E.Y. Hsie. Systematic variations in the concentration of NOx (NO plus NO2) at Niwot Ridge, Colorado. *Journal of Geophysical Research: Atmospheres*, 95(D2):1817–1836, 1990. ISSN 2156-2202.

[91] Y. Sadanaga, Y. Fukumori, T. Kobashi, M. Nagata, N. Takenaka, and H. Bandow. Development of a selective light-emitting diode photolytic NO2 converter for continuously measuring NO2 in the atmosphere. *Analytical chemistry*, 82(22):9234–9239, 2010. ISSN 0003-2700.

[92] I.B. Pollack, B.M. Lerner, and T.B. Ryerson. Evaluation of ultraviolet light-emitting diodes for detection of atmospheric NO2 by photolysis - chemiluminescence. *Journal of Atmospheric Chemistry*, 65(2-3):111–125, 2010. doi: 10.1007/s10874-011-9184-3.

[93] C. Reed, M.J. Evans, P.D. Carlo, J.D. Lee, and L.J. Carpenter. Interferences in photolytic NO2 measurements: explanation for an apparent missing oxidant? *Atmospheric Chemistry and Physics*, 16(7):4707–4724, 2016. ISSN 1680-7316.

[94] P.D. Townsend. Photocathodespast performance and future potential. *Contemporary Physics*, 44(1):17–34, 2003. ISSN 0010-7514.

[95] R.T. Borlinghaus. From Light to Mind: Sensors and Measuring Techniques in Confocal Microscopy, 2015. URL `http://www.leica-microsystems.com/science-lab/from-light-to-mind-sensors-and-measuring-techniques-in-confocal-microscopy/`.

[96] H.H. Tan. A statistical model of the photomultiplier gain process with applications to optical pulse detection. In *International Telemetering Conference Proceedings*. International Foundation for Telemetering, 1982. ISBN 0884-5123.

[97] P. Boylan, D. Helmig, and J-H. Park. Characterization and mitigation of water vapor effects in the measurement of ozone by chemiluminescence with nitric oxide. *Atmospheric Measurement Techniques*, 7(5):1231–1244, 2014. ISSN 1867-1381.

[98] R.D. Matthews, R.F. Sawyer, and R.W. Schefer. Interferences in chemiluminescent measurement of nitric oxide and nitrogen dioxide emissions from combustion systems. *Environmental Science & Technology*, 11(12):1092–1096, 1977. ISSN 0013-936X.

[99] M. Gerboles, F. Lagler, D. Rembges, and C. Brun. Assessment of uncertainty of NO2 measurements by the chemiluminescence method and discussion of the quality objective of the NO2 European Directive. *Journal of Environmental Monitoring*, 5 (4):529–540, 2003.

[100] B.A. Ridley, F.E. Grahek, and J.G. Walega. A small high-sensitivity, medium-response ozone detector suitable for measurements from light aircraft. *Journal of Atmospheric and Oceanic Technology*, 9(2):142–148, 1992. ISSN 1520-0426.

[101] J.D. Lee, S.J. Moller, K.A. Read, A.C. Lewis, L. Mendes, and L.J. Carpenter. Year-round measurements of nitrogen oxides and ozone in the tropical North Atlantic marine boundary layer. *Journal of Geophysical Research-Atmospheres*, 114, 2009. doi: ArtnD2130210.1029/2009jd011878.

[102] J.D. Ingle and S.R. Crouch. Critical comparison of photon counting and direct current measurement techniques for quantitative spectrometric methods. *Analytical chemistry*, 44(4):785–794, 1972. ISSN 0003-2700.

[103] J.A. Williamson, M.W. Kendall-Tobias, M. Buhl, and M. Seibert. Statistical evalua-

tion of dead time effects and pulse pileup in fast photon counting. Introduction of the sequential model. *Analytical Chemistry*, 60(20):2198–2203, 1988. ISSN 0003-2700.

[104] D. Silvia and J. Skilling. *Data analysis: a Bayesian tutorial*. OUP Oxford, 2006. ISBN 0191546704.

[105] J.W. Drummond, A. Volz, and D.H. Ehhalt. An optimized chemiluminescence detector for tropospheric NO measurements. *Journal of atmospheric chemistry*, 2(3): 287–306, 1985. ISSN 0167-7764.

[106] J.D. Lee, C. Helfter, R.M. Purvis, S.D. Beevers, D.C. Carslaw, A.C. Lewis, S.J. Moller, A. Tremper, A. Vaughan, and E.G. Nemitz. Measurement of NOx Fluxes from a Tall Tower in Central London, UK and Comparison with Emissions Inventories. *Environmental Science & Technology*, 49(2):1025–1034, 2015. doi: 10.1021/es5049072.

[107] P.K. Misztal, T. Karl, R. Weber, H.H. Jonsson, A.B. Guenther, and A.H. Goldstein. Airborne flux measurements of biogenic isoprene over California. *Atmospheric Chemistry and Physics*, 14(19):10631–10647, 2014. doi: DOI10.5194/acp-14-10631-2014.

[108] G. Burba. *Eddy covariance method for scientific, industrial, agricultural and regulatory applications: A field book on measuring ecosystem gas exchange and areal emission rates*. LI-Cor Biosciences, 2013. ISBN 061576827X.

[109] O. Reynolds. On the dynamical theory of incompressible viscous fluids and the determination of the criterion. *Proceedings of the Royal Society of London*, 56(336-339):40–45, 1894. ISSN 0370-1662.

[110] F.J. Scrase. Some characteristics of eddy motion in the atmosphere, Meteor. Offc.(Brit.), Geophys. Mem. No. 52, 1930.

[111] W.C. Swinbank. The measurement of vertical transfer of heat and water vapor by eddies in the lower atmosphere. *Journal of Meteorology*, 8(3):135–145, 1951. ISSN 0095-9634.

[112] D.D. Baldocchi, B.B. Hincks, and T.P. Meyers. Measuring biosphereatmosphere exchanges of biologically related gases with micrometeorological methods. *Ecology*, 69(5):1331–1340, 1988. ISSN 1939-9170.

[113] C. Field, J.A. Berry, and H.A. Mooney. A portable system for measuring carbon dioxide and water vapour exchange of leaves. *Plant, Cell & Environment*, 5(2): 179–186, 1982. ISSN 1365-3040.

[114] M.L. Goulden and P.M. Crill. Automated measurements of CO2 exchange at the moss surface of a black spruce forest. *Tree physiology*, 17(8-9):537–542, 1997. ISSN 0829-318X.

[115] D.D. Baldocchi. Assessing the eddy covariance technique for evaluating carbon dioxide exchange rates of ecosystems: past, present and future. *Global Change Biology*, 9(4):479–492, 2003. ISSN 1365-2486.

[116] T.G. Karl, C. Spirig, J. Rinne, C. Stroud, P. Prevost, J. Greenberg, R. Fall, and A. Guenther. Virtual disjunct eddy covariance measurements of organic compound fluxes from a subalpine forest using proton transfer reaction mass spectrometry. *Atmospheric Chemistry and Physics*, 2(4):279–291, 2002. ISSN 1680-7316.

[117] B. Davison, R. Taipale, B. Langford, P. Misztal, S. Fares, G. Matteucci, F. Loreto, J.N. Cape, J. Rinne, and C.N. Hewitt. Concentrations and fluxes of biogenic volatile organic compounds above a Mediterranean macchia ecosystem in western Italy. *Biogeosciences*, 6:1655–1670, 2009. ISSN 1726-4170.

[118] C. Park, G. Schade, and I. Boedeker. VOC flux measurements using a novel relaxed eddy accumulation GC-FID system in urban Houston, Texas. *Eos Trans. AGU*, 89: 53, 2008.

[119] B. Langford, B. Davison, E. Nemitz, and C.N. Hewitt. Mixing ratios and eddy covariance flux measurements of volatile organic compounds from an urban canopy (Manchester, UK). *Atmospheric Chemistry and Physics*, 9(6):1971–1987, 2009. ISSN 1680-7316.

[120] B. Langford, E. Nemitz, E. House, G.J. Phillips, D. Famulari, B. Davison, J.R. Hopkins, A.C. Lewis, and C.N. Hewitt. Fluxes and concentrations of volatile organic compounds above central London, UK. *Atmos. Chem. Phys.*, 10(2):627–645, jan 2010. ISSN 1680-7324. doi: 10.5194/acp-10-627-2010. URL `http://www.atmos-chem-phys.net/10/627/2010/http://www.atmos-chem-phys.net/10/627/2010/acp-10-627-2010.pdf`.

[121] T. Karl, E. Apel, A. Hodzic, D.D. Riemer, D.R. Blake, and C. Wiedinmyer. Emissions of volatile organic compounds inferred from airborne flux measurements over a megacity. *Atmospheric Chemistry and Physics*, 9(1):271–285, 2009.

[122] M. Mauder, R.L. Desjardins, and I. MacPherson. Scale analysis of airborne flux measurements over heterogeneous terrain in a boreal ecosystem. *Journal of Geophysical Research: Atmospheres*, 112(D13), 2007. ISSN 2156-2202.

[123] S. Metzger, W. Junkermann, M. Mauder, K. Butterbach-Bahl, B.T.Y. Widemann, F. Neidl, K. Schafer, S. Wieneke, X.H. Zheng, H.P. Schmid, and T. Foken. Spatially explicit regionalization of airborne flux measurements using environmental response functions. *Biogeosciences*, 10(4):2193–2217, 2013. doi: DOI10.5194/bg-10-2193-2013.

[124] T. Karl, P.K. Misztal, H.H. Jonsson, S. Shertz, A.H. Goldstein, and A.B. Guenther. Airborne Flux Measurements of BVOCs above Californian Oak Forests: Experimental Investigation of Surface and Entrainment Fluxes, OH Densities, and Damkohler Numbers. *Journal of the Atmospheric Sciences*, 70(10):3277–3287, 2013. doi: Doi10.1175/Jas-D-13-054.1.

[125] G.M. Wolfe, T.F. Hanisco, H.L. Arkinson, T.P. Bui, J.D. Crounse, J. DeanDay, A. Goldstein, A. Guenther, S.R. Hall, and G. Huey. Supporting information for Quantifying sources and sinks of reactive gases in the lower atmosphere using airborne flux observations. *Geophysical Research Letters*, 42(19):8231–8240, 2015. ISSN 1944-8007.

[126] A.J. Rinehart, S.A. McKenna, and T.A. Dewers. Using Wavelet Covariance Models for Simultaneous Picking of Overlapping Pand SWave Arrival Times in Noisy SingleComponent Data. *Seismological Research Letters*, 87(4):893–900, 2016. ISSN 0895-0695.

[127] C. Torrence and G.P. Compo. A practical guide to wavelet analysis. *Bulletin of the American Meteorological Society*, 79(1):61–78, 1998. doi: Doi10.1175/1520-0477(1998)079⟨0061:Apgtwa⟩2.0.Co;2.

[128] K.M. Beswick, M.W. Gallagher, A.R. Webb, E.G. Norton, and F. Perry. Application of the Aventech AIMMS20AQ airborne probe for turbulence measurements during

the Convective Storm Initiation Project. *Atmos. Chem. Phys.*, 8(17):5449–5463, 2008. doi: 10.5194/acp-8-5449-2008. URL `http://www.atmos-chem-phys.net/8/5449/2008/`.

[129] The MathWorks Inc. Continuous 1-D wavelet transform, 2017. URL `https://uk.mathworks.com/help/wavelet/ref/cwt.html`.

[130] D. Vickers, C. Thomas, and B.E. Law. Random and systematic CO2 flux sampling errors for tower measurements over forests in the convective boundary layer. *agricultural and forest meteorology*, 149(1):73–83, 2009. ISSN 0168-1923.

[131] J. Mann and D.H. Lenschow. Errors in Airborne Flux Measurements. *Journal of Geophysical Research-Atmospheres*, 99(D7):14519–14526, 1994. doi: Doi10.1029/94jd00737.

[132] P.H. Schuepp, M.Y. Leclerc, J.I. MacPherson, and R.L. Desjardins. Footprint prediction of scalar fluxes from analytical solutions of the diffusion equation. *Boundary-Layer Meteorology*, 50(1-4):355–373, 1990. ISSN 0006-8314.

[133] M.Y. Leclerc and G.W. Thurtell. Footprint prediction of scalar fluxes using a Markovian analysis. *Boundary-Layer Meteorology*, 52(3):247–258, 1990. ISSN 0006-8314.

[134] H.P. Schmid. Source areas for scalars and scalar fluxes. *Boundary-Layer Meteorology*, 67(3):293–318, 1994. ISSN 0006-8314.

[135] M.Y. Leclerc and T. Foken. *Footprints in micrometeorology and ecology*. Springer, 2014. ISBN 3642545459.

[136] T.W. Horst and J.C. Weil. Footprint estimation for scalar flux measurements in the atmospheric surface layer. *Boundary-Layer Meteorology*, 59(3):279–296, 1992. ISSN 00068314. doi: 10.1007/BF00119817.

[137] T.W. Horst and J.C. Weil. How Far is Far Enough?: The Fetch Requirements for Micrometeorological Measurement of Surface Fluxes, 1994. ISSN 0739-0572.

[138] H.P. Schmid. Experimental design for flux measurements: matching scales of observations and fluxes. *Agricultural and Forest Meteorology*, 87(2):179–200, 1997. ISSN 0168-1923.

[139] S.K. Kaharabata, P.H. Schuepp, S. Ogunjemiyo, S. Shen, M.Y. Leclerc, R.L. Desjardins, and J.I. MacPherson. Footprint considerations in BOREAS. *Journal of Geophysical Research: Atmospheres*, 102(D24):29113–29124, 1997. ISSN 2156-2202.

[140] R. Kormann and F.X. Meixner. An analytical footprint model for non-neutral stratification. *Boundary-Layer Meteorology*, 99(2):207–224, 2001. ISSN 0006-8314.

[141] A. Neftel, C. Spirig, and C. Ammann. Application and test of a simple tool for operational footprint evaluations. *Environmental Pollution*, 152(3):644–652, 2008. ISSN 0269-7491.

[142] K.K. Sabelfeld and O.A. Kurbanmuradov. Numerical statistical model of classical incompressible isotropic turbulence. *Russian Journal of Numerical Analysis and Mathematical Modelling*, 5(3):251–263, 1990. ISSN 1569-3988.

[143] T.K. Flesch. The footprint for flux measurements, from backward Lagrangian stochastic models. In *Boundary-Layer Meteorology 25th Anniversary Volume, 19701995*, pages 399–404. Springer, 1996.

[144] K.K. Sabelfeld and O.A. Kurbanmuradov. One-particle stochastic Lagrangian model for turbulent dispersion in horizontally homogeneous turbulence. *Monte Carlo Methods and Applications*, 4:127–140, 1998. ISSN 0929-9629.

[145] N. Kljun, M.W. Rotach, and H.P. Schmid. A three-dimensional backward lagrangian footprint model for a wide range of boundary-layer stratifications. *Boundary-Layer Meteorology*, 103(2):205–226, 2002. doi: Doi10.1023/A:1014556300021.

[146] A. Sogachev, G.V. Menzhulin, M. Heimann, and J.O.N. Lloyd. A simple threedimensional canopyplanetary boundary layer simulation model for scalar concentrations and fluxes. *Tellus B*, 54(5):784–819, 2002. ISSN 1600-0889.

[147] A. Sogachev, M.Y. Leclerc, A. Karipot, G. Zhang, and T. Vesala. Effect of clearcuts on footprints and flux measurements above a forest canopy. *Agricultural and forest meteorology*, 133(1):182–196, 2005. ISSN 0168-1923.

[148] T.V. Prabha, M.Y. Leclerc, and D. Baldocchi. Comparison of in-canopy flux footprints between large-eddy simulation and the Lagrangian simulation. *Journal of Applied Meteorology and Climatology*, 47(8):2115–2128, 2008. ISSN 1558-8432.

[149] X. Cai and M.Y. Leclerc. Forward-in-time and backward-in-time dispersion in the convective boundary layer: the concentration footprint. *Boundary-layer meteorology*, 123(2):201–218, 2007. ISSN 0006-8314.

[150] S. Metzger, W. Junkermann, M. Mauder, F. Beyrich, K. Butterbach-Bahl, H.P. Schmid, and T. Foken. Eddy-covariance flux measurements with a weight-shift microlight aircraft. *Atmospheric Measurement Techniques*, 5(7):1699–1717, 2012. doi: 10.5194/amt-5-1699-2012.

[151] N. Kljun, P. Calanca, M.W. Rotach, and H.P. Schmid. A simple parameterisation for flux footprint predictions. *Boundary-Layer Meteorology*, 112(3):503–523, 2004. doi: Doi10.1023/B:Boun.0000030653.71031.96.

[152] L.H. Kantha and C.A. Clayson. *Small scale processes in geophysical fluid flows*, volume 67. Academic press, 2000. ISBN 0080517293.

[153] A. Graf, A. van de Boer, A. Moene, and H. Vereecken. Intercomparison of Methods for the Simultaneous Estimation of Zero-Plane Displacement and Aerodynamic Roughness Length from Single-Level Eddy-Covariance Data. *Boundary-Layer Meteorology*, 151(2):373–387, 2014. doi: 10.1007/s10546-013-9905-z.

[154] D.R. Drew, J.F. Barlow, and S.E. Lane. Observations of wind speed profiles over Greater London, UK, using a Doppler lidar. *Journal of Wind Engineering and Industrial Aerodynamics*, 121:98–105, 2013. doi: 10.1016/j.jweia.2013.07.019.

[155] B.D. Amiro. Comparison of turbulence statistics within three boreal forest canopies. *Boundary-Layer Meteorology*, 51(1-2):99–121, 1990. ISSN 0006-8314.

[156] T. Foken and C.J. Nappo. *Micrometeorology*. Springer Berlin Heidelberg, 2008. ISBN 9783540746652. URL `https://books.google.com.au/books?id=CFzDNAEACAAJ`.

[157] M. Aubinet, T. Vesala, and D. Papale. *Eddy covariance: a practical guide to measurement and data analysis*. Springer Science & Business Media, 2012. ISBN 9400723504.

[158] V. Strand, M. Svartengren, S. Rak, C. Barck, and G. Bylin. Repeated exposure to an ambient level of NO2 enhances asthmatic response to a nonsymptomatic allergen dose. *European Respiratory Journal*, 12(1):6–12, 1998. doi: 10.1183/09031936.98.12010006.

[159] R.W. Atkinson, I.M. Carey, A.J. Kent, T.P. van Staa, H.R. Anderson, and D.G. Cook. Long-Term Exposure to Outdoor Air Pollution and Incidence of Cardiovascular Diseases. *Epidemiology*, 24(1):44–53, 2013. doi: 10.1097/EDE.0b013e318276ccb8.

[160] World Health Organization. Review of evidence on health aspects of air pollution REVIHAAP project: final technical report. Technical report, 2013.

[161] World Health Organization. Health risks of air pollution in Europe HRAPIE project. Recommendations for concentrationresponse functions for costbenefit analysis of particulate matter, ozone and nitrogen dioxide. Technical report, 2014.

[162] S. Sillman. The relation between ozone, NOx and hydrocarbons in urban and polluted rural environments. *Atmospheric Environment*, 33(12):1821–1845, 1999. doi: 10.1016/s1352-2310(98)00345-8.

[163] M. Weiss, P. Bonnel, R. Hummel, A. Provenza, and U. Manfredi. On-Road Emissions of Light-Duty Vehicles in Europe. *Environmental Science & Technology*, 45(19): 8575–8581, 2011. doi: 10.1021/es2008424.

[164] E.A. Mazzi and H. Dowlatabadi. Air quality impacts of climate mitigation: UK policy and passenger vehicle choice. *Environmental Science & Technology*, 41(2): 387–392, 2007. doi: 10.1021/es060517w.

[165] T. Bush, I. Tsagatakis, K. King, and N. Passant. NAEI UK emission mapping methodology 2006. Technical report, 2008.

[166] J. Brioude, S.W. Kim, W.M. Angevine, G.J. Frost, S.H. Lee, S.A. McKeen, M. Trainer, F.C. Fehsenfeld, J.S. Holloway, T.B. Ryerson, E.J. Williams, G. Petron, and J.D. Fast. Top-down estimate of anthropogenic emission inventories and their interannual variability in Houston using a mesoscale inverse modeling technique. *Journal of Geophysical Research-Atmospheres*, 116:19, 2011. doi: 10.1029/2011jd016215.

[167] Greater London Authority. London Datastore. URL `http://data.london.gov.uk/`.

[168] M.D. Shaw, J.D. Lee, B. Davison, A. Vaughan, R.M. Purvis, A. Harvey, A.C. Lewis, and C.N. Hewitt. Airborne determination of the temporo-spatial distribution of benzene, toluene, nitrogen oxides and ozone in the boundary layer across Greater

London, UK. *Atmospheric Chemistry and Physics*, 15(9):5083–5097, 2015. doi: 10.5194/acp-15-5083-2015.

[169] Natural Environment Research Council. The Dornier 228: G-ENVR. URL `http://arsf.nerc.ac.uk/aircraft/`.

[170] C. Thomas and T. Foken. Flux contribution of coherent structures and its implications for the exchange of energy and matter in a tall spruce canopy. *Boundary-Layer Meteorology*, 123(2):317–337, 2007. doi: 10.1007/s10546-006-9144-7.

[171] B. Yuan, L. Kaser, T. Karl, M. Graus, J. Peischl, T.L. Campos, S. Shertz, E.C. Apel, R.S. Hornbrook, A. Hills, J.B. Gilman, B.M. Lerner, C. Warneke, F.M. Flocke, T.B. Ryerson, A.B. Guenther, and J.A. de Gouw. Airborne flux measurements of methane and volatile organic compounds over the Haynesville and Marcellus shale gas production regions. *Journal of Geophysical Research-Atmospheres*, 120(12):6271–6289, 2015. doi: 10.1002/2015jd023242.

[172] A. Held. Spectral Analysis of Turbulent Aerosol Fluxes by Fourier Transform, Wavelet Analysis, and Multiresolution Decomposition. *Boundary-Layer Meteorology*, 151(1):79–94, 2014. doi: 10.1007/s10546-013-9889-8.

[173] H.P. Schmid. Footprint modeling for vegetation atmosphere exchange studies: a review and perspective. *Agricultural and Forest Meteorology*, 113(1):159–183, 2002. ISSN 0168-1923.

[174] T. Vesala, Ü. Rannik, M. Leclerc, T. Foken, and K. Sabelfeld. Flux and concentration footprints. *Agricultural and Forest Meteorology*, 127(3):111–116, 2004. ISSN 0168-1923.

[175] T. Vesala, N. Kljun, Ü. Rannik, J. Rinne, A. Sogachev, T. Markkanen, K. Sabelfeld, T. Foken, and M.Y. Leclerc. Flux and concentration footprint modelling: State of the art. *Environmental Pollution*, 152(3):653–666, 2008. ISSN 0269-7491.

[176] D.C. Carslaw and S.D. Beevers. Investigating the potential importance of primary NO2 emissions in a street canyon. *Atmospheric Environment*, 38(22):3585–3594, 2004. ISSN 1352-2310.

[177] DEFRA and DECC. NAEI data. URL `http://naei.defra.gov.uk/`.

[178] EEA. EMEP/EEA air pollutant emission inventory guidebook 2013. *European Environment Agency, Copenhagen*, 2013.

[179] D.P. Billesbach. Estimating uncertainties in individual eddy covariance flux measurements: a comparison of methods and a proposed new method. *Agricultural and Forest Meteorology*, 151(3):394–405, 2011. ISSN 0168-1923.

[180] T. Karl, A. Guenther, A. Turnipseed, G. Tyndall, P. Artaxo, and S. Martin. Rapid formation of isoprene photo-oxidation products observed in Amazonia. *Atmos. Chem. Phys.*, 9(20):7753–7767, oct 2009. ISSN 1680-7324. doi: 10.5194/acp-9-7753-2009. URL `http://www.atmos-chem-phys.net/9/7753/2009/http://www.atmos-chem-phys.net/9/7753/2009/acp-9-7753-2009.pdf`.

[181] A.B. Bjorkegren, C.S.B. Grimmond, S. Kotthaus, and B.D. Malamud. CO2 emission estimation in the urban environment: measurement of the CO2 storage term. *Atmospheric Environment*, 2015.

[182] A.R. Desai, K. Xu, H. Tian, P. Weishampel, J. Thom, D. Baumann, A.E. Andrews, B.D. Cook, J.Y. King, and R Kolka. Landscape-level terrestrial methane flux observed from a very tall tower. *Agricultural and Forest Meteorology*, 201:61–75, 2015. ISSN 0168-1923.

[183] D.H. Lenschow and E.G. Patton. Modeling the diurnal cycle of conserved and reactive species in the convective boundary layer using SOMCRUS. *Geoscientific Model Development*, 9(3):979, 2016. ISSN 1991-9603.

[184] D.C. Carslaw and G. Rhys-Tyler. New insights from comprehensive on-road measurements of NOx, NO2 and NH3 from vehicle emission remote sensing in London, UK. *Atmospheric Environment*, 81:339–347, 2013. doi: 10.1016/j.atmosenv.2013.09.026.

[185] A.L. Robinson, N.M. Donahue, M.K. Shrivastava, E.A. Weitkamp, A.M. Sage, A.P. Grieshop, T.E. Lane, J.R. Pierce, and S.N. Pandis. Rethinking organic aerosols: Semivolatile emissions and photochemical aging. *Science*, 315(5816):1259–1262, 2007. ISSN 0036-8075.

[186] A. Kansal. Sources and reactivity of NMHCs and VOCs in the atmosphere: A review. *Journal of Hazardous Materials*, 166(1):17–26, 2009. ISSN 0304-3894.

[187] K. Na, Y-P. Kim, I. Moon, and K-C. Moon. Chemical composition of major VOC emission sources in the Seoul atmosphere. *Chemosphere*, 55(4):585–594, 2004. ISSN 0045-6535.

[188] A. Srivastava, A.E. Joseph, A. More, and S. Patil. Emissions of VOCs at urban petrol retail distribution centres in India (Delhi and Mumbai). *Environmental Monitoring and Assessment*, 109(1-3):227–242, 2005. ISSN 0167-6369.

[189] K. Na, K. Moon, and Y. Kim. Source contribution to aromatic VOC concentration and ozone formation potential in the atmosphere of Seoul. *Atmospheric environment*, 39(30):5517–5524, 2005. ISSN 1352-2310.

[190] J.I. Rubin, A.J. Kean, R.A. Harley, D.B. Millet, and A.H. Goldstein. Temperature dependence of volatile organic compound evaporative emissions from motor vehicles. *Journal of Geophysical Research: Atmospheres*, 111(D3), 2006. ISSN 2156-2202.

[191] A. Guenther, C.N. Hewitt, D. Erickson, R. Fall, C. Geron, T. Graedel, P. Harley, L. Klinger, M. Lerdau, and W.A. McKay. A global model of natural volatile organic compound emissions. *Journal of Geophysical Research: Atmospheres*, 100(D5):8873–8892, 1995. ISSN 2156-2202.

[192] C. Thomas and T. Foken. Detection of long-term coherent exchange over spruce forest using wavelet analysis. *Theoretical and Applied Climatology*, 80(2):91–104, 2005. ISSN 0177-798X.

[193] A.R. Vaughan, J.D. Lee, P.K. Misztal, S. Metzger, M.D. Shaw, A.C. Lewis, R.M. Purvis, D.C. Carslaw, A.H. Goldstein, and C.N. Hewitt. Spatially resolved flux measurements of NOx from London suggest significantly higher emissions than predicted by inventories. *Faraday discussions*, 189:455–472, 2016. ISSN 1364-5498.

[194] J. de Gouw and C. Warneke. Measurements of volatile organic compounds in the earth's atmosphere using protontransferreaction mass spectrometry. *Mass Spectrometry Reviews*, 26(2):223–257, 2007. ISSN 1098-2787.

[195] C.N. Hewitt, S. Hayward, and A. Tani. The application of proton transfer reaction-mass spectrometry (PTR-MS) to the monitoring and analysis of volatile organic compounds in the atmosphere. *Journal of Environmental Monitoring*, 5(1):1–7, 2003.

[196] W. Lindinger and A. Hansel. Analysis of trace gases at ppb levels by proton transfer reaction mass spectrometry (PTR-MS). *Plasma Sources Science and Technology*, 6 (2):111, 1997. ISSN 0963-0252.

[197] O. Amador-Muñoz, P.K. Misztal, R. Weber, D.R. Worton, H. Zhang, G. Drozd, and A.H. Goldstein. Sensitive detection of n-alkanes using a mixed ionization mode proton-transfer-reaction mass spectrometer. *Atmospheric Measurement Techniques*, 9(11):5315–5329, 2016. ISSN 1867-1381.

[198] T.M. Rogers, E.P. Grimsrud, S.C. Herndon, J.T. Jayne, C.E. Kolb, E. Allwine, H. Westberg, B.K. Lamb, M. Zavala, and L.T. Molina. On-road measurements of volatile organic compounds in the Mexico City metropolitan area using proton transfer reaction mass spectrometry. *International Journal of Mass Spectrometry*, 252(1):26–37, 2006. ISSN 1387-3806.

[199] J.J. Schauer, M.J. Kleeman, G.R. Cass, and B.R.T. Simoneit. Measurement of emissions from air pollution sources. 2. C1 through C30 organic compounds from medium duty diesel trucks. *Environmental Science & Technology*, 33(10):1578–1587, 1999. ISSN 0013-936X.

[200] R. Taipale, T.M. Ruuskanen, J. Rinne, M.K. Kajos, H. Hakola, T. Pohja, and M. Kulmala. Technical Note: Quantitative long-term measurements of VOC concentrations by PTR-MSmeasurement, calibration, and volume mixing ratio calculation methods. *Atmospheric Chemistry and Physics*, 8(22):6681–6698, 2008. ISSN 1680-7316.

[201] J. de Gouw, C. Warneke, R. Holzinger, T. Klüpfel, and J. Williams. Inter-comparison between airborne measurements of methanol, acetonitrile and acetone using two differently configured PTR-MS instruments. *International Journal of Mass Spectrometry*, 239(2):129–137, 2004. ISSN 1387-3806.

[202] M.E. Jenkin, J.C. Young, and A.R. Rickard. The MCM v3. 3.1 degradation scheme for isoprene. *Atmos. Chem. Phys*, 15(20):11433–11459, 2015.

[203] J.A. Businger, J.C. Wyngaard, Y. Izumi, and E.F. Bradley. Flux-profile relationships in the atmospheric surface layer. *Journal of the atmospheric Sciences*, 28(2):181–189, 1971. ISSN 1520-0469.

[204] T. Foken. 50 years of the MoninObukhov similarity theory. *Boundary-Layer Meteorology*, 119(3):431–447, 2006. ISSN 0006-8314.

[205] N.R. Passant. Speciation of UK emissions of non-methane volatile organic compounds. *AEA Technology Report ENV-0545, Culham, Abingdon, United Kingdom*, 2002.

[206] M. Vieno, A.J. Dore, D.S. Stevenson, R. Doherty, M.R. Heal, S. Reis, S. Hallsworth, L. Tarrason, P. Wind, D. Fowler, D. Simpson, and M.A. Sutton. Modelling surface ozone during the 2003 heat-wave in the UK. *Atmos. Chem. Phys.*, 10(16):7963–7978, aug 2010. ISSN 1680-7324. doi: 10.5194/acp-10-7963-2010. URL `http://www.atmos-chem-phys.net/10/7963/2010/http://www.atmos-chem-phys.net/10/7963/2010/acp-10-7963-2010.pdf`.

[207] M. Vieno, M.R. Heal, S. Hallsworth, D. Famulari, R.M. Doherty, A.J. Dore, Y.S. Tang, C.F. Braban, D. Leaver, M.A. Sutton, and S. Reis. The role of long-range transport and domestic emissions in determining atmospheric secondary inorganic particle concentrations across the UK. *Atmos. Chem. Phys.*, 14(16):8435–8447, aug 2014. ISSN 1680-7324. doi: 10.5194/acp-14-8435-2014. URL `http://www.atmos-chem-phys.net/14/8435/2014/http://www.atmos-chem-phys.net/14/8435/2014/acp-14-8435-2014.pdf`.

[208] M. Vieno, M.R. Heal, M.L. Williams, E.J. Carnell, E. Nemitz, J.R. Stedman, and S. Reis. The sensitivities of emissions reductions for the mitigation of UK PM2.5. *Atmos. Chem. Phys.*, 16(1):265–276, jan 2016. ISSN 1680-7324. doi: 10.5194/acp-16-265-2016. URL `http://www.atmos-chem-phys.net/16/265/2016/http://www.atmos-chem-phys.net/16/265/2016/acp-16-265-2016.pdf`.

[209] M. Vieno, M.R. Heal, M.M. Twigg, I.A. MacKenzie, C.F. Braban, J.J.N. Lingard, S. Ritchie, R.C. Beck, A. Móring, R. Ots, C.F. Di Marco, E. Nemitz, M.A. Sutton, and S. Reis. The UK particulate matter air pollution episode of March-April 2014: More than Saharan dust. *Environmental Research Letters*, 11(4), 2016. ISSN 17489326 17489318. doi: 10.1088/1748-9326/11/4/044004.

[210] D. Simpson, A. Benedictow, H. Berge, R. Bergström, L.D. Emberson, H. Fagerli, C.R. Flechard, G.D. Hayman, M. Gauss, J.E. Jonson, M.E. Jenkin, A. Nyíri, C. Richter, V.S. Semeena, S. Tsyro, J-P. Tuovinen, Á. Valdebenito, and P. Wind.

The EMEP MSC-W chemical transport model technical description. *Atmos. Chem. Phys.*, 12(16):7825–7865, aug 2012. ISSN 1680-7324. doi: 10.5194/acp-12-7825-2012. URL http://www.atmos-chem-phys.net/12/7825/2012/http://www.atmos-chem-phys.net/12/7825/2012/acp-12-7825-2012.pdf.

[211] N.V. Heeb, A. Forss, C. Bach, S. Reimann, A. Herzog, and H.W. Jäckle. A comparison of benzene, toluene and C 2-benzenes mixing ratios in automotive exhaust and in the suburban atmosphere during the introduction of catalytic converter technology to the Swiss Car Fleet. *Atmospheric Environment*, 34(19):3103–3116, 2000. ISSN 1352-2310.

[212] I.R. Kaplan, Y. Galperin, H. Alimi, R. Lee, and S. Lu. Patterns of chemical changes during environmental alteration of hydrocarbon fuels. *Groundwater Monitoring & Remediation*, 16(4):113–124, 1996. ISSN 1745-6592.

[213] W. Xiong, R. Bernesky, R. Bechard, G. Michaud, and J. Lang. A tiered approach to distinguish sources of gasoline and diesel spills. *Science of the Total Environment*, 487:452–462, 2014. ISSN 0048-9697.

[214] Environment Agency. Motor fuel components: environmental occurrence and potential future risks, Science Summary SC040087/SS. Technical report, 2008.

[215] R. Bailey, R. Claxton, L. Jones, E. Kilroy, T. Misselbrook, Y. Pang, N. Passant, E. Salisbury, H. Smith, G. Thistlethwaite, D. Wakeling, and C. Walker. Air Quality Pollutant Inventories for England, Scotland, Wales and Northern Ireland: 1990 - 2014. Technical report, 2016.

[216] D.H. Lenschow, J. Mann, and L. Kristensen. How long is long enough when measuring fluxes and other turbulence statistics? *Journal of Atmospheric and Oceanic Technology*, 11(3):661–673, 1994. ISSN 1520-0426.

[217] C.C. Guenther. Estimates of global terrestrial isoprene emissions using MEGAN (Model of Emissions of Gases and Aerosols from Nature). *Atmospheric Chemistry and Physics*, 6, 2006. ISSN 1680-7316.

[218] A. Arneth, G. Schurgers, J. Lathiere, T. Duhl, D.J. Beerling, C.N. Hewitt, M. Martin, and A. Guenther. Global terrestrial isoprene emission models: sensitivity to

variability in climate and vegetation. *Atmospheric Chemistry and Physics*, 11(15): 8037–8052, 2011. ISSN 1680-7316.

[219] P.K. Misztal, J.C. Avise, H.H. Jonsson, A.B. Guenther, and A.H. Goldstein. Evaluation of regional isoprene emission factors and modeled fluxes in California. *Atmospheric Chemistry and Physics*, 16(15):9611, 2016. ISSN 1680-7324.